RADICAL AND NON-RADICAL CARBAZOLE DERIVATIVES FOR MOLECULAR ELECTRONICS.

MOLECULAR GLASSES AND LIQUID CRYSTALS.

Memòria per a aspirar al grau de Doctora en Química, dins el programa de doctorat de Química Orgànica (bienni 2005-2007)

Sonia Castellanos Ortega

Dirigida i revisada per:

Dra. Dolores Velasco Castrillo Dr. Lluis Julià Bargés

Barcelona, març de 2010.

¿Es inocente el hombre cuando no sabe?
¿Un idiota que ocupa el trono está libre de
toda culpa sólo por ser idiota?

(Milan Kundera)

A mis padres.

Agraïments

Agradecimientos

Aknowledgments

Han sido muchas las personas que, dentro y fuera del laboratorio, han contribuido durante estos últimos cuatro años en la realización de esta tesis. No quisiera que su ayuda pasara desapercibida porque ha sido, sin duda, imprescindible para llegar hasta aquí.

Per començar, voldria agrair-li a la Dra. Dolores Velasco i al Dr. Lluis Julià que m'oferissin la possibilitat de realitzar aquesta tesi doctoral sota la seva direcció. Gràcies per la confiança depositada en mi i per haver-me instruït durant aquests anys. Ha sigut una gran experiència a nivell personal i professional.

Quisiera también agradecerle al Dr. Francisco López-Calahorra que me animara a comenzar el doctorado (y llegar hasta el final). Gracias por haberme atendido siempre que lo he necesitado.

Al Dr. Joaquim Puigdollers per donar-me l'oportunitat de fer una col·laboració que m'ha obert una porta al món de l'electrònica molecular i ha despertat un gran interés científic en mi. I sobretot, pel seu bon humor i la seva paciència i ajuda en tot moment. Gràcies també al Dr. Cristòbal Voz, per la seva amabilitat i per ajudar-me tantes vegades amb les mesures dels dispositius. A Mónica Della-Pirriera, por dedicarme tanto tiempo con las células solares y a Stephanie Cheylan por las medidas

realizadas con los OLEDs. Muchas gracias a las dos por su simpatía. Volia agair-li també a l'Albert Marsal la seva ajuda amb els OTFTs.

I want to thank Prof. Grazulevizius to give me the opportunity of doing an internship in Lithuania. Thanks to Prof. Gaidelis for his supervision during my stay in the Solid State Electronics Department at Vilnius University, and to Vida for teaching me how to prepare the samples. Muchas gracias to Dr. Jankauskas for all the measurements and for attending so patiently and kindly all my requests. I also would like to thank all people that made my stay in Vilnius so nice, specially to Prof. Gytis Juska for introducing me in the world of the orientiring sport and for showing me so many nice places of Lithuania and of course to his son Giedrius Juska, for his help in the lab, his friendship and for inviting me to that great trip riding the bikes. Labai ačiu!

Thanks a lot to Prof. Getautis, for allowing me to work in his group at the Kaunas University of Technology and making me feel like at home. Thanks to all the people working in the lab there, Daiva, Simona, Jolanta, Giedre, Dainius and specially to Dr. Tadas Malinauskas for his help during and after the internship, not only from a scientific point of view but from a personal point of view.

Thank you very much to Dr. Laquai for giving me the opportunity of doing an internship in his group in the Max Plank Institute for Polymer Research and for all his help during and after the stay. Thanks to all members of the group, for their sympathy and all the fun I had there, to Alfons, Valentin, Michael and specially to Hun (der TOF-König) and Ralph, who patiently taught me how to use the TOF equipment. Moltes gràcies als dos valencians que em vaig trobar per allà, al Rafa i a la Mònica, y al mejicano y al argentino, Carlos y Pablo, respectivamente, por vuestro apoyo y por tantos ratos divertidos.

Gracias a todo el equipo técnico que ha realizado paciente y eficientemente todos los experimentos que fui necesitando. Al Xavi Alcobé, pel registre del raigs X, per estar sempre disposat a ajudar-me a millorar els resultats; a la Irene Fernández, pels seus consells i esforços per trobar els pics de masses dels meus compostos més rebels; a Venci Díez, por su amabilidad, por enseñarme a usar el equipo de IR y por el tiempo que ha dedicado a realizar los experimentos de EPR; a la Núria Clos pels esforços i el temps dedicat a l'estudi del magnetisme dels meus compostos. Quiero agradecer especialmente a Amelia López su trabajo en la realización de análisis térmicos y sobretodo su simpatía y el cariño que siempre me ha mostrado. I que el Dr. Josep Carilla no se senti gelòs perquè a ell també li agraeixo molt la seva ajuda i la seva simpatia.

Gràcies al Dr. Brillas per l'enregistrament de les voltamperometries cícliques dels radicals preparats durant aquesta tesis i a la Dra. Vallés per la seva paciència i el seu temps ensenyant-me a fer servir

l'equip de voltamperometria. Gracias a José Vidal del ICMAB por el registro de EPR de uno de los compouestos estrella de esta tesis.

A todos los que habéis conseguido crear un ambiente de trabajo tan agradable y divertido. ¡Y soys unos cuantos! A ver si no me dejo a nadie.

Al personal del departament, l'Ignasi, el Vicente, la Cristina, la Maria Pilar i a la gent de Secretaria, la Montse, la Maria Pía, la Conchita i la Maria Rosa. Als companys del grup de la UB, el Juan Fco. Chesa, la Sonia Latorre, el Raoul Kessels, el Toni Segade, que m'ha ajudat molt amb els cristalls líquids i el Marc Puigmartí . Vull agrair especialment als que heu treballat amb mi al laboratori: a la Maria Antonia Torroella, que em va ajudar amb la síntesi durant les seves pràctiques, a la Sandra Piñol, pels seus ànims tant a dins com a fora del laboratori i sobretot al Jaume García. A ti te agradezco en castellano, que no me quieres hablar en catalán. Gracias por tu ayuda a lo largo de toda la tesis, por tu paciencia, por haber dicho 18 y por todas las carcajadas, que no han faltado. A la Mireia Díaz, moltes gràcies per tots els dinars i altres activitats "extraescolars". Per escoltar sempre tan atentament. A Javi Abelairas, por los buenos ratos en el comedor y por todos los chupa-chups.

A tots el companys del CSIC. M'ho he passat molt i molt bé amb vosaltres! Heu aconseguit que els dies dolents deixessin de ser-ho amb la vostra companyia, sobretot durant aquesta etapa d'escriptura que m'ha resultat tan difícil. Sense que l'ordre vulgui dir res, al Jordi Calveras, al Jose Castillo, al Xavi Garrabou, a l'Ana Carreras, al Marc López, a Mariana Gutiérrez, al Bruno Almeida, a l'Aristotelis Kotronoulas, a Esther Galán, con su alegría y sus recibimientos que suben la moral, al Jordi Peracaula, a la Sara Barrachina, a Marisa Mateos, a Jara Pérez, al Carles Lozano, que sempre escolten els meus rotllos. Quiero agradecer especialmente a Alda Lisa y a Livia Gómez las escapadas por los rincones míticos de Barcelona y tantas conversaciones divertidas e interesantes. A la Sonia Touriño li agraeixo el seu bon humor, i la seva energia que s'encomana; la seva persona i la seva visió de les coses han estat uns referents per mi.

Als que m'heu recolzat fora del laboratori, en especial, al Guillem Rocasalbas, per tots aquests vespres tan divertits compartint el pis; per les converses, les pelis, la música, els sopars, les birres belgues... Tot en el moment que més ho necessitava. A Daniel Jacoby, por ser mi motivación y mi apoyo durante la mayor parte de esta tesis. Por aportarme tanto a nivel personal y a nivel profesional. Al Roger Bartra, per la seva paciència i per tots els moments tan constructius i divertits que hem compartit (no poso més, que no vull ser cursi). Al Ramon Pujol, per tots aquests capítols de sèrie de televisió no emesos (no com els teus programes a El Gran Dictat). A mi hermano por todo el apoyo técnico (pon un informático en tu vida). A l'Edgar González per donar-me un cop de mà sempre que li he demanat. A l'Albert Casán, alias el físico-músico, per omplir de música, literal i

figuradament, aquestes últimes setmanes. A Dani y a Lydia, que siempre han estado ahí, sin importar cuánto tiempo pasara. Y, sobretodo, a Míriam Arnaiz, que siempre está a mi lado, llenando mi vida de situaciones surrealistas y que ha sido un apoyo incondicional. Gracias por su amistad y por su frase célebre que se convirtió en un referente: “Los días caca también pasan”.

Y, por último, muchísimas gracias a mis padres. Porque siempre he podido contar con ellos, me han apoyado en los peores momentos y han celebrado todos mis éxitos.

Prólogo

En julio de 2009 tuve la oportunidad de visitar la Shirn Kunsthalle de Frankfurt, donde se mostraba la instalación de Aleksandra Mir, *Triumph*. Consistía en exponer más de 2.500 trofeos procedentes de Sicilia en una habitación. Los trofeos eran de cualquier campo imaginable y se repartían y amontonaban por toda la sala. Ahora miro esta tesis ya escrita y me siento como si levantara mi trofeo en medio de esa sala. Y es que, según el Instituto Estadístico de Catalunya, durante el curso 2007/08 se defendieron solo en Catalunya 1434 tesis doctorales. ¿Cuántas se defenderán cada año en todo el mundo? ¿Cuántas se habrán defendido en todo el mundo hasta hoy?

Pienso en cómo la Química nació de la curiosidad de unos pocos por entender el mundo, cuando aún no se llamaba química y era parte de un todo que se hacía llamar Ciencia. Pienso también en cómo a mediados del siglo XIX el famoso Kekulé y su amigo Karl Weltzien organizaron el primer congreso de químicos en Karlsruhe (Alemania) para tratar de resolver entre los químicos de todos los países los problemas que existían entonces respecto a la determinación de pesos atómicos y moleculares. Se reunieron para ponerse de acuerdo, para trabajar juntos. Una idea casi romántica.

No creo que los científicos fueran más nobles entonces que ahora. De hecho casi no se sacó nada en claro de aquel encuentro. Además, a mí nunca me ha gustado esa actitud de "en el pasado todo era mejor". Sin embargo, "quedan lejos los tiempos en los que un hombre podía saber cómo funcionaba todo a su alrededor".[1] La ciencia se ha ramificado y especializado tanto y la competitividad es tan fuerte que a veces siento que nos dedicamos a hacer como el hombre de aquel anuncio que salía en

[1] *La immortalidad*. Milan Kundera

televisión que quería ser el primero en llegar en coche al polo norte con su vestido de comunión, escuchando a Georgie Dann... ¡con Georgie Dann! Y cuando llega se encuentra a otros diez coches conducidos por otros diez hombres con su vestido de comunión, escuchando a Georgie Dann... ¡con Georgie Dann! (Pero no se rindió.)

"¿Es eso malo? Supongo que no hay una respuesta correcta".[2] Si el criterio para evaluar la importancia de la investigación científica es si tiene aplicación directa o no, muchas de las cosas que se investigan se pueden considerar totalmente irrelevantes. Personalmente prefiero pensar que la investigación es en parte como el arte: aunque no tenga una utilidad (ahora), marca una tendencia, indica la dirección en la que nos movemos y solo vemos sus efectos a largo plazo. Y que esta tesis es un trofeo más en medio de la sala.

[2] *Retorno de las estrellas*. Stanislaw Lem.

Index

Introduction

Most probably when Antonio Santi Giuseppe Meucci built the first telephone around 1854 he never imagined that flexible mobile phones, which could be worn as bracelets and would get the energy to work from sunlight, such as the Nokia Morph phone, would ever be designed. Neither could Johannes Gutenberg, the "inventor" of the printing press, think that someday people would read e-papers, that is, flexible displays, instead of paper books. No need to say that the revolution of the new technologies has a lot to acknowledge to the computer science revolution. But none of these gadgets that seemed impossible 50 years ago could now exist without the development of molecular electronics.

Molecular electronics is a relatively new and emerging technology, relating to the exploitation of organic and biological materials in electronic and opto-electronic devices. Two broad areas are involved in this field: molecular materials for electronics and molecular-scale electronics. The first area concerns the development of electronic and opto-electronic devices that utilize the unique macroscopic properties of organic compounds. The second area focuses on the use of single molecules or groups of molecules as components in electronic devices. The title of this thesis refers to the preparation of organic systems for their application in electronic devices and thus we will focus in the first area of molecular electronics.

Both small organic molecules and polymers have been used as molecular materials for electronics, that is, for the fabrication of electronic devices such as organic thin film transistors (OTFTs), organic photovoltaics (OPVs) and organic light emitting diodes (OLEDs), whose structures and operation

mechanisms will be explained in section 3.1. According to their organization states, molecular materials are classified into crystals -and polycrystals-, liquid crystals and amorphous glasses.

Since device performance is highly dependent on materials morphology as a result of the different charge transport mechanisms for the different kind of molecular arrangements, control over materials morphology is of crucial importance in materials science and for practical applications. Charge carrier transport as well as charge carrier generation (injection) play a main role in the operation of all these devices and thus the organic materials for electronics are often called organic semiconductors. Depending upon the kind of charge carriers transported, molecular materials are classified into hole- and electron-transporting materials, also referred to as p-type semiconductors and n-type semiconductors, respectively.

A. Charge carrier transport

The concept of mobility of a charge carrier is an important one in semiconductor device physics. It is a measure of how quickly the carriers (holes or electrons) will respond to an applied electric field. Carrier mobility is defined as

$$\mu = \frac{\vartheta}{E} \tag{1}$$

where υ is the average drift velocity of the carrier, that is, the common velocity at which the carriers, following random trajectories, move in the direction of the applied electric field, *E*. The mobility of electrons is related to the conductivity σ by the equation

$$\sigma = ne\mu \tag{2}$$

where *n* is the number of electrons per unit volume taking part in the conduction and *e* the charge of a single electron.

The charge carrier mobilities of organic materials greatly vary depending on the kind of charge carriers, whether they are holes or electrons, molecular structures, and materials morphologies. Different transport mechanisms are operative depending on the aggregation states of materials, for example, crystalline and amorphous states.

The charge carrier drift mobility has been determined by several methods but the time-of-flight (TOF) technique and the analysis of the performance of OTFTs have been most widely employed for this task. Each method will be discussed in detail in sections 2.1 and 3.1, respectively.

The band model

A useful model for the propagation of electron waves in a crystal was first formulated by Kronig and Penney in 1930. This model predicts that the motion of electrons in a periodic lattice is characterized by bands of allowed energies separated by forbidden regions or *band gaps*. These bands result from the splitting of the energy levels of an isolated atom into N energy levels close to each other, due to the potential lattice that is generated by the N atoms present in the crystalline arrangement.

The last (highest-energy) band that is completely filled is called the *valence* band, while any partly filled or empty bands above it are called the *conduction* bands. The *Fermi energy* represents the demarcation between filled and empty states at absolute zero. The key property that determines whether a material is an insulator, a conductor or a semiconductor is the location of the Fermi energy relative to the valence and conduction bands, and the size of the energy gap between these two bands.

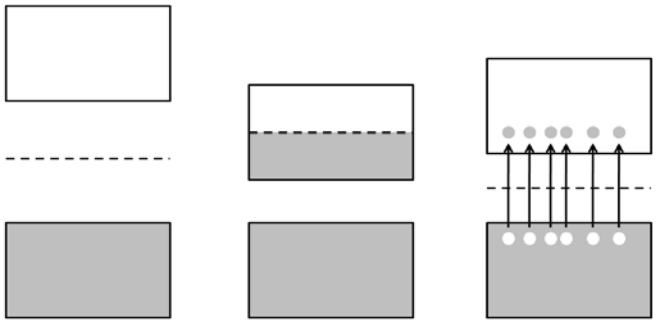

Figure 1. Energy band diagrams for an insulator (left), a conductor (middle) and a semiconductor (right). White areas represent empty band levels, grey areas full band levels and dashed lines the Fermi levels. Arrows in the semiconductor diagram indicate the "jump" of some electrons (grey circles) to the conduction band.

In the case of insulators (Figure 1 left) there is a large energy gap between the valence and conduction bands and the Fermi energy lies between the two bands. This means that the valence band is completely full and the conduction band is completely empty. Since there is a large energy gap between the valence and conduction bands, an electron would need a lot of energy to make a "jump" from the valence to the conduction band, an energy that is not available unless the applied

voltage is extremely high. Hence the electrons cannot move in response to an applied voltage, that is, no current flows within the material.

In the case of conductors (Figure 1 middle) the Fermi energy lies within the conduction band. As a result, the conduction band is partially full, while the valence band is completely full. When a voltage is applied across a sample of the material, electrons in the conduction band can easily jump to a free energy level only slightly higher than their own energy level and drift in the direction of the electric field.

Semiconductors are similar to insulators in the sense that the Fermi energy lies between the valence and conduction bands, with the result that the valence band is completely full and the conduction band is completely empty. However, they differ from insulators in that the energy gap between the valence and conduction bands is rather small, so that at room temperature some electrons near the top of the valence band can acquire enough energy from thermal fluctuations that they can be promoted to the conduction band, leaving behind a number of vacancies (holes) (Figure 1 right). The consequence is that, if a voltage is applied across a sample of the material, there are some electrons in the conduction band which can carry a current. At the same time, electrons in the valence band can jump between holes and move in the direction of the current. This makes the holes migrate in the opposite direction as the electrons. However, since the number of electrons in the conduction band is small, the conductivity will not be as high as that of a conductor; hence the name *semi*conductor. In the described situation, the current is carried by both the electrons and the holes. However, electrons or holes can be also injected in the conduction and valence band, respectively, so that the current is a consequence of either the electrons or the holes drift, in each case, thus giving place to n-type or p-type semiconductors.

Although these ideas have been developed in order to explain the electrical behavior of inorganic materials, such as silicon or gallium arsenide, they are also applicable to organic solids such as molecular crystals or polymers based on extended p-systems. The compound pentacene is a good example of a molecular crystal. If we consider a single molecule in the gas state, it presents a highest occupied molecular orbital HOMO of π nature and a lowest occupied molecular orbital (LUMO) of π^* nature with defined energies. However, when the molecules become embedded in the solid-state environment, a moderate splitting of the molecular energy levels into narrow bands is observed due to the Van der Waals intermolecular forces that hold the molecules together in the crystalline state.

Linear unsaturated polymers present π-electrons delocalized along the chain. Considering that an important feature of the band model is that the electrons are delocalized or spread over the

crystalline lattice, a completely delocalized electron system in one dimension is expected to lead to the metallic state. The Peierls transition, though, leads to a bond alternation and therefore a semiconductive rather than a metallic band structure is generated (Figure 2). Moreover, electrical conduction in polymers not only requires carrier transport along the polymer chains but also some kind of transfer (*hopping*) between the chains, which tend to lie tangled up like a plate of spaghetti.

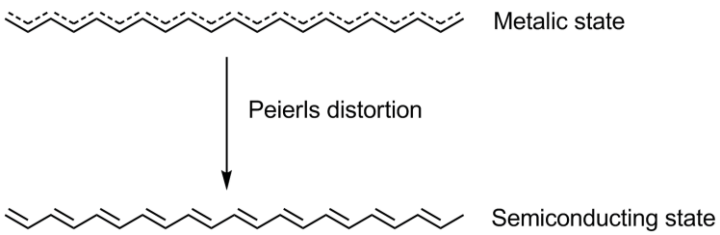

Figure 2. Schematic of Peierls distortion.

Studies of the hole-transport in high-purity naphtalene crystals revealed that for T < 150 K the conditions for the existence of band conductivity are well fulfilled. Naphtalene, as well as other structurally similar compounds like anthracene, tetracene or perylene, presents the temperature hole mobility (μ) dependence $\mu(T) \alpha T^n$ ($n < 0$) at low temperatures, like in the case of inorganic semiconductors, although the formers deviate from the ideal n value n = -3/2. These molecular crystals also show anisotropy in their conductivity. However, at room temperature and above the electrical conductivity, even in ultrapure molecular crystals, must be treated in terms of a hopping mechanism.

The hopping model

It has generally been accepted that charge transport in organic disordered systems, such as molecularly dispersed polymers and amorphous glasses, takes place by a hopping process. That is, charge transport in organic disordered systems is understood as a sequential redox process over molecules; electrons are sequentially transferred from the anion radical of one molecule to a neutral molecule through the lowest unoccupied molecular orbital (LUMO) for electron transport, and electrons are sequentially transferred from a neutral molecule to the cation radical of another molecule through the highest occupied molecular orbital (HOMO) for hole transport, as it is represented in Figure 3.

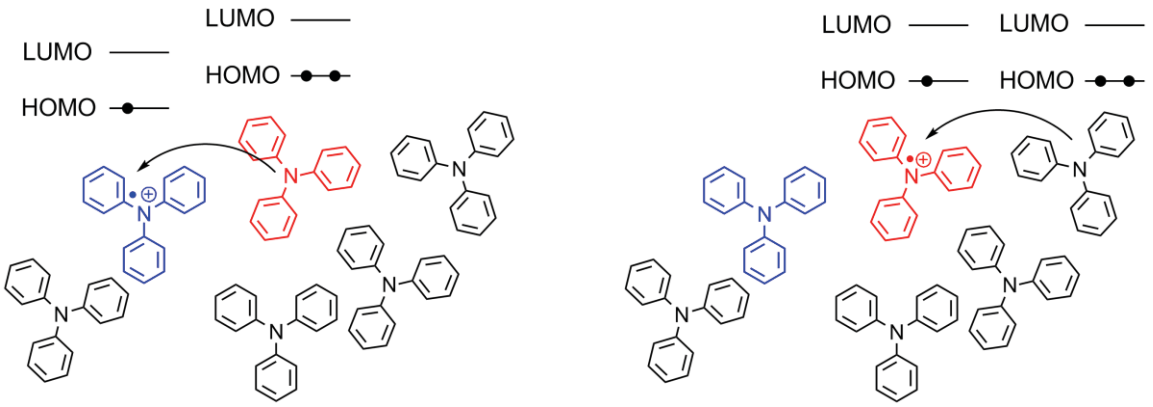

Figure 3. Schematic of a hole-transport hopping mechanism: the hole (radical cation) moves through the material by redox reactions involving the adjacent molecules, which are randomly distributed.

One of the most used models to explain the hopping mechanism is the *disorder formalism*, developed by Bässler et al. This model states that, given the absence of long-range order, hopping sites in polymers and amorphous materials are located in statistically different environments, thus both the hopping site energies and intersite distances are subject to a distribution. Due to the weak van der Waals coupling between hopping sites, electronic states of the molecules in the disordered state can be considered as completely localized. From a central-limit-theorem argument point of view, the density-of-states (DOS) distribution may be assumed to be of Gaussian shape because it depends on a large number of configurational coordinates, each varying randomly by a small amount. Hence, according to the disorder formalism, the distribution of the hopping site energy and the intermolecular distances follow Gaussian distributions.

Analytic treatment of the transport problem becomes difficult because of the asymmetry of the hopping rates, in particular if the DOS is of Gaussian shape. Predictions for the disorder formalism have been largely developed by Monte Carlo simulations, which will be explained in section 2.1.

B. Molecular materials

In the 1980s, conductive polymers based on polyheterocyclic compounds (e.g. polyaniline, polypyrrole, polythiophene) that were soluble in organic solvents and, consequently, could be processed into the form needed for many applications, were first produced. From then on it was noticed that polymer semiconductors could have significant advantages over their inorganic counterparts. For example, thin layers of polymers could easily be made by low-cost methods, such as spin-coating instead of the high-temperature deposition from vapor reactants that was generally needed for inorganic semiconductors. In addition, polymers were lightweight and could be manufactured in many different shapes, which were very attractive features for their use as

components in many devices. Other electroactive properties of these organic compounds could also be exploited as components in photocopying machines, organic light-emitting displays, and so on. The electrical properties of the last devices could not be directly compared with those based on single crystal silicon and gallium arsenide. The mobilities of charge carriers in OTFTs were low and similar to those found in amorphous silicon. Nevertheless, the simple fabrication techniques for polymers attracted several companies to work on polymers transistor applications, such as data storage and thin film device arrays to address liquid crystal displays.

Despite the importance of polymers in the development of the field of molecular electronics is unquestionable, much attention is addressed to low weight molecules for their application in electronic devices in the latest times. Namely, since they are discrete systems, the synthesis and characterization of small molecules is generally easier than in the case polymers, and, in addition, they can be purified by many methods, such as column chromatography, crystallization or sublimation. This allows an easier tuning of the electrochemical and photochemical properties via synthetic design, thus offering a huge range of possibilities. For these reasons, we will focus in molecular materials based in low-weight organic compounds.

Regarding the charge carriers that they transport, molecular materials can be classified as hole-transporting, electron-transporting or bipolar materials, that is, materials that can transport both holes and electrons. While most hole-transporting materials bear electron-donating moieties in order to: a) decrease their ionization potential (IP) values -make hole injection easier- and; b) stabilize the radical cation species that are involved in the charge migration, electron-transporting materials bear electron-accepting groups so that they show high electronaffinity (EA) values and their anion radicals are stabilized. Accordingly, bipolar materials are usually based on structures that contain both electron-donating and accepting moieties.[1-3] Bipolar materials usually function as materials for the emitting layer in OLEDs, since the emitting layer in OLEDs acts as the recombination center for holes and electrons injected from the anode and cathode, respectively.

Crystalline materials

Organic crystalline materials exhibit larger charge carrier mobilities than those in polymeric organic materials. Anthracene and naphthalene, showed hole mobilities of up to 1.8 and 2.0 $cm^2 V^{-1} s^{-1}$ and in rubrene crystals, values up to 15 $cm^2 V^{-1} s^{-1}$ have been achieved. Oligothiophenes with well-defined structures, which are highly crystalline in nature, constitute a new class of organic π-electron systems for various potential applications. In fact, the best currently-reported organic field-effect transistors with layered structures make use of oligo- and poly-thiophenes as semiconductor material. Also

pentacene and related condensed aromatic hydrocarbons have recently attracted attention as a new class of promising materials for use in OFETs.[4] The structures of the mentioned materials can be seen in Figure 4.

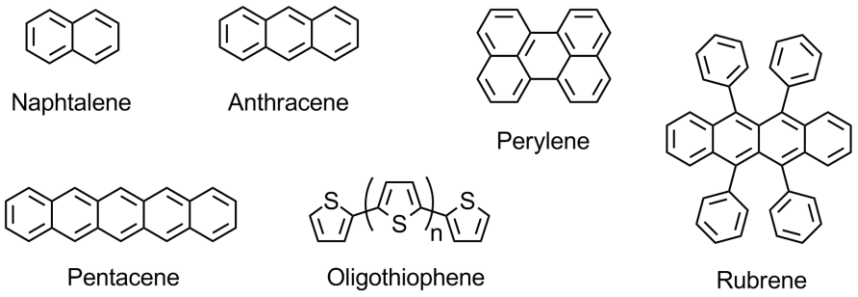

Figure 4. Examples of crystalline organic semiconductors.

Another important class of materials are the donor-acceptor complex crystals. They consist of two partner compounds in a stoichiometric ratio, one of which transfers charge to the other. When the charge transfer occurs only in an electronically excited state, they are termed weak D-A crystals (Figure 5). A good example of these is anthracene:tetracyanobenzene (TCNB). The crystal is constructed as a sandwich of planes which alternately contain the donor and the acceptor molecules. In the strong D-A or charge-transfer complexes, for example the compound tetrathiafulvalene: tetracyanoquinodimethane (TTF:TCNQ), the charge transfer takes place in the electronic ground state. This 1:1 TTF:TCNQ salt exhibits a high room temperature conductivity ($5x10^2$ S cm^{-1}) and metallic behavior is observed as the temperature is reduced to 54 K.[5]

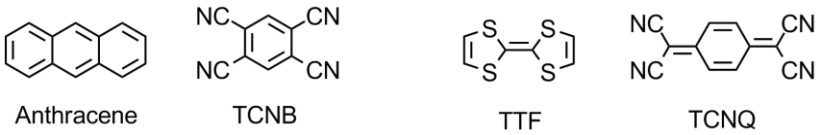

Figure 5. Examples of D-A crystalline charge-transfer complexes.

However, a main drawback of crystalline materials is that the single-crystal growth on the plane of a large-area substrate for device applications is not easy. The possibility of working with polycrystalline materials also exist. Polycrystals have been used mostly in OTFTs and OPVs, such as [6,6]-phenyl-C_{61}-butyric acid methyl ester (PCBM), titanium oxide phthalocyanine (TiOPc), perylene pigment, tris-(8-quinolinolato)aluminum (Alq_3), but the device performance is strongly affected by the grain size, grain boundaries, and molecular orientations and therefore a great control of the film morphology is required in order to obtain efficient and reproducible devices.

Amorphous molecular materials

Amorphous molecular materials or molecular glasses are low molar mass compounds with stable amorphous phases above room temperature. Although for a long time vitrification was regarded to be mainly a privilege of polymeric materials, Tammann described the glassy state of low molecular weight organic compounds at the end of the 19th century. Photoconduction of glassy β-carotene was reported by Rosenberg in 1959 and in 1981 Mikawa et al. compared hole mobilities of 1,3-diphenyl-5-(p-chlorophenyl)-2-pyrazoline in the single crystalline state (around 10^{-2} cm^2 V^{-1} s^{-1}) and in the glassy state (around 10^{-5} cm^2 V^{-1} s^{-1}).[6, 7]

Amorphous glasses are characterized by the presence of free volume and disorder in both molecular distance and orientation thus showing isotropic and homogeneous properties without grain boundaries, which allow uniform contact between organic/metal electrode and organic/organic layers. In other words, amorphous molecular materials readily form uniform amorphous thin films by themselves by vacuum deposition and spin coating from solution, like disordered polymers, but they contrast to the latest in that they are pure materials with well defined molecular structures and definite molecular weights without any distribution.

Molecular glasses are in the state of thermodynamic non equilibrium, and hence, they tend to undergo structural relaxation, exhibiting well-defined glass transition temperatures, T_g, in their differential scanning calorimetry (DSC) analyses. Some of them tend to crystallize on heating above their T_g, frequently exhibiting polymorphism. However, the stability of amorphous glasses greatly differs depending on the molecular structures of materials. Certain materials form very stable amorphous glasses that do not undergo any crystallization even upon heating above T_g.[4] Several guidelines for the molecular design of amorphous molecular materials have been presented, which include non planar molecular structures, coexistence of different conformers, incorporation of bulky and heavy substituents, and the enlargement of molecular size. The latter two guidelines also serve for increasing T_g and for enhancing the stability of the amorphous glassy state. The introduction of structurally rigid moieties to form non planar molecules or the promotion of intermolecular interactions, e.g., by hydrogen bonding or dipolar interaction are other important guidelines for increasing T_g.[4, 6]

In Figure 6 are represented the most representative basic structures for hole-transporting molecular glasses. Many of them present one or more star-shaped units in order to avoid the planarity of the aromatic system. The presence of a nitrogen atom fulfill the electron-donor character required to attain low IP, while the aromatic moieties gives stability to the corresponding cation radicals that are

formed by injecting holes in the material. Similarly the molecular design of electron-transporting amorphous molecular materials is to incorporate electron-withdrawing moieties, such as pyridine, triazine, 1,3,4-oxadiazole, triazole, and silacyclopentadiene (silole), dimesitylboranes, and triarylboranes into non-planar structures. Figure 7 shows some molecular glasses that present electron-transport.

Many compounds used in OLEDs as emitting layer showing bipolar redox characteristics, that is, reversible oxidation and reduction, are based in structures that bear both electron donating and withdrawing groups, like compounds **NPAFN**, **NPAMLMe** or **BMA-nT**. However, bipolar transport had been observed in other kind of compounds presented in Figure 8.[8-10] In Table 1 the mobility values registered by time-of-flight (TOF) method for some of some representative compounds are given.

Liquid crystals

Nowadays the letters LCD are found on the stickers of televisions, digital cameras, mobile phones and many other products that are sold in electronics stores. LCD stands for liquid crystal display and LCDs are the proof of the main role that liquid crystals played in the history of electronics. So, what is a liquid crystal?

At the end of the 19th century when Friedrich Reinitzer, Otto Lehmann and others introduced the liquid crystalline state of matter into science. They observed that cholesteryl benzoate and other similar compounds did not underwent a direct transition from the solid state to the liquid state, like the rest of known organic compounds, but presented a “double melting” behavior, that is, a new phase in between the solid and the liquid states. Liquid crystals (LCs) exhibit a phase in which their molecules are arranged with some order but at the same time have some freedom to move, that is, the material possesses fluidness. They can be divided in *lyotropic*, if they present phase transition as a function of their concentration, or *thermotropic*, if the phase transition into a liquid crystal occurs as the temperature is changed. Thermotropic liquid crystals can be further subdivided into two main classes, according to their structure: *calamitic*, based on a rod-like molecules, and *discotic*, based on disk-like molecules.

The application of calamitic liquid crystals in displays dates to the early 1970s. These devices took profit of the capability of this kind of molecules of respond to an applied external electric field, so that the arrangement of the LC layer between two electrodes could be changed with moderate voltages and thus the anisotropic optical properties could be controlled. Since then on, calamitic LCs have been widely exploited in the field of electronics. They have been used as components of polymeric materials, both as main chain and as side group mesogens.

Table 1. Ionization potentials (IP), electron affinities (EA) and mobility values (μ) of holes (h) and/or electrons (e) measured by the TOF technique under a certain electric field (E) according to reference [4].

	IP / eV	EA / eV	type	μ / $cm^2 V^{-1} s^{-1}$	E / $V cm^{-1}$
o-MTDAB			h	$3.0x10^{-3}$	$2.0x10^5$
TPD	5.5	2.4	h	$1.1x10^{-3}$	$1.0x10^5$
DPN			h	$2.2x10^{-4}$	$2.0x10^5$
Alq3	5.8	3.1	e	$1.2x10^{-6}$~$2x10^{-4}$	~$5x10^5$
S(PyPy)2	~5.9	~3.2	e	$2.0x10^{-4}$	$6.4x10^5$
TPDB			e	$1.2x10^{-6}$	$7.0x10^5$
B3	~5.6	~2.5	h	$2.0x10^{-3}$	$3.5x10^5$
			e	$5.9x10^{-4}$	$6.4x10^5$
T3	~5.4	~2.3	h	$2.8x10^{-4}$	$3.6x10^5$
			e	$1.2x10^{-3}$	$6.4x10^5$

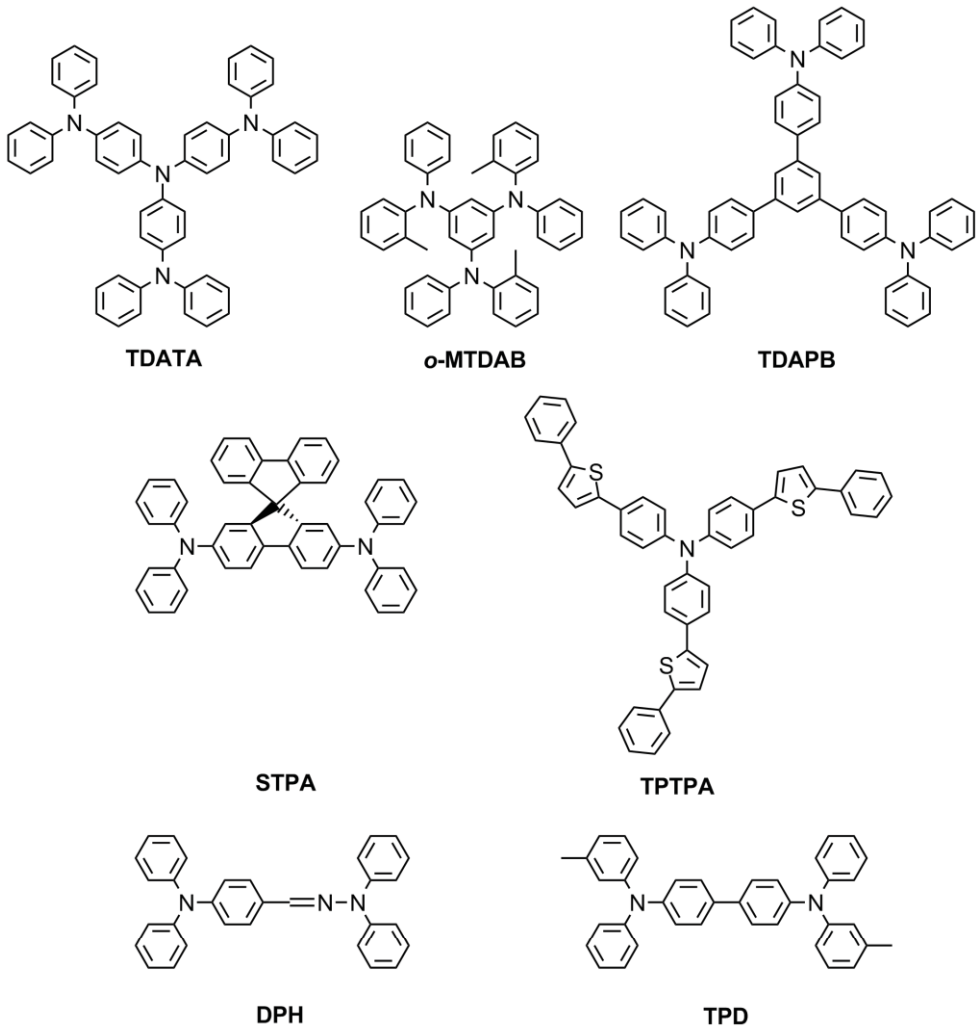

Figure 6. Representative molecular glasses presenting hole-transport properties.

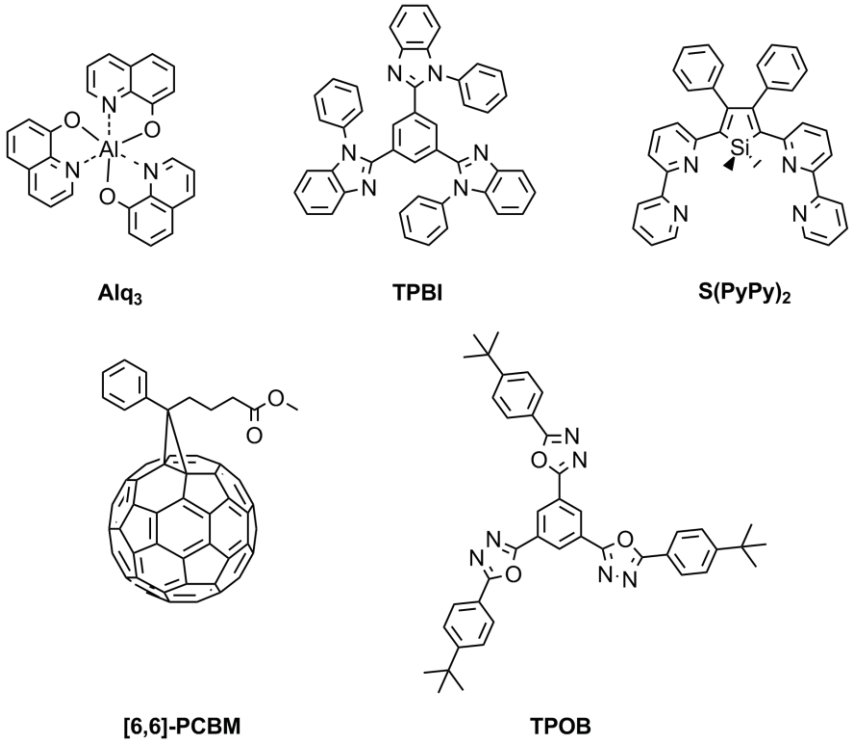

Figure 7. Representative molecular glasses presenting electron-transport properties.

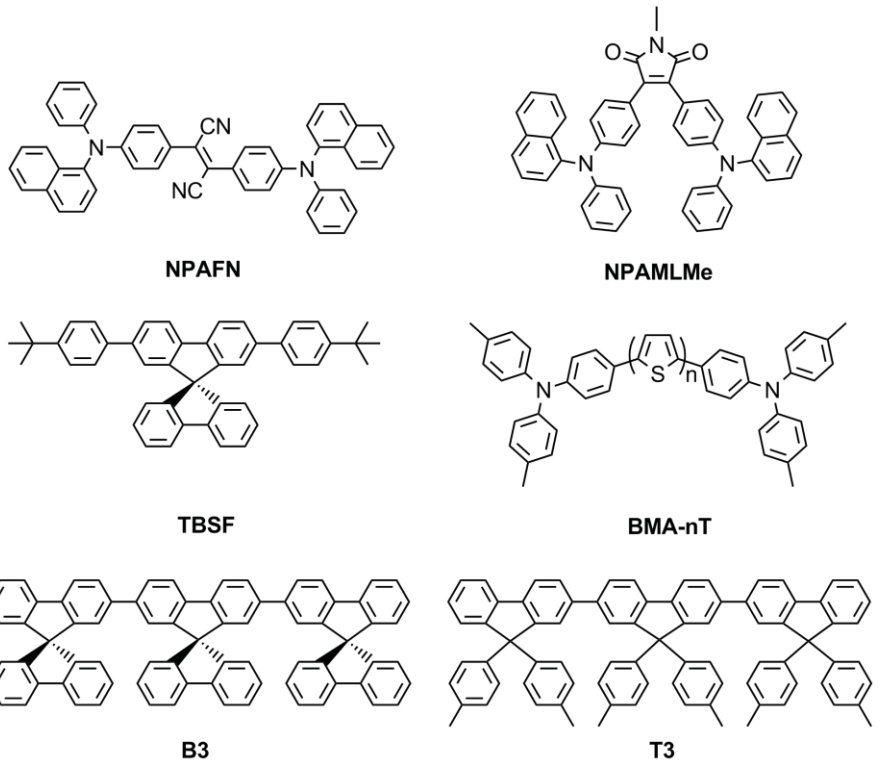

Figure 8. Representative molecular glasses presenting bipolar transport properties.

Despite the background of calamitic LCs, the work presented in this thesis was aimed to the preparation of discotic liquid crystals. Namely, discotic LCs, which were discovered in 1977 by Chandrasekhar et al., offer further applications as a result of their orientation in the columnar mesophase. The disk-like mesogens pile up into extended one-dimensional (1D) columns, making them ideal candidates for molecular wires in electroluminescence, photovoltaic and field-effect transistor devices.

Discotic liquid crystals represent a solution to the limitations of crystalline and amorphous organic semiconductors. On the one hand, while molecular glasses suffer mostly due to their low charge carrier mobility, well-aligned columnar LCs samples, which experience a much larger orbital overlap to adjacent molecules within the columns than their calamitics counterparts, can reach values of 1–5 $cm^2\ V^{-1}\ s^{-1}$, comparable to amorphous silicon. On the other hand, they allow the combination of high local order with the absence of grain boundaries, which is a main drawback in polycrystalline materials.[11] In addition, their liquid crystalline character favors a self-healing process of structural defects. It is remarkable that, despite the high degree of order in the columns, the transport seems not to be described by a bandlike model but rather by a hopping process, and thus photocurrent can be predicted by Monte Carlo simulations.[12-14]

One of the most used methods to evaluate the semiconducting properties of columnar LCs is the time of flight (TOF) technique.[11-19] This technique gives the macroscopic mobility, which is strongly dependent on the number of defects, and clearly indicates the type of charge carrier.[11] The disadvantage of the TOF method is that monodomains with the columns aligned perpendicular to the electrodes (homeotropic *face-on* alignment) are required. Any defect in the path has a strong effect on the mobility, so the values can underestimate the true transport potential of the material. Discotics that do not align accordingly might be impossible to investigate with the TOF method.[14] However, the orientation of molecules within these large domains can be manipulated by various means, such as a concentration or temperature gradient, irradiation with polarized light, or surface alignment layers.[19, 20]

Moreover, the liquid crystalline phase characteristics can be tuned by the proper modifications of the discotic molecules. Taking into account that disk-like molecules should consist of a central aromatic core surrounded by floppy chains, the variation of the symmetry and size of the π-conjugated core and of the nature of the connecting groups between the core and the flexible side chains allows a wide range of synthetic possibilities that are translated in a wide range of chemical-physical properties.

Necessarily, discotic LCs for electronic applications should be well-soluble in organic solvents to allow easy processing by spin coating or other solution methods. Processing of the material by thermal annealing requires also reasonably low clearing points: the upper temperature limit for fabrication of devices on flexible plastic substrates is often considered to be ca. 200 °C. Further, the materials should be liquid crystalline at the ambient temperature and LC mesophases should be stable over a sufficiently broad temperature range.[19] In Figure 9 are shown some of the most usual core structures for discotic molecules showing columnar liquid crystal arrangements.[11, 19, 21, 22]

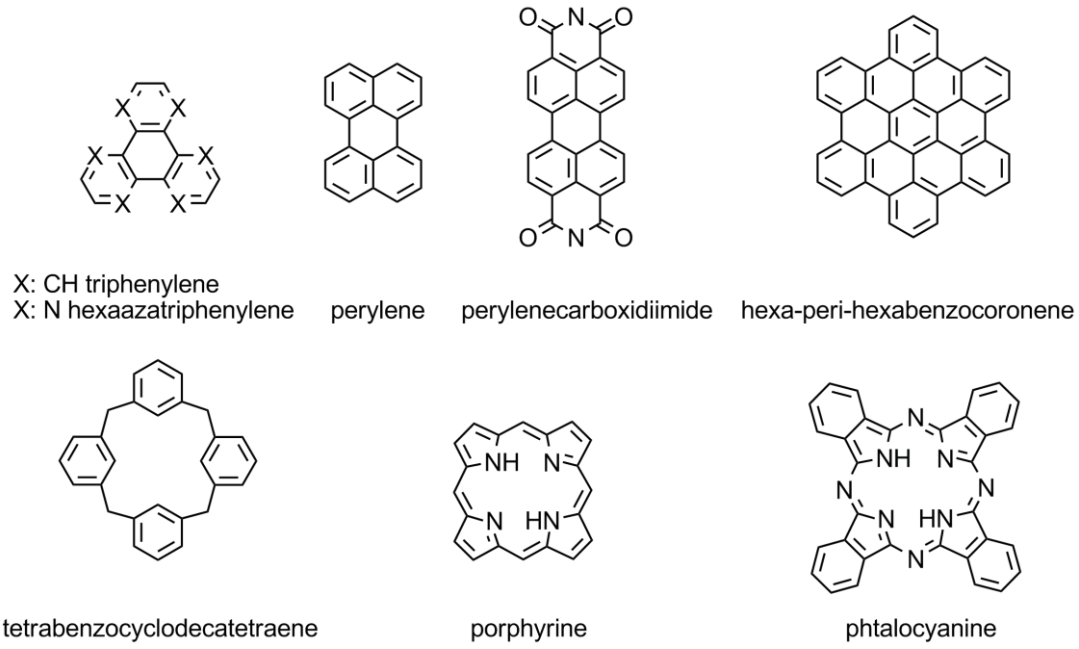

Figure 9. Representative core units for discotic molecules presenting columnar liquid crystal phases.

It is also worth to mention the role of doping in the preparation of ordered columnar liquid crystal phases. The disk-shaped molecules generally have an extended aromatic core, and with the appropriate substituents, they can act as electron-rich "donors" when complexed with planar electron-deficient molecules. Commonly, 2,4,7-trinitro-9-fluorenone (TNF) or its derivatives are used, but other nitro-, cyano-, or fluoro-substituted arenes have been employed as well. By charge transfer (CT) interactions, mesophases can be induced (via complexing of two non liquid-crystalline compounds), modified (another mesophase appears), or stabilized (by extending of the temperature window of mesophase formation).[15, 23-30]

The use of columnar LCs in OTFTs and in OPVs is a promising research area. In a field-effect transistor (FET), the charge carriers migrate between the source and drain electrode close to the interface under an applied gate voltage. For an optimized FET device, the molecules have to adopt an *edge-on* organization with their molecular plane perpendicular to the surface (Figure 10 right). The columns

lying on surface permit a charge carrier transport parallel to the surface. Hexaalkylhexa-peri-benzocoronene (HBC) derivatives showed promising device performance with mobilities up to 10^{-3} cm^2 V^{-1} s^{-1} along the alignment direction. The corresponding values for non-aligned films of the same material were two orders of magnitude lower, confirming the importance of the long-range order for the performance of devices. The on/off ratio was more than 10^4 with a turn-on voltage of ca. -5 V to -10 V.[31]

The optimal situation for the fabrications of solar cells with discotic semiconductors would be the homeotropic alignment of mutually non-miscible electron-donor (D) and electron-acceptor (A) discotics with a 10-100 nm phase separation scale, so that rapid hole and electron transport along the D and A columnar stacks could take place once the exciton is dissociated (Figure 10 left). However, the only attempt that proved to be close to this arrangement was a photovoltaic cell prepared with an HBC derivative as hole-transporting material and perylene diimide (PDI) as electron transporting material, which showed an efficiency of 34% at a wavelength of ca. 490 nm.[19]

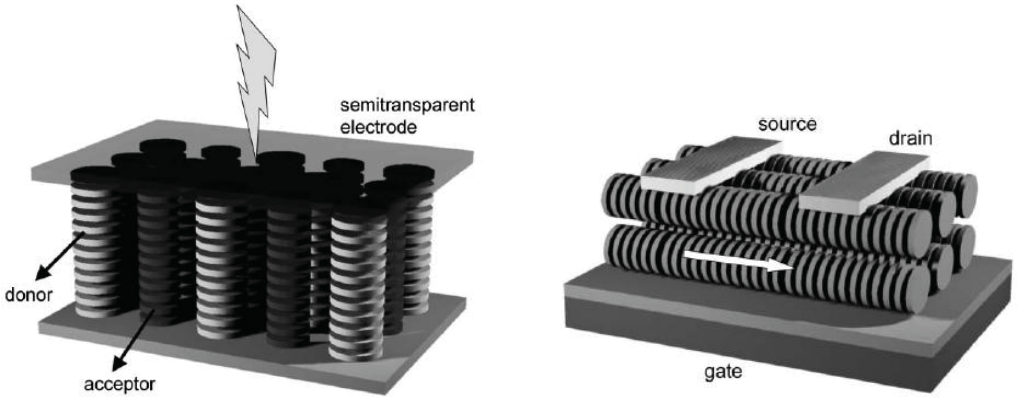

Figure 10. Schematic illustration of an OPV device (left) and a top-contact OTFT (right) based on columnar liquid crystals.

C. Radical and non-radical carbazole derivatives.

The interest in carbazole-based compounds as photoconductors or charge-transporting materials arises from the advantageous characteristics that they present, e.g. their ability of forming stable radical cations (holes), their high thermal and photochemical stability, the possibility of easily introducing different substituents into the carbazole ring and the low cost of carbazole raw material. In fact, polymers containing carbazole have proven to perform efficiently enough as to be used in practical applications: in 1970 IBM introduced its Copier I series, in which the charge transfer

complex formed by polyvinylcarbazole (PVK) and 2,4,7-trinitrofluorenone (TNF) was used as photorefractive material.[32]

Regarding the area of low-weight molecular materials, 3,6(2,7),9-substituted carbazoles proved to be effective charge transporting, electroluminescent and host materials with improved thermal and morphological stabilities.[33] More precisely, the *N*-arylcarbazoles, in which a phenyl or a naphthyl group is attached on the 9-position of carbazole, have shown excellent thermal stability and good electro-optical properties.[34, 35] Namely, 9-arylcarbazole structure can be seen as a more planar analog of the triphenylamine, some derivatives of which are exceptional hole-transporting molecular materials, as it was already discussed. The rigidness of carbazole gives intense photoluminescence properties to this moiety. *N*-arylcarbazoles have been also used as pigments in dye sensitized solar cells (DSSCs).[36] Figure 11 shows some molecular glasses derived from carbazole.

Although carbazole derivatives play an important role as organic materials for electronic applications, not many carbazole containing discotic LCs have been reported so far. Most of these systems bear the carbazole moiety as a pendant group of the rigid core.[15, 28-30] Only some examples of disk-like liquid crystal carbazole systems in which the carbazole unit constitutes the central part of the mesogen have been prepared.[37-39] Some of these systems were synthesized in our group and showed rectangular and lamellar mesophases.

For these reasons carbazole fragment is a promising building block for the preparation of both amorphous molecular glasses and liquid crystals that may present the sought properties for their application in optoelectronic/electronic devices. But where does the interest of working with stable radicals lay?

The use of crystalline radical compounds is a challenging approach to obtain organic materials with high conductivities because the arrangement of the unpaired electrons in a crystal lattice could lead to the generation of a half-filled energy band like in an elemental metal by orbital overlapping between adjacent radicals. Aiming to this target, Haddon et al. prepared a mixed valence salt that resulted from treating the 1,4-phenylene-bisdithiazolyl diradical with iodine that presented conductivities of 100 S cm^{-1} at r.t.[40] This research group also reported the preparation of spiro-bis(1,9-disubstituted phenalenyl)boron neutral radicals among which some of the most highly conducting neutral organic solids can be found.[41-43] However, despite these radicals proved to present excellent electronic properties, their application in electronic devices with large and flexible areas might be a problem, since they require a crystalline arrangement.

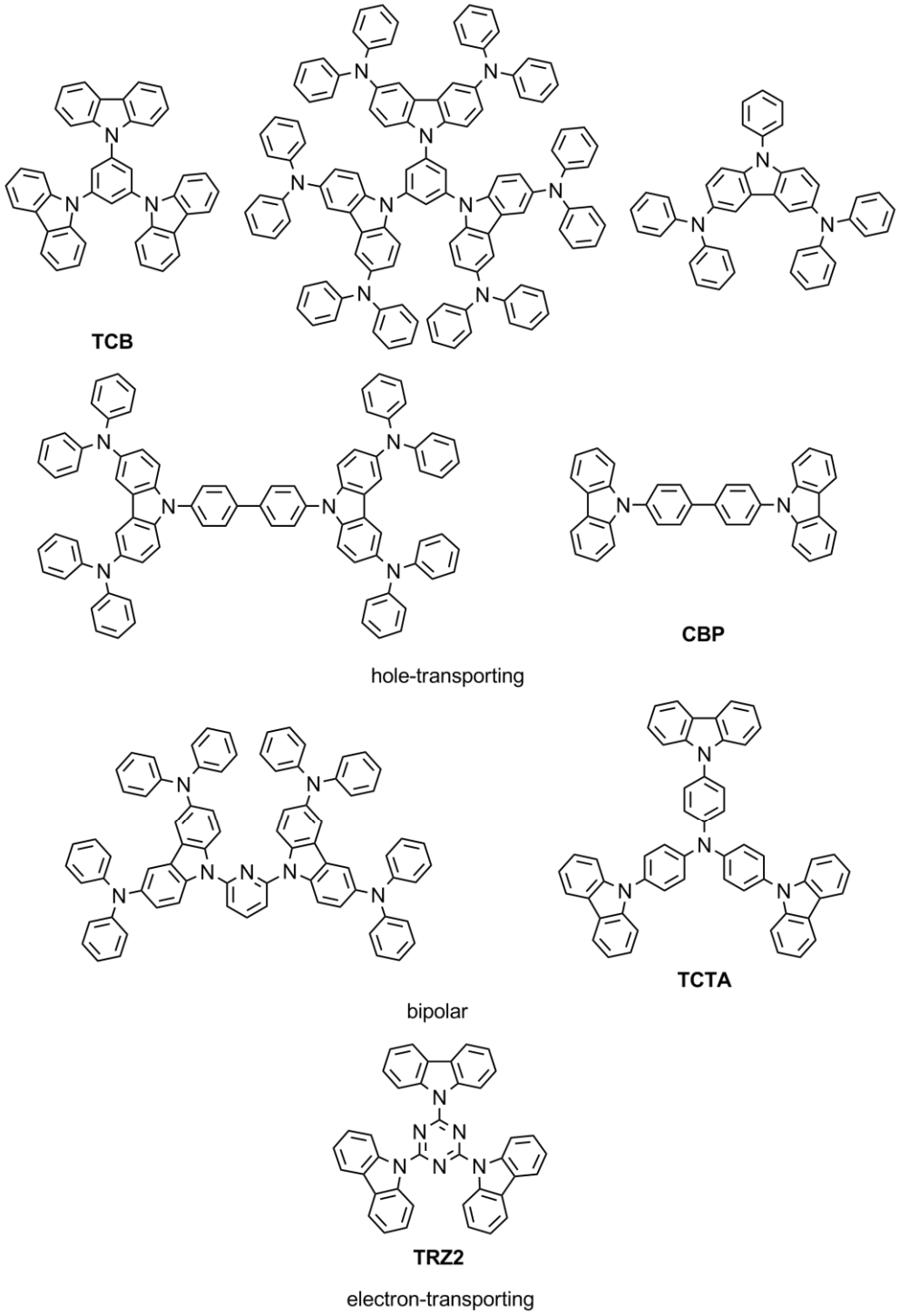

Figure 11. Molecular glasses bearing carbazole moieties.

A different approach in the preparation of radical organic semiconductors was given by Nishide et al.[44] who developed a new kind of organic radicals combining triphenylamine and nitroxide radical moieties. These radical adducts presented hole-transport in the amorphous state, that is, by hopping mechanism, with mobility values in the range of 10^{-3} cm^2 V^{-1} s^{-1}, which are comparable to the values found for typical hole-transporting organic materials. Although in a previous work the charge-transport properties of a polymer doped with stable organic radical were studied,[45] this is the only work to be found in the literature dealing with hole-hopping in organic neutral radicals.

To the best of our knowledge, only three examples of electronic devices built with organic radicals exist: single-layer hole-only device of the radical polymer dispersed in polycarbonate (ITO/radical:polycarbonate/Al),[46] an organic field efect transistor (OFET)[47] based on 1-imino nitroxide pyrene, both of them using compounds bearing a radical nitroxide fragment, and an OPV[48] whose photoactive layer is based on the radical **poly-Ply** shown in Figure 12.

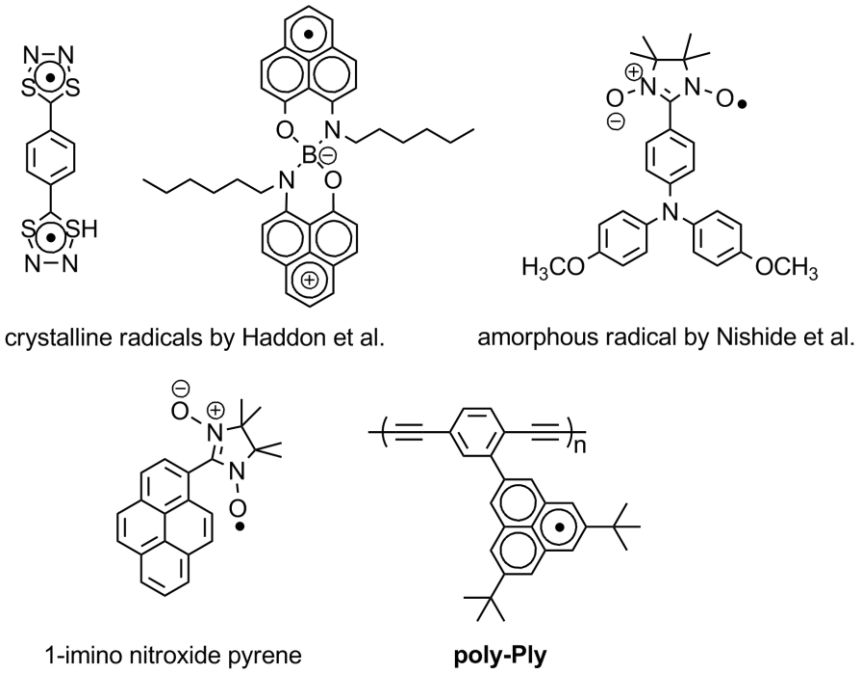

Figure 12. Examples of radical semiconductors.

Previously to this thesis, our group reported the electrochemical and photoluminescence properties of the radical compound that resulted from coupling a unit of carbazole and a unit of tris(2,4,6-trichlorophenyl)methyl radical (**TTM**), which is shown in Figure 13.[49, 50] The new *N*-carbazolylTTM radical (**1**) showed high quantum yield fluorescence emission in the red region of the visible spectrum and reversible oxidation and reduction processes in its cyclic voltammetries. This bipolar

redox behavior was attributed to the radicalary character of this kind of compounds, since this feature was also observed in the **TTM** radical. Both the intense fluorescence emission in the visible range and the electrochemical bipolarity were two interesting features for the study of this system and other systems derived from it as materials for electronic and/or optoelectronic devices.

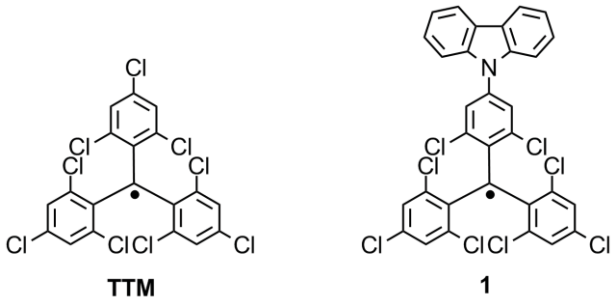

Figure 13. Structures of the tris(2,4,6-trichlorophenyl)methyl radical (**TTM**) and of the *N*-carbazolylTTM radical (**1**).

Another field in which organic radicals are promising materials is the field of *spintronics* or magnetoelectronics. Spintronics is an emerging technology that exploits the intrinsic spin of the electron and its associated magnetic moment, in addition to its fundamental electronic charge, in solid-state devices. In other words, it is the field of solid-state physics that takes profit of the combined magnetic and electric properties that some materials present. Although most of the materials developed for spintronic devices are inorganic, the weak spin–orbit and hyperfine interactions in organic molecules leads to the possibility of preserving spin-coherence over times and distances much longer than in conventional metals or semiconductors.[51, 52] Thus, organic radicals, bearing unpaired electrons and therefore being paramagnetic compounds, are good candidates for the development of organic molecular spintronics.[52]

Closely related to spintronics, the development of spin systems with liquid crystalline properties is particularly interesting in the field of magnetism because of the alteration of the magnetic properties derived from the spin intermolecular interactions through the phase transition, or the modulation of the magnetic response by external fields.[53-71] That is, organic liquid crystalline systems may allow the electrical manipulation of magnetic anisotropy. Calamitic all-organic radical LCs containing TEMPO and PROXYL as spin sources,[60, 61, 64, 67, 68] which can be ordered into a variety of liquid crystal phases as nematic or layered phases are found in the literature. Among them, magneto-responsive nematic or chiral nematic phases have been described for cyclic nitroxides.[56, 68] Despite all these examples devoted to the preparation of rod-like self-assembling paramagnetic organic molecules, there is only a single reference in the literature with two examples of disk-like all-organic radical,[70]

whose spin-supporting unit is introduced to the disk-like triphenylene core as a lateral chain bonded moiety (Figure 14). This is mainly due to the fact that radical-stabilizing substituients are in detrimental of the stability of liquid-crystalline phases.

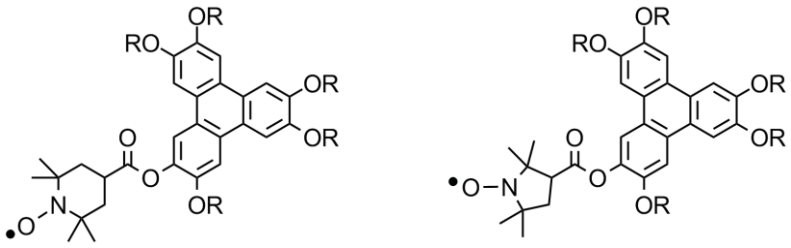

Figure 14. Structures of the first discotic radical compounds showing columnar liquid crystal phases.

Hence, in the above described context, the preparation of new carbazole derivatives, new compounds that combine carbazole and **TTM** radical units among them, both in the amorphous state, i.e. as molecular glasses, and in the liquid crystal state turns to be highly attractive and challenging for their application in molecular electronics.

References

[1] M. Guan, Z. Q. Bian, Y. F. Zhou, F. Y. Li, Z. J. Li, C. H. Huang, *Chem. Commun.* **2003**, 2708-2709.
[2] T. H. Huang, J. T. Lin, L. Y. Chen, Y. T. Lin, C. C. Wu, *Adv. Mater.* **2006**, *18*, 602-606.
[3] Y. Zhu, A. P. Kulkarni, S. A. Jenekhe, *Chem. Mater.* **2005**, *17*, 5225-5227.
[4] Y. Shirota, H. Kageyama, *Chem. Rev.* **2007**, *107*, 953-1010.
[5] H. Alves, A. S. Molinari, H. Xie, A. F. Morpurgo, *Nat Mater* **2008**, *7*, 574-580.
[6] P. Strohriegl, J. V. Grazulevicius, *Adv. Mater.* **2002**, *14*, 1439-1452.
[7] H. Kitayama, M. Yokoyama, H. Mikawa, *Mol. Cryst. Liq. Cryst.* **1981**, *69*, 257-271.
[8] Y.-L. Liao, C.-Y. Lin, Y.-H. Liu, K.-T. Wong, W.-Y. Hung, W.-J. Chen, *Chem. Commun.* **2007**, 1831-1833.
[9] T.-C. Tsai, W.-Y. Hung, L.-C. Chi, K.-T. Wong, C.-C. Hsieh, P.-T. Chou, *Org. Electron.* **2009**, *10*, 158-162.
[10] C.-c. Wu, T.-L. Liu, W.-Y. Hung, Y.-T. Lin, K.-T. Wong, R.-T. Chen, Y.-M. Chen, Y.-Y. Chien, *J. Am. Chem. Soc.* **2003**, *125*, 3710-3711.
[11] P. Wojciech, Z. Matthias, C. Ji Young, M. Klaus, Z. Rudolf, *Macromol. Rapid Commun.* **2009**, *30*, 1179-1202.
[12] I. Hiroaki, H. Jun-ichi, J. B. Richard, M. Bijan, J. W. Benjamin, *J. Appl. Phys.* **2006**, *100*, 043716.
[13] K. Marcel, L. Frederic, M. Klaus, W. Gerhard, *Appl. Phys. Lett.* **2006**, *89*, 252103.
[14] L. Sabine, B. Angelika, S. Nelli, G. Frank, H. Constanze, S. Giusy, J. Roxana, K. Elisabeth, S. Sven, S. Alina, T. Martin, *Angew. Chem. Int. Ed.* **2007**, *46*, 4832-4887.
[15] K. J. Donovan, K. Scott, M. Somerton, J. Preece, M. Manickam, *Chem. Phys.* **2006**, *322*, 471-476.
[16] I. Hiroaki, H. Jun-ichi, J. B. Richard, M. Bijan, J. W. Benjamin, J. C. Michael, *Appl. Phys. Lett.* **2005**, *87*, 132102.
[17] S. Laschat, a. et, et al., *ChemInform* **2007**, *38*.

[18] C.-y. Liu, A. Fechtenkotter, M. D. Watson, K. Mullen, A. J. Bard, *Chemistry of Materials* **2002**, *15*, 124-130.
[19] S. Sergeyev, W. Pisula, Y. H. Geerts, *Chem. Soc. Rev.* **2007**, *36*, 1902-1929.
[20] J. Piris, M. G. Debije, N. Stutzmann, A. M. v. d. Craats, M. D. Watson, K. Müllen, J. M. Warman, *Adv. Mater.* **2003**, *15*, 1736-1740.
[21] S. Kumar, *Chem. Soc. Rev.* **2006**, *35*, 83-109.
[22] L. Sabine, a. et, et al., *ChemInform* **2007**, *38*.
[23] R. Helmut, B. Holger, K. Olaf, W. Renate, E. Martina, H. W. Joachim, K. Bernd, P. Klaus, *Adv. Mater.* **1990**, *2*, 141-144.
[24] P. H. J. Kouwer, W. F. Jager, W. J. Mijs, S. J. Picken, *Macromolecules* **2001**, *34*, 7582-7584.
[25] P. H. J. Kouwer, W. F. Jager, W. J. Mijs, S. J. Picken, *Macromolecules* **2002**, *35*, 4322-4329.
[26] P. H. J. Kouwer, W. F. Jager, W. J. Mijs, S. J. Picken, *J. Mater. Chem.* **2003**, *13*, 458-469.
[27] P. H. J. Kouwer, O. van den Berg, W. F. Jager, W. J. Mijs, S. J. Picken, *Macromolecules* **2002**, *35*, 2576-2582.
[28] M. Manickam, M. Belloni, S. Kumar, S. K. Varshney, D. S. S. Rao, P. R. Ashton, J. A. Preece, N. Spencer, *J. Mater. Chem.* **2001**, *11*, 2790-2800.
[29] M. Manickam, G. Cooke, S. Kumar, P. R. Ashton, J. A. Preece, N. Spencer, *Mol. Cryst. Liq. Cryst.* **2003**, *397*, 1-1.
[30] M. Manickam, S. Kumar, J. A. Preece, N. Spencer, *Liq. Cryst.* **2000**, *27*, 703-706.
[31] W. Pisula, A. Menon, M. Stepputat, I. Lieberwirth, U. Kolb, A. Tracz, H. Sirringhaus, T. Pakula, K. Müllen, *Adv. Mater.* **2005**, *17*, 684-689.
[32] J. V. Grazulevicius, P. Strohriegl, J. Pielichowski, K. Pielichowski, *Prog. Polym. Sci.* **2003**, *28*, 1297-1353.
[33] S. Grigalevicius, *Synth. Met.* **2006**, *156*, 1-12.
[34] H.-y. Fu, H.-r. Wu, X.-y. Hou, F. Xiao, B.-x. Shao, *Synth. Met.* **2006**, *156*, 809-814.
[35] P. Kundu, K. R. J. Thomas, J. T. Lin, Y. T. Tao, C. H. Chien, *Adv. Funct. Mater.* **2003**, *13*, 445-452.
[36] D. Kim, J. K. Lee, S. O. Kang, J. Ko, *Tetrahedron* **2007**, *63*, 1913-1922.
[37] M. J. Sienkowska, H. Monobe, P. Kaszynski, Y. Shimizu, *J. Mater. Chem.* **2007**, *17*, 1392-1398.
[38] E. Perea, F. López-Calahorra, D. Velasco, H. Finkelmann, *Mol. Cryst. Liq. Cryst.* **2001**, *365*, 695 - 702.
[39] E. Perea, F. López-Calahorra, D. Velasco, *Liq. Cryst.* **2002**, *29*, 421-428.
[40] C. D. Bryan, A. W. Cordes, R. M. Fleming, N. A. George, S. H. Glarum, R. C. Haddon, R. T. Oakley, T. T. M. Palstra, A. S. Perel, L. F. Schneemeyer, J. V. Waszczak, *Nature* **1993**, *365*, 821-823.
[41] S. K. Pal, M. E. Itkis, F. S. Tham, R. W. Reed, R. T. Oakley, B. Donnadieu, R. C. Haddon, *J. Am. Chem. Soc.* **2007**, *129*, 7163-7174.
[42] S. K. Pal, M. E. Itkis, R. W. Reed, R. T. Oakley, A. W. Cordes, F. S. Tham, T. Siegrist, R. C. Haddon, *J. Am. Chem. Soc.* **2004**, *126*, 1478-1484.
[43] S. K. Mandal, M. E. Itkis, X. Chi, S. Samanta, D. Lidsky, R. W. Reed, R. T. Oakley, F. S. Tham, R. C. Haddon, *J. Am. Chem. Soc.* **2005**, *127*, 8185-8196.
[44] T. Kurata, K. Koshika, F. Kato, J. Kido, H. Nishide, *Chem. Commun.* **2007**, 2986-2988.
[45] T. Kurata, Y.-J. Pu, J. Kido, H. Nishide, *J. Photopolym. Sci. Technol.* **2003**, *16*, 297-298.
[46] T. Kurata, K. Koshika, F. Kato, J. Kido, H. Nishide, *Polyhedron* **2007**, *26*, 1776-1780.
[47] Y. Wang, H. Wang, Y. Liu, C.-a. Di, Y. Sun, W. Wu, G. Yu, D. Zhang, D. Zhu, *J. Am. Chem. Soc.* **2006**, *128*, 13058-13059.
[48] X. Lv, J. Mao, Y. Liu, Y. Huang, Y. Ma, A. Yu, S. Yin, Y. Chen, *Macromolecules* **2008**, *41*, 501-503.
[49] O. Armet, J. Veciana, C. Rovira, J. Riera, J. Castaner, E. Molins, J. Rius, C. Miravitlles, S. Olivella, J. Brichfeus, *J. Phys. Chem.* **1987**, *91*, 5608-5616.
[50] D. Velasco, S. Castellanos, M. Lopez, F. Lopez-Calahorra, E. Brillas, L. Julia, *J. Org. Chem.* **2007**, *72*, 7523-7532.

[51] A. R. Rocha, V. M. Garcia-Suarez, S. W. Bailey, C. J. Lambert, J. Ferrer, S. Sanvito, *Nat Mater* **2005**, *4*, 335-339.
[52] M. Mas-Torrent, N. Crivillers, V. Mugnaini, I. Ratera, C. Rovira, J. Veciana, *J. Mater. Chem.* **2009**, *19*, 1691-1695.
[53] N. Ikuma, R. Tamura, K. Masaki, Y. Uchida, S. Shimono, J. Yamauchi, Y. Aoki, H. Nohira, *Ferroelectrics* **2006**, *343*, 119-125.
[54] N. Ikuma, R. Tamura, S. Shimono, N. Kawame, O. Tamada, N. Sakai, J. Yamauchi, Y. Yamamoto, *Angew. Chem. Int. Ed.* **2004**, *43*, 3677-3682.
[55] D. Ionescu, G. R. Luckhurst, D. S. D. Silva, *Liq. Cryst.* **1997**, *23*, 833-843.
[56] M. Mazzoni, L. Franco, A. Ferrarini, C. Corvaja, G. Zordan, G. Scorrano, M. Maggini, *Liq. Cryst.* **2002**, *29*, 203-208.
[57] Z. Min-Yan, A. Zhong-Wei, *Chin. J. Chem .* **2006**, *24*, 1754-1757.
[58] M. Mizumoto, H. Ikemoto, H. Akutsu, J.-I. Yamada, S. I. Nakatsuji, *Mol. Cryst. Liq. Cryst.* **2001**, *363*, 149-156.
[59] S. Nakatsuji, *Adv. Mater.* **2001**, *13*, 1719-1724.
[60] S. i. Nakatsuji, H. Ikemoto, H. Akutsu, J.-i. Yamada, A. Mori, *J. Org. Chem.* **2003**, *68*, 1708-1714.
[61] I. Naohiko, T. Rui, S. Satoshi, K. Naoyuki, T. Osamu, S. Naoko, Y. Jun, Y. Yukio, *Angew. Chem.* **2004**, *116*, 3763-3768.
[62] Y. Noda, S. Shimono, M. Baba, J. Yamauchi, N. Ikuma, R. Tamura, *J. Phys. Chem. B* **2006**, *110*, 23683-23687.
[63] Y. Noda, S. Shimono, M. Baba, J. Yamauchi, Y. Uchida, N. Ikuma, R. Tamura, *Appl. Magn. Reson.* **2008**, *33*, 251-267.
[64] N. Shin'ichi, M. Masako, I. Hiroshi, A. Hiroki, Y. Jun-ichi, *Eur. J. Org. Chem.* **2002**, *2002*, 1912-1918.
[65] M. J. Sienkowska, J. M. Farrar, P. Kaszynski, *Liq. Cryst.* **2007**, *34*, 19-24.
[66] R. Tamura, S. Susuki, N. Azuma, A. Matsumoto, F. Toda, Y. Ishii, *J. Org. Chem.* **1995**, *60*, 6820-6825.
[67] R. Tamura, Y. Uchida, N. Ikuma, *J. Mater. Chem.* **2008**, *18*, 2872-2876.
[68] Y. Uchida, N. Ikuma, R. Tamura, S. Shimono, Y. Noda, J. Yamauchi, Y. Aoki, H. Nohira, *J. Mater. Chem.* **2008**, *18*, 2950-2952.
[69] Y. Uchida, R. Tamura, N. Ikuma, S. Shimono, J. Yamauchi, Y. Aoki, H. Nohira, *Mol. Cryst. Liq. Cryst.* **2007**, *479*, 213-221.
[70] C. V. Yelamaggad, A. S. Achalkumar, D. S. S. Rao, M. Nobusawa, H. Akutsu, J.-i. Yamada, S. i. Nakatsuji, *J. Mater. Chem.* **2008**, *18*, 3433-3437.
[71] J. Zienkiewicz, A. Fryszkowska, K. Zienkiewicz, F. Guo, P. Kaszynski, A. Januszko, D. Jones, *J. Org. Chem.* **2007**, *72*, 3510-3520.

Consulted bibliography

Michael C. Petty. *Molecular Electronics. From principles to practice.* Chichester, Wiley & Sons Ltd. (2008).

Markus Schwoerer, Hans Christoph Wolf. *Organic Molecular Solids*. Weinheim, Wiley-VCH Verlag GmbH & Co. (2007).

Paul M. Borsenberger, David S. Weiss. *Organic Photoreceptors in Xerography.* Vol. 49, Optical Engineering Series. New York, Marcel Dekker Inc. (1998).

Objectives

The aim of this thesis is the preparation of carbazole derivatives for molecular electronics. This task involves three main stages: 1) the synthesis and characterization of carbazole derivatives; 2) the study of their behavior as semiconductors; 3) their application in electronic devices. A chapter of the dissertation is dedicated to each one of these stages.

As it was already mentioned in the introduction, a carbazole derivative bearing a radical core of the tris(2,4,6-trichlorophenyl)methyl (TTM) series, as well as non-radical carbazole derivatives showing liquid crystalline phases had been obtained previously in our research group. The work presented in this thesis was therefore focused on the derivatization of the already known systems and the synthesis of analog compounds in order to attain two kinds of materials: molecular glasses and liquid crystals. Such compounds could be, at the same time, of radical nature or not, thus classifying the target materials in radical or non-radical materials, respectively. In addition some novel systems were targeted in order to perform either comparative studies or to get novel properties.

This last point included the separation of the carbazole and TTM fragments through some alkyl chain or the functionalization of the 1,3,5-tris(*N*-carbazolyl)benzene (TCB) core with electron-withdrawing moieties. Also the attainment of materials that combine the radical nature with the liquid-crystalline behavior was a most sought objective in this thesis, given the promising features that could derive from such combination, which were exposed in the introduction. In the area of non-radical compounds, the preparation of molecular glasses bearing more than one unit of carbazole and the attachment of functional groups that may lead to photoluminescence properties in the visible range was targeted.

Regarding the modification of the carbazole derivatives previously prepared in the group, it was proposed as synthetic target the introduction of terminal functional groups, such as carboxylic acids, that might give rise to new intermolecular interactions between the known carbazolic mesogens and/or allow the attachment of such mesogens to larger architectures, like polymers or dendrimers. Also the synthesis of molecular glasses with aromatic cores analog to the carbazolic mesogens was proposed, in order to compare the physical properties of the liquid-crystalline phases with the properties of the amorphous state for the same aromatic core.

Hence, the objectives of the thesis can be summarized as follows:

- Optimization of the coupling reaction between carbazole and **TTM** radical. Study of the effect of the attachment of acyl and alkyl chains of different length to the aromatic core in the thermal behavior of radicals derivatives belonging to the *N*-carbazolylTTM family. Specifically, preparation of discotic compounds based on the *N*-carbazolylTTM core aiming to the attainment of columnar liquid crystal phases.
- Preparation of molecular glasses based on the *N*-phenylcarbazole system with attractive photoluminescence and/or electrochemical properties. That is, synthesis of polymethoxy *N*-phenylcarbazole derivatives analogs to the *N*-phenylcarbazole mesogens previously developed in our research group; and synthesis of TCB derivatives bearing triscyanovinyl fragments.
- Providing polyalkoxylated *N*-phenylcarbazole derivatives that present liquid-crystalline phases with terminal carboxylic acids and studying the effect of the modification in the liquid-crystalline behavior. Study of the effects of doping with an electron acceptor molecule in the mesophases of some of the synthesized systems.
- Study of the absorption and luminescence properties, as well as electrochemical characteristics, of all the prepared compounds in order to estimate the important parameters for their application as active materials in electronic devices
- Study of the charge mobilities of the most representative materials by the xerographic time-of-flight (XTOF) technique–in the case of molecular glasses- and by the time-of-flight (TOF) technique–in the case of liquid crystals-.
- Preparation and evaluation of electronic devices based on the organic materials that show the proper properties.

1. Materials

1.1. Theoretical basis

In this chapter some useful concepts about the techniques used for the characterization of the prepared materials will be explained.

1.1.1. Study of the electrochemical properties.

The redox properties of the prepared materials should be studied in order to determine if they fulfill the requirements to operate as organic semiconductors. These requirements are low ionization potentials (IP) values and reversible oxidations, for their potential application as hole-transporting materials and high electronaffinities (EA) and reversible reductions for their potential application as electron-transporting materials.

Proper IP and EA values are necessary to allow the charge injection from the electrodes to the organic material. That is, the work function of the electrode injecting holes (anode) should be higher than the IP value of the hole-transporting material and the work function of the electrode injecting electrons should be lower than the EA of the electron-transporting material. Namely, injecting a charge carrier in chemical terms consists in oxidating (for holes) or reducing (for electrons) the organic compound and the redox reaction between the electrodes and the organic layer would only occur for certain IP and EA values. In addition, such oxidation and reduction processes should be reversible, since the transport of the charge carrier by hopping mechanism involves the transfer of a single electron between the ionic species and the adjacent neutral species, as it was already explained in the introduction.

The study of such properties, that is, reversibility of the oxidation or reduction processes and the approximate IP and EA values, can be performed through the cyclic voltammetry (CV) electrochemical technique. For this technique the compound is dissolved in a proper solvent (inert in the potential range in which the compound is electroactive) in the presence of a supporting electrolite and three electrodes are used: a working electrode, a contraelectrode and a reference electrode. The potential, measured between the working electrode and the reference electrode, is increased and decreased linearly within an initial potential value and an inversion potential value, which are selected according to the electroactive range of the studied compound. Simultaneously, the current intensity between the working electrode and the contraelectrode produced during the reduction and oxidation processes due to the potential variation is measured. Thus, a current vs. potential curve is obtained (Figure 1.1). The supporting electrolyte makes possible the conduction of

electric current through the solution by ionic migration. The transport of the substrate to the working electrode takes place by ionic diffusion.

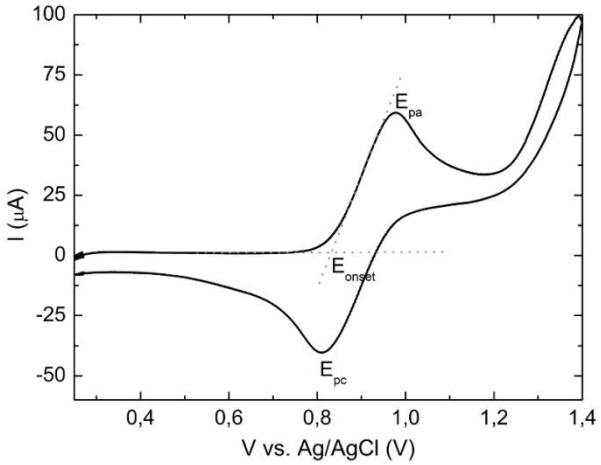

Figure 1.1. Cyclic voltammetry of a reversible oxidation process.

Although much information can be obtained from CVs, the important parameters regarding the potential application of the studied material as a semiconductor are the symmetry of the anodic and cathodic curves, which is an indicative of the reversibility of the redox process, and the onset redox potential, E_{onset}, from which the IP and EA can be estimated. A reversible oxidation or reduction process should present a profile like the one shown in Figure 1.1, so that the condition

$$E_{pa} - E_{pc} = \frac{59.6}{n} \tag{1.1}$$

is fulfilled at 25 °C, where E_{pa} and E_{pc} are the potentials of the anodic and cathodic peak, respectively, and *n* is the number of electrons involved in the redox process. However, the separation of the anodic and cathodic peaks might be slightly larger as a consequence of the slow diffusion of the substrate through the solution for fast potential rates, thus giving place to *semi-reversible* oxidation and reduction processes. In both cases, the standard redox potential, E^0, of the oxidation or the reduction coincides with the half-sum of the potentials of the cathodic and anodic peaks.

$$E^0 = \frac{E_{pa} + E_{pc}}{2} \tag{1.2}$$

From the E_{onset} of the anodic peak observed in the oxidation and the E_{onset} of the cathodic peak observed in the reduction, the IP and EA values, respectively, can be calculated on the basis of the reference energy level of ferrocene using the formula:[1]

$$EA, IP = 4.8 + E_{onset} - E^0(Fc/Fc^+) \tag{1.3}$$

where 4.8 is the vacuum level of ferrocene in eV and $E^0(Fc/Fc^+)$ is the redox potential for the oxidation of ferrocene versus the used reference electrode. Naturally, the IP and EA values of the oganic material in the solid state may differ from the values obtained in solution, since the solvation effects in the solution might be not inconsiderable.

1.1.2. Study of the absorption and photoluminescence properties.

Not intending to go into a quantum-physics discussion, it might be useful to recall some basic aspects about the light absorption and photoluminescence phenomena represented in the Perrin-Jablonski diagram (Figure 1.2).

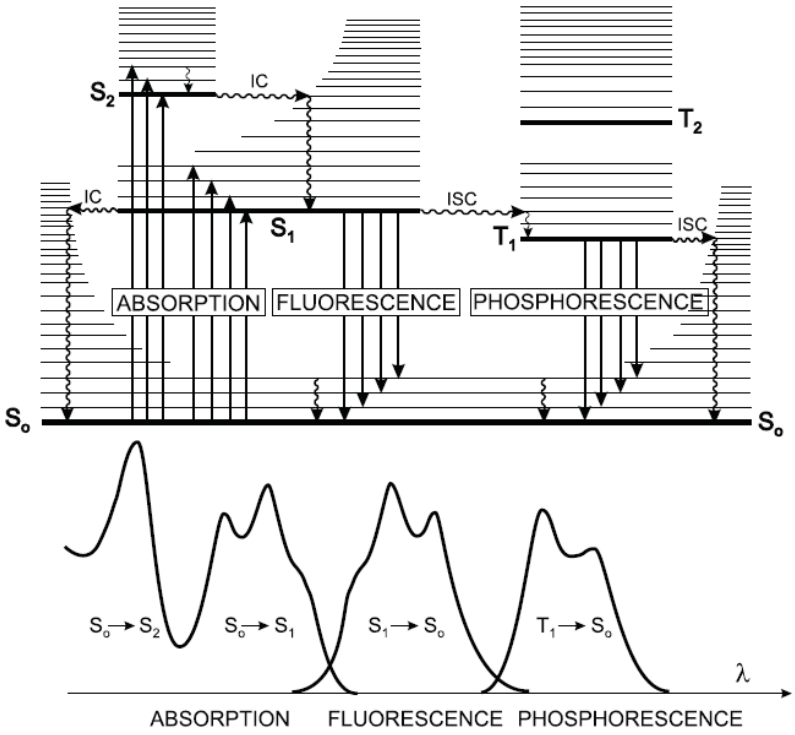

Figure 1.2. Perrin-Jablonski diagram (top) and illustration of the absorption, fluorescence and phosphorescence spectra (bottom).

In terms of electronic energy levels, a molecule in its ground state can absorb a photon of light if the photon energy is equal to the difference between two energy levels in the system. When this occurs, the molecule is excited into a higher energy state so that

$$E_1 - E_0 = h\upsilon \tag{1.4}$$

where υ is the frequency of the radiation in Hz and E_1 and E_0 are the excited and ground states of the molecule respectively.

Let us consider a molecule with closed-shell electronic configuration, that is, with an even number of electrons, each molecular orbital bearing a pair of electrons. Within each pair, the opposing electron spins cancel and the molecule has no electronic spin. Such an electronic structure is called a singlet state. When a ground-state singlet, labeled S_0, absorbs a photon of sufficient energy, it is converted to an excited singlet state in which the initial spin of the molecule is not altered. The process is so fast that the excited state has the same geometry of bond distances and bond angles as the ground state. This is the *Franck-Condon principle*. Thus, the minimum photon energy required for absorption will be when E_0 corresponds to the HOMO and E_1 to the LUMO level, which corresponds to the $S_0 \rightarrow S_1$ electronic transition. However, the most stable geometry of the excited state often differs from that of the ground state, so that the excited electronic state is formed in an excited vibrational state. In other words, each electronic state presents vibrational levels represented by the thinner lines with quantum numbers j associated to them (j = 0, 1, 2, 3..., n). The probability and intensity of an electronic transition will not be a maximum between the j = 0 levels of the ground and excited states. There might be a λ_{max} corresponding to the transition to a j = n level of the excited state. On each side of this, the absorption intensities will decrease to zero, producing the familiar bell-shaped absorption bands. According to this, the gap between the HOMO and the LUMO of a certain compound can be estimated from the onset of the absorption band assigned to the $S_0 \rightarrow S_1$ transition.

Experimentally, the efficiency of light absorption (*A*) at a wavelength λ by an absorbing medium is characterized by the absorbance defined as

$$A = \log \frac{I^0}{I} \tag{1.5}$$

where I^0 and I are the light intensities of the beams entering and leaving the absorbing medium, respectively. For low concentrations, the absorbance of a dissolved compound follows the Lamber-Beer law

$$A = \varepsilon l c \tag{1.6}$$

where ε is the molar absorption coefficient (usually in $dm^3\ mol^{-1}\ cm^{-1}$), c is the concentration (in mol dm^{-3}) and l the absorption path length (in cm). From the value of ε the nature of the molecular orbitals involved in the electronic transition can be presumed. The most usual transitions involving the HOMO and LUMO are of $\pi \rightarrow \pi^*$ and $n \rightarrow \pi^*$ nature, which correspond to bands showing ε values of the order 10^5 and 10^2-10^3, respectively.

There are two major selection rules for absorption transitions. Transitions between states of different spin multiplicities are forbidden, i.e. singlet-singlet and triplet-triplet are allowed but not singlet-triplet or triplet-singlet. However, crossing from the first singlet state S_1 to the triplet state T_1, known as *intersystem crossing*, is possible thanks to spin-orbit coupling and gives rise to phosphorescence phenomena. The second selection rule is related to the symmetry of the ground and the excited states. The role of symmetry groups theory in the transition probabilities are beyond the scope of this thesis. But it is important to note that small ε values might be indicative of a forbidden transition.

Excited molecules undergo deexcitation after a certain time. The emission of photons accompanying the $S_1 \rightarrow S_0$ relaxation is called fluorescence. Apart from a few exceptions, fluorescence emission occurs from S_1 and therefore its characteristics do not depend on the excitation wavelength. According to this, the corrected excitation spectrum is identical to the absorption spectrum, provided that there is a single species in the ground state. Namely, the excitation spectrum is obtained by registering the variations in fluorescence intensity at a chosen wavelength as a function of the excitation wavelength.

The fluorescence spectrum is located at higher wavelengths (lower energy) than the absorption spectrum because of the energy loss in the excited state due to vibrational relaxation. The fluorescence spectrum often resembles the first absorption band, something called the *mirror image rule*.

The gap expressed in wavenumbers (cm^{-1}) between the maximum of the first absorption band and the maximum of fluorescence is called the *Stokes shift*. This parameter can provide information on the excited states. For instance, when the dipole moment of a fluorescent molecule is higher in the excited state than in the ground state, the Stokes shift increases with solvent polarity. This effect is specially pronounced in molecules possessing an electron-donor (D) group conjugated to an electron-acceptor (A) group that undergo intermolecular charge transfer (ICT). For such molecules the excited state reached upon excitation (locally excited state, LE) is not in equilibrium with the surrounding solvent molecules if the later are polar. Thus, the system undergoes relaxation to give a solvated ICT state, which in some cases may imply conformational changes. Moreover, DA molecules can present dual fluorescence as a result of the emission of both the LE state and the ICT state.

The fraction of excited molecules that return to the ground state S_0 with emission of fluorescence photons is the fluorescence quantum yield, Φ_F. In other words, the fluorescence quantum yield is the ratio of the number of emitted photons to the number of absorbed photons. For routine

characterization, the Φ_F is determined regarding to the Φ_F of a reference compound according to the formula:[2, 3]

$$\Phi_{F[1]} = \frac{A_r}{A_x}\frac{F_x}{F_r}\frac{n_x^2}{n_r^2}\,\Phi_{F(r)} \tag{1.7}$$

where A is the absorbance, F the area of the emission band, n the refractive index and the subscripts x and r refer to the sample and the reference, respectively.

The reference compound should absorb and emit at close wavelengths to those corresponding to the studied compound. The absorbance of both compounds should have a value within the 0.04-0.05 range so that it can be assumed that the emission intensity is proportional to the concentration of the analyte.[2, 3]

The excited molecule may undergo many processes that may lead to the decrease and even the loss of the fluorescence intensity, phenomena known as *quenching*. Intra and intermolecular electron or energy transfer or the formation of excimers or exciplexes, which can be more or less favored for certain solvents, are some examples of quenching causes.

1.1.3. Determination of liquid-crystalline phases

While differential scanning calorimetry (DSC) allows the determination of the phase transition energies and temperatures, the experimental identification and characterization of the liquid crystal phases of discotic molecules is performed by polarized optical microscopy (POM) and X-ray diffraction.

1.1.3.1. Polarized optical microscopy (POM)

Due to their anisotropic nature, liquid crystals are birefringent. They possess two refractive indices, one for light polarized parallel to the director, and the other, for light polarized perpendicular to the director. The former gives rise to the slow ray, or extraordinary ray, (n_e in Figure 1.3) whereas the latter is responsible for the fast ray, or ordinary ray (n_o in Figure 1.3), propagating through the sample. The birefringence is characterized by the difference in the refractive indices for the ordinary and extraordinary rays. The magnitude of the optical anisotropy is generally lower for discotics than for calamitics.

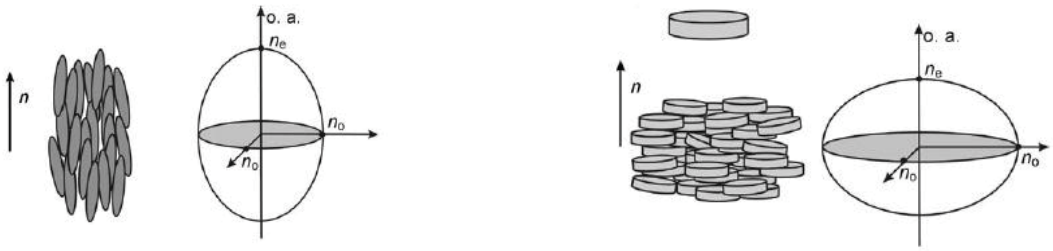

Figure 1.3. Ordinary (n_o) and extraordinary (n_e) rays in calamitic (left) and discotic (right) molecules.

If an isotropic transparent material is placed between two polarizers, oriented at 90° to each other (crossed polarizers), no light will normally emerge because the light from the first polarizer is completely absorbed by the second. Insertion of an isotropic material does not change this situation because the polarization of light is unchanged. The polarized light propagating through a liquid crystal may be considered to comprise two components –light polarized along the director and light polarized perpendicular to the director. As the radiation propagates through the material, these two polarizations get out of phase and emerge from the material as elliptically polarized light. Therefore, the field of view will appear bright unless the incident polarized light has its polarization direction either parallel or perpendicular to the director.

Normally a liquid crystal introduced between the two parallel glass plates for its observation by POM show multiple patterns, indicating that the alignment of the molecules is only local, with the director varying continuously over large distances. Discontinuities in the optical image suggest the presence of discontinuities in director distribution, in the form of singular points, lines and walls, that is, defects. The regular arrangement of defects and domains of the liquid crystal is called *texture*, which is useful in the identification of the formed liquid crystal phase. For example, for hexagonal columnar mesophases conic fan-shaped (Figure 1.4 left) or flower like textures are characteristics, while for lamellar mesophases the most typical texture is the broken fanlike texture (Figure 1.4 right).

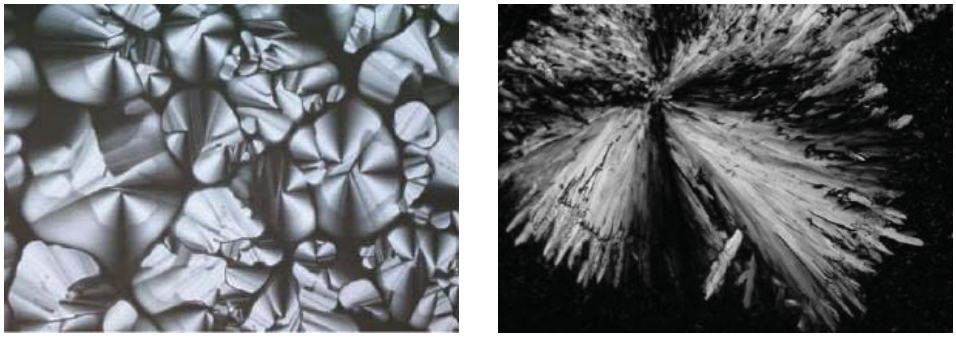

Figure 1.4. Conic fan-shaped (left) and broken fanlike (right) textures observed by a POM in a hexagonal columnar and in a lamelar mesophase, respectively.

1.1.3.2. X-ray diffraction

When electromagnetic energy is incident on the surface of a material, some of it will be reflected specularly, so that the angle of incidence is equal to the angle of reflection. For materials presenting a crystal-like arrangement, such as the liquid crystals, constructive and destructive interference between the radiation reflected from successive crystal planes will occur when the wavelength of the incident radiation is of the same order as the lattice spacing. The condition for maxima in the reflected radiation is provided by Bragg's law.

$$\lambda = 2d_{hkl} \sin\theta \tag{1.8}$$

where θ is the angle of incidence, conventionally measured from the plan of reflection in X-ray crystallography and d_{hkl} is the interplanar spacing. The crystal planes are noted using the Miller indices, three integers (lmn), where each index denotes an intersection of a plane with a direction (l,m,n) in the basis of the reciprocal lattice vectors.

The columns formed by piled discotic molecules arrange in bidimensional lattices, the most usual being the hexagonal and the rectangular lattices (Figure 1.5).[4] The 2D diffraction patterns of samples of this kind of mesophases present reflection peaks in the small-angle regime, which belong to the large periods of the 2D lattice, and reflections in the wide-angle regime, which belong to the short distances. A broad diffuse halo is normally found in the wide-angle regime, which corresponds to the liquid-like order of the alkyl side chains. Additionally, a second relatively sharp peak can be also detected related to the regular stacking of the mesogenic cores along the column long axis.

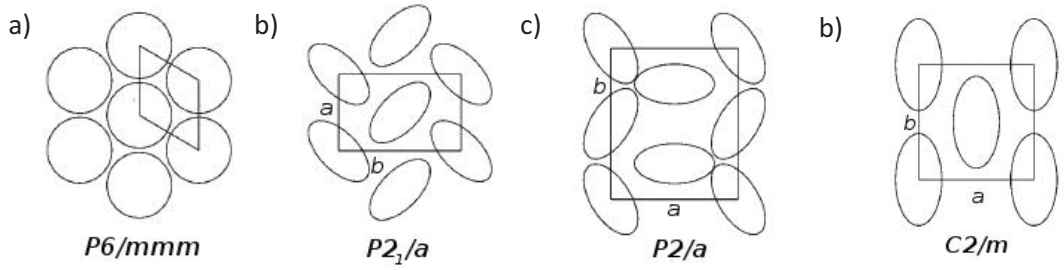

Figure 1.5. Most usual bidimensional arrangements of the columns in hexagonal (a) and rectangular (b,c and d) columnar mesophases

The hexagonal columnar (Col_h) arrangement can be detected from the characteristic *d* spacing ratios in the low angle region, which are 1:1/√3:1/2:1/√7:1/3:1/√12 for the first peaks, that is, for the reflexions of the planes with Miller indices (10), (11), (20), (21), (30), (22). The *d* spacings follow the equation:

$$\frac{1}{d_{hk}^2} = \frac{4}{3}\frac{h^2 + k^2 + hk}{a^2} \tag{1.9}$$

where *a* is the lattice parameter shown in Figure 1.5.

The 2D X-ray patterns of the columnar rectangular mesophase (Col_r) resemble those of a Col_h mesophase with a diffuse halo in the wide-angle regime and sharp reflections in the small-angle regime. However, in the Col_r the (10) peak of the Col_h arrangement splits in the (20) and (11) reflections. This observation is explained graphically in figure 1.6. The Col_r presents two lattice parameters *a* and *b* that can be calculated from the equation:

$$\frac{1}{d_{hk}^2} = \frac{h^2}{a^2} + \frac{k^2}{b^2} \tag{1.10}$$

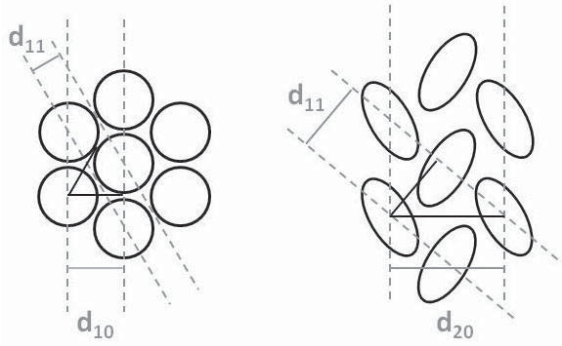

Figure 1.6. Interplanar distances in a Col_h (left) and a Col_r (right) mesophases.

The indexation of the rest of peaks in the low angle region according to equation 1.10, once the lattice parameters have been found, allows the determination of the space group to which the rectangular arrangement belongs, according to the reflection conditions shown in Table 1.1. However the identification of the space group is complex and often not completely unambiguous.

Table 1.1. Reflection conditions for rectangular columnar phases.

Space group	Reflection conditions	
$P2_1/a$	hk:	-
	h0:	h = 2n
	0k:	k = 2n
P2/a	hk:	-
	0k:	k = 2n
C2m	hk:	h+k = 2n

Both kinds of columnar arrangements may present a sharp peak in the wide angle region within the range 3.3-3.7 Å corresponding to the core-core spacing. This reflection indicates the existence of π-π intermolecular interactions. In those cases the mesophases are called ordered hexagonal columnar, (Col_{ho}) and ordered rectangular columnar (Col_{ro}) mesophases.

Discotic molecules can present other liquid-crystalline phases in which they do not pile in columns. This is the case of lamelar (L) and nematic (N) mesophases. In lamelar mesophase the disk-like molecules arrange in layers as it is represented in Figure 1.7 thus giving place to *d* spacing ratios in low angle regime of the X-ray profile 1:2:3:4 and so on. The interlayer spacing is normally comparable to the molecule diameter. In the nematic mesophases only orientational order is present so that no crystalline planes are formed and thus no reflections are registered in the low angle regime of the diffractograms.

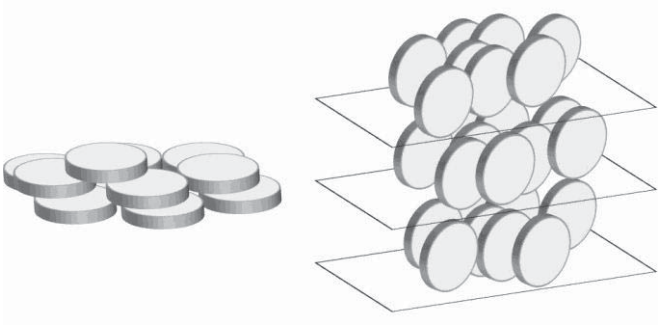

Figure 1.7. Nematic (left) and lamelar (right) arrangement of discotic molecules.

1.1.4. Study of radical compounds

1.1.4.1. Electronic paramagnetic resonance (EPR)

The EPR is a spectroscopic technique based in the interaction of the paramagnetic species, that is, species with a permanent magnetic moment, with an external magnetic field. Organic radicals, bearing an unpaired electron, are paramagnetic systems and thus the EPR technique allows the detection of radicals and the study of some of their features, e. g. the distribution of the magnetic spin density over their structure or the intermolecular interactions that may exist.

The magnetic moment of an electron, $\boldsymbol{\mu}$, is given by the expression

$$\boldsymbol{\mu} = g\beta\boldsymbol{S} \tag{1.11}$$

Where $\boldsymbol{S}$ is the spin angular momentum vector of the electron, *g* is a dimensionless constant called *Landé factor* and β is the electronic Bohr magneton. The interaction between the electron magnetic moment and an applied magnetic field $\boldsymbol{H}$ is represented by the Hamiltonian

$$\mathcal{H} = \boldsymbol{\mu} \times \boldsymbol{H} \tag{1.12}$$

which becomes

$$\mathcal{H} = g\beta H S_z \tag{1.13}$$

if the applied magnetic field is in the z direction. Quantum theory demands that the allowable electron spin states are quantized. Thus the states of the spin m_S in any given direction can only take up one of a set of discrete values going from *S*, *S*-1, ..., -*S*. Since *S* = 1/2 for the electron, there are only two allowed values for m_S, +1/2 and -1/2, that is, two orientations of the spin, parallel or antiparallel to H_z, as it is illustrated in Figure 1.8, also called the electronic Zeeman energies.

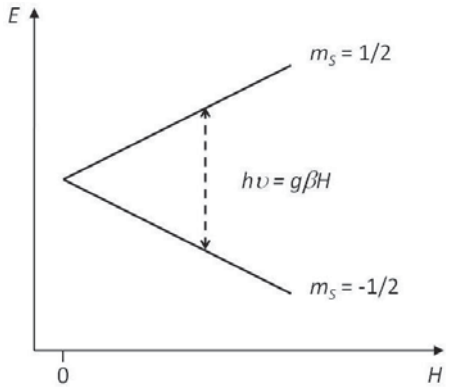

Figure 1.8. Energy levels for a *S* = 1/2 system as a function of the applied magnetic field *H*.

Application of an oscillating field perpendicular to *H* induces transitions provided the frequency υ is such that the resonance condition

$$h\upsilon = g\beta H \tag{1.14}$$

is satisfied. To make transitions possible, the electromagnetic field has a component perpendicular to the static magnetic field. Moreover the conservation of angular momentum imposes a selection rule of $\Delta m_S = 1$.

The equipments used for the EPR experiments in this thesis detected the resonant energy absorption by keeping the oscillating electromagnetic radiation (microwaves) fixed and varying the magnetic field, that is, the difference between the Zeeman levels. From the first derivative of the absorption curve the following parameters can be obtained:

- *The g factor*. This parameter is analog to the chemical shift in nuclear magnetic resonance (NMR). The effective *g* value varies according to the electronic structure of the molecule leading to a deviation from the *g* value of the free electron g_e = 2.0023. Namely, the spin orbit coupling

endows the unpaired electron with a small orbital angular momentum and alters its effective magnetic moment. This deviation is the characteristic *g* value of a species.

Specifically, the simple resonance expression (eq. 1.14) with a single numerical value of parameter *g* is applicable only to systems that behave isotropically. In the general case there are three principal *g* values, g_{xx}, g_{yy} and g_{zz}, since different levels are coupled by the magnetic field along the direction of the three axes x, y and z of the magnetic entity. Thus a truly isotropic system, when the radical species is in solution, is the one for which $g_{xx} = g_{yy} = g_{zz}$. If the molecular system has an axial symetry, the values of *g* are reduced to values in the parallel direction, $g_{\|}$, and the perpendicular direction, $g_{\perp}$, to the magnetic field for an anisotropic system.

- *Hyperfine structure.* The hyperfine structure is the magnetic coupling that can occur between the spin of the unpaired electron and those of nearby magnetic nuclei in the molecule, that is, nuclei with a magnetic spin $I \neq 0$. Before the application of an external field, the electron and nuclear spins are already coupled and are properly treated in terms of their combined spins. For nuclei with $I = 1/2$, commonly ^{1}H, ^{13}C, ^{14}N or ^{18}O, this leads to $2nI+1$ energy levels for each value of m_S where *n* is the number of nuclei coupled with the electron. Thus, in the presence of an applied magnetic field, the states diverge the 0 states being unaffected, and $2nI+1$ lines might be observed in the spectrum (Figure 1.9). The hyperfine constant with each nucleus, A_0, is measured directly from the experimental spectra as the separation between component peaks.

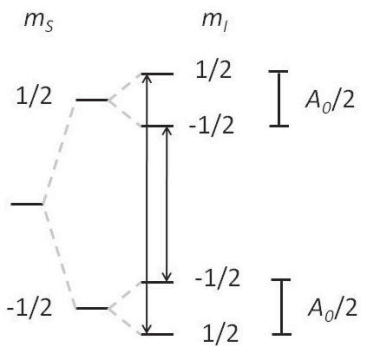

Figure 1.9. Energy levels of a system with one unpaired electron and one nucleus with $I = 1/2$. The arrows correspond to the allowed EPR transitions with hyperfine coupling operative.

- *Linewidth.* The linewidth of the EPR signal is understood as the ΔH between the minimum and the maximum of the first derivative. It depends on the relaxation processes that the spin undergoes after the absorption. Two parameters are related to the relaxation processes, the spin-lattice relaxation time, usually denoted t_1, and the spin-spin relaxation time, t_2.

A collection of spins at thermal equilibrium in an applied magnetic field has a bulk magnetization, or magnetic moment, because of the excess population in the lower level. The parameter t_1 characterizes the rate of decay of this magnetization when the field is switched off. Moreover, in an applied field the spins are all brought into phase and if there are magnetic interactions then different spins will experience slightly different local fields and thus there will be a spread in their precession frequencies. A gradual dephasing will then take place, which often follows an exponential rate characterized by a time, t_2.

For a sample in liquid solution with a Lorenzian lineshape,

$$\frac{1}{t_2} = \frac{\sqrt{3}}{2}\,\Delta H \tag{1.15}$$

However, in a solid containing radicals which have no hyperfine interactions and an isotropic *g*-factor, the EPR line will be a superposition of shapes from all the spins with a random distribution of the local fields so that the total lineshape will be Gaussian. Therefore the study of the linewidth might be very complex and particular for each sample.

- *Intensity.* The intensity of the EPR signal depend on many parameters: the number of paramagnetic centers in the sample; the transition probability per second per spin, where the population difference ΔN between the lower energy states (N_1) and the higher energy states (N_2), whose relation at thermal equilibrium is given by the Boltzmann distribution,

$$\frac{N_\alpha}{N_\beta} = e^{g\beta H/kT} \tag{1.16}$$

play an important role; the number of lines in the spectrum (the fine and hyperfine structure); the sample temperature, among others. In fact, for a given population of a paramagnetic state, the intensity of EPR absorption *I* is given by a Curie-law dependence, that is, $I \propto 1/T$.

A remark should be done concerning the EPR study of molecules presenting triplet states, i. e. molecules bearing two parallel unpaired electrons that couple together so that its total spin is $S = 1$. Since the total spin is 1, three sublevels will be obtained under a magnetic field. If there is only exchange and electrostatic interactions between electrons, the three sublevels of a triplet state would be exactly degenerate and the EPR spectra would be very like those of radicals with spin 1/2. However the magnetic dipole-dipole forces between the two unpaired electrons remove the degeneracy and lead to highly anisotropic spectra in most molecules. Not aiming to go deep in the

analysis of EPR spectra of triplet states, it should be said that a parameter to detect triplet states is the recording of the *half-field line*. That is, recording the $\Delta m_s = 2$ transition that occurs at the same frequency as for the $\Delta m_s = 1$ transitions by applying a field with half the strength, $H/2$ (Figure 1.10).

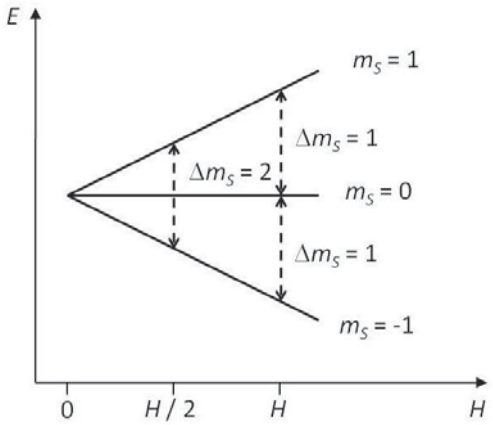

Figure 1.10. Allowed ($\Delta m_s = 1$) and forbidden ($\Delta m_s = 2$) transitions in a triplet state.

1.1.4.2. Magnetic susceptibility

The definition of magnetic susceptibility can be given from the equation

$$M = \chi H \tag{1.17}$$

Where M is the magnetization or magnetic moment per unit of volume and H is the magnetic field strength. Although the volume magnetic susceptibility χ is dimensionless, it is usually expressed as emu cm^{-3}. Therefore, the molar susceptibility χ_M is given in emu mol^{-1}. In order to simplify we will note molar susceptibility as χ. In principle χ is the algebraic sum of two contributions associated with different phenomena:

$$\chi = \chi_P + \chi_D \tag{1.18}$$

where χ_P and χ_D are the diamagnetic an paramagnetic susceptibilities, respectively. For the purpose of this thesis, it is sufficient to specify that χ_D is due to the interaction of the magnetic field with the motion of the electrons of the molecule in their orbits and that it is independent of the temperature and the strength of the applied field.

χ can also be expressed as

$$\chi = \frac{N\mu^2}{3kT} \tag{1.19}$$

where μ, the module of magnetic moment, is

$$\mu^2 = g^2\beta^2 S(S+1) \tag{1.20}$$

and β is the Bohr magneton, *g* is the Landé factor and *S* the total electronic spin. For a monoradical μ is estimated to be 1.73β. At low temperatures, paramagnetic species follow the Curie-Weiss law

$$\chi_P = \chi - \chi_D = \frac{C}{T - \Theta} \tag{1.21}$$

where *C* is the Curie constant and Θ is the Weiss temperature. The plot of $\chi(T)$ versus *T* (Figure 1.11) is a hyperbole that fits the equation

$$A + B\chi + CT = \chi T \tag{1.22}$$

so that coefficients $B = \Theta$ and $C = \chi_D$. Once the χ_P is obtained by extracting χ_D to the observed χ, the plot of the product $\chi_P T$ as a function of the temperature allows to determine if the nature of the intermolecular interactions between the paramagnetic molecules when the temperature is close to 0 K. The decrease of $\chi_P T$ values at lower temperatures indicates antiferromagnetic interactions while their increase indicates ferromagnetic interactions. It should be remarked that for a monoradical $\chi_P T$ = 0.37 emu mol^{-1} K.

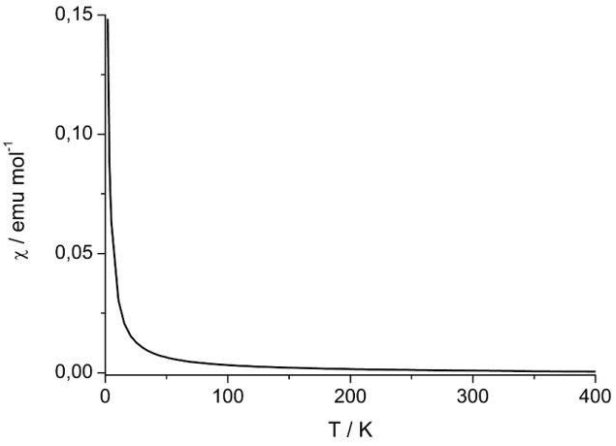

Figure 1.11. Molar magnetic susceptibility of a monoradical in function of the tempertaure.

References

[1] P. Bauer, H. Wietasch, S. M. Lindner, M. Thelakkat, *Chem. Mater.* **2006**, *19*, 88-94.
[2] S. Fery-Forgues, D. Lavabre, *J. Chem. Educ.* **1999**, *76*, 1260.
[3] D. F. Eaton, *Pure Appl. Chem.* **1988**, *60*, 1107-1114.
[4] L. Sabine, B. Angelika, S. Nelli, G. Frank, H. Constanze, S. Giusy, J. Roxana, K. Elisabeth, S. Sven, S. Alina, T. Martin, *Angew. Chem. Int. Ed.* **2007**, *46*, 4832-4887.

Consulted bibliography

Manuel M. Baizer. *Organic Electrochemistry. An introduction and a guide*. New York, Marcel Dekker (1973).

Bernard Valeur. *Molecular Fluorescence. Principles and applications.* Weinheim, Wiley-VCH (2002).

Martyn Symons. *Chemical and biochemical aspects of electron-spin resonance spectroscopy.* Workingham, Van Nostrand Reinhold Company Ltd. (1978)

Alan Carrington, Andrew D. McLachlan. *Introduction to magnetic resonance.* London, Science Paperback (1979).

Neil M. Atherton. *Electron Spin Resonance.* Chichester, Ellis Horwood Ltd. (1973).

John A. Weil, James R. Bolton, John E. Wertz. *Electron paramagnetic resonance.* New York, John Wiley & Sons Inc. (1994)

Olivier Kahn. *Molecular Magnetism.* New York, VCH Publishers Inc. (1993).

Michael C. Petty. *Molecular Electronics. From principles to practice.* Chichester, Wiley & Sons Ltd. (2008).

Richard L. Carlin. *Magnetochemistry.* Berlin, Springer-Verlag (1986)

Dietrich Demus, John W. Goodby, George W. Gray, Hans-Wolfgang Spiess, Vokmar Vill. *Handbook of Liquid Crystals.* Weinheim, Wiley-VCH (1998)

1.2. Radical carbazole derivatives

1.2.1 Radical molecular glasses.

In this section the synthesis and characterization of small molecules that combine radical units of the tris(2,4,6-trichlorophenyl)methyl series and carbazole units in their structure is presented. The target products were both derivatives in which these two units were conjugated and in which they were separated by an alkyl chain. The aim for the conjugated derivatives was the attainment of radical adducts showing glassy states while for the non-conjugated carbazole/TTM systems the aim was the study of the photochemical properties.

1.2.1.1. Synthesis

1.2.1.1.1. Introduction of carbazole and indole units in a trisphenylmethyl radical core.

Preparation of the tris(2,4,6-trichlorophenyl)methyl (**TTM**) radical was performed as reported.[1] The tris(2,4,6-trichlorophenyl)methane (**αH-TTM**) resulting from the Friedel-Crafts condensation of 1,3,5-trichlorobenzene and chloroform in presence of $AlCl_3$, was deprotonated and oxidised to give **TTM** radical in good yields (Scheme 1.1).

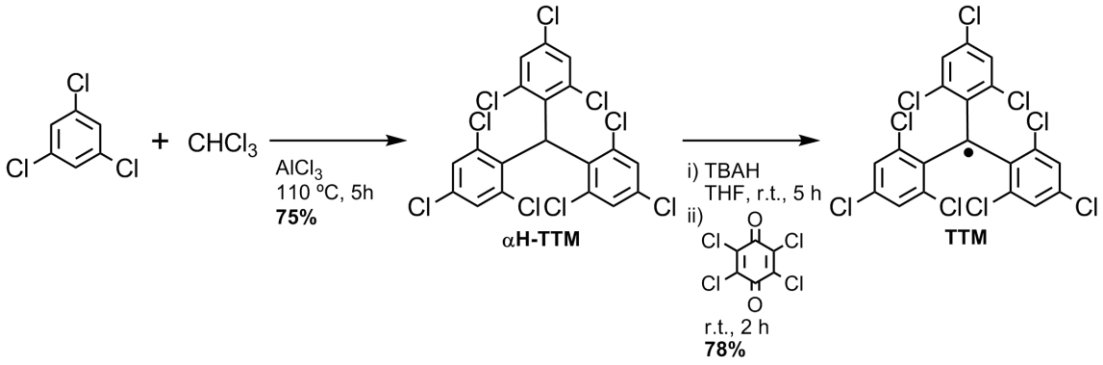

Scheme 1.1

[4-(*N*-carbazolyl)-2,6-dichlorophenyl]bis(2,4,6-trichlorophenyl)methyl radical (**1**) was first synthesized through a direct coupling between *N*H-carbazole and TTM radical in boiling DMF solution and in the presence of a base (scheme 1.2).[2] In this reaction, a mixture of [4-(*N*-carbazolyl)-2,6-dichlorophenyl]bis(2,4,6-trichlorophenyl)methane (**1H**) and the corresponding triphenylmethyl radical **1** was obtained in moderate yields, together with a mixture of **αH-TTM** and the starting **TTM** radical, and the products that resulted from the substitution of two and three chlorines in *para* position regarding the trivalent carbon of the **TTM** radical core in their protonated and radical forms, the compounds bis[4-(*N*-carbazolyl)-2,6-dichlorophenyl](2,4,6-trichlorophenyl)methane (**2H**) and the corresponding triphenylmethyl radical **2**, and tris[4-(*N*-carbazolyl)-2,6-dichlorophenyl]methane (**3H**)

and the corresponding triphenylmethyl radical **3**, respectively. In all the mixtures, the majority was the protonated form. The corresponding pure radicals were then obtained by the deprotonation and oxidation of the resulting anions as shown in Scheme 1.3.

The lack of control in the stechiometry of this reaction was considered a main inconvenience to obtain good synthetic yields for each mixture. Hence, new synthetic paths were sought to optimize the preparation of the mixture **1H**+**1**. The two considered strategies were: 1) the use of a metallic catalyst in the coupling processes and; 2) the decrease from three to one in the number of *para*-chlorines that act as leaving groups in the starting triphenylmethyl radical.

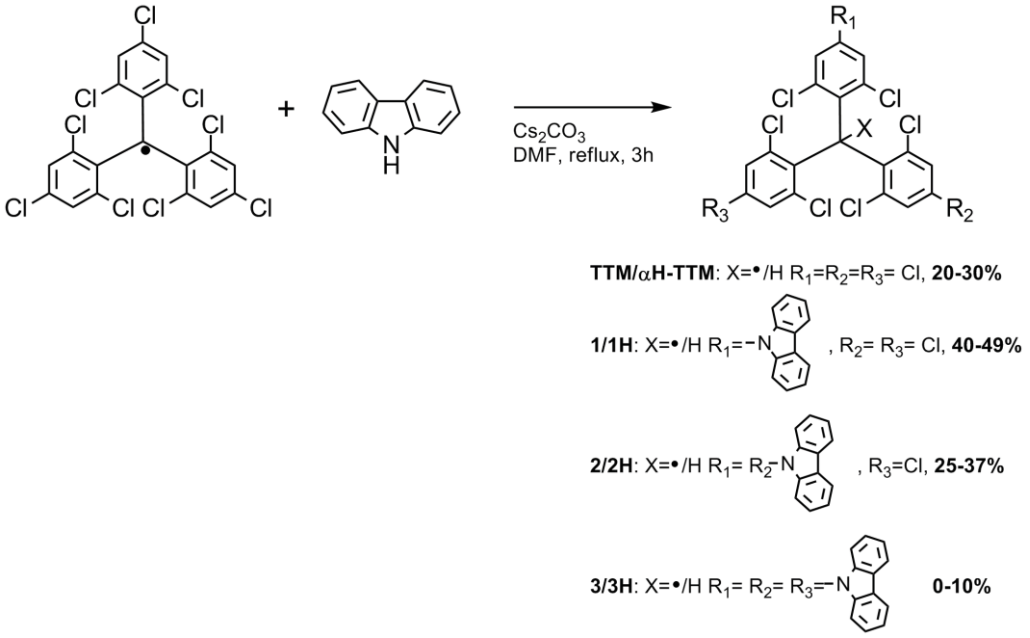

Scheme 1.2

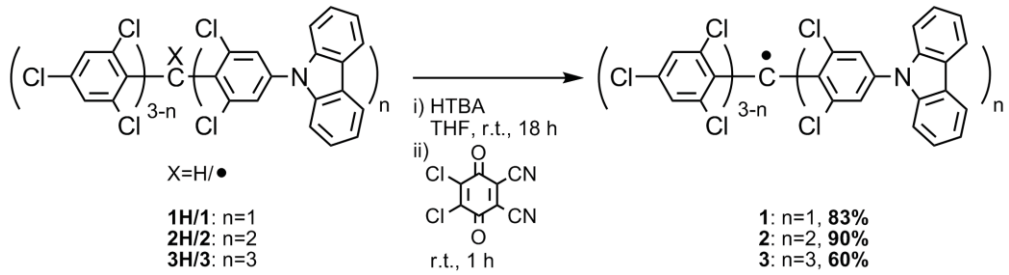

Scheme 1.3

The metal chosen for the first strategy was Cu (0), since this catalyst had been widely used in our group for the preparation of *N*-phenylcarbazole derivatives by Ullmann's reaction.[3] The reaction was set by using commercial *N*H-carbazole and either the **TTM** radical or its precursor **αH-TTM** as starting materials. Yields of **1H** + **1** were higher when the **TTM** radical was the reagent, even though reaction times must be much shorter with **TTM** radical than with **αH-TTM** as reagent, due to the less stability

of the former species in the used reaction conditions. However, no improvements were achieved regarding the traditional method for the preparation of **1**. Another example in the literature for catalyzed carbazole arylation was the use of Pd (0) as catalyst.[4, 5] In this case, no formation of the target products was detected after a long time of reaction (48 h), using **αH-TTM** as starting material. Table 1.2 displays the reaction conditions and yields obtained in all these processes.

Table 1.2. Reaction conditions and yields of **1H** + **1** for the catalyzed couplings of carbazole and **TTM/αH-TTM**

catalyst/base	Solvent	TTM /αH-TTM[a]	base[a]	cat. / %	t / h	yield / %
Cu / K_2CO_3	DMA	3[b]	1.2	10	3	8
Cu / K_2CO_3	DMA	2.5[b]	1.2	5	2.5	8
Cu / K_2CO_3	DMA	1.1[c]	1.2	5	20	5
Pd-DPPF/ ^{t}BuONa	Toluene	1.5[c]	1.5	5	48	X

[a]Relative to *N*H-carbazole molar concentration. [b]**TTM**. [c]**αH-TTM**.

The second strategy was concerned with the coupling reaction of the *N*H-carbazole and bis(2,6-dichlorophenyl)(2,4,6-trichlorophenyl)methyl radical (**4**).[6] The stability of radical **4** is similar to that of TTM, since it keeps the six chlorine atoms around the central carbon that bears the unpaired electron. But radical **4** presents only one reaction site, assuming that the coupling reaction between the radical and *N*H-carbazole proceeds through a S_NAr mechanism in which the chloride ion acts as leaving group.

The first step in the seven-stage synthesis of radical **4**, shown in Scheme 1.4, consisted in the preparation of a diphenylmethane system. This was achieved by the attack of the organolithium generated from the 1,3-dichlorobenzene with nBuLi on 2,6-dichlorobezaldehyde to give the bis(2,6-dichlorophenyl)methanol (**5**). Chlorination of methanol **5** to get compound **6** was performed with good yields by using $AlCl_3$ in carbon disulfide and with quantitative yields by using $SOCl_2$, as solvent and reagent. In both cases, the Lewis acid coordinates the hydroxy group, thus activating the corresponding carbon atom in front of the nucleophilic substitution, and also it acts as a nucleophilic chloride ion source.

The Friedel-Crafts reaction of compound **6** with 1,3,5-trichlorobenzene would lead to the formation of byproducts resulting from the autocondensation of **6**. First of all, the compound **6** must be deactivated with electron-withdrawing nitro groups so that the Friedel-Crafts takes place only with 1,3,5-trichlorobenzene as nucleophile. Attempts of nitration of **6** with fuming nitric acid produced the degradation of the starting material, while using a mild nitrating agent such as $Cu(NO_2)$ left the starting material unmodified. For this reason, nitration was finally performed, as it had been

previously described, by treating compound **6** with nitronium tetrafluoroborate giving moderate yields of the target product **7** and a small amount of the mononitrated methane.

By a Friedel-Crafts reaction between **7** and 1,3,5-trichlorobenzene in the presence of $AlCl_3$ the triphenylmethane system **8** was obtained in good yield. Then, elimination of the nitro groups of **8** was achieved by reducing them to amino groups with $SnCl_2$, generation of the corresponding diazonium salt with isoamyl nitrite and easily denitrogenation giving compound bis(2,6-dichlorophenyl)(2,4,6-trichlorophenyl)methane (**4H**).

The last stage of the synthesis was the preparation of the corresponding triphenylmethyl radical **4** from the parent compound **4H**. This reaction consisted in the deprotonation of the methyl carbon and the oxidation of the resulting anion to give the neutral radical **4**. Several reaction conditions were tested to obtain pure radical **4** (Table 1.3). Identification as well as determination of the purity of radical **4** was possible by means of IR spectroscopy, showing a characteristic stretching aromatic peak at 1525 cm^{-1}, assigned exclusively to the radical species, and the lack of a peak at 996 cm^{-1}, corresponding exclusively to the precursor **4H**. It was proved that the best method was the use of the DMSO conjugated base (DMSO and sodium hydroxide) for a week to generate the anion and then I_2 as oxidant agent (Scheme 1.4). All other methods did not give a pure radical **4**.

Table 1.3. Radicalization attempts of **4H**.

base/ox./solvent	base[a]	t_1 / h[b]	ox.[a]	t_2 / h[b]	4+4H / %	4 / %
HTBA/p-chloroanyl/THF	1.5	5	4	18	74	-
	4	5	4	18	95	-
	4	18	4	72	80	-
HTBA/CrO_3/THF	2	6	6	18	90	-
	1.5	2	5	18	-	-
DMSONa/I_2/Et_2O	> 10	72	> 10	2	80	-
	> 10	144	> 10	2	-	91

[a]Relative to molar concentration of **4H**. [b]Reaction times for the deprotonation (t_1) and oxidation (t_2) stages.

Coupling reaction between *N*H-carbazole and radical **4** was performed in the same conditions as for the **TTM** counterpart (Scheme 1.5). However, an unexpected product was formed instead of the target product. In addition to the reduced and protonated **4H**, obtained in a very high yield (75%), a coupling fraction identified by mass spectrometry as **10H** was isolated. The generation of [4-(*N*-carbazolyl)-2,6-dichlorophenyl](2,6-dichlorophenyl)(2,4,6-trichlorophenyl)methyl radical (**10**) from this new adduct allowed to confirm by EPR measurements that the carbazole group had substituted a hydrogen in *para* position regarding the trivalent carbon instead of the chlorine in *para* position (see section 1.2.1.3). The mechanism proposed to explain this result is presented in Scheme 1.6.

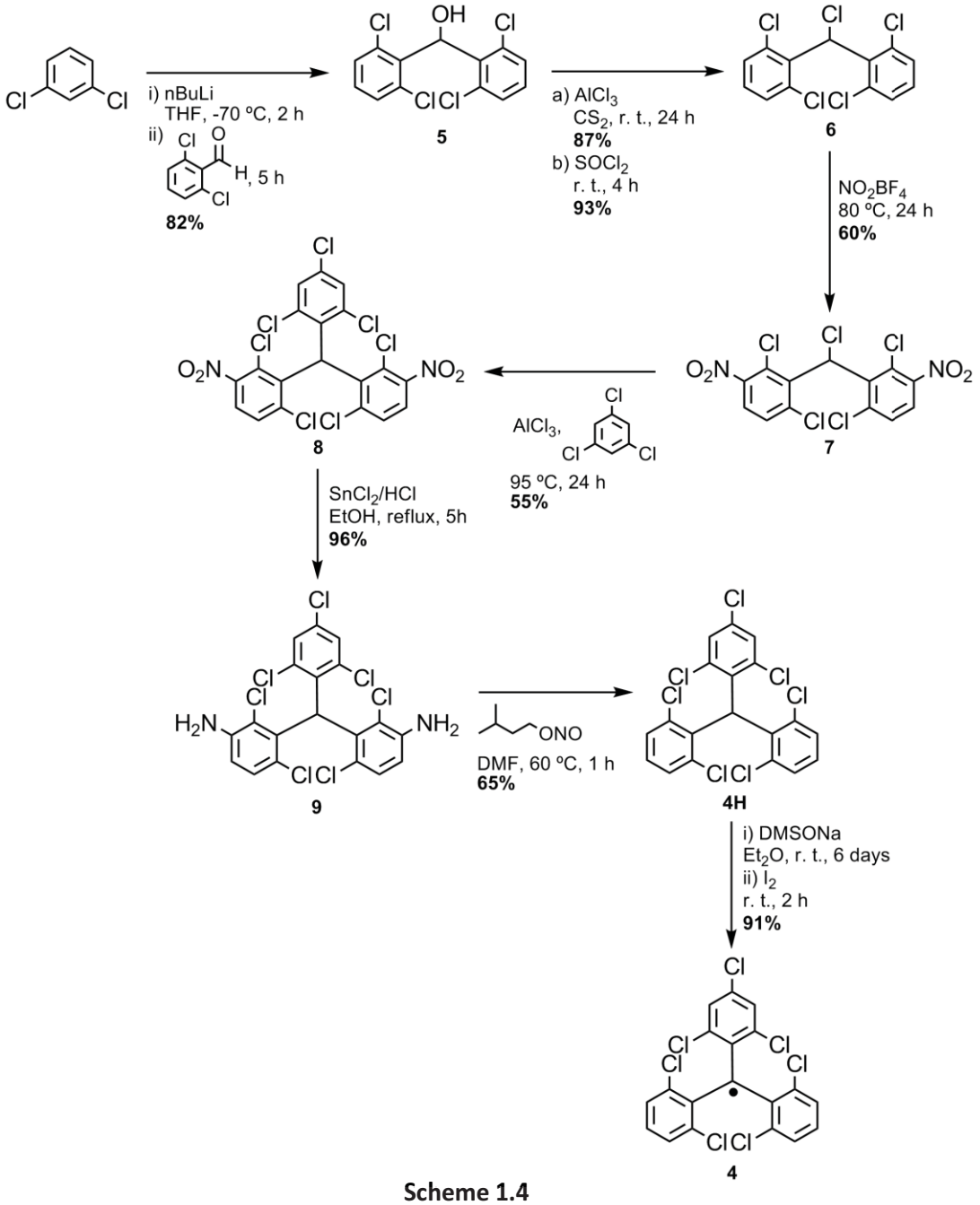

Scheme 1.4

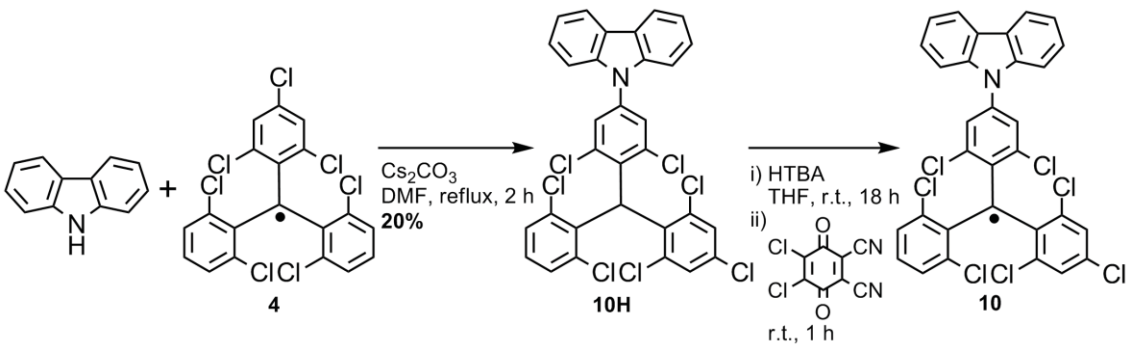

Scheme 1.5

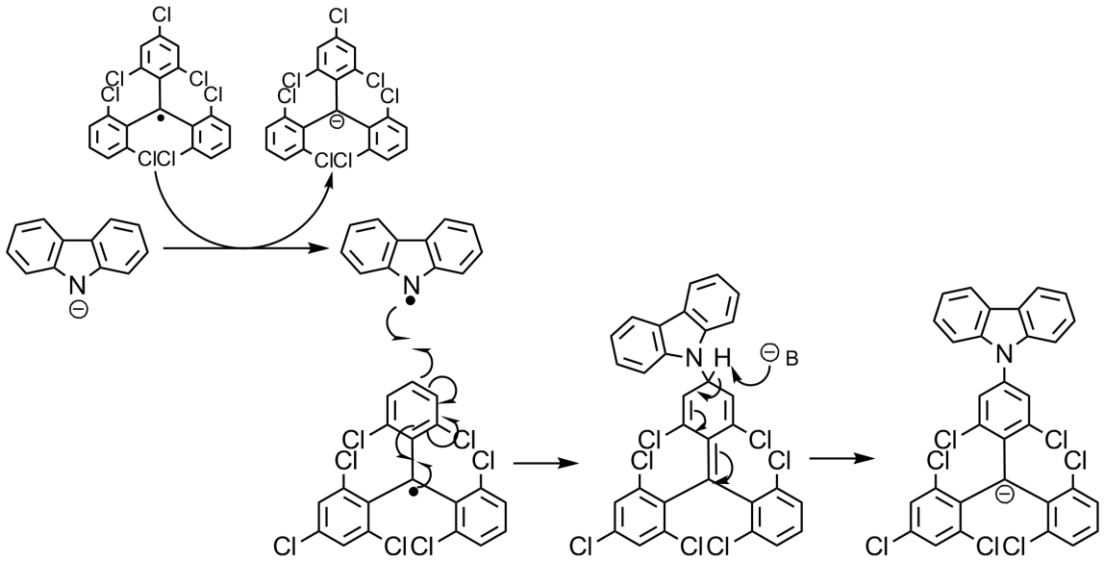

Scheme 1.6

Taking this reaction into account, coupling between *N*H-carbazole and **TTM** radical may proceed as shown in Scheme 1.7, that is, through a radicalary mechanism instead of a S_NAr mechanism, as it had been previously supposed. The radical mechanism gives a possible explanation for the lack of improvement in the reaction yield when a Cu (0) catalyst was used and for the total lack of products when the Pd (0) catalyst was used in the reaction with αH-TTM as starting material

Hence, preparation of *N*-carbazolylTTM radical family was performed with the classical method from then on. This method was also applied for the preparation of the radicals of the *N*-indolylTTM radical family,[7] by synthesizing [2,6-dichloro-4-(*N*-indolyl)phenyl]bis(2,4,6-trichlorophenyl)methane (**11H**), bis[2,6-dichloro-4-(*N*-indolyl)phenyl](2,4,6-trichlorophenyl)methane (**12H**) and tris[2,6-dichloro-4-(*N*-indolyl)phenyl]methane (**13H**) (Scheme 1.8) and then oxidizing them to the corresponding triphenylmethyl radicals **11**, **12** and **13** (scheme 1.9).

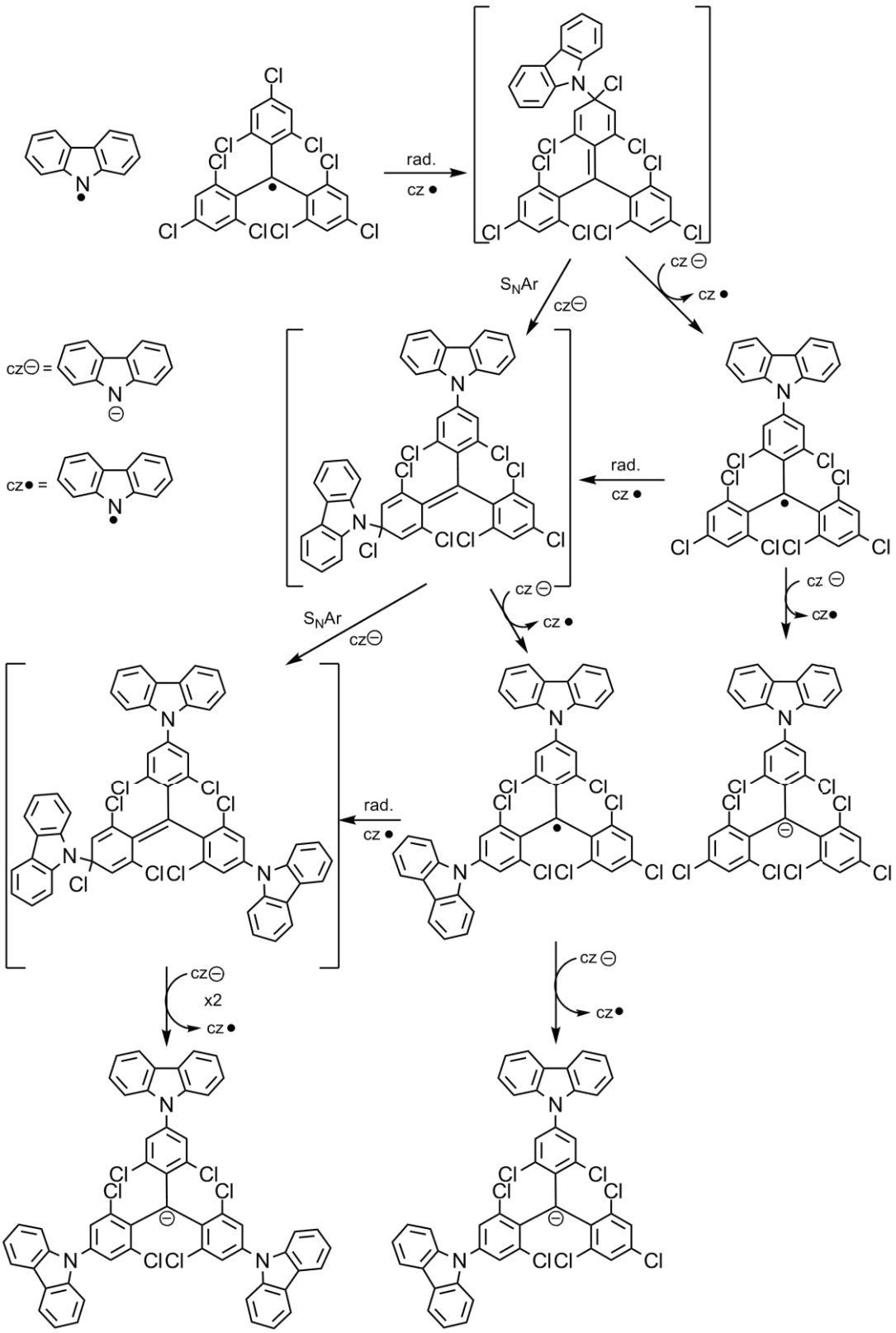

Scheme 1.7

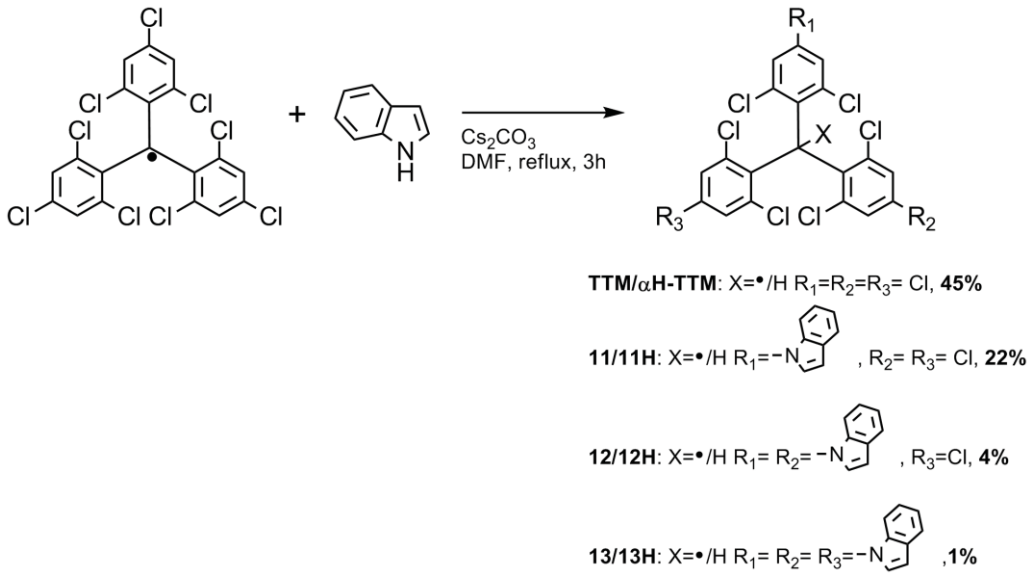

Scheme 1.8

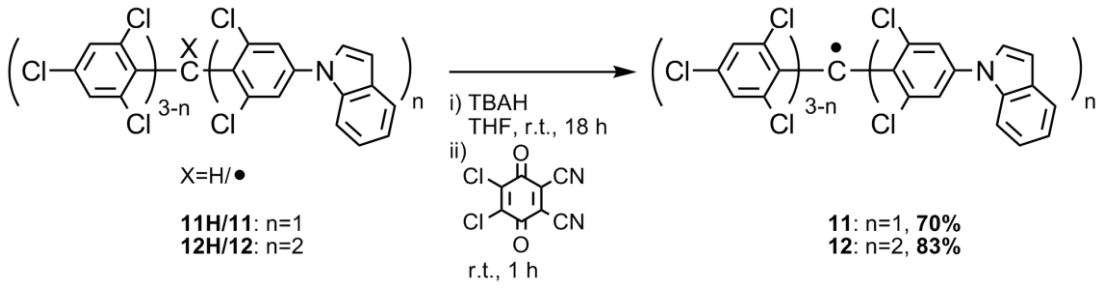

Scheme 1.9

1.2.1.1.2. Acylated and alkylated radicals of the *N*-carbazolylTTM family.

In light of the results discussed in the previous section, the synthesis of acylated and alkylated derivatives of **1** was performed by coupling between the properly substituted *N*H-carbazole and the **TTM** radical and the subsequent preparation of the corresponding triphenylmethyl radicals from the products of the coupling reaction [4-(3,6-diacetyl-*N*-carbazolyl)2,6-dichloro-phenyl]bis(2,4,6-trichlorophenyl)methane (**14H**) and [2,6-dichloro-4-(3,6-diethyl-*N*-carbazolyl)phenyl]bis(2,4,6-trichlorophenyl)methane (**15H**). The acetylation of *N*H-carbazole by Friedel-Crafts reaction took place with good yields on the most active positions of the heterocylce to give 3,6-diacetyl-*N*H-carbazole (**16**). The Clemmensen reduction of the carbonyl groups gave 3,6-diethyl-*N*H-carbazole (**17**) in moderate yields. The coupling between either **16** or **17** with the TTM radical, though, worked with very low yields (Scheme 1.10). In addition, compound **14H** could not be isolated from the mixture of byproducts that were formed during the coupling reaction.

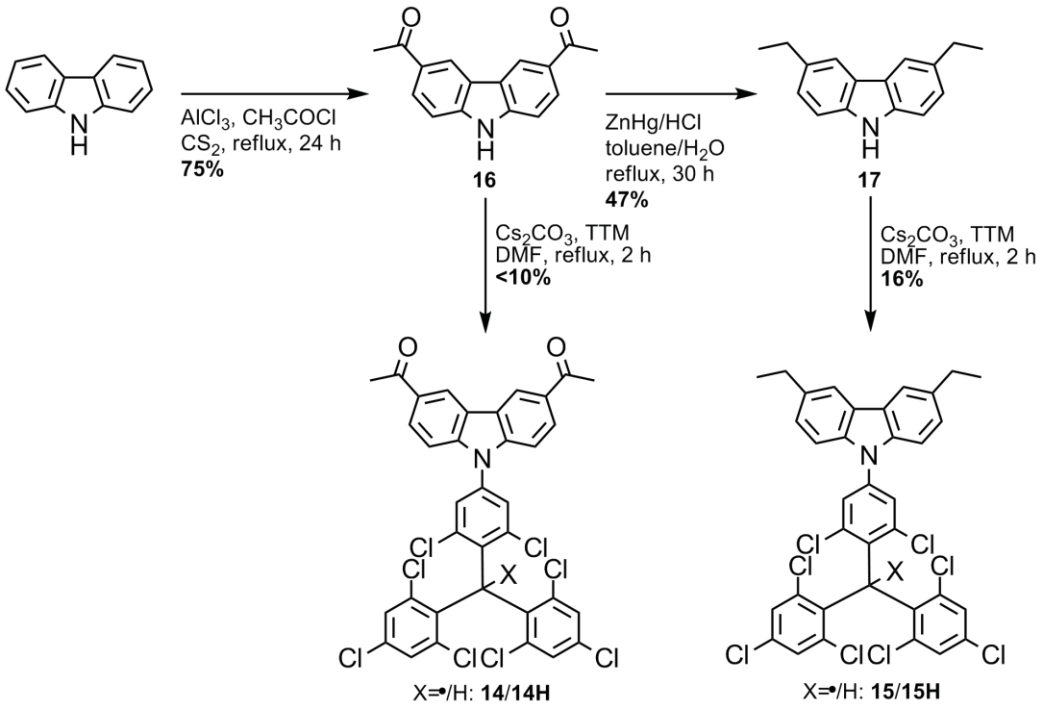

Scheme 1.10

For this reason, the acetylation and alkyation of radical **1** by direct Friedel-Crafts were performed. The first reaction worked successfully after very short times of reaction and gave [2,6-dichloro-4-(3,6-diethyl-*N*-carbazolyl)phenyl]bis(2,4,6-trichlorophenyl)methyl radical (**14**), preserving the radical nature of the starting material **1**. However, Friedel-Crafts alkylation with ethylchloride led to the formation of many products, very difficult to isolate and identify. Therefore, an alternative synthetic path was applied consisting on the Clemmensen reduction of the ketones of **14**. The carbonyl groups were effectively reduced, as well as the central carbon, so that a subsequent preparation of the

corresponding [2,6-dichloro-4-(3,6-diethyl-*N*-carbazolyl)phenyl]bis(2,4,6-trichlorophenyl)methyl radical (**15**) by the usual deprotonation of **15H** and oxidation of the corresponding anion was required (Scheme 1.11).[8]

These acylation conditions proved to work with good yields for longer acylchlorides (Scheme 1.12), as well as the reduction of the carbonyl group (Scheme 1.13), thus allowing the preparation of a wide range of new radicals. By using either radical adducts **1**, **2** or **3,** [2,6-dichloro-4-(3,6-dioctanoyl-*N*-carbazolyl)phenyl]bis(2,4,6-trichlorophenyl)methyl radical (**18**), bis[2,6-dichloro-4-(3,6-dioctanoyl-*N*-carbazolyl)phenyl](2,4,6-trichlorophenyl)methyl radical (**19**) and tris[2,6-dichloro-4-(3,6-dioctanoyl-*N*-carbazolyl)phenyl]methyl radical (**20**) were obtained in good yields, respectively.[9]

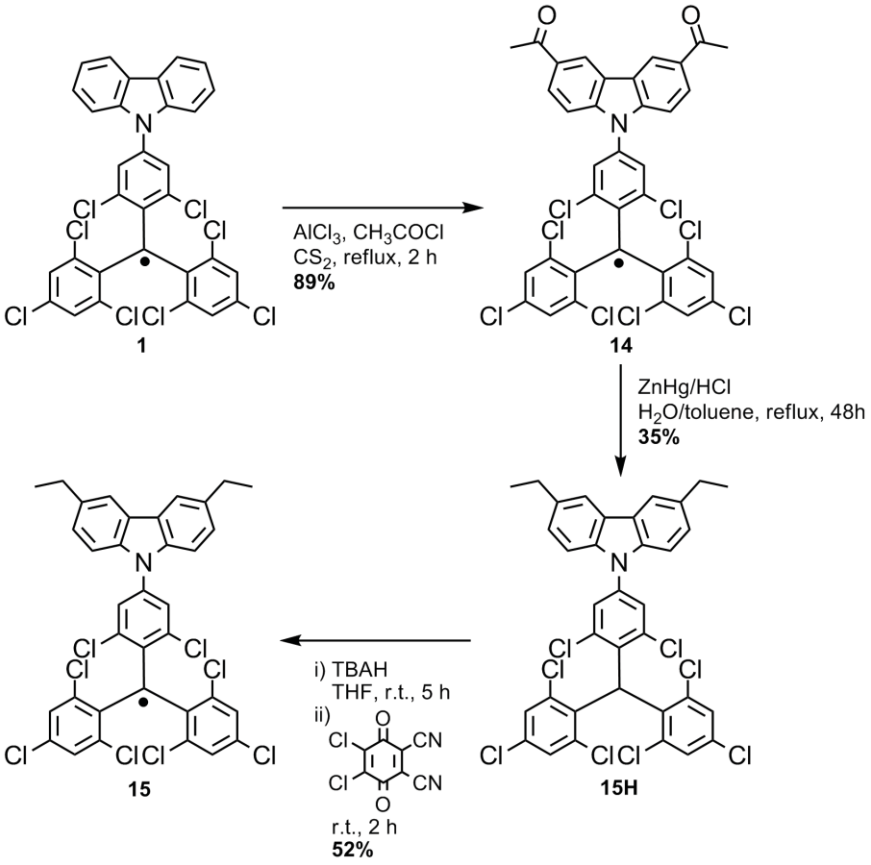

Scheme 1.11

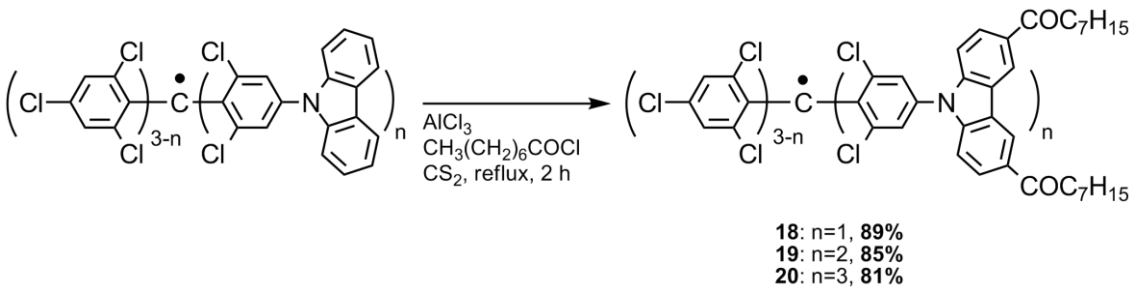

Scheme 1.12

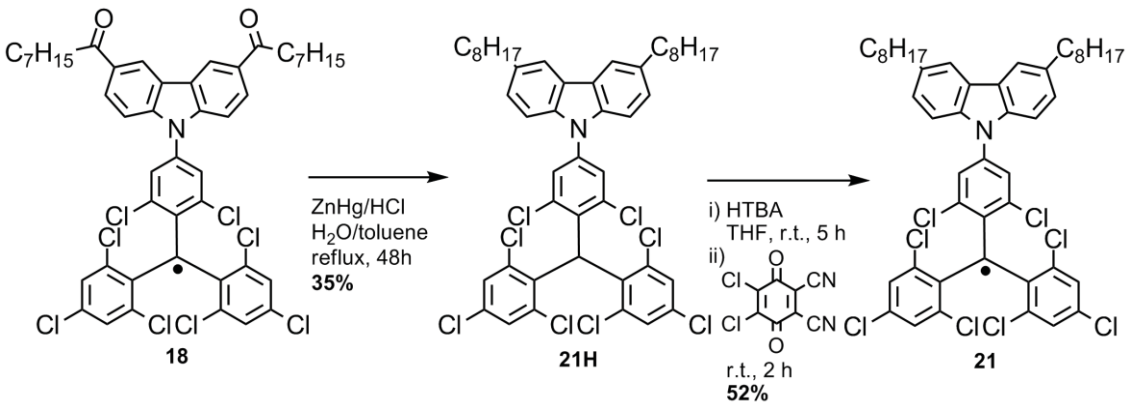

Scheme 1.13

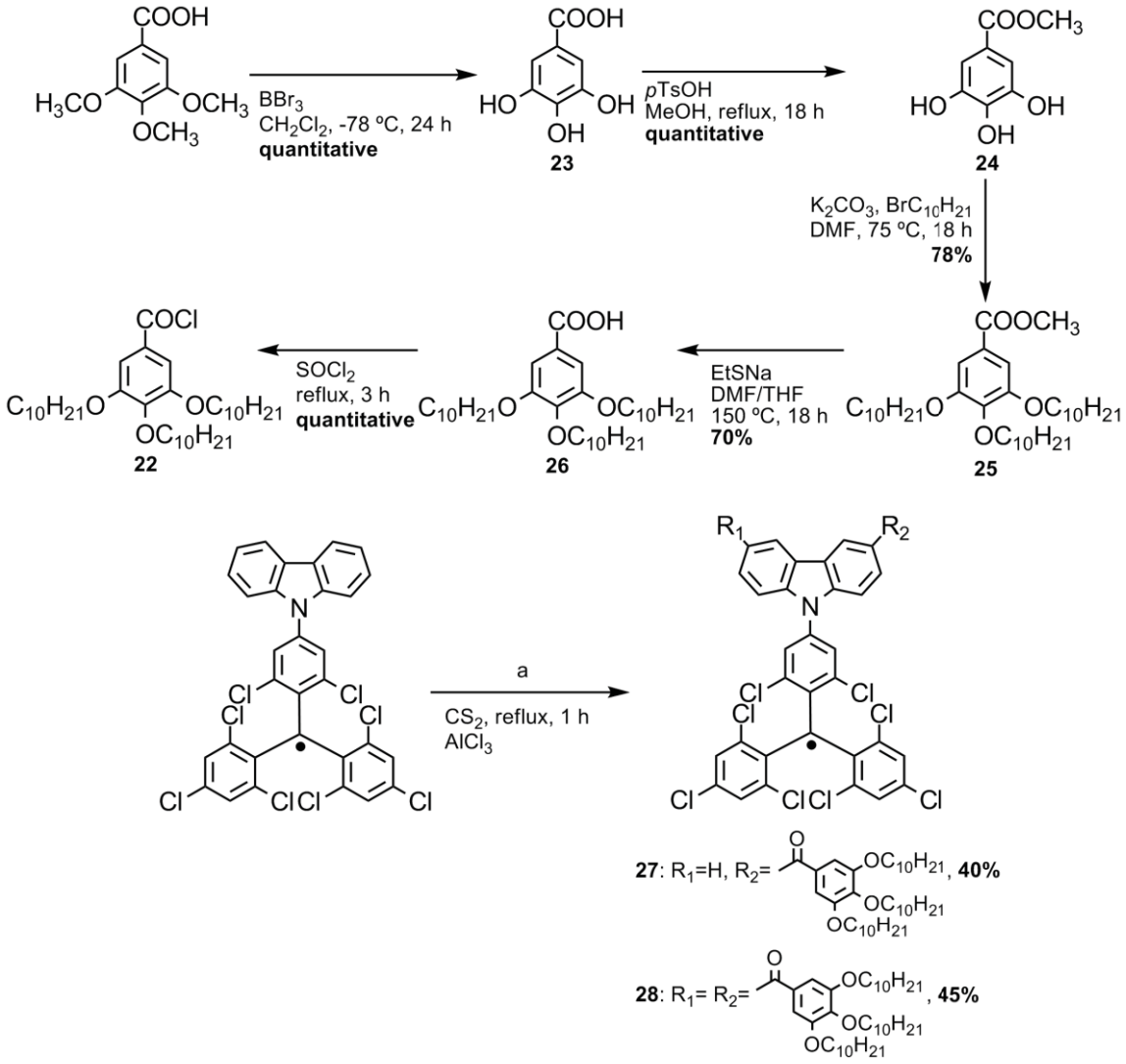

a. **27**: **22** (1 eq.); **28**: **22** (2 eq.)

Scheme 1.14

Radical **1** underwent acylation also with more complex acylchlorides such as 3,4,5-trisdecyloxybenzoyl chloride (**22**) thus giving {2,6-dichloro-4-[3-(3,4,5-tridecyloxybenzoyl)-*N*-carbazolyl]phenyl}bis(2,4,6-trichlorophenyl)methyl radical (**27**) and {2,6-dichloro-4-[3,6-bis(3,4,5-tridecyloxybenzoyl]-*N*-carbazolyl)phenyl}bis(2,4,6-trichlorophenyl)methyl radical (**28**), by the addition of one or two equivalents of **22** in the reaction, respectively (Scheme 1.14). The aim of attaching these benzoyl systems was to modify the photoluminescence properties as a result of a more extended aromaticity and, in addition, to attain stronger intermolecular interactions ought to the greater number of chains, which may promote the Van der Waals interactions, and thus may favor the formation of a liquid crystal phase

1.2.1.1.3. Non-conjugated carbazole-bridge-TTM systems.

Aiming to the study of charge and/or energy transfer processes derived from the combination of the carbazole fragment -which has an electron-donor nature- and the **TTM** radical fragment –which has a bipolar nature, i.e. which can act as electron-acceptor or as electron-donor moiety-, two new systems with a donor-bridge-acceptor (D-B-A) configuration were prepared. Photoinduced intramolecular electron-transfer processes in donor-acceptor systems are of considerable interest and importance from the aspects of light-energy conversion. Specifically, photoinduced charge separation is a key process in the operation of molecular photovoltaic devices, and D-B-A systems present a proper structural design to achieve it.[10-16]

The prepared D-B-A compounds consisted in one carbazole unit and one **TTM** radical unit linked by an alkyl spacer of different length, {{4-[3-(*N*-carbazolyl)propyl]amino}-2,6-dichlorophenyl}bis(2,4,6-trichlorophenyl)methyl radical (**29**) and {{4-[8-(*N*-carbazolyl)octyl]amino}-2,6-dichlorophenyl) bis(2,4,6-trichlorophenyl)methyl radical (**30**) (Scheme 1.15). The chosen starting radical for the synthesis of these systems was (4-amino-2,6-dichlorophenyl)bis(2,4,6-trichlorophenyl)methyl radical (**31**)[17] for two reasons: 1) its close similarity to the electronic nature of *N*-carbazolylTTM, due to the presence of a nitrogen in a *para* position regarding to the central carbon and 2) the greater functionalization possibilities of the amino group, which allows easy *N*-alkylation. The preparation of **31** was already known in the research group and was performed as shown in Scheme 1.16. The cationic salt of the **TTM** radical, generated with the oxidizing agent $SbCl_5$, was treated with a saturated solution of NH_3 in CH_2Cl_2 to give the corresponding protonated imine. The reduction of this imine with $SnCl_2$ led to radical **31** in good yields.

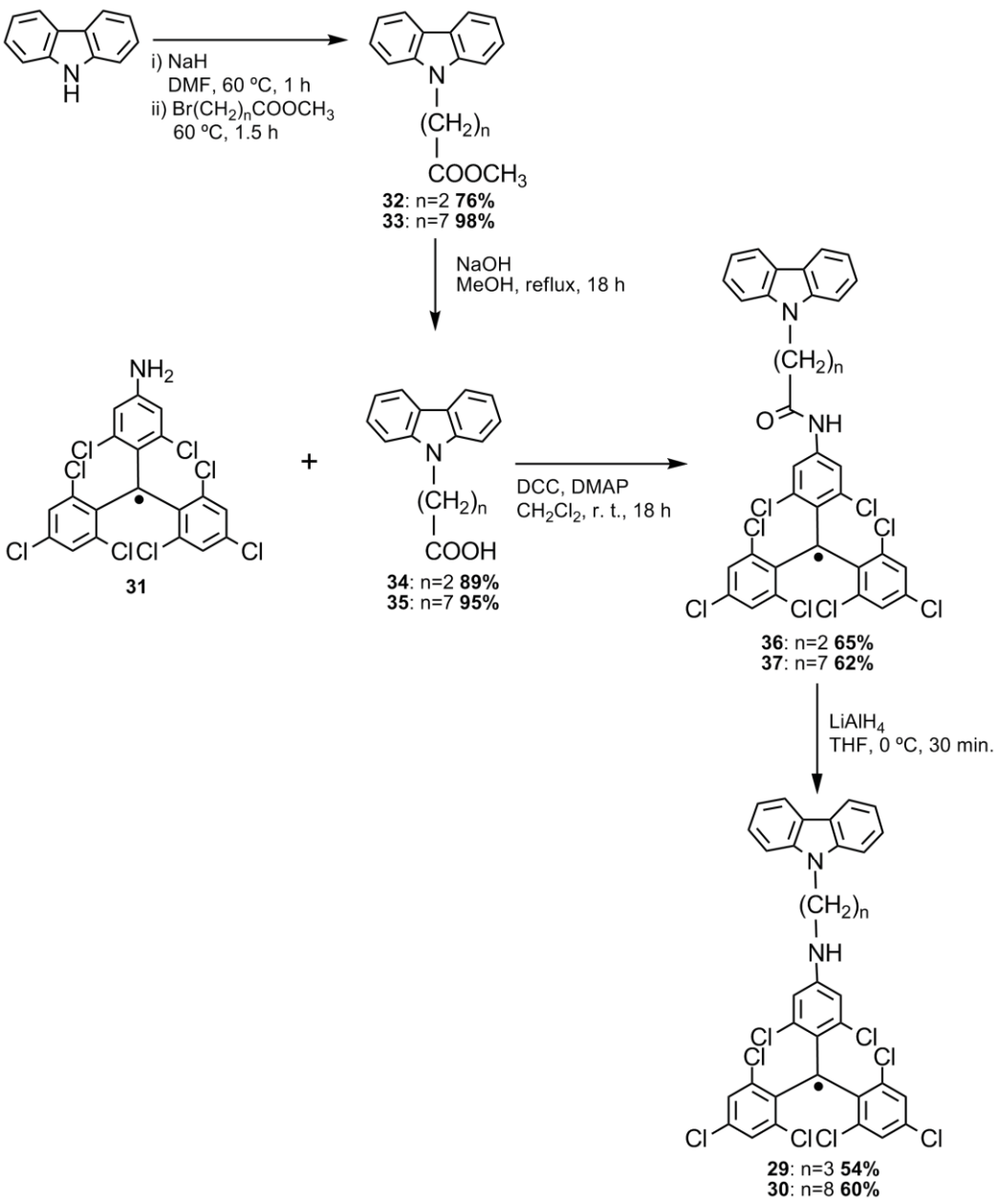

Scheme 1.15

The *N*-alkylation of the *N*H-carbazole with the corresponding alkylbromides bearing a terminal methyl ester, methyl 3-bromopropionate and methyl 8-bromooctanoate, by using sodium hydride as a base and the subsequent saponification of the terminal esters with NaOH in methanolic medium gave the *N*-alkylcarbazoles with terminal carboxilic acids **34** and **35** in good yields. Amidation of **34** and **35** with radical **31** was achieved using DMAP as a catalytic base and DCC as activating agent of the carboxylic group and gave radicals **36** and **37** with good yields. Finally, the reduction of the amide with $LiAlH_4$[18] gave the secondary amines **29** and **30**, preserving the radical center.

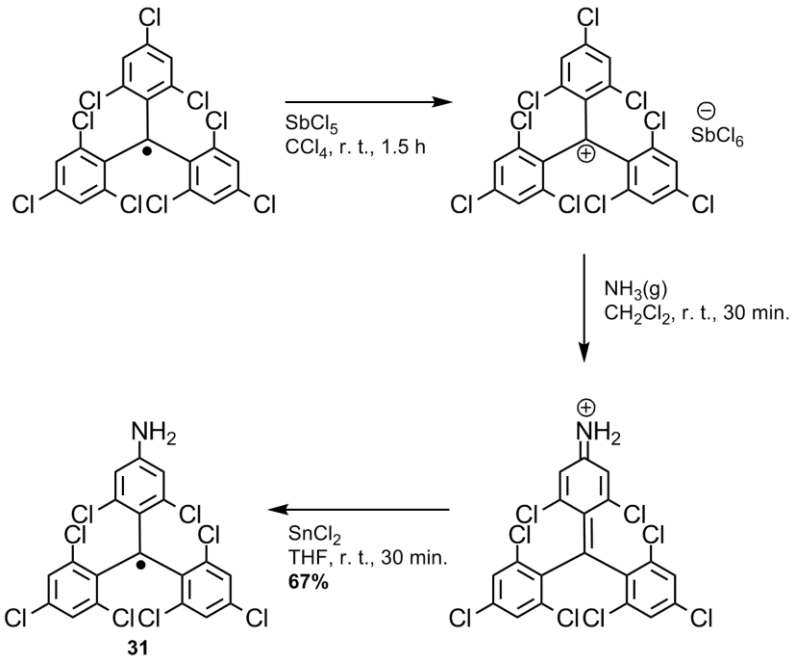

Scheme 1.16

[4-(*N*-ethyl)amino-2,6-dichlorophenyl]bis(2,4,6-trichlorophenyl)methyl radical (**38**) was prepared as a reference compound for the fluorescence comparative studies (see section 1.2.3). Its preparation consisted in the two step synthesis shown in Scheme 1.17. The synthesis involved the amidation of radical **31** with acetylchloride in the presence of triethylamine as a base and the subsequent reduction of the resulting amide with $LiAlH_4$.

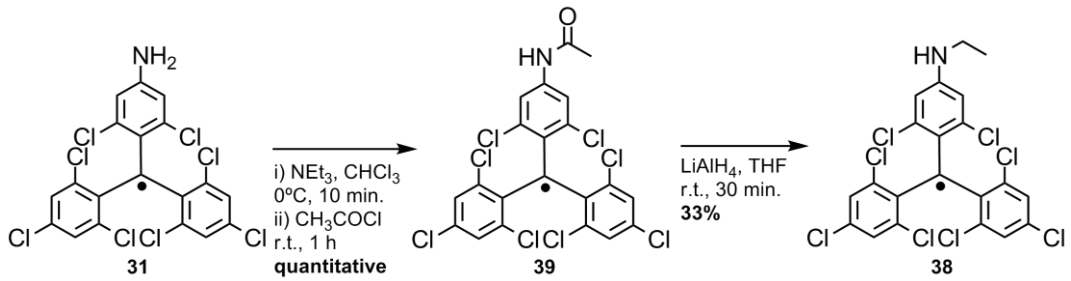

Scheme 1.17

1.2.1.2. Differential Scanning Calorimetry analyses.

The number of carbazole units attached to the triphenylmethyl aromatic core, as well as the attachment of different side groups in the carbazolyl fragment of the various radical adducts, lead to variation in their thermal properties (Table 1.4).

The increase of the carbazole fragments in the aromatic structure of the radicals **1**, **2** and **3** results in higher melting points, all radicals undergoing decomposition during the melting process. Also the

attachment of two acetyl chains in positions 3 and 6 of the carbazole fragment of radical **1** produces an increase in the melting temperature in radical **14**. The same effect, though much weaker, is observed in radical **15**, which bears a 3,6-diethylcarbazolyl moiety. However, by lengthening the acyl and the alkyl chains (radical adducts **18** and **21**) the melting point drops, thus allowing the melting of the materials without any degradation. This behavior is also observed in radical **19** regarding its precursor radical **2**, but not in radical **20**, which seems to undergo some degradation despite showing a lower m.p. than its precursor **3**. Namely, the endothermic peak associated to the melting of radical **20** in the first heating process displace to higher temperatures and shows a different ΔH associated to it in the second heating curve of the cyclic DSCs.

The observation of radicals **18**, **19** and **21** in the polarized optical microscope (POM) revealed that these materials do not crystallize during their cooling after melting. Their cyclic DSC analyses are in agreement with these observations, since no exothermic peaks are observed in their cooling curves from the liquid state, but the inflexions corresponding to their glass transition temperatures, T_g (Figure 1.12 left). These inflexions are symmetrically reproduced in their second heating curves, which do not present any endothermic peak associated to the melting of a crystalline phase. Thus, the three radicals have the ability of forming amorphous films by a proper thermal treatment, i.e. a rapid cooling of their liquid state.[9]

Radicals **1**, **2** and **3** can also form amorphous films by spin coating of their THF or $CHCl_3$ solutions. However, these glassy layers undergo crystallization with time or by the supplying of heat and the determination of their T_g by DSC analyses was only possible in the case of **1**, which presented the inflexion associated to the glass transition in the first heating curve, followed by an exothermic peak attributed to its crystallization (Figure 1.12 right).

Table 1.4. Melting points and glass transition temperatures determined by DSC analyses.

	m. p. / °C	T_g / °C		m. p. / °C	T_g / °C
1	298[a]	80[b]	**2**	347[a]	-
14	359[a]	-	**19**	143	56
15	300[a]	-	**3**	355[a]	-
18	188	67	**20**	249[a]	-
21	136	25	**11**	258	97
28	-	-	**12**	224	105

[a]Melting with decomposition. [b]Amorphous layer prepared by spin-coating of a chloroformic solution

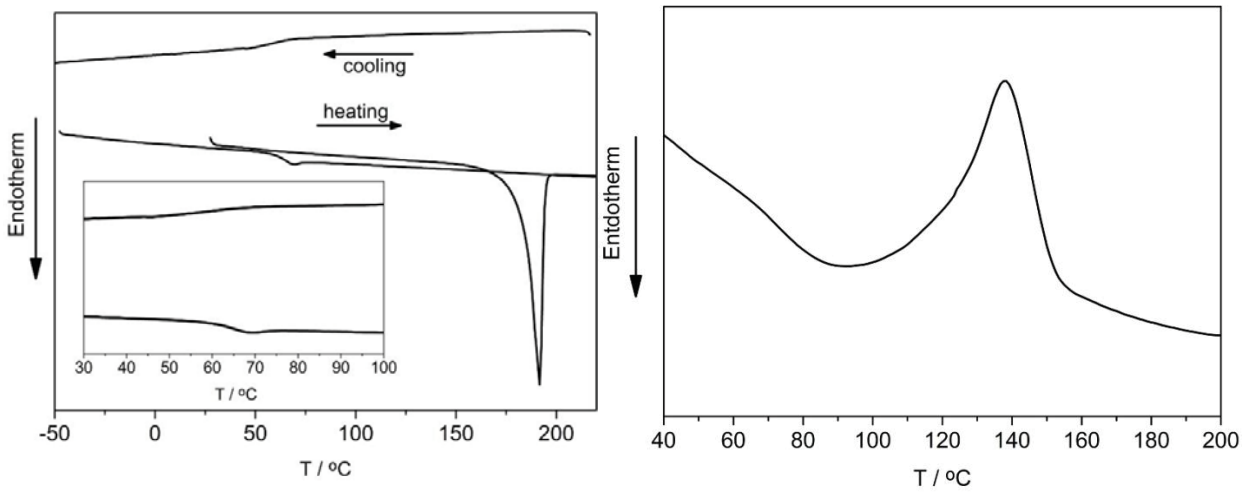

Figure 1.12. Cyclic DSC of radical **18** (left) and DSC curve of the first heating process of an amorphous layer of **1** prepared by spin-coating of a chloroformic solution (right). The inflexion before the exothermic peak in the DSC of **1** is attributed to the glass transition temperature.

Despite the original aim of attaching benzoyl groups bearing long alkoxyl chains to the radical core **1** was to attain greater Van de Waals interactions and to promote the formation of a liquid-crystalline phase, no birefringent texture was observed by POM observations of radical **28** in a wide range of temperatures. Cyclic DSC analyses of radical **28** did not present any peak or inflexion in a wide range of temperatures covering from -70 °C till 130 °C. Hence, this material only presents an amorphous state but its T_g could not be detected.

Unlike the carbazolic systems, radicals of the *N*-indolylTTM family, **11** and **12**, melt without decomposition and the rapid cooling of their liquid state leads to a glassy state. These amorphous layers present higher glass transition temperatures than their carbazolic counterparts (Table 1.4), a favoring feature for their application as molecular materials.

1.2.1.3. Electron Paramagnetic Resonance studies

EPR spectra of the prepared radicals, **1**-**3** and **14**, **15**, **18**-**20**, in CH_2Cl_2 solution (10^{-3} - 10^{-4} M) were recorded at 298 $\pm$ 3 K and at 160 $\pm$ 15 K and the spectra parameters are displayed in Table 1.5. All spectra at room temperature consist of a broad and single line, along with a small equidistant pair of lines in both sides of the main band. This small pair corresponds to the strong coupling of the free electron with the trivalent ^{13}C nucleus. At low temperature, the EPR signals split and the spectra show an overlapped multiplet of very close 7 lines corresponding to the weak coupling with the six equivalent aromatic hydrogens in the *meta* positions of the phenyl rings, and two weak multiplets in both sides of the central multiplet attributed to the coupling with the three bridgehead- ^{13}C nuclei

adjacents to the α-carbon atom. In all cases, *g* values are similar and very close to that of the TTM radical (*g* = 2.0034 ± 0.0002) and of the free electron (g_e = 2.0023), thus indicating small spin-orbit interaction. As an example, spectrum of **18** is displayed in Figure 1.13.

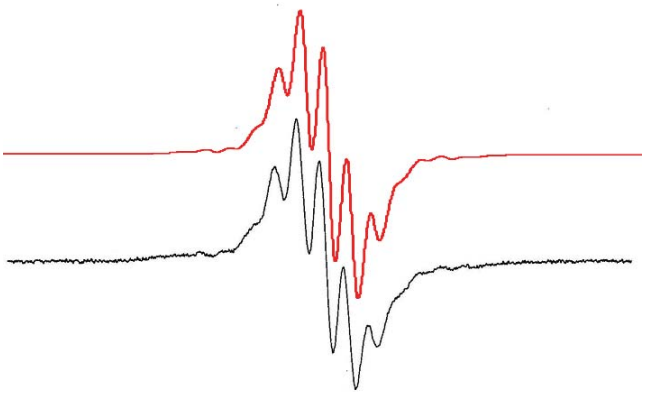

Figure 1.13. EPR spectrum of radical **18** in CH_2Cl_2 at 160 K ± 5 K (black) and computer simulation (red)

It can be observed in Table 1.5 that the couplings of the free electron with the α and the bridgehead ^{13}C atoms have relatively large values, while coupling with the *m*-hydrogens is quite weak and the coupling with the carbazole fragments is not even appreciable. In addition, the registered parameters are very similar irrespective to the number of carbazole units or the electronic nature of the attached chains to them, all of them being very close to those presented by the **TTM** radical. These results suggest that the distribution of the semioccupied molecular orbital (SOMO) in these molecules is localized mainly around the central carbon atom and is not influenced by the carbazolyl ring, as a consequence of the propeller-like conformation of the triphenylmethyl core.

Table 1.5. *g* Values and hyperfine coupling of the studied radicals.

	g	^{1}H / G	^{13}C (α)/ G	^{13}C / G	ΔH_{pp} / G
1	2.0032	1.25	28.0	9.0	0.80
14	2.0032	1.20	27.9	10.5	0.65
15	2.0033	1.20	27.9	10.5	0.65
18	2.0039	1.25	26.8	10.5	0.95
2	2.0029	1.25	28.2	9.9	0.80
19	2.0026	1.25	27.2	10.5	1.10
3	2.0028	1.25	27.8	10.1	0.85
20	2.0029	1.25	28.8	10.5	1.20

DFT calculations of the geometry and spin density distribution of radical **1** using the UB3LYP/6-31G method are in agreement with this interpretation. The calculated dihedral angles between the phenyl groups and the plane defined by the central sp^2 cabon atom, 45.7 48.5 and 48.9 are close to those observed in the **TTM** radical by X-ray crystallographic analyses, 48.1, 47.1 and 48.1.[19] These

out-of-plane torsions of the phenyl rings due to the presence of the six chlorine atoms in the *ortho* position do not allow a high delocalization of the unpaired electron on them. Thus, the free electron resides mainly on the trivalent carbon atom (Figure 1.14)

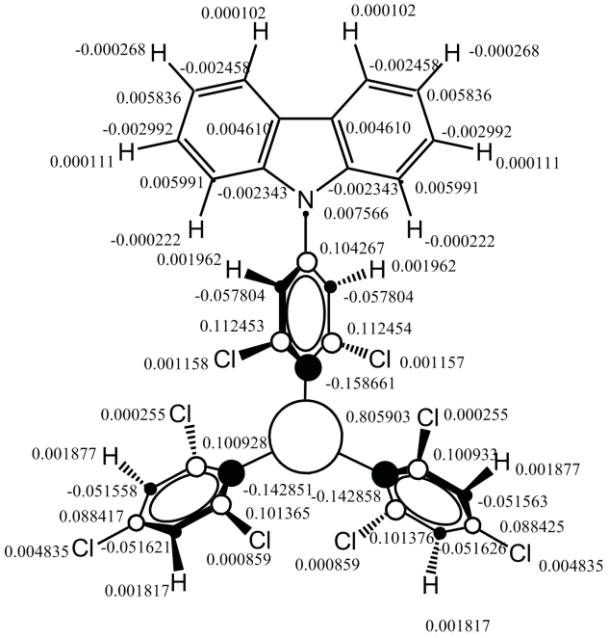

Figure 1.14. Spin densities of radical **1** according to DFT calculations (UB3LYP/6-31G)

The same spin density distribution is expected for radicals **4** and **10**, since they share the six-chlorinated triphenylmethyl radical core with the other radicals. However CH_2Cl_2 solutions of these two compounds present different EPR spectrum profiles as a result of the extra couplings of the free electron with the hydrogens in *para* position (Figure 1.15). Table 1.6 lists the EPR parameters registered for these two radicals.

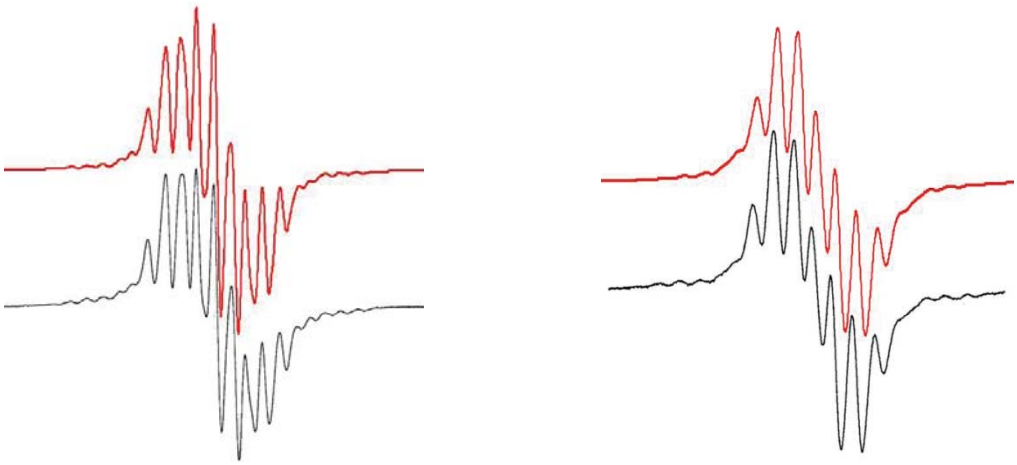

Figure 1.15. EPR spectra of **4** (a) and **10** (b) in CH_2Cl_2 at 160 $\pm$ 5 K (black) and computer simulations (red)

Table 1.6. *g* Values and hyperfine couplings of **4** and **10**.

	g	^{1}Hp / G	^{1}Hm / G	^{13}C (a) / G	^{13}C / G	ΔH_{pp} / G
4	2.0029	2.05	1.25	27.9	13.0	0.55
10	2.0027	1.95	1.18	27.9	10.5	0.65

Taking into account the electron-donor nature of carbazole and the ability of this heterocycle of forming stable cationic radicals, it seemed reasonable that the cationic derivative of **1** could present a resonant form based on a birradical in which the nitrogen atom bears the positive charge (Scheme 1.18). Oxidation of radical **1** by means of $SbCl_5$ in CH_2Cl_2 led to the isolation of the stable salt $\mathbf{1}^{+}SbCl_6^{-}$ EPR spectra of a CH_2Cl_2 solution of the $\mathbf{1}^{+}SbCl_6^{-}$ salt were registered during a cooling process going from rt. to 2 K. A wide signal was registered within the whole range of temperatures and a half-field band was observed at the lowest temperature (Figure 1.16). This result proves that, at least at low temperatures, $\mathbf{1}^{+}$ exists in the form of a biradical that gives rise to a triplet, evidenced by the forbidden $\Delta m_s = 2$ transition detected at half-field.

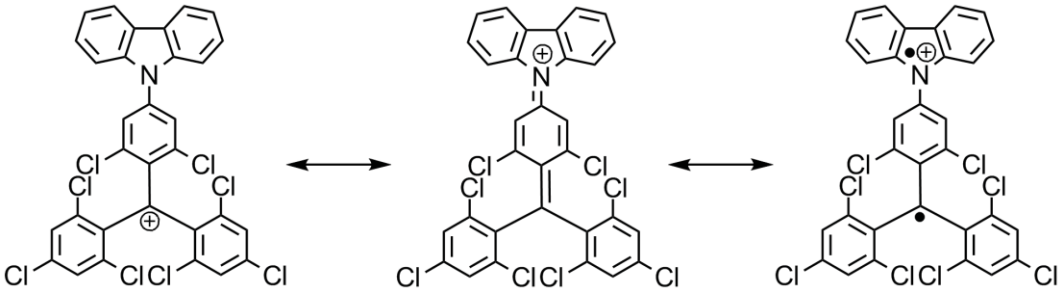

Scheme 1.18

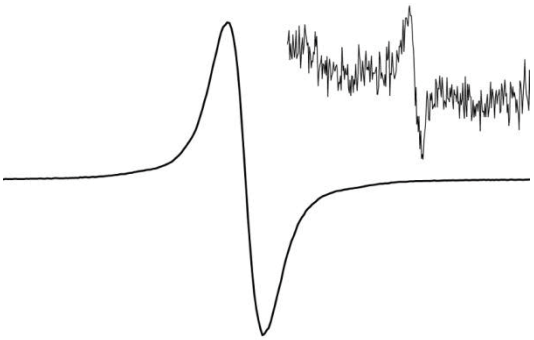

Figure 1.16. EPR spectrum of a solution of $\mathbf{1}^{+}SbCl_6^{-}$ in CH_2Cl_2 at 2 K (g= 2.0030 ± 0.0005; peak to peak linewidth, ΔH = 8.3 G). Insert shows the half-field band (g = 4.0090 ± 0.0005).

EPR spectra of **18** and **19** presented some differences when they were in their microcrystalline or in their amorphous states. Room temperature spectra of the polycrystalline samples of **18** and **19** presented a single line with a ΔH_{pp} of 4.7 G and 3.4 G, respectively. When the samples were heated

to their melting point and then cooled to room temperature to obtain amorphous glasses, their ΔH_{pp} values became of 2.7 and 5.0 G, respectively (Figure 1.17).

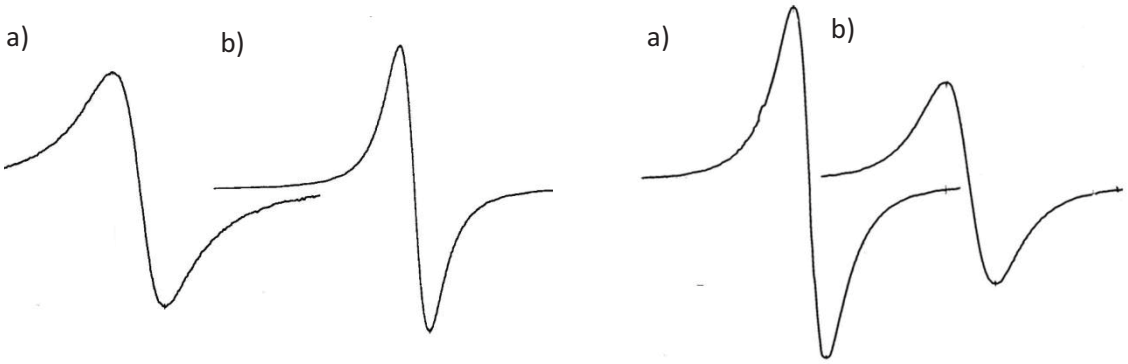

Figure 1.17. EPR spectra of **18** and **19** in two different disordered solid states: microcrystalline (a) and amorphous (b).

It is assumed that the spectrum of a polyoriented paramagnetic sample, either microcrystalline or amorphous, is made up of a broad envelope of homogeneously peaks from spins resonating at different frequencies, each associated with a certain orientation. This is a consequence of the anisotropic Zeeman and hyperfine interactions. However, there is a small difference in the spin-diffusion conditions between microcrystalline and amorphous states. While the spins associated with a particular orientation within each microcrystalline are isolated in space and the magnetization of each microcrystalline develops independently thus minimizing spin diffusion, in the amorphous glassy state all the spins can interact with each other because all the regions overlap and are more sensitive to cross correlation, increasing the spin-spin relaxation rate and diminishing the mean lifetime of a given spin-orientation state. In order to preserve the Heisenberg uncertainty principle, the line width of the peak must increase. This might be an explanation for the behavior of radical **19**. Surprisingly, the opposite results were obtained for radical **18**, that is, a narrowing of the EPR signal when going from the polycrystalline to the amorphous state, the causes of this behavior being unknown.

1.2.2. Radical liquid crystals

In this section the preparation and study of the properties of discotic molecules based on a triphenylmethyl radical core in order to attain columnar arrangements of the radical molecules is described. For this purpose, the attachment of side chains to the aromatic core bearing the radical trivalent carbon was required. The main objective of the preparation of such discotic molecules was to study the electronic and magnetic properties that could derive from the anisotropy of the columnar mesophases.

1.2.2.1. Synthesis

The first attempts to obtain a discotic radical consisted in providing the triphenylmethane unit with alkyl chains. The two synthetic paths shown in Scheme 1.19 were tried to prepare the target product: direct alkylation of the **αH-TTM** and condensation of previously alkylated 1,3,5-trichlorobenzene with chloroform.

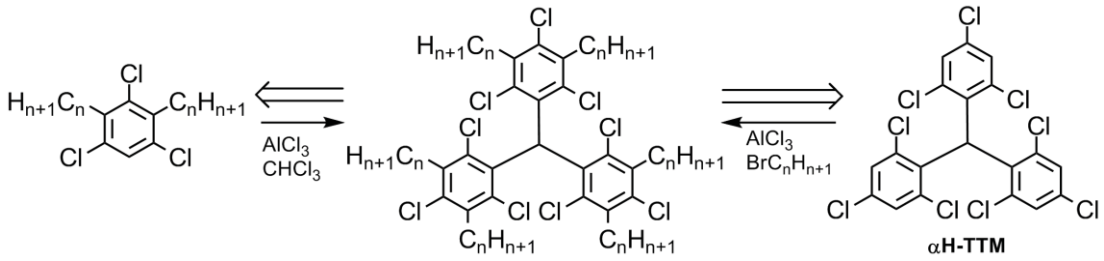

Shcheme 1.19

Friedel-Crafts alkylation conditions in a pressure reactor were used for the first synthetic method, using both acetylchloride as acylating agent and bromobutane as alkylating agent, but **αH-TTM** did not undergo any electrophilic attack by any of these reagents.

Alkylation of commercial 1,3,5-tirchlorobenzene with bromobutane and bromohexane via the generation of the organolithium intermediate[20] gave mixtures of mono-, the di- and the tri-alkylated products. Isolation of the dialkylated trichlorobenzene was not fully achieved via low pressure distillation and some rests of the trialkylated byproduct remained in the distilled fraction. Taking into account that the trialkylated products could not interfere in the next reaction, the Friedel-Crafts condensation between the impure fractions of 2,4-dibutyl-1,3,5-trichlorobenzene or 1,3,5-trichloro-2,4-dihexylbenzene with $CHCl_3$ were performed but with no results.

Our attention was then focused in the use of a radical of the TTM series bearing carbazole moieties as aromatic core of the discotic molecule. Such a system offers very interesting electrochemical and photoluminescence properties and easy functionalization of the carbazole fragment. The system chosen for this purpose was radical **3** due to its more symmetric structure in front of radicals **1** and **2**. Moreover, it allowed the attachment of acyl chains all around the rigid core due to the presence of one carbazole unit in each phenyl ring. It had been previously observed that 8-carbon acyl chains were not long enough to promote either the formation of a liquid crystal phase or to avoid the degradation during the melting process of the radical bearing them (see section 1.2.1.2). Therefore, it was decided to use much longer acylchlorides in order to attain stronger intermolecular interactions that might lead to the arrangement of the disk-like molecules into columns.

Preparation of stearyl chloride was achieved by treating stearic acid with thionyl chloride. Friedel-Crafts acylation of radical **3** with the prepared stearyl chloride worked in good yields (Scheme 1.20) and the resulting tris[2,6-dichloro-4-(3,6-dioctadecyl-*N*-carbazolyl)phenyl]methyl radical (**40**) proved to present the sought liquid crystalline properties.[21] For this reason, the synthesis of an analog bearing acyl chains of a length in between eight and eighteen carbons was also performed in order to study the influence of a shortening of the side chains in the observed properties. Tris[2,6-dichloro-4-(3,6-didodecyl-*N*-carbazolyl)phenyl]methyl radical (**41**) was prepared in the same conditions as the previous counterparts, and with similar yield.

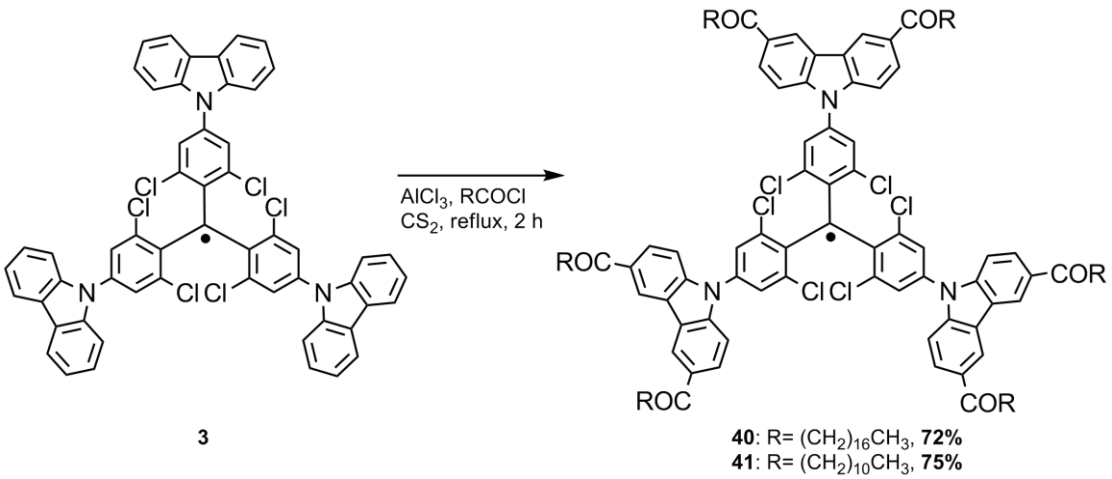

Scheme 1.20

1.2.2.2. Study of the liquid-crystalline phases.

1.2.2.2.1. Differential Scanning Calorimetry analyses

The attachment of long acyl chains, specifically of 18 carbons, in the carbazole moieties of radical **3** provides the resulting new radical **40** with a different thermal behavior regarding its counterpart radical **20** that bears 8-carbon acyl chains. Radical adduct **40** does not crystallize and exhibits the typical features of a disk-like mesogen with different phases, which were studied by optical, calorimetric and diffractometric methods.

Two exothermic peaks are observed in the cooling curve of the DSC of radical adduct **40** (Figure 1.18): one peak at T = 351 K with an enthalpy value of ΔH = -2.8 kJ/mol and a broad transition covering the range of temperatures going from 300 K to 274 K with an enthalpy value of ΔH = -74.1 kJ/mol. The former corresponds to the formation of a hexagonal columnar (Col_h) mesophase, as it was evidenced by X-ray diffraction analyses. The broad peak is associated to a transition to a glassy rectangular columnar mesophase, according to the lack of fluidness of the material in the POM observations at these temperatures and the X-ray diffractogram recorded at 253 K (see next section). The symmetric profile of the DSC analyses of **40** during the second heating process proves an enantiotropic character of the mesophase. The broad endothermic peak (from T = 274 K to T = 312 K) with an enthalpy of ΔH =45.0 kJ/mol is associated with the arrangement of the molecules in the Col_h phase observed during the cooling process. Isotropization of the liquid crystal phase occurs at 379 K with an associated enthalpy of 10.7 kJ/mol.

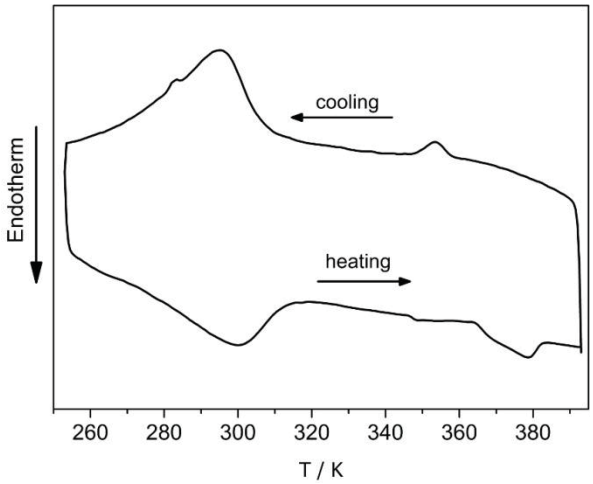

Figure 1.18. DSC curves of **40** (10 K/min.).

The shortening of the alcyl chains in six carbons leads to the disappearance of the broad peak corresponding to the Col_h-Col_r transition and the rising of the isotropization temperature in 65 K (Figure 1.19). The DSC curves of radical **41** presented a single exothermic peak at 425 K (ΔH = 17.6

kJ/mol) during the cooling process and single endothermic peak at 444 K (ΔH = 18.8 kJ/mol) during the heating process. These two peaks correspond to the formation of a ordered rectangular columnar (Col_{ro}) liquid crystal phase, characterized by X-ray diffraction, and its transition to the isotropic state, respectively. As in the case of **40**, no crystallization of the material takes place, but the vitrification of the columnar phase. Thus, the small inflexion at 348 K observed in the heating curve of the DSC is attributed to the T_g associated to this process.

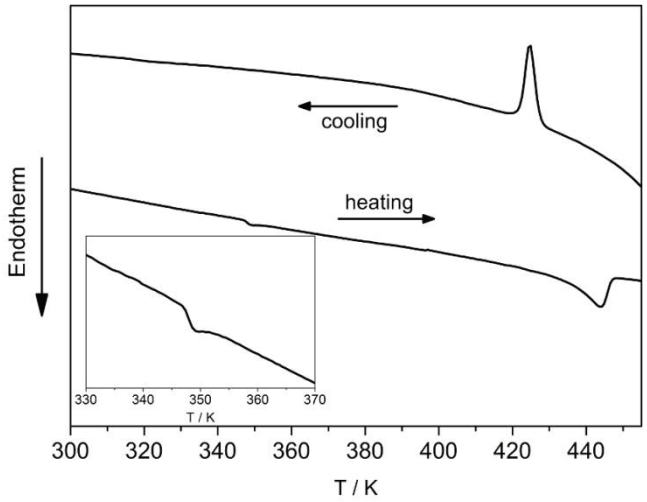

Figure 1.19. DSC curves of radical **41** (10 K/min.).

1.2.2.2.2. X-ray diffraction

Identification of the liquid crystal phases presented by radicals **40** and **41** was achieved by X-ray diffraction studies of the materials at different temperatures. X-ray data of the phases found for radical **40** are shown in Table 1.7. At 253 K (Figure 1.20 left), the X-ray diffractogram presents two sharp peaks in the low angle region, indexed as (200) and (110), according to the two-dimensional lattice structure of a rectangular arrangement (see section 1.1.3.2). The broad peak at lower angles corresponding to the distance of 4.3 Å indicated liquid-like order of the alkyl chains.

By heating the sample to higher temperatures (333 K), a diffraction profile corresponding to a Col_{ho} phase was observed (Figure 1.20 right). The first intense reflection peak at low angles is indexed as (100). Next peak is attributed to the (110) plane and subsequent low angle peaks are assigned to reflections of (200), (300), (500) and (600). The presence of these periodical reflection peaks proves that the material have a strong long range 2D order. Two diffuse peaks can be seen in the wide angle region, a broad one at 4.5 Å, characteristic of the packing of floppy alkyl chains, and a smaller one at 3.5 Å derived from the core-core intermolecular interaction, thus revealing the ordered nature of the columnar mesophase.

Radical **41** shows the same diffractogram at high and low temperatures (Figure 1.21), which indicates that molecular arrangement remains unaltered in a wide range of temperatures. Indexation of the diffraction peaks is shown in Table 1.8. It is noticeable that the intercolumnar distances and cell parameters for **41** are smaller than those of **40**, as it could be expected by the smaller diameter of the molecule bearing shorter acyl chains. The proposed indexation of the low-angle reflections corresponds to a rectangular lattice of the $P2_1/a$ space group. The reflection at 3.6 Å attributed to the intercore distance evidences π-π interactions, so that this mesophase can be labeled as Col_{ro}. Thus, the attachment of acyl chains of twelve carbons to the aromatic core of radical **3** does not promote the 2D columnar arrangement in a hexagonal lattice but promotes the rapprochement of the molecules close enough along the columns to establish π-π interactions.

Table 1.7. Indexation of the XRD profiles of **40** at 253 K and 333K.

T/ K	Phase[a]	d/ Å	Miller Indices (hkl)	Lattice Parameters/ Å
253	Col_r	40.2	200	a= 80.4
		34.6	110	b= 38.3
		20.1	400	
		4.3		
333	Col_{ho}	43.1	100	a= 49.8
		25.6	110	c= 3.5
		21.5	200	
		14.4	300	
		8.5	500	
		7.2	600	
		6.1	700	
		4.5		
		3.5	001	

[a] Col_r= glassy rectangular columnar; Col_{ho}= ordered hexagonal columnar mesophase.

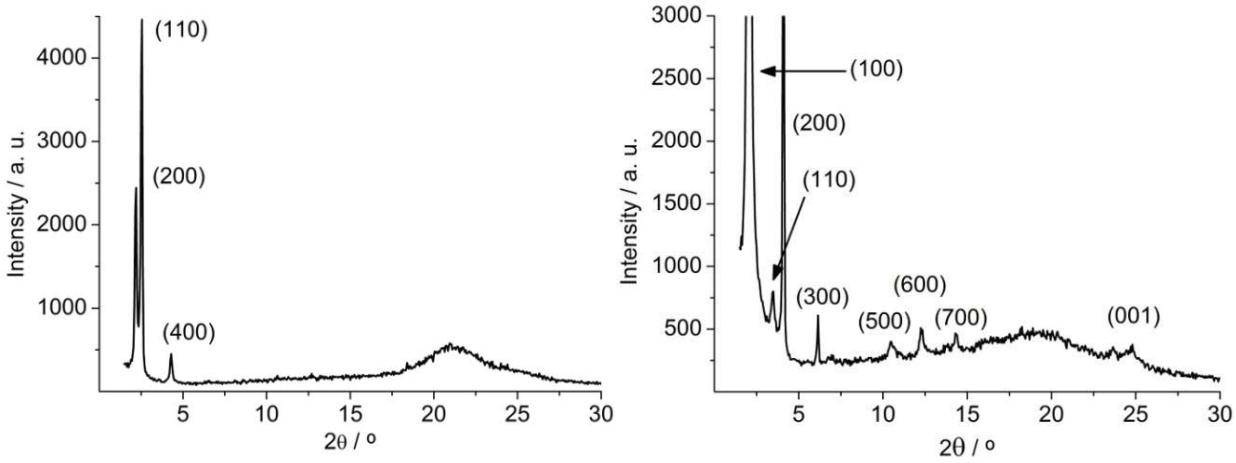

Figure 1.20: X-ray diffractograms of radical adduct **40** at 253 K (left) and at 333 K (right).

Table 1.8. Indexation of the XRD profiles of **41** at 373 K.

T/ K	Phase[a]	d/ Å	Miller Indices (hkl)	Lattice Parameters/ Å
373	Col_{ro}	33.3	(200)	a= 66.6
		25.2	(110)	b= 27.2
		14.0	(410)	c= 3.6
		10.2	(420)	
		8.5	(330)	
		8.2	(800)	
		7.2	(910)	
		7.0	(820)	
		6.7	(240)	
		6.5	(340)	
		4.6		
		3.6	(001)	

[a]Col_{ro}= ordered rectangular columnar mesophase.

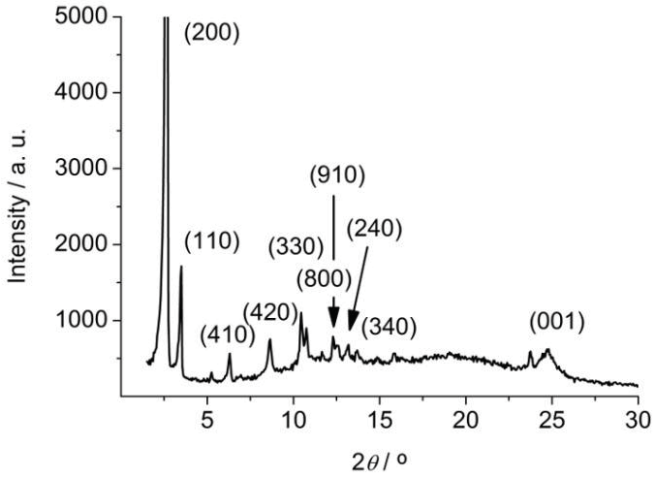

Figure 1.21. XR-diffractograme of **41** at 293 K and at 373 K.

1.2.2.2.3. Polarized Optical Microscopy observations

Homeotropic alignment during the cooling from the isotropic state of radical adduct **40** was evidenced by using polarized optical microscopy (POM) at 333 K and it is shown in Figure 1.22. The sample was uniformly black when polarizers were crossed[22-26] (Figure 1.22 left) and birefringence could only be observed when pressure was applied upon the sample. Though the transitions between Col_r and Col_h were detected by DSC analyses, no changes in the texture associated to the phase transitions were recorded by POM during the cooling or the heating processes. The columnar mesophase of radical **41** presented a very similar sand-like texture, also in the vitrified state (Figure 1.23). However, no homeotropic alignment was detected.

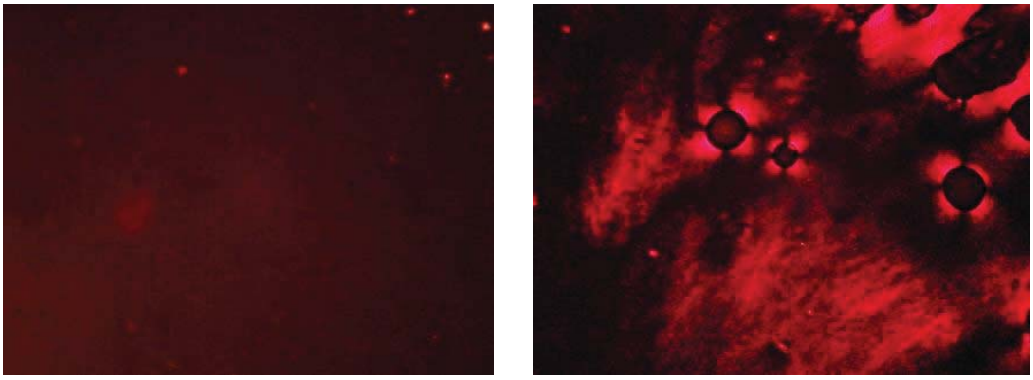

Figure 1.22. Textures observed for **40** in the POM with crossed polarizers before (left) and after (right) applying pressure at 363 K.

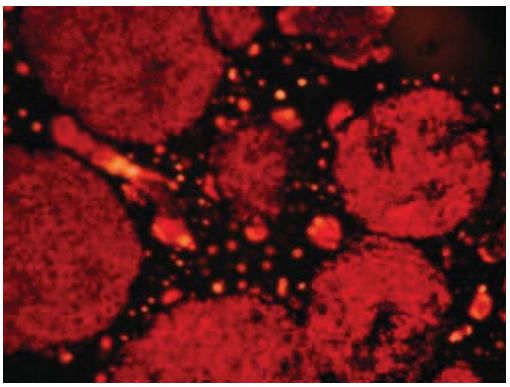

Figure 1.23. Texture observed for **41** in the POM with crossed polarizer at 333 K

1.2.2.2.4. Magnetic susceptibility studies

Given the intracolumnar core-core interactions, the magnetic intermolecular interactions in the mesophase of radical **40** were investigated. The studies were made in a wide range of temperatures covering the isotropic state, the liquid crystal phase and the glassy state until low temperatures near to 2 K.

Magnetic susceptibility of radical adduct **40** was measured in the temperature range 2-400 K. Figure 1.24 displays the variation of the product of the paramagnetic molar susceptibility and the temperature, $\chi_P T$ (emu mol^{-1} K), with the temperature. From the isotropic liquid state, radical **40** showed an increase in the $\chi_P T$ from 0.32 to 0.35 at 313K during the cooling, in agreement with the beginning of the endothermic peak in the DSC analysis (T = 310K) and, therefore, coinciding with the transition from the Col_h phase to the Col_r glassy state. The new value $\chi_P T$ = 0.35 corresponds to the value of a monoradical (S = 1/2; $\chi_P T$ = 0.37), and suggests that the core-core interaction in the Col_{ho} phase has an antiferromagnetic character. Values of $\chi_P T$ remain constant during the glassy rectangular phase until it smoothly decreases with decreasing temperature from T = 100 K, and

drastically from T = 20 K, due to strong antiferromagnetic interactions. A reversible magnetic behavior comes out during the second heating from 2 K. Values of $\chi_P T$ close to the monoradical are recovered from 2 K to T = 100 K and then are kept until the transition from the rectangular glassy phase to the hexagonal ordered columnar mesophase, which is fully formed at approximately 330 K, as it is evidenced by a drop in the $\chi_P T$ values from 0.35 to 0.31 due to the reappearance of the intermolecular antiferromagnetic interaction. This reversibility in the magnetic interactions is also seen in the identical values of the Curie constant, *C*, and the Weiss temperature, θ, obtained from values of magnetic susceptibility of radical **40** in the heating and the cooling processes given in Table 1.9.

Table 1.9. Magnetic susceptibility data of radical **40**.

Process	magnetic interactions	*C* / emu mol^{-1} K	θ / K	Phase transtion / K[a]
Cooling	Antiferromagnetic	0.34	-0.30	Col_r 265-308 Col_h 348-359 I
Heating	Antiferromagnetic	0.34	-0.30	Col_r 299-316 Col_h 364-383 I

[a]Transition temperatures determined by DSC analysis between the different found states: glassy rectangular state (Col_r), columnar hexagonal mesophase (Col_h) and isotropic state (I).

The same experiment was performed on radical **41** (Figure 1.25). Given that this compound shows a similar core-core distance along the columns in its Col_{ro} mesophase to the core-core distance detected in the Col_{ho} of its counterpart radical **40**, an antiferromagnetic interaction could be expected within the whole range of temperatures in which the Col_{ro} is formed. However, values of the $\chi_P T$ product (emu mol^{-1} K), around 0.35 were registered within the range going from 100 K to 250 K and only from this temperature on a decrease of $\chi_P T$ values with the temperature was observed. These results suggest that no magnetic interaction takes place while molecules are frozen in the glassy columns, but some intermolecular interactions appear and become stronger as the system becomes more fluid. A possible explanation could be that, despite presenting similar intracolumnar distances, aromatic cores in the **41** glassy Col_r phase are tilt regarding the column axis so that the central carbons are not aligned, unlike in the case of **40** mesophase. Then, in the range covering from 300 K to 400 K, the gain of fluidness allows the movement of the disks leading to greater intermolecular interaction that give rise to an antiferromagnetic behavior. The Weiss temperature and the Curie constant deduced from the magnetic susceptibility measurements are given in Table 1.10.

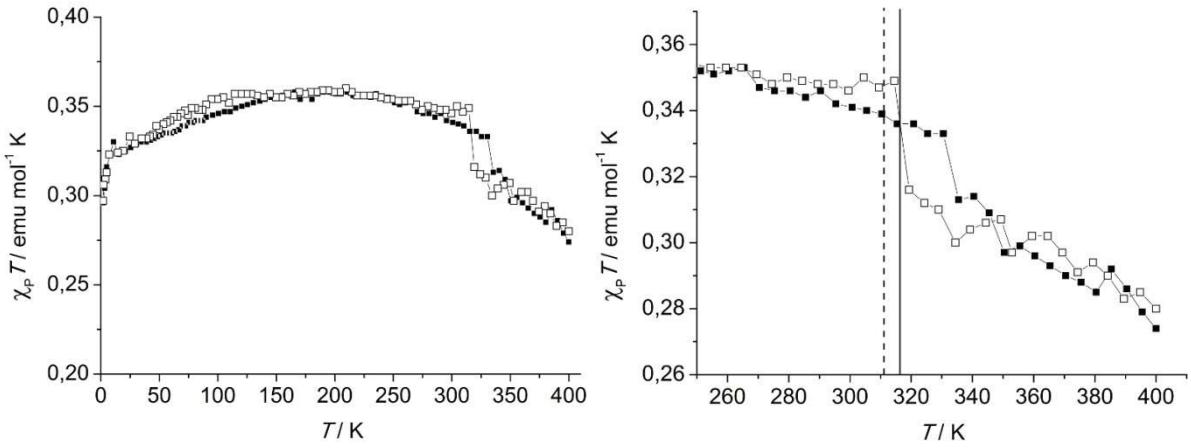

Figure 1.24. Temperature dependence of the product $\chi_P T$ of radical **40** at a rate of 10 °C/min during the cooling (white squares) and the second heating (black squares) processes between 2 and 400 K at a field of 5 T (left) and a detailed aspect of the function between 250 and 400 K (right). Dashed line indicates the temperature at which the Col_{ho} disappears during the cooling process, the solid line indicates the temperature at which the Col_{ho} is completely formed during the heating process, according to the DSC analyses.

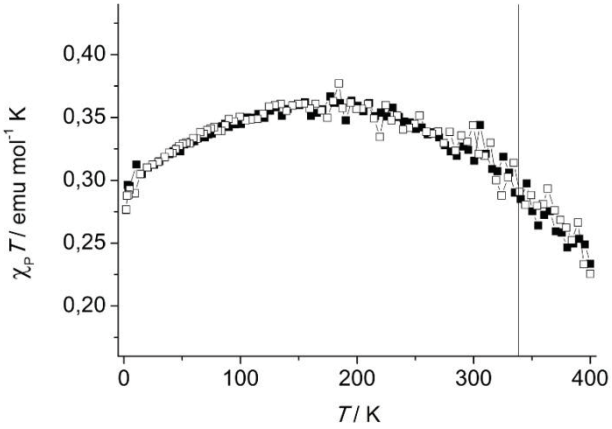

Figure 1.25. Temperature dependence of the $\chi_P T$ product of radical **41** at a rate of 10ºC/min during the cooling (white squares) and the second heating (black squares) processes. between 2 and 400 K at a field of 5 T. The solid line indicates the temperature at which the T_g takes place, according to the DSC analyses.

Table 1.10. Magnetic susceptibility data of radical **40**.

Process	magnetic interactions	C / emu mol^{-1} K	θ / K	T_g / K[a]
Cooling	antiferromagnetic	0.33	-0.40	Not detected
Heating	antiferromagnetic	0.33	-0.40	346 K

[a]Glass temperature transition according to DSC analyses

1.2.2.2.5. Electron Paramagnetic Resonance studies

In order to confirm the changes of the magnetic intermolecular interactions in the different phases, so that the drop of the $\chi_P T$ values could be unequivocally assigned to a core-core rapprochement in the Col_{ho} phase, the Landé *g*-value and the band intensity and linewidth values in the electron paramagnetic resonance (EPR) spectrum of the radical **40** were registered as a function of the temperature.

Variable-temperature EPR spectra of radical **40** were recorded during the cooling process from the isotropic melted state (400 K) to the glassy Col_r phase (230 K) and during the second heating process going from the glassy Col_r to the Col_h mesophase (300 K) (Figure 1.26). The *g*-value only showed a slight increase from 2.0026 to 2.0032 during the cooling process and remained almost constant during the heating, keeping the value reached before (Figure 1.26 a). As a general rule, polychlorotriphenylmethyl radicals have axial symmetry showing anisotropic *g*-values: $g_\perp$= 2.0019 ± 0.0004 and $g_\parallel$= 2.00046 ± 0.0005. Considering that the $g_\parallel$ component is set along the semi-occupied 2p orbital of the trivalent carbon, the small increase of the *g* might be attributed to a slight major contribution of the $g_\parallel$. Hence, once molecules form columns from the melted isotropic state they do not experience changes in their orientation during the phase transitions and they tend to align the 2p orbital closer to the direction of the magnetic field.

While intensity of the band in the EPR spectrum of **40** increased with decreasing temperature from 400 K to 220 K according to the Curie's law, the linewidth dropped almost in a linear rate in the range 400-340 K corresponding to the isotropic state, due to an increase of the spin-relaxation times with the decrease of the temperature (Figure 1.26 b). Under 340 K, the linewidth became constant, thus indicating a stabilization of the relaxation times that can be attributed to the formation of the columnar mesophase, where molecules occupy positions in a columnar order and intracolumnar core-core interaction and spin-relaxation mechanisms remain unaltered within the temperature range in which this intramolecular order is preserved. After the $Col_{ho} \rightarrow Col_r$ transition, however, the linewidth values increased slightly in the temperature range in which the magnetic susceptibility values indicate a monoradical behavior and thus the loss of intermolecular intracolumnar interactions. The intensity and linewidth values are reproduced during the second heating as a consequence of the enantiotropic character of the phases.

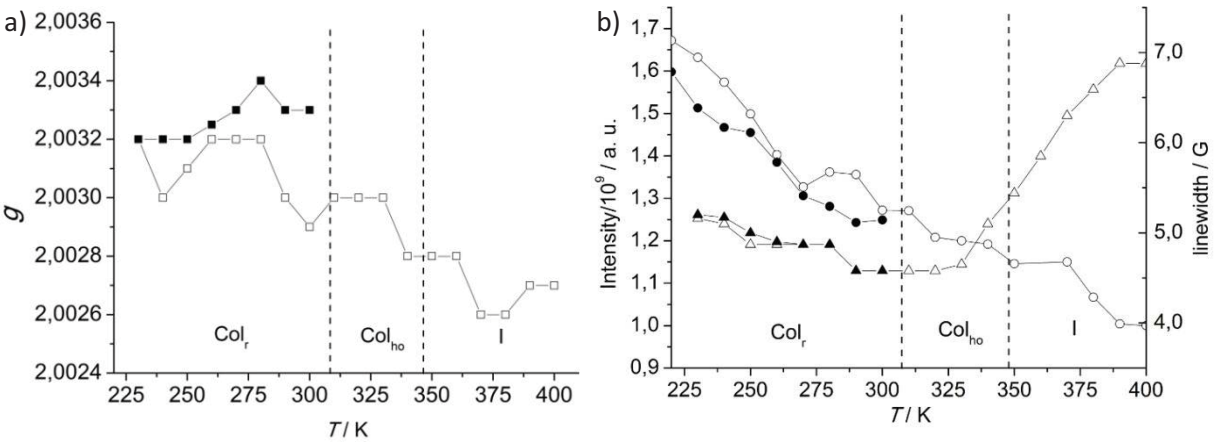

Figure 1.26. a) Variation of *g* (squares) and b) variation of the band intensity (circles) and the band linewidth (triangles) values in the EPR spectra of radical **40** during the cooling process (white) from the isotropic melted state and the second heating process (black). Dashed lines limit the temperature range for Col_h phase determined by DSC analysis during the cooling process.

The EPR spectrum of a CH_2Cl_2 solution of radical **40** recorded at 300 K (Figure 1.27) shows an overlapped multiplet of seven lines corresponding to the weak coupling (1.22 G) with the six equivalent aromatic hydrogens in the meta positions, and two weak multiplets in both sides of the central multiplet attributed to the coupling with the *ortho*-^{13}C nuclei (10.22 G) and the three bridgehead-^{13}C nuclei (12.75 G) next to the trivalent α-carbon atom. Though the strong coupling with the α-^{13}C could not be detected, the spectrum of **40** shows very similar parameters to those registered for the radical precursor **3** (see section 1.2.1.3) and for all the radical adducts based on the TTM core. The weak coupling of the unpaired electron with the six *meta*-hydrogens proves that, like in the previous referred adducts, the unpaired electron is mainly located in the central trivalent carbon.

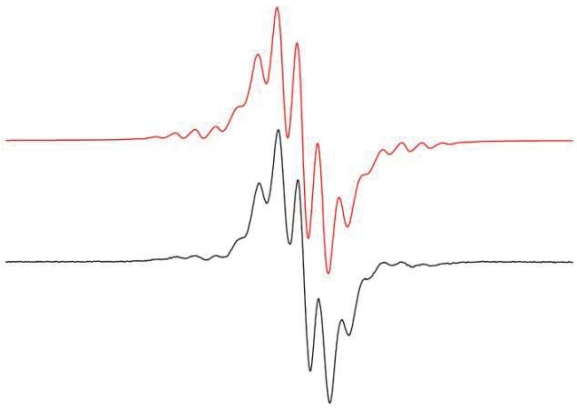

Figure 1.27. EPR spectra of **40** in CH_2Cl_2 at 298 K (black) and computer simulations (red).

1.2.3. Absorption and photoluminescence studies

1.2.3.1. Light absorption studies.

Absorption spectra of the compounds belonging to the *N*-carbazolylTTM radical family (Figure 1.28) are complex ones and the peaks assignation is not a trivial task. Taking the **TTM** radical absorption spectrum as a starting point, it presents one band that shows some fine structure in the visible region (λ_{max}= 497 nm and 541 nm). Its low molar absorption coefficient, ε, indicates it is a forbidden transition. The other band is located in the UV region of the spectrum (λ_{max}= 371 nm) and has much higher ε values. These two absorption peaks were already observed in the perchlorotrisphenylmethyl (PTM) radical by Ballester et al.[19] and were assigned to the transitions to the two first excited states, which involved the promotion of an electron from the HOMO to the SOMO and from the SOMO to the LUMO, respectively. Given that the ground and excited states present an unpaired electron, they should be noted as D_0, the ground state, D_1 and D_2, the two first excited states, where D stands for doublet. Moreover, taking into account that the unpaired electron is mainly located on the trivalent carbon (see sections 1.2.1.3 and 1.2.2.2.5), the atomic orbital 2p might have a major contribution in the SOMO, thus providing this MO with a non-bonding (n.b.) nature. Therefore, the band in the visible region corresponds to a $\pi \rightarrow$n.b. electronic transition, in agreement with its low ε values, and the band in the UV region to a n.b.$\rightarrow \pi^*$ transition.

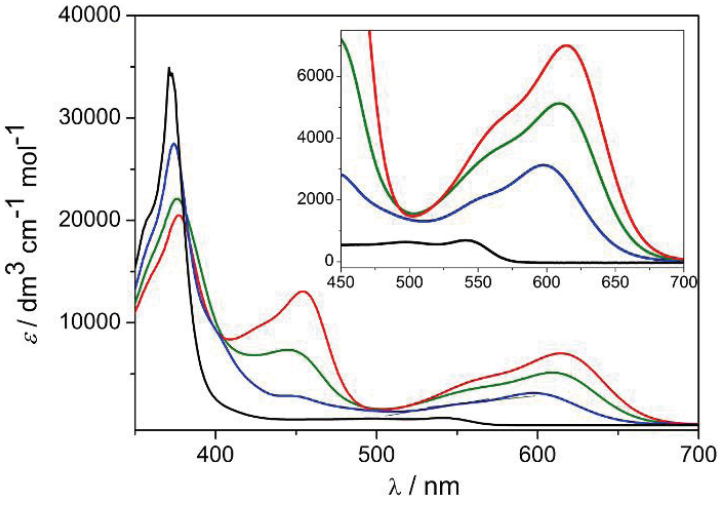

Figure 1.28. Absorption spectra of TTM (black), **1** (blue), **2** (green) and **3** (red) in $CHCl_3$

If the spectrum of **TTM** is compared with the spectra of the radicals bearing carbazole moieties, radicals **1**, **2** and **3**, many differences can be detected. Two new absorption bands appear, one in the orange region (> 600 nm) and another near the blue region (~450 nm) of the visible spectrum. In

addition, the band observed in the **TTM** radical around 540 nm is bathochromically shifted in the new radicals and represents a shoulder on the left side of the less energetic band, due to the overlapping of both peaks. The band in the UV range at λ_{max} ~370 nm remains almost unaltered, just decreasing its ε along with the increase of carbazole units.

A possible explanation for the changes in the absorption spectra would be the following. The less energetic band could be an intramolecular charge transfer (ICT) band arising from the electron-donor nature of the carbazole fragment, which can transfer an electron to the trivalent carbon, an electron-deficient fragment, through the phenyl bridge linking both units to give a zwitterionic species. The intensity of this band follows a 1:2:3 ratio, following the number of carbazole units, and thus the probability of the electronic transition to take place. The overlapped band observed as a shoulder could be assigned as the HOMO→SOMO transition by analogy to the **TTM** precursor, that is, a $D_0 \rightarrow D_1$ transition. Assuming that the SOMO orbital remains unaltered in the *N*-carbazolylTTM radicals regarding the **TTM** radical, as the EPR analyses seem to indicate, the lower E_{gap} between these two orbitals might be due to a higher HOMO level.

Since the *N*-carbazolylTTM radicals still present a peak around 370 nm, the LUMO orbital of the **TTM** radical might be kept in the new radicals as an antibonding π^* molecular orbital, which is not affected by the presence of the carbazole fragment. The less energetic band at 450 nm could be then explained by the transition to a new excited state in which the carbazole units play a main role. This excited state might be the result of promoting the electron of the SOMO to a new π^* molecular orbital, in which the carbazole has a major contribution and which was not present in the **TTM** radical. In other words, the $D_0 \rightarrow D_2$ transition of the **TTM** radical is now the $D_0 \rightarrow D_3$ transition and the band with λ_{max} ~450 nm is attributed to the $D_0 \rightarrow D_2$ transition, the SOMO→LUMO transition, in the *N*-carbazolylTTM radical derivatives. This assignation would be in agreement with the increase of the intensity of the band with λ_{max} ~450 nm and the simultaneous decrease of the intensity of the bands with λ_{max} ~370 nm by the increase of the number of carbazole units in the structures of the radicals.

Figure 1.29 gives a simplified scheme of the electronic levels involved in the transitions of the **TTM** radical and radical adducts **1**, **2**, and **3**. As it was discussed above, the radicals bearing carbazole units preserve the molecular orbitals derived from the **TTM** core and present new ones due to the carbazolyl moieties with a lower E_{gap}.

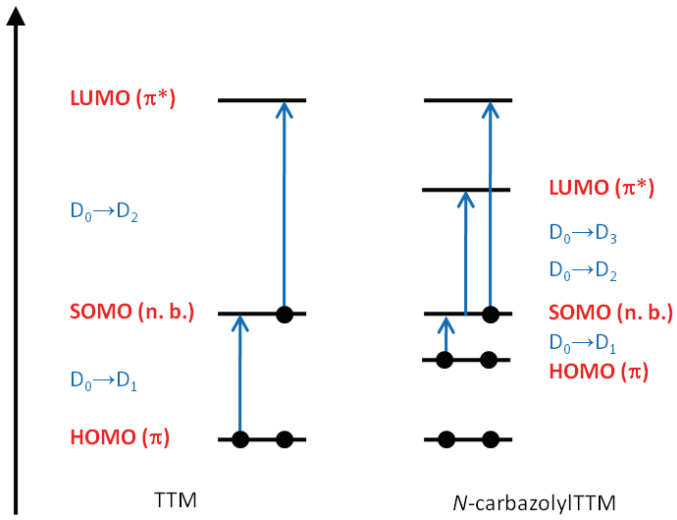

Figure 1.29. Scheme of the proposed energetic levels and electronic transitions for the TTM radical and the radicals bearing carbazole fragments.

Table 1.11 presents the λ_{max} of the absorption bands registered for the synthesized radical systems classified according to the interpretation discussed above. The systems are grouped regarding the number of carbazolyl moieties they present in their structure. In radicals bearing a single carbazole unit an increase in the wavelength and a decrease of the ε of the ICT band accompany the decrease of the electron-donor nature of the substituents in positions 3 and 6 of the carbazole, as it could be expected. The spectra of radicals **27** and **28** show an ICT band with a wavelength slightly higher than in the case of **18**. This could be due to the electron-donating character of the alkoxyl chains in the phenyl rings. However, the absorption spectra for these adducts was registered in cyclohexane, a less polar solvent, and they are not comparable to the spectra registered in chloroform.

Table 1.11. Absorption maxima and molar absorption coefficients of the studied radicals in $CHCl_3$

	$D_0 \rightarrow D_3$ (ε)/ nm ($dm^3\ mol^{-1}\ cm^{-1}$)	$D_0 \rightarrow D_2$ (ε)/ nm ($dm^3\ mol^{-1}\ cm^{-1}$)	$D_0 \rightarrow D_1$ (ε)/ nm ($dm^3\ mol^{-1}\ cm^{-1}$)	CT (ε)/ nm ($dm^3\ mol^{-1}\ cm^{-1}$)
21	375 (28740)	458 (3100)[a]	-	627 (4600)
1	374 (27500)	446 (2800)[a]	550 (2000)[a]	597 (3130)
18	373 (32400)	440 (4080)[a]	537 (1900)[a]	570 (1980)
27[b]	373 (15800)	447 (2580)[a]	544 (1950)	588 (1740)
28[b]	373 (22470)	447 (4077)[a]	543 (4370)	586 (2670)[a]
2	376 (22100)	445 (7350)	553 (3300)[a]	609 (5130)
19	374 (21500)	440 (9540)	540 (2980)[a]	582 (3480)
3	377 (20100)	454 (13060)	554 (4090)[a]	615 (7000)
20	377 (20100)	446 (14200)	548 (4070)[a]	593 (5450)

[a]Shoulder [b]Registered in cyclohexane

The lower HOMO levels and/or higher LUMO levels of the compounds bearing acyl groups in the carbazolyl moieties, that is, electron-withdrawing groups, might be the responsible of their more energetic $D_0 \rightarrow D_1$ and $D_0 \rightarrow D_2$ transitions, respectively, regarding the non-substitued counterparts. The same behavior for all the absorption bands was detected in radical compounds with two (**2** and **19**) and three (**3** and **20**) carbazole units.

Absorption profiles of the *N*-carbazolylTTM system containing an even number of electrons, that is, of the cationic ($\mathbf{1}^+$) and anionic analogs ($\mathbf{1}^-$), are simpler than the absorption profile of the radical adduct **1,** as a consequence of their closed-shell electronic configuration (Figure 1.30). The anionic species presents a single absorption band in the visible region of the spectra with a maximum at λ_{max}= 506 nm. It was reported that the PTM anion absorbed at almost the same wavelength,[19] which may lead to the conclusion that, once more, only the molecular orbitals based on the **TTM** cores are involved in this transition. Thus, this peak is assigned to the promotion of an electron from the n. b. MO, which used to be the SOMO in the radical adduct and is now fully occupied in the anion, to the $LUMO^2$, which used to be the LUMO in the **TTM** radical.

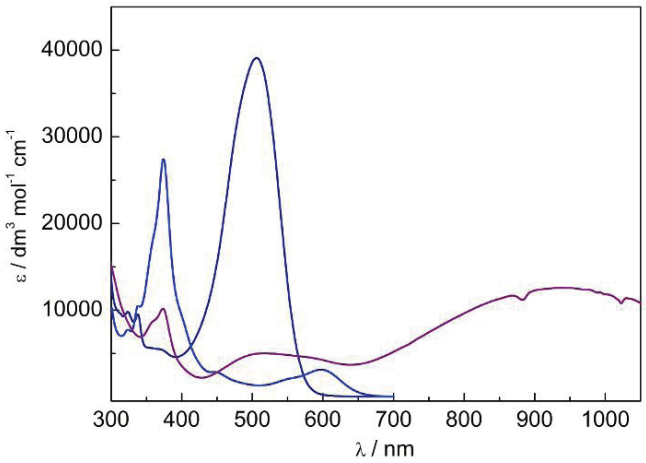

Figure 1.30. Absorption spectra of **1** (blue) in $CHCl_3$, $\mathbf{1}^-$ (dark blue) in THF and $\mathbf{1}^+$ (lilac) in CH_2Cl_2.

The cationic species, in turn, shows a low intensity band with a maximum at λ_{max} = 518 nm and a shoulder at λ_{max} ~580 nm, and a wide absorption band whose maximum is located in the infrared region at 940 nm. The first peak could be attributed to the transition to a localized excited state (LE) of the cation, the HOMO→LUMO electronic transition, where the HOMO is the same orbital as in the radical adduct and the LUMO the former SOMO. The less energetic broad band is a charge transfer band from the carbazole to the central carbon. This intramolecular charge transfer was evidenced by EPR studies (see section 1.2.1.3), which proved the existence of a biradical form resulting from the electron transfer from the carbazole fragment to the triphenylmethyl core. The surprisingly low energy associated to this transition is attributed to the close energies of the HOMO and LUMO

orbitals, a feature associated to the triplet detected by EPR, since it indicates that the orbitals containing the two unpaired electrons are almost degenerated.

1.2.3.2. Light emission studies.

Emission spectra of the most representative radicals were registered in an apolar solvent (cyclohexane) and a polar solvent (chloroform). The obtained fluorescence parameters are listed in Table 1.12, grouped regarding the number of carbazole units present in their aromatic core.

Table 1.12. Emission parameters of the prepared radical systems.

	Cyclohexane			Chloroform			
	λ_{em} / nm	ϕ_f	Stokes shift / cm^{-1}	λ_{em} / nm	ϕ_f	Stokes shift / cm^{-1}	ΔS / cm^{-1}
21	661	0.13	594	-	-	-	-
1	628	0.53	771	680	0.04	2016	1245
18	606	0.51	950	621	0.46	1534	584
2	651	0.54	1113	680	0.10	1714	1601
19	621	0.56	991	631	0.49	1364	373
3	654	0.52	1077	680	0.07	1581	504
20	631	0.48	902	642	0.45	1146	244
40	631	0.34	902	642	0.32	1146	244

All compounds were excited with light of around 450 nm, thus promoting the transition indexed as $D_0 \rightarrow D_2$. The radiative emission is attributed to the relaxation of the less energetic excited state ($D_1 \rightarrow D_0$), to which the system evolve from the D_2 state through non-radiative processes. Thus, Stokes shifts are calculated as the difference between the λ_{max} of the emission band and the λ_{max} of the absorption band in the visible region, which is close to the λ_{max} of the $D_0 \rightarrow D_1$ transition.

All radicals emit in the orange-red region in cyclohexane solution. Two clear trends are observed in the emission wavelenghts related to two variables: the number of carbazolic moieties and the electronic nature of the side-groups. The addition of carbazole units leads to a red shift of the emission band while a blue shift is observed when the attached chains in the carbazole unit go from electron-donating to electron-withdrawing.

Chloroformic solutions of these radicals present a quenching phenomenon in all cases except for the systems that bear electron-withdrawing groups, **18**, **19**, **20** and **40**. It is known that many CT states undergo non-radiative relaxation so that they are responsible of quenching. Thus, this result can be attributed to the solvent-polarity-assisted transition $D_2 \rightarrow CT$. Certainly, the Stokes shift increase is much higher in the non-acylated radical adducts **21**, **1**, **2**, and **3** than in the acylated ones, **18**-**20** and

40, indicating a much polar state for the first radical adduct, which is in agreement with the formation of the CT state.

The fluorescence emission of the radicals bearing benzoyl groups, **27** and **28**, was first registered in cyclohexane (Table 1.13). Despite the differences in their structure, they presented emission bands in the same range as the rest of the radical compounds but with lower quantum efficiencies. Therefore, the luminescence properties of radicals **27** and **28** were not further studied.

Table 1.13. Emission parameters of **27** and **28** in cyclohexane.

	λ_{em} / nm	ϕ_f
27	618	0.17
28	616	0.21

1.2.3.3. Non-conjugated carbazole-bridge-TTM systems.

The absorption spectra of radicals **29** and **30** are an overlap of the absorption spectra of *N*-ethylcarbazole and radical **38**, a characteristic that indicates that the two aromatic fragments are acting independently (Figure 1.31).[10, 11] This profile could be expected given that no conjugation can take place between both units, since they are linked by a saturated alkyl chain. The lack of extra absorption bands at longer wavelength indicates that no intramolecular interactions, such as the formation of excimers, take place.

Accordingly, the fluorescence spectra of these two species are also an overlap of the emission spectra of their two units, as it is displayed in Figure 1.34. However, some changes in their intensity are observed regarding the emission of the *N*-ethylcarbazole and radical **38**. The emission band attributed to the carbazole moiety is strongly quenched in radical adducts **29** and **30**, while the intensity of the emission in the visible region, which is exclusively due to the radical core, is higher in these adducts than in radical **38** when all compounds are excited in the UV region.* That is, compounds **29** and **30** presented higher quantum efficiencies than what would correspond to the absorption of the radical fragment. This phenomenon was not observed in the solution containing *N*-ethylcarbazole and **38** in a 1:1 molar ratio and with the same concentration.

*Absorption at the excitation wavelength of radicals **29** and **30** was considered the addition of the proportional absorption of each unit at this wavelength, so that at the chosen concentrations and wavelength all radical units had the same absorption.

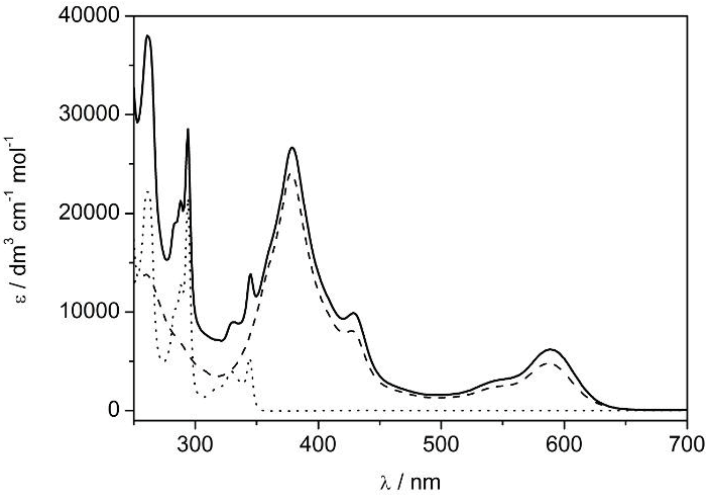

Figure 1.31. Absorption spectra of *N*-ethylcarbazole (dotted line), **31** (dashed line) and **30** radical (solid line).

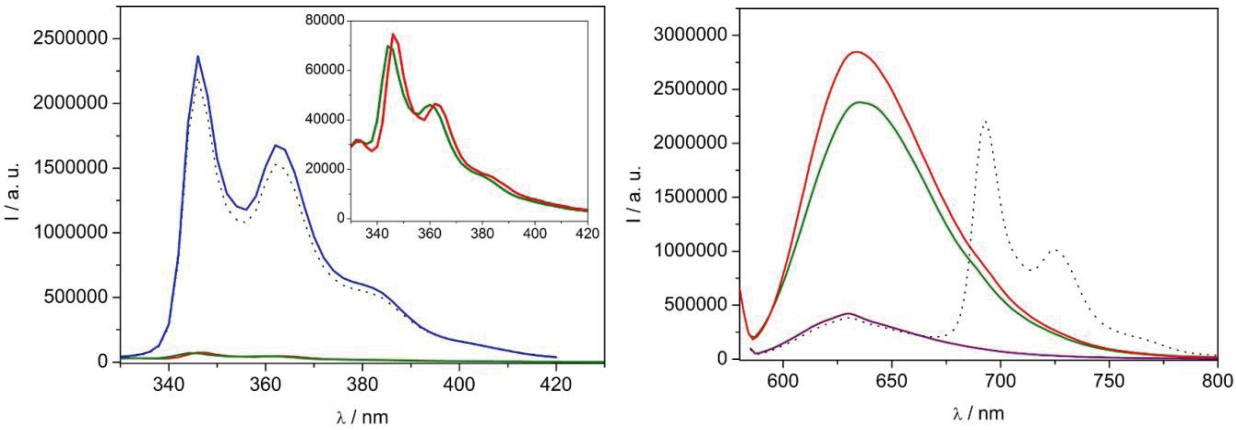

Figure 1.32. Emission bands in the UV region (left) and in the visible region (right) registered by exciting around 285 nm the cyclohexane solutions of *N*-ethylcarbazole (blue), **38** (lilac), a 1:1 molar ratio mixture of *N*-ethylcarbazole and **38** (dotted line), **29** radical (green) and **30** (red).

This behavior is attributed to an intramolecular energy transfer from the excited carbazolyl moiety, which acts as a donor of photons, and the radical moiety, the acceptor, so that the emission of the first is quenched and the emission of the latest is enhanced.[10] Thus, no charge transfer takes place and, accordingly, no charge-separation in cyclohexane solution.[11, 15, 27]

The same experiments were performed using a more polar medium in order to favor a possible CT state resulting from the transfer of an electron from the carbazole fragment to the radical fragment (Figure 1.33). The obtained results when radicals **29** and **30** were excited in the UV region were similar to those recorded for the cyclohexane solutions: a drop in the emission intensity of the fluorescence band attributed to the carbazole accompanied by the increase of the emission intensity

of the band in the visible region. This behavior indicates that an intramolecular energy transfer occurs also in chloroform, regardless the higher polarity of the media. However, the quantum yields of all bands in the chloroform solutions resulted lower than in the cyclohexane solutions, even for the isolated *N*-ethylcarbazole and **38** (Table 1.14).

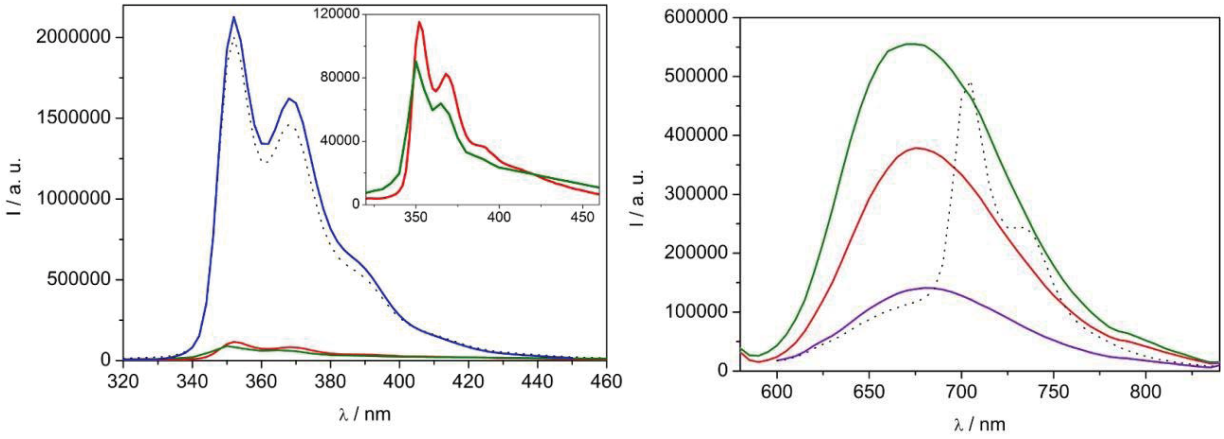

Figure 1.33. Emission bands in the UV region (left) and in the visible region (right) registered by exciting at 284 nm the chloroform solutions of *N*-ethylcarbazole (blue), **38** (lilac), a 1:1 molar ratio mixture of *N*-ethylcarbazole and **38** (dotted line), **29** (green) and **30** (red).

The excitation spectra of radicals **29** and **30** in chloroform solution recorded at 675 nm resembles the corresponding absorption spectra (Figure 1.34). However the relative intensities of the bands corresponding to the carbazole fragment are lower in the excitation spectra than in the absorption spectra. This indicates that the radical fragment emits when the carbazole fragment is absorbing light, but not proportionally to the absorbed light, which is in agreement with the energy transfer process discussed above.

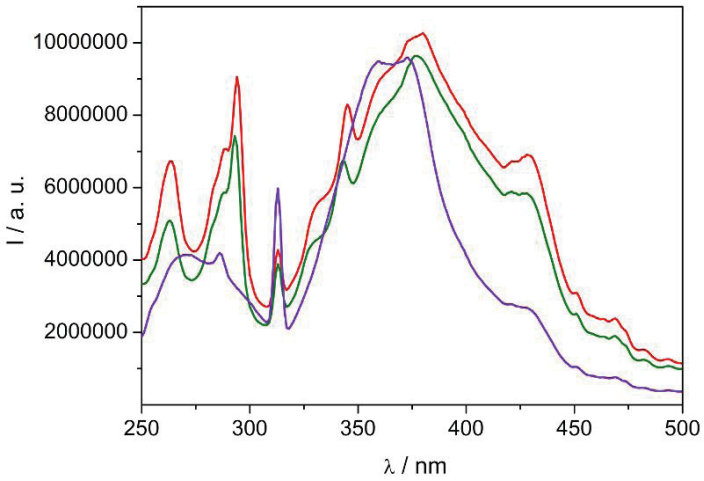

Figure 1.34. Excitation spectra of **29** (green), **30** (red) and **38** (lilac) in chloroform solution at 675 nm.

Table 1.14. Emission wavelengths and quantum yields registered for the cyclohexane solutions of the different systems in the UV region (λ_{em1}) and the visible region (λ_{em2}) of the spectrum, by exciting at two different wavelengths.

	λ_{exc} / nm	λ_{em1} / nm	ϕ_f	λ_{em2} / nm	ϕ_f	λ_{exc} / nm	λ_{em} / nm	ϕ_f
etcz	285	346, 362	0.40	-	-			
38	289	-		630	0.01	565	630	0.09
mix	289	346, 362	0.36	630	0.01	-	-	-
29	289	345, 360	0.01	634	0.12	565	634	0.06
30	289	345, 360	0.01	634	0.14	565	634	0.11

etcz = *N*-ethylcarbazole, mix: equimolecular mixture of *N*-ethylcarbazole and **31**.

According to the previous studies performed on the *N*-carbazolylTTM radical family, a CT to the trivalent carbon should lead to a quenching of the fluorescence emission in the visible region. Thus, if by exciting the carbazole moiety a CT takes place, a decrease of the intensity in the emission band in the visible region should be observed comparing with the fluorescence activity of radical **38** in the same conditions. Therefore, radicals **29** and **30** do not seem to present any CT from the heterocycle to the radical and, consequently, no charge separation. However, the lower quantum yields observed in all radicals regarding the quantum yields obtained for the cyclohexane solutions, even when they were excited in the visible region, suggest that they present some CT from the amino group attached to the triphenylmethyl fragment to the central carbon.

Table 1.15. Emission wavelengths and quantum yields registered for the cyclohexane solutions of the different systems in the UV region (λ_{em1}) and the visible region (λ_{em2}) of the spectrum, by exciting at two different wavelengths.

	λ_{exc} / nm	λ_{em1} / nm	ϕ_f	λ_{em2} / nm	ϕ_f	λ_{exc} / nm	λ_{em} / nm	ϕ_f
Etcz	286	352, 368	0.11	-	-			
31	284	-		683	-	550	683	0.02
Mix	284	352, 368	0.10	683	0.01	-	-	-
29	284	350, 365	0.01	683	0.02	540	683	0.03
30	284	352, 368	0.01	683	0.01	550	683	0.02

etcz= *N*-ethylcarbazole, mix: equimolecular mixture of *N*-ethylcarbazole and **31**.

1.2.4. Electrochemical studies

Electrochemical behavior proved to be very similar in all radicals. All of them present two reversible redox processes: a reversible oxidation to the cationic species and a reversible reduction to the anionic species (Figure 1.35). This electrochemical bipolarity is due to the ability of the SOMO of losing and gaining a single electron so that the resulting systems acquire a closed-shell electronic configuration.[2, 8, 9] The electrochemical parameters deduced from the cyclic voltammetries of radicals **21**, **1**, **18**, **11**, **2**, **19**, **3** and **29** are listed in table 1.16.

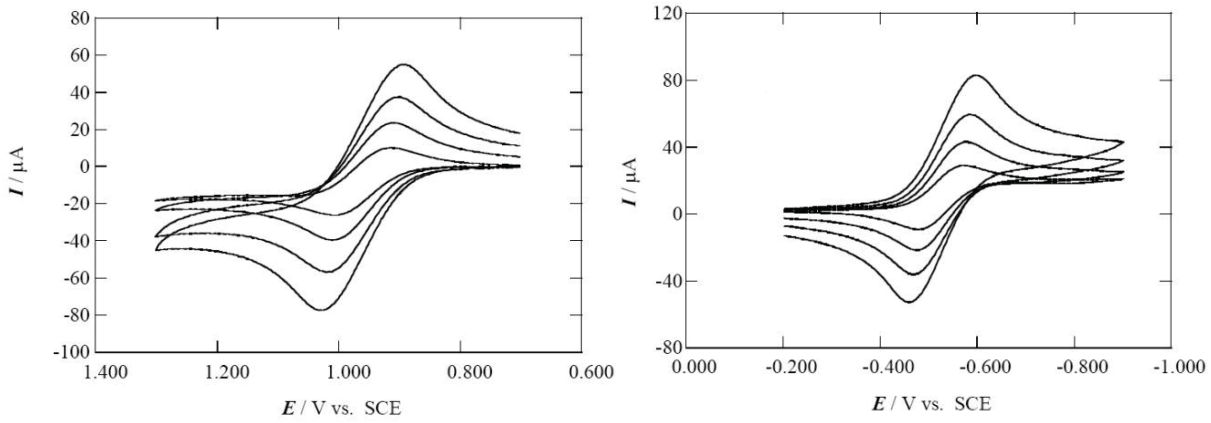

Figure 1.35. Typical cyclic voltammetries of the oxidation process (left) and the reduction process (right) registered for the different radicals.

Table 1.16. Standard oxidation (E^0_{ox}) and reduction (E^0_{red}) potentials vs. SCE electrode and calculated ionization potential and electron-affinity values of some synthesized radicals.

	E^0_{ox} / V[a]	E^0_{red} / V[a]	IP / eV[b]	EA / eV[b]	IP / eV[c]
21	0.95	-0.54	5.52	4.18	
1	1.03	-0.52	5.59	4.19	5.78
18	1.18	-0.47	5.74	4.25	5.90
11	1.00	-0.54	5.56	4.18	5.83
2	0.96	-0.53	5.52	4.19	5.62
19	1.13	-0.43	5.71	4.29	
3	0.90	-0.52	5.48	4.19	
20	1.12	-0.39	5.69	4.33	

[a]Experimental conditions are described in the experimental section. [b]Calculated using the formula E^{onset}-E^0(Fc/Fc+)+4.8, where E^0(Fc/Fc+) = 0.16 V is the standard oxidation potential of ferrocene vs. SCE electrode; [c]Determination of IP values by photoemission in air was only performed for materials whose charge transport properties were studied (see section 2.2.1).

The attachment of carbonyl groups produces an increase of the standard oxidation potentials and of the IP values, as well as an increase of the standard reduction potentials and of the electron-affinities, which is attributed to the electron-withdrawing nature of the acyl chains. The inverse effect is observed by increasing the number of carbazole units, that is, the greater the electron-donor character the less energy needed to extract an electron. The substitution of the carbazole fragment for the indole fragment does not lead to significant changes in the electrochemical properties, only to a weak increase of the IP.

While for molecules bearing an even number of electrons IP and EA are used to estimate the HOMO and LUMO energy levels, in the case of the neutral radicals it must be considered that the energy involved in the oxidation and the reduction processes is used to remove or attach an electron in the same orbital, the SOMO. In other words, oxidizing a molecule means supplying the necessary energy to overcome the binding energy of the electron that is removed. Since this electron is located in the highest energy level, the energy required to promote it to the infinity is taken as the HOMO energy. Similarly, the EA is the energy released when an electron is attached to a neutral molecule, which is taken as the LUMO energy, that is, the energy of the MO where the electron remains. In the case of these neutral radicals, though, the removed electron and the attached electron comes from and ends up, respectively, in the same molecular orbital, the SOMO. Therefore, it could be expected that the IP and the EA have the same value corresponding to the SOMO energy. However, in the case of the reduction, the new electron is not attached to an empty MO, but to a half-filled one. Thus, some repulsion energy must be overcome and the energy released in the reduction process (EA) is lower than the energy supplied in the oxidation process (IP).

By combining the information about the electronic transitions that take place in the radical systems from the absorption spectra and the information deduced from the cyclic voltametries, the values of the HOMO, the SOMO and the LUMO energies can be proposed (Figure 1.36). Assuming that the IP value corresponds to the SOMO energy, the HOMO energy can be calculated by extracting the λ_{onset} in eV of the absorption band assigned to the $D_0 \rightarrow D_1$. However, this band is overlapped with the CT band, and thus the absorption onset is used to approximate the E_{gap} instead. Since it was determined that the band at 450 nm corresponds to the SOMO→LUMO transition, the LUMO energy is estimated by the addition of the λ_{onset} in eV of this band to the SOMO energy.

The proper theoretical calculations must be done to confirm the proposed approximation of the energy levels of the radicals. Nevertheless, a further discussion of the role of the different orbitals in the operation of the different electronic devices will be exposed in chapter 3.

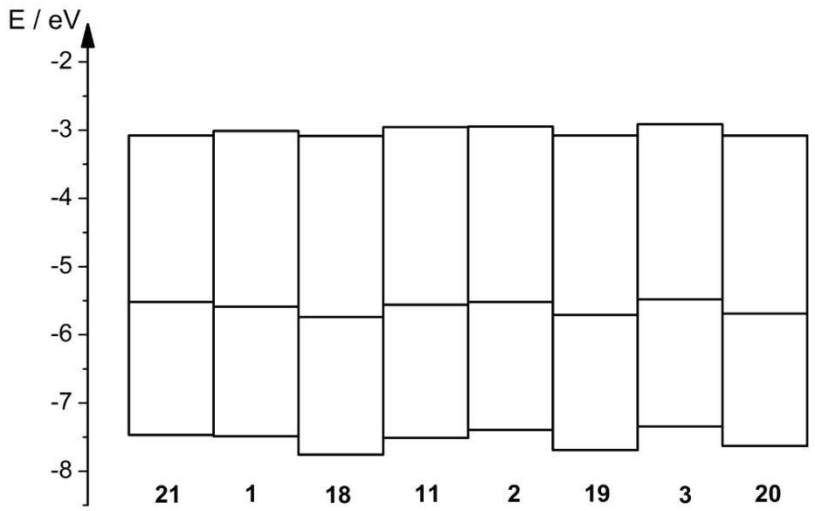

Figure 1.36. Energetic levels of the different radicals estimated from the UV-vis. absorption spectra and the cyclic voltammetries.

1.2.5. Summary

The coupling reaction between *N*H-carbazole and **TTM** radical proceeds through a radicalary mechanism that starts with the formation of a cationic radical of *N*H-carbazole by the electron transfer to a molecule of **TTM** radical.

The acylation of positions 3 and 6 of the carbazole unit in the radical adducts of the *N*-carbazolylTTM with 8-carbon acyl chains allows the attainment of stable radical molecular glasses (**18** and **19**) with high glass transition temperatures.

The disk-like radical adduct prepared by the attachment of acyl chains of 18 carbons in positions 3 and 6 of the carbazole moieties in the tris[4-(*N*-carbazolyl)-2,6-dichlorophenyl]methyl radical core (**3**), radical adduct **40**, piles in two columnar arrangements: a glassy rectangular columnar phase (Col_r) under room temperature and an ordered hexagonal columnar liquid crystalline phase (Col_{ho}) above room temperature. The closeness of the aromatic cores in the Col_{ho} leads to the antiferromagnetic interaction of the spins of the radicals along the columns. However, the 12 carbon acyl chain counterpart, radical adduct **41**, shows a single Col_{ro} arrangment in which no intermolecular magnetic interactions were detected. Radical **40** is the first reported example of all organic radical discotic liquid-crystal bearing the spin in the center of the core.

All radical adducts present a wide range of light absorption with two main absorption bands, one in the UV and another in the red region of the visible spectrum. These bands are attributed to the existence of the SOMO, so that the two electronic transitions SOMO→LUMO and HOMO→SOMO take place. Solvatochromic emission in the red region of the visible spectrum was also detected for all *N*-carbazolylTTM radical derivatives. The number of carbazole units, as well as the electron-donor or electron-withdrawing nature of the functional groups attached to the carbazole units, produce bathochromic or hipsochromic shifts in the absorption and emission bands in the visible region. As a general rule, the more favored the charge transfer from the carbazole fragment to the trivalent carbon of the radical fragment, the more bathochromic shift and the more the emission is quenched. However, no charge transfer from the carbazole unit to the radical core was detected in carbazole-bridge-TTM radical systems, but an energy transfer process.

All radical adducts present a bipolar redox behavior, that is, they present both reversible oxidations and reductions, a feature attributed to the ability of the SOMO of losing or gaining an electron to attain stable charged closed-shell configurations. The IP values, deduced from the electrochemical studies proved to depend on the electronic nature of the groups attached to the radical core.

1.2.6. Experimental section.

1.2.6.1. Materials and methods.

^{1}H spectra were recorded in Varian Geminy (300 MHz), Varian Inova (300 MHz), Varian Unity (300 MHz) and Varian Mercury (400 MHz) spectrometers. Signals are noted as singlet (s), doublet (d), triplet (t) and multiplet (m).

Mass spectra were recorded by the Mass spectrometry service at the Chemistry faculty of the Universitat de Barcelona using the techniques: chemical ionization (CI) with a ThermoFinniganTRACE DSQ spectrometer using NH_3 as reagent gas; electronic impact (EI) and MALDI-TOF with a Voyager-DE RP spectrometer.

IR spectra were registered in a Fourier transform NICOLET Avatar 360. Peaks intensity is expressed as strong (s), medium (m) and weak (w).

UV-vis. absorption spectra were recorded in two Varian spectrometers, models Cary 300-Bio and Cary 500. Emission and excitation spectra were recorded in a PTI fluorimeter equipped with a 220B lamp power supply, an 815 photomultiplier detection system and a Felix 32 software. Quartz cuvettes of 1 cm optical path were used.

EPR spectra were recorded with a Varian spectrometer, model E-109 (E-Line Century Series), using a frequency υ = 9.5 Hz (X-band frequency). Temperature was regulated with a variable temperature Varian system, model E-257. Solutions of the radicals were prepared with spectrophotometric CH_2Cl_2 and introduced in quarz tubes. Study of the liquid-crystalline radicals were performed in an X-Band Bruker ESP 300 E spectrometer, equipped with an ER 412HT temperature controller, a field frequency (F/F) lock accessory and a built-in NMR gaussmeter.

Magnetic susceptibility measurements were performed by the Serveis Cientificotècnics of the University of Barcelona using a SQUID MPMS-XL Quantum Design (5T).

Cyclic voltammetries were registerd by Dr. Brillas from the Physical Chemistry Department at the University of Barcelona using an Eco Chemie Autolab PGSTAT00 potentiostat-galvanostat. The working electrode was a platinum sphere (0.0093 cm^2), the contraelectrode was a platinum wire and the reference electrode was an SCE electrode. The studied compounds were dissolved in distilled CH_2Cl_2 (~10^{-3} M) with *tert*-buthylamonium perchlorate, TBAP, (~0.1 M) as supporting electrolite and the temperature of the solution was kept at 25 °C during the measurements.

DSC diagrams were registered by the Thermal Analysis service at the Institut de Química Avançada de Catalunya (IQAC-CSIC) with a Mettler-Toledo DSC821 apparatus.

X-ray diffractograms were registered by the Serveis Cientificotècnics of the Universitat de Barcelona using a CPS-120 Debye-Scherrer diffractometer and a Siemens D-500 diffractometer with a Bragg-Bentano geometry theta/2theta, both apparatus equipped with temperature control devices.

Theoretical calculations were performed using the software Gaussian03.

1.2.6.2. Experimental.

1.2.6.2.1. Tris(2,4,6-trichlorophenyl)methane (αH-TTM)

A mixture of 1,3,5-trichlorobenzene (40 g; 220 mmol), chloroform (2.1 ml; 26 mmol) and aluminum chloride (10.3 g; 77 mmol) is heated at 110 °C in a hermetically closed glass reactor (5 h). The crude is poured on HCl/H_2O/ice and extracted with $CHCl_3$. The organic layer was dried over $MgSO_4$ and the solvent was eliminated by evaporation. The resulting solid was stirred in boiling hexane and **αH-TTM** was isolated as a white powder by filtering.

IR (KBr): 3079 (w), 1721 (w), 1573 (s), 1542 (s), 1430 (m), 1371 (w), 1337 (w), 1245 (m), 1188 (m), 1166 (m), 1138 (m), 1122 (w), 1074 (w), 896 (w), 856 (w), 803 (w), 778 (w), 764 (w) cm^{-1}.

^1H NMR (300 MHz, $CDCl_3$) δ: 7.36 (d, 3H, *J* = 2.1 Hz, ph); 7.24 (d, 3H, *J* = 2.4 Hz, ph); 6.68 (s, 1H, CH) ppm.

1.2.6.2.2. Tris(2,4,6-trichlorophenyl)methyl radical (TTM)

An aqueous solution of TBAH (1.5M) (7.5 ml; 11.0 mmol) was added to a solution of **αH-TTM** (4.0 g; 7.0 mmol) in THF (130 ml) and stirred (5 h) in an inert atmosphere at rt. and then tetrachloro-*p*-benzoquinone (2.0 g; 8.0 mmol) was added. The solution was stirred in the dark (45 min) and evaporated to dryness. The crude is dissolved in $CHCl_3$, the organic layer is washed with water and dried over $MgSO_4$. The solvent is removed under vacuum, giving a residue which was filtered on silica gel with hexane to give **TTM** radical (3.1 g; 78%).

IR (KBr): 1551 (s), 1519 (s), 1383 (m), 1366 (m), 1280 (w), 1237 (w), 1179 (m), 1134 (m), 1079 (w), 919 (m), 857 (s), 813 (s), 786 (s), 721 (w), 562 (s) cm^{-1}.

1.2.6.2.3. [4-(*N*-carbazolyl)-2,6-dichlorophenyl]bis(2,4,6-trichlorophenyl)methane radical (1H) and bis[4-(*N*-carbazolyl)-2,6-dichlorophenyl](2,4,6-trichlorophenyl)methane (2H)

A mixture of *N*H-carbazole (500 mg; 3.0 mmol), **TTM** (0.500 g; 0.73 mmol), anhydrous Cs_2CO_3 (541 mg; 1.6 mmol) and DMF (9 ml) was stirred at reflux (3 h) in an inert atmosphere and in the dark. The resulting mixture was poured into an excess of diluted aqueous HCl acid and the precipitate was filtered off. The solid was chromatographed in silica gel with hexane:$CHCl_3$ (4:1) to give **1H** (0.246 g; 49%) and bis(4-(*N*-carbazolyl)-2,6-dichlorophenyl)(2,4,6-trichlorophenyl)methane **2H** (0.177 g; 30%).

[4-(*N*-carbazolyl)-2,6-dichlorophenyl]bis(2,4,6-trichlorophenyl)methane (1H)

IR (KBr): 3058 (w), 1598 (s), 1576 (s), 1541 (s), 1494 (m), 1478 (m), 1465 (s), 1452 (s), 1442 (m), 1370 (s), 1334 (m), 1314 (m), 1232 (s), 1173 (m), 1142 (m), 1076 (m), 998 (m), 928 (m), 899 (m), 861 (s), 838 (m), 808 (s), 748 (s), 722 (s) cm^{-1}.

^1H NMR (400 MHz, $CDCl_3$) δ: 8.13 (d, 2H, *J* = 6 Hz, cz), 7.61 (d, 1H, *J* = 1.6 Hz, ph), 7.48 (d, 1H, *J* = 1.6 Hz, ph), 7.44-7.46 (m, 4H, cz), 7.43 (d, 1H, *J* = 1.6 Hz, ph), 7.40 (d, 1H, *J* = 1.6 Hz, ph), 7.30-7.3 (m, 3H, cz+ph), 7.28 (d, 1H, *J* = 1.6 Hz, ph), 6.85 (s, 1H, CH) ppm

Bis[4-(*N*-carbazolyl)-2,6-dichlorophenyl](2,4,6-trichlorophenyl)methane (2H).

IR (KBr) 3058 (w), 1598 (s), 1576 (s), 1543 (s), 1493 (s), 1479 (m), 1464 (s), 1452 (s), 1442 (m), 1334 (m), 1310 (m), 1228 (s), 1174 (m), 1074 (m), 998 (m), 921 (m), 884 (m), 878 (m), 831 (m), 797 (s), 748 (s), 721 (s) cm^{-1}.

^1H NMR (400 MHz, $CDCl_3$) δ: 8.14 (d, 4H, *J* = 6.4 Hz, cz), 7.68 (d, 1H, *J* = 1.6 Hz, ph), 7.65 (d, 1H, *J* = 1.6 Hz, ph), 7.55 (d, 1H, *J* = 1.6 Hz, ph), 7.52 (d, 1H, *J* = 1.6 Hz, ph), 7.45-7.50 (m, 10H, cz+ph), 7.35-7.32 (m, 6H, cz+ph), 7.03 (s, 1H, CH) ppm.

Anal. Calcd for $C_{43}H_{23}Cl_7N_2 \cdot CHCl_3$ (1:5): C, 61.8; H, 2.8; Cl, 32.1; N, 3.3. Found: C, 61.7; H, 2.8; Cl, 31.5; N, 3.3.

1.2.6.2.4. Tris[4-(*N*-carbazolyl)-2,6-dichlorophenyl]methane (3H).

A mixture of *N*H-carbazole (500 mg; 3.0 mmol), radical **2** (500 mg; 0.61 mmol), anhydrous Cs_2CO_3· (500 mg; 1.5 mmol) and DMF (10 ml) was stirred at reflux (2.5 h) in an inert atmosphere and in the dark. The resulting mixture was poured into an excess of diluted aqueous HCl acid and the precipitate was filtered off. The solid was chromatographed in silica gel with CCl_4 to give **2H** (415 mg; 83%), identified by IR and **3H** (0.071 g; 12%).

IR (KBr): 3055 (w), 2953 (m), 2923 (m), 2853 (m), 1596 (s), 1574 (m), 1543 (w), 1493 (m), 1463 (s), 1453 (s), 1333 (m), 1310 (m), 1227 (m), 1172 (w), 1151 (w), 1073 (w), 996 (w), 921 (w), 878 (w), 799 (m), 746 (s), 721 (m), 652 (w) cm^{-1}.

^1H NMR (300 MHz, $CDCl_3$) δ: 8.15 (d, 6H, *J* = 7.4 Hz, cz), 7.72 (d, 3H, *J* = 2.4 Hz, ph), 7.59 (d, 3H, *J* = 2.1Hz, ph), 7.53-7.46(m, 12H, cz), 7.37-7.32(m, 6H, cz), 7.21(s, 1H, CH) ppm.

Anal. Calcd for $C_{55}H_{31}Cl_6N_3$: C, 69.8; H, 3.3; Cl, 22.5; N, 4.4. Found: C, 69.8; H, 3.8; Cl, 21.7; N, 4.2.

1.2.6.2.5. [2,6-Dichlorophenyl-4-(*N*-indolyl)]bis(2,4,6-trichlorophenyl)methane (11H), bis[2,6-dichlorophenyl-4-(*N*-indolyl)](2,4,6-trichlorophenyl)methane (12H) and tris[2,6-dichlorophenyl-4-(*N*-indolyl)]methane (13H).

A mixture of *N*H-indole (0.320 g; 2.7 mmol), **TTM** radical (1.5 g; 5.4 mmol), anhydrous Cs_2CO_3 (0.880 g; 2.7 mmol) and DMF (25 ml) was stirred at reflux (2 h) in an inert atmosphere and in the dark. The resulting mixture was poured into an excess of diluted aqueous HCl acid and the precipitate was filtered off. The solid was chromatographed in silica gel with hexane:$CHCl_3$ (4:1) to give **αH-TTM** (0.470 g; 31%) identified by IR, **11H** (0.485 g; 28%), **12H** (0.480 g; 25%) and **13H** (0.065 g; 3%).

[2,6-Dichlorophenyl-4-(*N*-indolyl)]bis(2,4,6-trichlorophenyl)methane (11H).

IR (KBr): 3070(w), 1598(s), 1579 (m),1545 (s), 1476 (s), 1468 (s), 1449 (w), 1372 (m), 1332(m), 1296 (w), 1259 (w),1236 (w), 1211 (m), 1193 (w), 1175 (m), 1136 (m), 1023 (m), 899 (m), 859 (s),837 (w), 804 (s), 761 (m), 742 (s), 714 (w), 677 (w) cm^{-1}.

^1H NMR (300 MHz, $CDCl_3$) δ: 7.65 (d, 1H, *J* = 7.8 Hz, ind), 7.57 (d, 1H, *J* = 7.8 Hz, ind), 7.51 (d, 1H, *J* = 2.4 Hz, ph), 7.37-7.35 (m, 3H, ph), 7.29 (d, 1H, *J* = 3.3 Hz, ind), 7.27–7.22 (m, 3H, ind+ph), 7.16 (t, 1H, *J* = 7.5 Hz, ind), 6.75 (s, 1H, CH), 6.67 (d, 1H, *J* = 3.3 Hz, ind) ppm.

MS (MALDI-TOF): *m/z* = 633.3 (M^+-1).

Anal. Calcd for $C_{27}H_{13}Cl_8N$: $CHCl_3$ (8:3) C, 48.4; H, 2.0; N, 2.1. Found: C, 48.7; H, 2.1.

Bis[2,6-dichlorophenyl-4-(*N*-indolyl)](2,4,6-trichlorophenyl)methane (12H)

IR (KBr): 3072 (w), 2922 (w) 1595 (s), 1577 (m), 1542 (s), 1518 (m), 1468 (s), 1449 (m), 1396 (m), 1374 (m), 1332 (m), 1297 (w), 1235 (w), 1212 (m), 1193 (w), 1174 (w), 1137 (m), 1071 (w), 1015 (w), 898 (w), 883 (w), 870 (w), 859 (m), 832 (w), 808 (m), 763 (m), 739 (s), 730 (m), 684 (w) cm^{-1}.

^1H NMR (400 MHz, $CDCl_3$) δ: 7.68 (d, 2H, *J* = 7.6 Hz, ind), 7.63 (d, 2H, *J* = 7.6 Hz, ind), 7.58 (d, 1H, *J* = 2.4 Hz, ph), 7.57 (d, 1H, *J* = 2.4 Hz, ph), 7.34 (d, 2H, *J* = 3.6 Hz, ind), 7.30-7.26 (m, 3H, ind+ph), 7.21 (t, 2H, *J* = 7.6 Hz, ind), 6.90 (s, 1H, CH) ppm

MS (EI): *m/z*= 714.5 (M^+-1)

Tris[2,6-dichlorophenyl-4-(*N*-indolyl)]methane (13H)

IR (KBr): 3072 (w), 2924 (w), 2853 (w), 1595 (s), 1545 (m), 1519 (m), 1468 (s), 1449 (m), 1394 (w), 1332 (m), 1297 (w), 1236 (w), 1210 (m), 1177 (w), 1135 (m), 1071 (w), 1016 (w), 870 (w), 799 (w), 763 (w), 740 (m), 171 (w) cm^{-1}.

^1H NMR (400 MHz, $CDCl_3$) δ: 7.69 (d, 3H, J = 7.5 Hz, ind), 7.66 (d, 3H, *J* = 7.5 Hz, ind), 7.61 (d, 3H, *J* = 2.5 Hz, ph), 7.47 (d, 3H, *J* = 2.5 Hz, ph), 7.36 (d, 3H, *J* = 3.5 Hz, ind), 7.30 (t, 3H, *J* = 7.5 Hz, ind), 7.22 (t, 3H, *J* = 7.5 Hz, ind), 7.01 (s, 1H, CH), 6.73 (d, 3H, *J* = 3.5 Hz, ind) ppm.

MS (EI): *m/z* = 793.1 (M^+-1)

1.2.6.2.6. 3,6-diacetyl-*N*H-carbazole (16)

Acetyl chloride (2.8 ml; 39.6 mmol) is added to a stirred mixture of carbazole (3.0 g; 18 mmol), $AlCl_3$ (5.33 mg; 40 mmol), and CS_2 (45 ml) at reflux in an anhydrous atmosphere. The mixture was further refluxed (6 h), and then the solvent was evaporated off and the crude was chromatographed on silica gel with chloroform to give **16** (3.38 g, 75%).

IR (KBr) 3277 (s), 1673 (s), 1662 (s), 1623 (s), 1599 (s), 1490 (w), 1451 (w), 1406 (w), 1358 (m), 1293 (m), 1267 (m), 1240 (m), 1227 (m), 1140 (w), 1127 (w), 1053 (w), 1021 (w), 956 (w), 904 (w), 882 (w), 829 (w), 820 (w), 802 (w), 638 (w) cm^{-1}

^1H NMR (300 MHz; $CDCl_3$) δ: 8.79 (d, *J* = 1.5 Hz, 2H, $H_{(4,5)}$), 8.15 (dd, *J* = 8.4 Hz, *J* = 1.5 Hz, 2H, $H_{(2,7)}$), 7.51 (d, *J* = 8.4 Hz, 2H, $H_{(1,8)}$), 2.77 (s, 6H, CH_3 x 2) ppm.

UV (cyclohexane) λ_{max}/nm (ε/dm^3 mol^{-1} cm^{-1}): 260 (34800), 292 (20600), 325 (10300)

EI-HRMS: calcd for $C_{16}H_{13}NO_2$ 252.097984, found *m/z* = 252.097546.

1.2.6.2.7. 3,6-diethyl-*N*H-carbazole (17)

A mixture of $HgCl_2$ (2.5 mg), metallic Zn (26 g), and concentrated aqueous HCl acid (2.5 ml) in water (50 ml) was stirred at rt. (15 min) to generate an amalgam. Concentrated aqueous HCl acid (40 ml) and 3,6-diacetylcarbazole (1 g, 5.99 mmol) were added, and the mixture was stirred vigorously (2 h) and then allowed to stand (12 h). Toluene (15 ml) was added, and the mixture was stirred to reflux (48 h). The resultant phases were separated, the aqueous phase was extracted with diethyl ether, and the combined organic phases were washed with water, dried, and evaporated to dryness. The residue was filtrated through silica gel with hexane to give **17** (417 mg, 47%).

IR (KBr): 3417 (m), 2968 (m), 2926 (w), 2868 (w), 2853 (w), 1866 (w), 1765 (w), 1610 (w), 1574 (w), 1494 (s), 1465 (s), 1371 (w), 1326 (m), 1303 (m), 1248 (s), 1147 (w), 1055 (w), 920 (w), 883 (s), 813 (s), 752 (w) cm^{-1}

^1H NMR (300 MHz; $CDCl_3$) 7.89 (s, 2H, $H_{(4,5)}$), 7.85 (s, 1H, NH), 7.32 (d, *J* = 8.1 Hz, 2H, $H_{(2,7)}$), 7.25 (d, *J* = 8.1 Hz, 2H, $H_{(1,8)}$), 2.83 (q, *J* = 7.8 Hz, 4H, CH_2 x 2), 1.35 (t, *J* = 7.8 Hz, 6H, CH_3 x 2) ppm

EI-HRMS calcd for $C_{16}H_{17}N$ 223.136100, found *m/z* = 223.136365.

1.2.6.2.8. [2,6-dichloro-4-(3,6-diethyl-*N*-carbazolyl)phenyl]bis(2,4,6-trichlorophenyl)methane (15H)

A mixture of **17** (300 mg; 1.35 mmol), **TTM** (500 mg; 0.9 mmol), anhydrous Cs_2CO_3 (500 mg; 1.5 mmol), and DMF (8 mL) was stirred at reflux (2 h) in an inert atmosphere and in the dark. The resulting mixture was poured into an excess of diluted aqueous HCl acid, and the precipitate was filtered off. The solid was chormatographed in silica gel with hexane/chloroform (9:1) to give **15H** (115 mg; 17%). Characterization of this compound is given in section 1.2.6.2.26.1.

1.2.6.2.9. General procedure for the preparation of radical adducts of the *N*-carbazolylTTM and the *N*-indolylTTM families from the corresponding triphenylmethane precursors.

An aqueous solution of TBAH (1.5 M) (2 eq.) was added to a solution of the corresponding triphenylmethane precursor in THF and stirred (overnight) in an inert atmosphere at rt. 2,3-Dichloro-5,6-dicyano-*p*-benzoquinone (DDQ) (3 eq.) was then added and the solution was stirred in the dark (45 min) and evaporated to dryness, giving a residue which was filtered through silica gel with a hexane:$CHCl_3$ mixture to give the corresponding radical.

1.2.6.2.9.1. [4-(*N*-Carbazolyl)-2,6-dichlorophenyl]bis(2,4,6-trichlorophenyl)methyl radical (1)

Starting materials: **1H** (0.510 g, 0.75 mmol), TBAH (1 ml, 1.5 mmol), DDQ (255 mg, 1.13 mmol), THF (35 ml)

Eluent: hexane/$CHCl_3$ (8:2)

η = 83%

m. p. (DSC): 298 °C (dec)

IR (KBr): 3068 (w), 1573 (s), 1553 (s), 1522 (s), 1492 (m), 1477 (w), 1461 (s), 1368 (m), 1322 (m), 1306 (m), 1281 (w), 1232 (m), 1183 (m), 1137 (m), 1076 (w), 994 (w), 922 (w), 861 (m) 814 (m), 747 (s), 722 (m), 661 (w) cm^{-1}.

UV ($CHCl_3$) λ_{max}/nm (ε/dm^3 mol^{-1} cm^{-1}): 291 (14 400), 324 (6900), 339 (9600), 374 (25 800), 446 (2600), 564 (sh) (2100), 598 (2940)

EI-HRMS: calcd for $C_{31}H_{14}Cl_8N$: 679.863446; found: *m/z* = 679.862383.

1.2.6.2.9.2. Bis[4-(*N*-carbazolyl)-2,6-dichlorophenyl](2,4,6-trichlorophenyl)methyl radical (2)

Starting materials: **2H** (0.730 g, 0.90 mmol), HTBA (1.2 ml, 1.8 mmol), DDQ (306 mg, 1.35 mmol),THF (35 ml)

Eluent: hexane/$CHCl_3$ (7:3)

η = 93%

m. p. (DSC): 347 °C (dec)

IR (KBr): 3053 (w), 1573 (s), 1524 (m), 1493 (s), 1471 (s), 1341 (m), 1333 (s), 1310 (m), 1226 (m), 804 (m), 748 (s), 720 (m) cm^{-1}

UV ($CHCl_3$) λ_{max}/nm (ε/dm^3 mol^{-1} cm^{-1}): 292 (28000), 323 (10300), 337 (12200), 376 (22100), 445 (7350), 571 (sh) (3840), 609 (5130)

EI-HRMS: calcd for $C_{43}H_{22}Cl_7N_2$ 810.960268, found *m*/z = 810.959629.

1.2.6.2.9.3. Tris[4-(*N*-carbazolyl)-2,6-dichlorophenyl]methyl radical (3)

Starting materials: **3H** (0.150 g, 0.16 mmol), HTBA (0.21 ml, 0.32 mmol), DDQ (54 mg, 0.24 mmol), THF (30 ml)

Eluent: hexane/$CHCl_3$ (6:4)

η= 59%

m.p. (DSC): 355 °C (dec)

IR (KBr): 3065 (w), 1571 (s), 1524 (m), 1493 (m), 1453 (s), 1335 (s), 1312 (m), 1224 (m), 806 (m), 746 (s), 723 (s) cm^{-1}.

UV ($CHCl_3$) λ_{max}/nm (ε/dm^3 mol^{-1} cm^{-1}): 291 (36200), 323 (12700), 337 (14050), 377 (20500), 454 (13050), 575 (sh) (4930), 614 (7000)

MS (MALDI-TOF) HRMS calcd for $C_{55}H_{30}Cl_6N_3$ 942.0590, found *m*/*z* = 942.0565

1.2.6.2.9.4. [2,6-dichlorophenyl-4-(*N*-indolyl)]bis(2,4,6-trichlorophenyl)methyl radical (11)

Starting materials: **11H** (480 mg, 0.76 mmol), HTBA (1.01 ml, 1.52 mmol), DDQ (259 mg, 1.14 mmol), THF (30 ml)

Eluent: hexane/$CHCl_3$ (7:3)

η = 70%

m.p. (DSC): 258 °C

IR (KBr): 3070 (w), 1577 (s), 1554 (m), 1525 (s), 1474 (m), 1464 (s), 1370 (m), 1332 (m), 1297 (w), 1235 (w), 1210 (m), 1183 (m), 1134 (m), 1082 (w), 924 (w), 858 (m), 812 (m), 799 (m), 764 (w), 740 (m), 716 (w) cm^{-1}.

UV ($CHCl_3$) λ_{max}/nm (ε/dm^3 mol^{-1} cm^{-1}): 262 (19320), 310 (8880), 374 (28050), 540 (sh) (2395), 584 (3420)

MS (MALDI-TOF): *m/z* = 634.4 (M_++1).

Anal. Calcd for $C_{27}H_{12}Cl_8N$: $CHCl_3$ (8:1) C, 50.2; H, 1.9; N, 2.2. Found: C, 50.3; H, 1.9; N, 2.0

1.2.6.2.9.5. Bis[2,6-dichlorophenyl-4-(*N*-indolyl)](2,4,6-trichlorophenyl)methyl radical (12)

Starting materials: **12H** (0.450 g, 0.62 mmol), HTBA (0.82 ml, 1.24 mmol), DDQ (211 mg, 0.93 mmol), THF (30 ml)

Eluent: hexane/$CHCl_3$ (6:4)

η = 85%

m.p. (DSC): 224 °C

IR (KBr): 3060 (w), 2924 (w), 1576 (s), 1524 (m), 1474 (m), 1463 (s), 1400 (w), 1370 (w), 1330 (m), 1296 (w), 1236 (w), 1210 (m), 1184 (w), 1134 (m), 1081 (w), 1018 (w), 923 (w), 881 (w), 858 (m), 821 (w), 802 (m), 765 (m), 731 (s), 651 (w) cm^{-1}

UV ($CHCl_3$) λ_{max}/nm (ε/dm^3 mol^{-1} cm^{-1}): 266 (27280), 301 (14570), 382 (21500), 413 (sh) (17400), 544 (sh) (3620), 592 (5170)

MS (EI): *m/z* = 715.4 (M^++1)

1.2.6.2.10. Bis(2,6-dichlorophenyl)methanol (5)

To a solution of 1,3-dichlorobenene (10 ml, 87.6 mmol) in anhydrous THF (150 ml) at -78 °C was added dropwise n-BuLi in hexane (1.5 M) (36 ml, 90.0 mmol) under N_2 atmosphere. The reaction is kept at -78 °C (2 h) with stirring and then a solution of 2,6-dichlorobenzaldehyde (15.5 g, 80.7 mmol) in anhydrous THF (50 ml) was added dropwise. The reaction was allowed to attemperate to room temperature (5 h) and then treated with $NH_4Cl_{(aq)}$ (5%). The aqueous layer was extracted with AcOEt and the organic layer was dried over Na_2SO_4. The solvent is removed by evaporation and the crude was filtered on silica gel eluating with $CHCl_3$ to isolate methanol **5** (21.2 g, 82%).

m.p.: 189 °C

^{1}H NMR (300 MHz, $CDCl_3$) δ: 7.32-7.29 (m, 4H, $H_{(m)}$), 7.16 (dd, 2H, *J* = 9 Hz, *J* = 6.9 Hz, $H_{(p)}$), 6.83 (d, 1H, *J* =10.8 Hz, CHOH), 3.56 (d, 1H, *J* = 10.8 Hz, -OH) ppm.

IR (KBr) = 3579 (w), 3530 (w), 3074 (w), 2976 (w), 1943 (w), 1864 (w), 1790 (w), 1675 (w), 1547 (m), 1553 (m), 1420 (w), 1280 (m), 1250 (m), 1182 (s), 1146 (s), 1079 (s) 1012 (s), 866 (m), 817 (s), 775 (s) cm^{-1}.

1.2.6.2.11. Chlorobis(2,6-dichlorophenyl)methane (6)

Methode 1

Methanol **5** (5 g, 15.5 mmol) and $AlCl_3$ (6.2 g, 46.5 mmol) in CS_2 (100 ml) were stirred in a P_2O_5 atmosphere (24 h). The reaction is treated with H_2O/ice, the resulting layers were separated and the aqueous layer is extracted with Et_2O. The combined organic layers were dried over Na_2SO_4 and evaporated to dryness. The crude is chromatographied on silica gel eluating with chloroform:hexane (1:1) to give chlorobis(2,6-dichlorophenyl)methane (6) (4.4 g, 87%).

Methode 2

A solution of **5** in boiling $SOCl_2$ was kept (4 h) under anhydrous atmosphere and then treated with H_2O/ice. The waters were neutralized with $NaHCO_3$ and extracted with $CHCl_3$. The organic layer was dried over Na_2SO_4 and the solvent was removed by evaporation. The resulting solid, identified as chlorobis(2,6-dichlorophenyl)methane (**6**) (4.2 g, 97%), was used in the following reaction without further purification.

m. p.: 161 °C

^{1}H NMR (300 MHz, $CDCl_3$) δ: 7.34-7.32 (m, 4H, $CH_{(m)}$), 7.18 (dd, 2H, J = 9.0 Hz, J = 7.5 Hz, $CH_{(p)}$), 7.15 (s, 1H, CHCl) ppm.

IR (KBr): 3078 (w), 2976 (w), 1931 (w), 1859 (w), 1788 (w), 1675 (w), 1578 (s), 1560 (s), 1497 (m), 1436 (s), 1341 (m), 1284 (m), 1237 (m), 1198 (s), 1168 (m), 1148 (m), 1087 (m), 963 (m), 873 (s), 841 (s), 800 (s), 782 (s), 746 (m), 721 (m), 699 (m), 654 (m), 633 (m), 481 (w), 459 (m) cm^{-1}.

1.2.6.2.12. Chlorobis(2,6-dichloro-3-nitrophenyl)methane (7)

A solution of **6** (2.8 g, 8.3 mmol) and NO_2BF_4 (2.5 g, 18.8 mmol) in sulfolane (50 ml) at 80 °C was stirred (24 h) and then treated with H_2O/ice. The aqueous layer was extracted with Et_2O and the organic layer was washed abundant water to remove all the sulfolane, then dried over Na_2SO_4 and evaporated to dryness. The crude was chromatographied on silica-gel with $CHCl_3$ and compound **7** was isolated (2.1 g, 60%).

m. p.: 163 °C

^{1}H NMR (300 MHz, $CDCl_3$) δ: 7.67 (d, 2H, *J* = 8.7 Hz, $CH_{(4,4')}$), 7.52 (d, 2H, *J* = 8.7 Hz, $CH_{(5,5')}$), 7.19 (s, 1H, CHCl) ppm.

IR (KBr): 3579 (w), 3066 (m), 1902 (w), 1704 (m), 1581 (s), 1564 (s), 1538 (s), 1434 (m), 1366 (m), 1234 (w), 1203 (w), 1174 (w), 1099 (m), 1064 (d), 954(m), 930 (s), 837 (s), 810 (m), 755 (w), 676 (w) cm^{-1}.

1.2.6.2.13. Bis(2,6-dichloro-3-nitrophenyl)(2,4,6-trichlorophenyl)methane (8)

A mixture of compound **7** (2 g, 4.6 mmol), 1,3,5-trichlorobenzene (8 g, 44 mmol) and $AlCl_3$ (1.4 g, 10.5 mmol) was heated (95 °C) in a hermetically closed glass reactor (24 h). The crude was poured on HCl/H_2O/ice and extracted with $CHCl_3$. The organic layer was dried on $MgSO_4$ and the solvent was eliminated by evaporation. The residue was chromatographed on silica gel eluating with hexane:$CHCl_3$ (1:1) to give **8** (1.46 g, 55%).

m. p.: 168 °C

^{1}H NMR (300 MHz, $CDCl_3$) δ: 7.72-7.62 (m, 2H, ph), 7.54-7.49 (m, 1H, ph), 7.42-7.37 (m, 2H, ph), 7.28-7.29 (m, 2H,ph), 6.935 (s, 1H, $C_{(\alpha)}$), 6.93 (s, 1H, $C_{(\alpha)}$), 6.91 (s, 1H, $C_{(\alpha)}$) ppm.

IR (KBr): 3079 (w), 2922 (w), 1580 (s), 1565 (s), 1533(f), 1432(d), 1351(m), 1251(d), 1176(d), 1141(d), 1098(d), 935(d),872-808(m), 753(m) cm^{-1}

1.2.6.2.14. Bis(3-amino-2,6-dichlorophenyl)(2,4,6-trichlorophenyl)methane (9)

A solution of **8** (436 mg, 0.74 mmol), anhydrous $SnCl_2$ (842 mg, 4.44 mmol) and HCl (35%) (0.8 ml, 8.88 mmol) in ethanol (25 ml) is kept at reflux (5 h) and then evaporated to dryness. The collected crude is dissolved in Et_2O and washed with $NaHCO_{3(sat)}$ and water. The organic layer is dried over Na_2SO4 and the solvent is removed by evaporation. Compound **9** is isolated by silica-gel column chromatography of the crude using $CHCl_3$ as eluent (0.364 g, 96%).

^{1}H NMR (300 MHz, $CDCl_3$) δ: 7.35-7.33 (m, 1H, ph), 7.23-7.20 (m, 1H, ph), 7.15-7.13 (m, 1H, ph), 7.00-6.95 (m, 1H, ph), 6.72-6.66 (m, 3H, ph+CH), 4.07-4.04 (m, 4H, NH) ppm.

IR (KBr): 3475 (w), 3385 (w), 3075 (w) 2974-2870 (w) 1610 (s), 1576 (s), 1544 (s), 1464 (s), 1451 (s), 1397 (w), 1375 (m), 1312 (w), 1267 (w), 1252 (w), 1219 (w), 1205 (w), 1150 (w), 1108 (w), 1050 (w), 860 (m), 804 (m), 744 (w), 642 (w) cm^{-1}.

1.2.6.2.15. Bis(2,6-dichlorophenyl)(2,4,6-trichlorophenyl)methane (4H)

To a solution of 9 (366 mg, 0.71 mmol) in DMF (4 ml) is added isoamyl nitrite (0.4 ml, 2.85 mmol) at rt. and then is heated to 60 °C and kept with stirring 1.5 h. HCl (20%) is then poured into the reaction to eliminate the nitrite in excess and the resulting phases are separated. The aqueous layer is extracted with Et_2O and the combined organic layer is washed with HCl (20%) and water, dried over Na_2SO_4 and evaporated to dryness. The crude is filtered through silica eluating with hexane to isolate bis(2,6-dichlorophenyl)(2,4,6-trichlorophenyl)methane (**4H**) (0.192 g, 56%).

m. p.: 195-6 °C

^{1}H NMR (300 MHz, $CDCl_3$) δ: 7.36-7.31 (m, 3H, ph), 7.23-7.13 (m, 5H, ph), 6.80 (s, 1H, CH) ppm.

IR (KBr): 3074 (w), 2921 (w), 1923 (w), 1851 (w), 1780 (w), 1727 (w), 1655 (w), 1576 (s), 1560 (s), 1542 (s), 1437 (s), 1421 (s), 1375 (m), 1341 (w), 1248 (w), 1207 (w), 1194 (w), 1175 (w), 1141 (w), 1088 (w), 966 (w), 897 (m), 860 (m), 828 (s), 806 (s), 770 (s), 754 (s), 723 (w), 667 (w), 651(w) cm^{-1}.

1.2.6.2.16. Bis(2,6-dichlorophenyl)(2,4,6-trichlorophenyl)methyl radical (4)

To a solution of **4H** (350 mg, 0.71 mmol) in anhydrous Et_2O/DMSO (10:3, 26 ml) is added NaOH powder (450 mg, 11.25 mmol). The mixture was kept (7 days) at rt. under Ar atmosphere with mechanical agitation. The reaction was then filtered with vacuum and a solution of I_2 (1.8 g, 7 mmol) in anhydrous Et_2O (25 ml) was poured into the filtrated. After magnetic stirring (2 h) at rt., the reaction was treated with aqueous Na_2SO_3 (10%) to reduce the iodine in excess. The phases are separated, the aqueous layer is extracted with Et_2O and the combined organic layers were washed with abundant water. By drying the organic layer over Na_2SO_4 and evaporating the solvent, bis(2,6-dichlorophenyl)(2,4,6-trichlorophenyl)methyl radical (**4**) was isolated (0.203 g, 59%).

IR (KBr): 2922 (w), 2851 (w), 1927 (w), 1850 (w), 1779 (w), 1733 (w), 1663 (w), 1545 (m), 1523 (m), 1423 (s), 1369 (m), 1286 (w), 1192 (m), 1184 (m), 1137 (w), 1080 (w), 923 (w), 863 (m), 816 (m), 775 (s), 723 (m) cm^{-1}.

UV ($CHCl_3$) λ_{max}/nm (ε/dm^3 mol^{-1} cm^{-1}): 221 (48500), 364 (27960), 527 (470).

1.2.6.2.17. [4-(N-carbazolyl) -2,6-dichlorophenyl](2,6-dichlorophenyl)(2,4,6-trichlorophenyl)methyl radical (10)

A mixture of *N*H-carbazole (68 mg, 0.41 mmol), **4** (200 mg, 0.41), anhydrous Cs_2CO_3 (200 mg; 0.61 mmol) and DMF (12 ml) was stirred at reflux (3 h) in an inert atmosphere and in the dark. The resulting mixture was poured into an excess of diluted aqueous HCl acid and the precipitate was filtered off. The solid was chromatographed in silica gel with hexane/$CHCl_3$ (9:1) to give **10H** (53 mg,

20%, MS (EI): *m/z* = 649.3 (M^+-1)). The subsequent preparation of the corresponding radical **10** was performed as described in 1.2.6.2.9.

Starting materials: **10H** (35 mg, 0.06 mmol), HTBA (0.15 ml, 0.1 mmol), DDQ (14 mg, 0.06 mmol)

Eluent: hexane/$CHCl_3$ (9:1)

η = 60%

MS (EI): *m/z* = 650.0 (M^++1)

IR (KBr): 3065 (w), 2919 (s), 2850 (m), 1597 (w), 1572 (m), 1553 (m), 1524 (m), 1493 (w), 1478 (w), 1452 (s), 1423 (m), 1370 (w), 1333 (w), 1314 (w), 1232 (m), 1181 (w), 1137 (w), 1081 (w), 923 (w), 860 (m), 820 (m), 793 (m), 776 (m), 747 (s), 722 (m), 683 (w) cm^{-1}.

1.2.6.2.18. General procedure for the acylation of radicals of the *N*-carbazolylTTM family.

A mixture containing the suitable radical precursor, powdered $AlCl_3$, and CS_2 was stirred at reflux under P_2O_5 atmosphere. The corresponding acylchloride was added and evolution of gas was observed. After 2-3 h of reaction, the solvent was evaporated and the crude was treated with an ice/water/HCl mixture and extracted with chloroform. The organic layer was dried and evaporated to dryness and the resulting residue was purified by silica-gel column chromatography.

1.2.6.2.18.1. [4-(3,6-Diacetyl-*N*-carbazolyl)-2,6-dichlorophenyl]bis(2,4,6-trichlorophenyl)methyl radical (14).

Starting materials: **1** (200 mg; 0.29 mmol), $AlCl_3$ (100 mg; 0.75 mmol), acetyl chloride (0.8 ml; 1.12 mmol), CS_2 (8 ml).

Reaction time: 2 h.

Eluent: $CHCl_3$

η = 89%

m.p. (DSC): 359 °C (dec)

IR (KBr): 3061 (w), 1678 (s), 1624 (m), 1593 (s), 1575 (s), 1554 (s), 1523 (m), 1478 (m), 1359 (m), 1290 (m), 1257 (s), 1217 (m), 1182 (m), 1137 (m), 858 (m), 815 (s), 799 (m), 757 (m) cm^{-1}.

UV ($CHCl_3$) λ_{max}/nm (ε/dm^3 mol^{-1} cm^{-1}): 263 (51 700), 293 (18 800), 328 (20 400), 373 (28 700), 555 (1900)

MS (EI): *m/z* = 768.2 (M^+)

CI-HRMS calcd for $C_{35}H_{18}Cl_8NO_2$ 767.878666, found *m/z* 767.888208.

1.2.6.2.18.2. [2,6-Dichloro-4-(3,6-dioctanoyl-*N*-carbazolyl)phenyl]bis(2,4,6-trichlorophenyl)methyl radical (18).

Starting materials: **1** (300 mg; 0.44 mmol), $AlCl_3$ (117 mg; 0.88 mmol), octanoyl chloride (0.17 ml; 1 mmol), CS_2 (18 ml).

Reaction time: 2 h.

Eluent: $CHCl_3$

η = 89%

m. p.: (DSC) 188 °C

IR (KBr) 3060 (w), 2953 (m), 2925 (s), 2853 (m), 1676 (s), 1594 (m), 1574 (s), 1555(m), 1524 (m), 1479 (m), 1370 (m), 1334 (m), 1290 (m), 1232 (m), 1183 (m), 1137 (m), 924 (m), 858 (s), 814 (s), 798 (s), 724 (m) cm^{-1}

UV ($CHCl_3$) λ_{max}/nm (ε/dm^3 mol^{-1} cm^{-1}): 263 (66700), 290 (sh) (36900), 328 (22700), 373 (32400), 438 (sh) (4400), 567 (1900)

EI-HRMS calcd for $C_{47}H_{42}Cl_8NO_2$ 932.072377, found *m/z* = 932.070085.

1.2.6.2.18.3. Bis[2,6-dichloro-4-(3,6-dioctanoyl-*N*-carbazolyl)phenyl](2,4,6-trichlorophenyl)methyl Radical (19).

Starting materials: **2** (200 mg; 0.25 mmol), $AlCl_3$ (207 mg; 1.55 mmol), octanoyl chloride (0.26 ml; 1.55 mmol), CS_2 (18 ml).

Reaction time: 3 h.

Eluent: $CHCl_3$/hexane (7:3)

m.p. (DSC): 143 °C

IR (KBr): 3060 (w), 2954 (m), 2928 (s), 2850 (m), 1676 (s), 1624 (m), 1595 (m), 1574 (s), 1526 (m), 1482 (m), 1369 (m), 1338 (m), 1291 (m), 1237 (m), 1189 (m), 818 (m), 806 (m) cm^{-1}.

UV ($CHCl_3$) λ_{max}/nm (ε/dm^3 mol^{-1} cm^{-1}): 263 (105200), 292 (62800), 327 (38000), 375 (21500), 438 (sh) (9600), 581 (3500)

MS (MALDI-TOF)-HRMS calcd for $C_{75}H_{78}Cl_7N_2O_4$ 1315.3776, found *m/z* = 1315.3776.

1.2.6.2.18.4. Tris[2,6-dichloro-4-(3,6-dioctanoyl-*N*-carbazolyl)phenyl]methyl radical (20).

Starting materials: **3** (35 mg; 0.037 mmol), $AlCl_3$ (40 mg; 0.3 mmol), octanoyl chloride (0.05 ml; 0.3 mmol), and CS_2 (8 ml).

Reaction time: 2 h.

Eluent: $CHCl_3$

m.p. (DSC): 249 °C (dec)

IR (KBr): 3060 (w), 2953 (m), 292 (s), 2851 (m), 1678 (s), 1623 (m), 1593 (m), 1571 (s), 1522 (m), 1476 (m), 1357 (m), 1333 (m), 1287 (m), 1230 (m), 1184 (m), 802 (s) cm^{-1}

UV ($CHCl_3$) λ_{max}/nm (ε/dm^3 mol^{-1} cm^{-1}): 263 (142500), 293 (87000), 326 (51800), 378 (20100), 446 (14200), 593 (5450)

MS (MALDI-TOF)-HRMS calcd for $C_{103}H_{114}Cl_6N_3O_6$ 1698.6833, found *m/z* = 1698.6899

1.2.6.2.18.5. Tris[2,6-dichloro-4-(3,6-dioctadecanoyl-*N*-carbazolyl)phenyl]methyl radical (40).

Starting materials: **3** (120 mg; 0.13 mmol), $AlCl_3$ (139 mg; 1.04 mmol), stearyl chloride (315 mg; 1.04 mmol), and CS_2 (15 ml).

Reaction time: 2.5 h.

Eluent: $CHCl_3$/Et_2O (99:1)

m.p. (DSC): 104 °C

IR (KBr): 2922 (s), 2852 (s), 1680 (s), 1624 (m), 1595 (s), 1574 (s), 1525 (m), 1478 (s), 1467 (s), 1363 (m), 1334 (m), 1290 (m), 1248 (m), 1188 (m), 1120 (w), 805 (m) cm^{-1}.

UV ($CHCl_3$) λ_{max}/nm (ε/dm^3 mol^{-1} cm^{-1}): 263(127800), 291(79500), 326(45740), 377(22900), 446(15550), 593(6100)

MS (MALDI-TOF): *m/z*= 2544 (M^+)

Anal. Calcd for $C_{163}H_{234}Cl_6N_3O_6$: C, 77.0; H, 9.3; N, 1.7. Found: C 76.34, H 9.2; N, 1.6

1.2.6.2.18.6. Tris[2,6-dichloro-4-(3,6-didodecanoyl-*N*-carbazolyl)phenyl]methyl radical (41).

Starting materials: **3** (40 mg; 0.04 mmol), $AlCl_3$ (53 mg; 0.4 mmol), dodecyl chloride (0.1 ml; 0.4 mmol), and CS_2 (8 ml).

Reaction time: 2.5 h.

Eluent: $CHCl_3$/Et_2O (99:1)

m.p. (DSC): 171 °C

IR (KBr)/cm^{-1}: 2922 (s), 2852 (s), 1680 (s), 1624 (m), 1595 (s), 1574 (s), 1525 (m), 1478 (s), 1467 (s), 1363 (m), 1334 (m), 1290 (m), 1248 (m), 1188 (m), 1120 (w), 805 (m) cm^{-1}.

UV ($CHCl_3$) λ_{max}/nm (ε/dm^3 mol^{-1} cm^{-1}): 263(127800), 291(79500), 326(45740), 377(22900), 446(15550), 593(6100)

MS (MALDI-TOF): *m/z* = 2039 (M^+)

1.2.6.2.19. 3,4,5-Trihydroxybenzoic acid (23)

BBr_3 in CH_2Cl_2 (1M) (18.8 ml, 18.8 mmol) was poured on 3,4,5-trimethoxybenzoic acid (1 g, 4.7 mmol) at -78 °C under N_2 atmosphere. The reaction was allowed to atemperate and it was stirred at rt. overnight and then poured into water. The aqueous layer was extracted with AcOEt. The organic layer was dried over Na_2SO_4 and the solvent removed by evaporation. The resulting solid was identified as 23 (802 mg, quantitative) and was used in the next step without further purification.

^{1}H NMR (300 MHz, acetone-d_6) δ: 8.18 (s, 2H, $OH_{(m)}$), 7.98 (s, 1H, $OH_{(p)}$), 7.15 (s, 2H, $H_{(2,6)}$) ppm.

1.2.6.2.20. Methyl 3,4,5-trihydroxybenzoate (24)

A solution of 3,4,5-trishydroxybenzoic acid (802 mg, 4.7 mmol) and *p*-TsOH (80 mg, 0.46 mmol) in MeOH (15 ml) was stirred at reflux temperature overnight. The solvent is evaporated to dryness and the resulting crude was filtered on silica using AcOEt/hexane (9:1) as eluent to obtain compound **24** (0.870 g, quantitative).

^{1}H NMR (300 MHz, acetone-d_6) δ: 8.10 (s, 2H, $OH_{(m)}$), 8.02 (s, 1H, $OH_{(p)}$), 7.11 (s, 2H, $H_{(2,6)}$), 3.79 (s, 3H, CH_3) ppm.

1.2.6.2.21. Methyl 3,4,5-tridecyloxybenzoate (25)

A solution of **24** (540 mg, 2.9 mmol), decylbromide (2.26 ml, 10.3 mmol) and anhydrous K_2CO_3 (1.6 g, 11.7 mmol) in anhydrous DMF (12 ml) was stirred under N_2 atmosphere at 50 °C (48 h). The solution was poured over water and the aqueous layer was extracted with AcOEt. The separated organic layer was washed with abundant water to eliminate the DMF and then dried over Na_2SO_4 and evaporated to dryness. The crude was chromatographed on silica-gel column eluating with hexane/AcOEt (95:5) to isolate **25** (1.45 g, 84%).

^{1}H NMR (300 MHz, $CDCl_3$) δ: 7.25 (s, 2H, $H_{(2,6)}$), 4.01 (t, *J* = 6.6 Hz, 6H, OCH_2 x 3), 3.89 (s, 3H, $COOCH_3$), 1.85-1.69 (m, 6H, CH_2 x 3), 1.50-1.26 (m, 42H, CH_2 x 21), 0.88 (t, *J* = 6.6 Hz, 9H, CH_3 x 3) ppm.

1.2.6.2.22. 3,4,5-Tridecyloxybenzoic acid (26)

To a suspension of NaH (1.26 g, 31.4 mmol) in anhydrous DMF (20 ml) at 0 °C EtSH (2.35 ml, 31.4 mmol) was added under N_2 atmosphere. The reaction was kept with stirring at 0 °C (30 min). A solution of compound **25** (1.53 g, 2.53 mmol) in anhydrous THF (10 ml) was then added and the reaction temperature was raised to 150 °C. The reaction was kept overnight and poured over water. The aqueous layer was neutralized with HCl (5%) and extracted with AcOEt. The organic layer was dried over Na_2SO_4, evaporated to dryness and the residue was chromatographied on silica gel eluating with hexane/AcOEt mixture increasing the polarity from 9:1 to 7:3 to give **26**.

^{1}H NMR (300 MHz, $CDCl_3$) δ: 7.31 (s, 2H, $H_{(2,6)}$), 4.07-4.00 (m,6H, OCH_2 x 3), 1.88-1.70 (m, 6H, CH_2 x 3), 1.53-1.26 (m, 42H, CH_2 x 21), 0.88 (t, *J* = 6.6 Hz, 9H, CH_3 x 3) ppm.

1.2.6.2.23. 3,4,5-Tridecyloxybenzoyl chloride (22).

3,4,5-Tridecyloxybenzoic acid (**26**) (500 mg, 0.85 mmol) was treated with $SOCl_2$ (1 ml) at reflux (2 h). The solvent is removed by vacuum distillation, to give **22.**

IR (KBr): 3399 (m), 3090 (m), 3019 (m), 2962 (m), 2948 (m), 2839 (m), 1762 (w), 1687 (s), 1603 (s), 1467 (s), 1445 (m), 1416 (s), 1325 (s), 1270 (m), 1232 (s), 1183 (m), 1129 (s), 1002 (m), 941 (w), 859 (w), 793 (w), 765 (w), 741 (w) cm^{-1}.

1.2.6.2.24. {2,6-Dichloro-4-[3-(3,4,5-tridecyloxybenzoyl)-*N*-carbazolyl]phenyl}bis(2,4,6-trichlorophenyl)methyl radical (27).

The synthesis of radical **27** was performed following the general procedure for the acylation of radicals of the *N*-carbazolylTTM family described above in 1.2.6.2.18.

Starting materials: **1** (30 mg; 0.04 mmol), $AlCl_3$ (6 mg; 0.05 mmol), **22** (32 mg; 0.05 mmol), CS_2 (8 ml).

Reaction time: 2 h.

Eluent: $CHCl_3$

η = 40%

IR (KBr): 2923 (s), 2853 (s), 1730 (m), 1652 (w), 1597 (w), 1575 (w), 1556 (w), 1525 (w), 1489 (w), 1462 (m), 1434 (w), 1377 (w), 1334 (w), 1287 (w), 1229 (w), 1211 (w), 1122 (w), 1105 (w), 1073 (w), 923 (w), 858 (w), 815 (w), 797 (w), 743 (w), 724 (w) cm^{-1}.

UV (cyclohexane) λ_{max}/nm (ε/dm^3 mol^{-1} cm^{-1}): 588 (1740), 575 (1970), 446 (sh) (2580), 373 (15800), 321 (16270), 289 (22840), 268 (24080)

MS (MALDI-TOF): *m/z* = 1256.6 (M^+)

1.2.6.2.25. bis{2,6-Dichloro-4-[3,6-bis(3,4,5-tridecyloxybenzoyl)-*N*-carbazolyl]phenyl} (2,4,6-trichlorophenyl)methyl radical (28).

The synthesis of radical **28** was performed following the general procedure for the acylation of radicals of the *N*-carbazolylTTM family described above in 1.2.6.2.18.

Starting materials: **1** (100 mg; 0.15 mmol), $AlCl_3$ (44 mg; 0.33 mmol), **22** (200 mg; 0.33 mmol), CS_2 (12 ml).

Reaction time: 2 h.

Eluent: hexane/Et_2O (94:6)

η = 45%

IR (KBr): 2924 (s), 2853 (s), 1734 (m), 1652 (w), 1597 (w), 1575 (w), 1558 (w), 1525 (w), 1489 (w), 1462 (m), 1429 (w), 1372 (w), 1335 (w), 1287 (w), 1230 (w), 1211 (w), 1182 (w), 1115 (w) 923 (w), 858 (w), 812 (w), 798 (w), 745 (w), 724 (w) cm^{-1}.

UV (cyclohexane) λ_{max}/nm (ε/dm^3 mol^{-1} cm^{-1}): 588 (2650), 543 (4360), 446 (4080), 373 (22470), 321 (25000), 289 (41660), 268 (42300)

MS (MALDI-TOF): *m/z* = 1709.7 (M^+-$(CH_2)_6CH_3$ –Cl), 1639.6 (M^+-$O(CH_2)_{10}H_{21}$ -Cl)

1.2.6.2.26. General procedure for the Clemmensen reduction of acylated *N*-carbazolylTTM radicals.

A Hg(Zn) amalgam was prepared by stirring a mixture of Zn pellets, $HgCl_2$ and HCl in H_2O (10-15 min.). The mixture was then further acidified by pouring more HCl and the suitable acylated radical together with toluene were added. The biphasic solvent was kept at reflux 2 days and then the phases were separated. The aqueous layer was extracted with Et_2O and the combined organic layers were dried over Na_2SO_4. The solvent was evaporated to dryness and the crude was chromatographed on silica-gel.

1.2.6.2.26.1. [2,6-dichloro-4-(3,6-diethyl-*N*-carbazolyl)phenyl]bis(2,4,6-trichlorophenyl)methane (15H)

Starting materials: Zn (3 g), $HgCl_2$ (0.250 g; 0.92 mmol), **14** (100 mg; 0.13 mmol), H_2O (5 ml), HCl (0.3 ml + 4 ml), toluene (9 ml).

Eluent: hexane

η = 17%

m.p. (DSC): 281°C

^{1}H NMR (300 MHz, $CDCl_3$) δ: 7.92 (s, 2H, cz); 7.60 (d, *J* = 2.1 Hz, 1H); 7.46 (d, *J* = 2.1 Hz, 1H, ph); 7.42 (d, *J* = 2.1 Hz, 1H, cz); 7.40 (d, *J* = 2.1 Hz, 1H, ph); 7.37 (d, *J* = 8.4 Hz, 2H, 1-H); 7.30-7.25 (m, 4H, cz + ph); 6.84 (s, 1H, CH); 2.84 (q, *J* = 7.5 Hz, 4H, CH_2 x 2); 1.34 (t, *J* = 7.5 Hz, 6H, CH_3 x 2);

IR (KBr): 3072 (w), 2961 (m), 2927 (m), 2856 (w), 1726 (w), 1594 (s), 1577 (s), 1481 (s), 1436 (w), 1372 (m), 1329 (w), 1302 (w), 1233 (m), 1191 (w), 1174 (w), 1140 (w), 1075 (w), 1057 (w), 922 (w), 900 (m), 857 (s), 835 (m), 806 (s) cm^{-1}

UV (cyclohexane) λ_{max} / nm (ε / dm^3 mol^{-1} cm^{-1}): 235 (53 600), 297 (20 700), 328 (17 300), 344 (7900)

CI-HRMS calcd for $C_{35}H_{23}Cl_8N$ = 740.927966, found *m/z* = 740.973128

1.2.6.2.26.2. [2,6-dichloro-4-(3,6-dioctyl-*N*-carbazolyl)phenyl]bis(2,4,6-trichlorophenyl)methane (21H)

Starting materials: Zn (10 g), $HgCl_2$ (0.820 g; 3.03 mmol), **18** (0.630 mg; 0.67 mmol), H_2O (17 ml), HCl (1 ml + 12 ml), toluene (25 ml).

Eluent: hexane/$CHCl_3$ (7:3)

η = 46%

^{1}H NMR (300 MHz, $CDCl_3$) δ: 7.89 (d, *J* = 1.2 Hz, 2H, cz), 7.60 (d, *J* = 2.4 Hz, 1H, ph), 7.47 (d, *J* = 2.4 Hz, 1H, ph), 7.42 (d, *J* = 2.4 Hz, 1H, ph), 7.40 (d, *J* = 2.4 Hz, 1H, ph), 7.36 (d, *J* = 8.4 Hz, 2H, cz), 7.30 (d, *J* = 2.4 Hz, 1H, ph), 7.27 (d, *J* = 2.4 Hz, 1H, ph), 7.24 (dd, *J* = 8.4 Hz, *J* = 1.5 Hz, 2H, cz), 6.84 (s, 1H, CH), 2.79 (t, *J* = 7.8 Hz, 4H, $CH_{2(\alpha)}$ x 2), 1.75-1.68 (m, 4H, $CH_{2(\beta)}$ x 2), 1.40-1.25 (m, 20H, CH_2 x 10), 0.88 (t, I = 6.6 Hz, 6H, CH_3 x 2) ppm.

IR (KBr): 3072 (m), 2958 (s), 2927 (s), 2854 (m), 1726 (w), 1594 (s), 1577 (s), 1481 (s), 1436 (w), 1372 (m), 1329 (w), 1302 (w), 1233 (m), 1191 (w), 1174 (w), 1140 (w), 1075 (w), 1057 (w), 922 (w), 900 (m), 857 (s), 835 (m), 806 (s) cm^{-1}

1.2.6.2.27. (2,6-dichloro-4-(3,6-diethyl-*N*-carbazolyl)phenyl)bis(2,4,6-trichlorophenyl)methyl radical (15)

The general procedure for the preparation of radical **15** from **15H** was followed as described in section 1.2.6.2.9.

Starting materials: **15H** (0.115 g, 0.16 mmol), THF (7 ml)

Eluent: hexane

η = 52%

m. p. (DSC): 300 °C (dec)

IR (KBr): 2961 (m), 2927 (w), 1575 (s), 1555 (s), 1523 (s), 1479 (s), 1467 (s), 1372 (m), 1350 (m), 1329 (m), 1303 (w), 1232 (m), 1184 (m), 1136 (m), 1082 (w), 1059 (w), 925 (w), 857 (m), 811 (s), 797 (s), 761 (w) cm^{-1}.

UV ($CHCl_3$) λ_{max}/nm (ε/dm^3 mol^{-1} cm^{-1}): 240 (62 500), 297 (20 100), 375 (27 000), 452 (sh) (2250), 622 (3800)

CI-HRMS calcd for $C_{35}H_{22}Cl_8N$ = 739.919740, found *m/z* = 739.907785.

1.2.6.2.28. [2,6-dichloro-4-(3,6-dioctyl-*N*-carbazolyl)phenyl]bis(2,4,6-trichlorophenyl)methyl radical (21)

The general procedure for the preparation of radical **21** from **21H** was followed as described in section 1.2.6.2.9.

Starting materials: **21H** (0.230 g, 0.25 mmol), THF (30 ml)

Eluent: hexane

η = 50%

m. p. (DSC): 136 °C

IR (KBr): 2954 (m), 2925 (s), 2853 (m), 1575 (s), 1557 (m), 1524 (m), 1478 (m), 1464 (m), 1370 (w), 1348 (w), 1325 (w), 1302 (w), 1230 (w), 1182 (w), 1137 (w), 1082 (w), 924 (w), 876 (w), 858 (m), 828 (w), 810 (m), 797 (m), 760 (w), 723 (w) cm^{-1}.

UV (cyclohexane) λ_{max}/nm (ε/dm^3 mol^{-1} cm^{-1}): 296 (21960), 374 (35300), 588 (sh)(3220), 636 (8040).

1.2.6.2.29. General procedure for the alkylation of *N*H-carbazole with bromoalkyl chains with terminal carboxylic esters.

To a solution of NH-carbazole in DMF under N_2 atmosphere at rt. NaH (60% in oil) was added and the reaction was heated (60 °C). After 1 h the suitable methyl bromoalkylester was added and the reaction was kept with stirring at 60 °C (1.5 h) and then treated with H_2O and neutralized with HCl 5%. The aqueous layer was extracted with AcOEt and the organic layer was dried over Na_2SO_4. The solvent was removed by evaporation and the resulting crude was cromatographed on silica-gel to isolate the corresponding *N*-alkylcarbazole.

1.2.6.2.29.1. Methyl 3-(*N*-carbazolyl)propionate (32)

Starting materials: *N*H-carbazole (1 g, 6 mmol), NaH (0.360 g, 9 mmol), methyl 3-bromopropionate (1.3 ml, 12 mmol), DMF (15 ml)

Eluent: hexane/$CHCl_3$ (2:3)

η = 73%

^{1}H NMR (400 MHz, acetone-d_6) δ: 8.13 (d, *J* = 6.4Hz, 2H, $H_{4,5}$), 7.61 (d, *J* = 6.4 Hz, 2H, $H_{1,8}$), 7.46 (t, *J* = 6.4 Hz, 2H, $H_{2,7}$), 7.21 (t, *J* = 6.4 Hz, 2H, $H_{3,6}$), 4.73 (t, *J* = 5.6 Hz, 2H, $CH_{2(\alpha)}$), 3.55 (s, 3H, CH_3), 2.86 (t, *J* = 5.6 Hz, $CH_{2(\beta)}$) ppm.

MS (CI): *m/z* = 254.5 (M^++1)

1.2.6.2.29.2. Methyl 8-(*N*-carbazolyl)octanoate (33)

Starting materials: *N*H-carbazole (1 g, 6 mmol), NaH (0.360 g, 9 mmol), methyl 8-bromopropionate (2.9 g, 12 mmol), DMF (15 ml)

Eluent: hexane/CH_2Cl_2 (3:7)

η = 98%

^{1}H NMR (300 MHz, $CDCl_3$) δ: 8.09 (d, *J* = 7.2 Hz, 2H, $H_{4,5}$), 7.45 (t, *J* = 8.1 Hz, 2H, $H_{2,7}$), 7.39 (d, *J* = 8.1 Hz, 2H, $H_{1,8}$), 7.22 (t, *J* = 8.1 Hz, 2H, $H_{3,6}$), 4.29 (t, *J* = 7.2 Hz, 2H, $CH_{2(\alpha)}$), 3.65 (s, 3H, CH_3), 2.27 (t, J = 7.2 Hz, 2H, $CH_{2(\beta)}$), 1.92-1.82 (m, 2H, CH_2), 1.63-1.54 (m, 2H, CH_2), 1.43-1.26 (m, 6H, CH_2 x 3) ppm.

1.2.6.2.30. General procedure for the saponification of methyl esters 32 and 33

To a solution of the suitable methyl ester in MeOH and $NaOH_{(aq)}$ was added and the reaction was refluxed overnight. The reaction was poured over H_2O/ice and then neutralized with HCl (5%). The aqueous layer was extracted with AcOEt and the organic layer was dried over Na_2SO_4 and evaporated to dryness. The crude was chromatographed on silica-gel eluating with $CHCl_3$/acetone to give the corresponding terminal acid.

1.2.6.2.30.1. 3-(*N*-carbazolyl)propionic acid (34)

Starting materials: **33** (0.880 g, 3.5 mmol), NaOH (0.736 g, 18.4 mmol), MeOH (15 ml), H_2O (30 ml)

Eluent: $CHCl_3$/acetone (1:1)

η = 89%

H NMR (400 MHz, acetone-d_6) δ: 8.13 (d, *J* = 6.4Hz, 2H, $H_{(4,5)}$), 7.64 (d, *J* = 6.4 Hz, 2H, $H_{(1,8)}$), 7.46 (t, *J* = 6.4 Hz, 2H, $H_{(2,7)}$), 7.21 (t, *J* = 6.4 Hz, 2H, $H_{(3,6)}$), 4.73 (t, *J* = 5.6 Hz, 2H, $CH_{2(\alpha)}$), 2.90 (t, *J* = 5.6 Hz, $CH_{2(\beta)}$) ppm.

IR (KBr): 3400-2200 (wide), 1709 (s), 1628 (w), 1593 (m), 1486 (m), 1463 (m), 1451 (m), 1397 (w), 1352 (w), 1316 (m), 1272 (m), 1230 (m), 1196 (w), 1153 (m), 1129 (w), 1069 (w), 1056 (w), 1019 (w), 992 (w), 926 (m), 881 (w), 820 (w), 750 (s), 727 (s) cm^{-1}.

1.2.6.2.30.2. 8-(*N*-carbazolyl)octanoic acid (35)

Starting materials: **33** (0.800 g, 2.5 mmol), NaOH (0.240 g, 6 mmol), MeOH (25 ml), H2O (10 ml)

Eluent: $CHCl_3$/acetone (1:1)

η = 95%

^{1}H NMR (400 MHz, $CDCl_3$) δ: 8.10 (dt, *J* = 8.0 Hz, *J*= 1.2 Hz, 2H, $H_{(4,5)}$), 7.47 (td, *J* = 6.8 Hz, *J* = 1.2 Hz, 2H $H_{(1,8)}$), 7.40 (d, *J* = 8.0 Hz, 2H, $H_{(2,7)}$), 7.23 (td, *J* = 8.0 Hz, *J* = 1.2, $H_{(3,6)}$), 4.30 (t, *J* = 7.2 Hz, 2H, $CH_{2(\alpha)}$), 2.32 (t, *J* = 7.2 Hz, $CH_{2(\beta)}$), 1.91-1.84 (m, 2H, CH_2), 1.64-1.55 (m, 2H, CH_2), 1.18-1.12 (m, 6H, CH_2 x 3) ppm.

1.2.6.2.31. Synthesis of the salt 1^+ $SbCl_6^-$

To a solution of **1** (380 mg, 0.59 mmol) in CCl_4 (20 ml) under N_2 atmosphere $SbCl_5$ (0.27 ml, 2.08 mmol) was added The reaction mixture was stirred at rt. (2.5 h) and the resulting precipitate was filtered off and washed with CCl_4, keeping the N_2 atmosphere (600 mg; quantitative yield).

IR (KBr): 1612 (m), 1554 (s), 1523 (m), 1378 (m), 1296 (m), 1178 (w), 1134 (s), 859 (w), 815 (w), 714 (w), 522 (m) cm^{-1}.

UV (CH_2Cl_2) λ_{max}/nm (ε/dm^3 mol^{-1} cm^{-1}): 936 (12570), 580 (sh, 4550), 516 (5000), 373 (10160).

Anal. Calcd for $C_{31}H_{14}Cl_{14}NSb$:CCl_4 1:1.6 C 31.04, H 1.12, N 1.11 Found C 31.01, H 1.03, N 1.10.

1.2.6.2.32. [(4-amino-2,6-dichlorophenyl)bis(2,6-dichlorophenyl)]methyl radical (31)

A solution of salt $\mathbf{1}^+$ $SbCl_6^-$ (1.6 g, 1.8 mmol) in anhydrous CH_2Cl_2 (40 ml) was treated with CH_2Cl_2 (30 ml) saturated with gaseous NH_3 and was stirred (30 min) under Ar atmosphere. The solvent was then evaporated, the crude was dissolved in anhydrous THF (100 ml) and anhydrous $SnCl_2$ (0.530 g, 2.8 mmol) was added to the solution. The reaction was kept under Ar atmosphere at rt. (30 min) and the solvent was removed by evaporation. The crude was dissolved in $CHCl_3$, washed with a saturated solution of $NaHCO_3$ and evaporated to dryness. The residue was chromatographed on silica-gel eluating with hexane/$CHCl_3$ (1:1) to give radical **31** (0.640 g, 67%).

IR (KBr): 3500 (w), 3400 (m), 3100 (w), 3070 (w), 1620 (s), 1590 (s), 1555 (m), 1525 (m), 1420 (m), 1385 (w), 1370 (m), 1305 (m), 1280 (m), 1240 (w), 1180 (m), 1135 (m), 1080 (w), 1060 (w), 920 (w), 850 (m), 835 (w), 820 (w), 800 (m), 785 (m), 715 (w) cm^{-1}

UV (cyclohexane) λ_{max}/nm (ε/dm^3 mol^{-1} cm^{-1}): 215 (38 100), 249 (6000 sh), 273 (12 300 sh), 360 (18 600 sh), 375 (27 700), 416 (6770 sh), 528 (2070), 566 (3450).

MS (EI): *m/z* = 534.4 (M^+)

1.2.6.2.33. General procedure for the amidation of radical 31

A solution of radical **31**, the suitable carboxylic acid, *N*,*N'*-dicyclohexylcarbodiimide and 4-dimethylaminopyridine in anhydrous CH_2Cl_2 is stirred at rt. under N_2 atmosphere 24 h. The solvent is evaporated and the crude is chromatographed through silica-gel to isolate the target radical.

1.2.6.2.33.1. 3-(*N*-carbazolyl)-*N*-{4-[bis(2,4,6-trichlorophenyl)methyl-1-yl]-3,5-dichlorophenyl} propionamide (36)

IR (KBr): 3333 (w), 3069 (w), 2926 (w), 1662 (s), 1576 (s), 1554 (s), 1526 (m), 1485 (m), 1461 (w), 1453 (m), 1381 (s), 1370 (s), 1325 (m), 1298 (w), 1230 (w), 1218 (w), 1181 (m), 1170 (w), 1156 (w), 1137 (w), 1083 (w), 1062 (w), 924 (w), 857 (s), 825 (w), 809 (m), 795 (m), 749 (s), 722 (s) cm^{-1}.

MS (CI): *m/z* = 771.7 (M^++ NH_3)

1.2.6.2.33.2. 8-(*N*-carbazolyl)-*N*-{4-[bis(2,4,6-trichlorophenyl)methyl-1-yl]-3,5-dichlorophenyl} octanoamide (37)

IR (KBr): 3300 (w), 2927 (w), 2853 (w), 1700 (w), 1683 (m), 1670 (m), 1570 (s), 1558 (s), 1522 (w), 1506 (w), 1483 (m), 1463 (m), 1452 (m), 1371 (m), 1324 (w), 1298 (w), 1234 (w), 1181 (w), 1152 (w), 1135 (w), 1082 (w), 923 (w), 857 (m), 825 (w), 809 (m), 795 (m), 794 (s), 722 (s) cm^{-1}.

MS (MALDI-TOF): *m/z* = 825.0 (M^+)

1.2.6.2.34. *N*-{4-[bis(2,4,6-trichlorophenyl)methyl-1-yl]-3,5-dichlorophenyl}acetamide (39)

Triethylamine (0.07 ml, 0.49 mmol) was added to a solution of radical **31** (150 mg, 0.28 mmol) in CH_2Cl_2 (3 ml) at 0 °C under N_2 atmosphere and the reaction was stirred at 0 °C (10 min). Acetyl chloride (0.03 ml, 0.42 mmol) was added and the reaction was allowed to atemperate and was poured over water. The resulting phases were separated, the aqueous layer was extracted with $CHCl_3$ and the combined organic layer was washed with water, dried over Na_2SO_4 and evaporated to dryness. The crude was chromatographed on a silica-gel column eluating with $CHCl_3$/Et_2O (99:1) to isolate radical **38** (160 g, quantitative).

IR (KBr): 3290 (w), 3136 (w), 3066 (w), 2958 (w), 1676 (s), 1572 (s), 1525 (m), 1498 (m), 1426 (w), 1410 (w), 1370(m), 1296 (m), 1246 (w), 1181 (w), 1134 (w), 1083 (w), 1013 (w), 913 (w), 860 (s), 809 (m), 796 (m), 757 (w), 723 (w), 694 (w) cm^{-1}.

MS (CI): *m/z* = 575 (M^+)

1.2.6.2.35. General procedure for the reduction of amides

$LiAlH_4$ is added in small portions to a solution of amide in anhydrous THF at 0 °C under Ar atmosphere producing gas evolution. The reaction is screened by TLC after every addition. When the reaction is completed, water is poured carefully into the reaction and the resulting layers are separated. The organic layer is dried over Na_2SO_4 and evaporated to dryness. The target compound is purified by column chromatography.

1.2.6.2.35.1. {{4-[3-(*N*-carbazolyl)propyl]amino}-2,6-dichlorophenyl}bis(2,4,6-trichlorophenyl) methyl radical (29)

Starting materials: **36** (78 mg, 0.1 mmol), $LiAlH_4$ (3 mg, 0.05 mmol), Et_2O (20 ml)

Eluent: hexane/$CHCl_3$ (3:7)

η = 54%

IR (KBr): 3391 (m), 3055 (w), 2924 (w), 2854 (w), 1591 (s), 1553 (w), 1521 (w), 1484 (m), 1463 (w), 1451 (m), 1402 (w), 1369 (w), 1324 (w), 1307 (w), 1239 (w), 1195 (w), 1180 (w), 1154 (w), 1135 (w), 1121 (w), 1080 (w), 1057 (w), 923 (w), 857 (m), 837 (w), 825 (w), 807 (m), 794 (m), 751 (s), 721 (m) cm^{-1}.

UV ($CHCl_3$) λ_{max}/nm (ε/dm^3 mol^{-1} cm^{-1}): 594 (5080), 430 (8470), 380 (23360), 346 (10410), 327 (sh)(5920), 294 (18460), 274 (27070).

MS (EI): *m/z* = 741 (M^+)

1.2.6.2.35.2. {{4-[8-(*N*-carbazolyl)octyl]amino}-2,6-dichlorophenyl}bis(2,4,6-trichlorophenyl) methyl radical (30)

Starting materials: **37** (0.153 g, 0.19 mmol), $LiAlH_4$ (0.007 g, 0.19 mmol), THF (30 ml)

Eluent: hexane/$CHCl_3$ (1:1)

η = 60%

IR (KBr): 3405 (w), 2928 (w), 2854 (w), 1591 (s), 1558 (w), 1524 (w), 1484 (m), 1464 (w), 1452 (m), 1369 (w), 1324 (w), 1239 (w), 1195 (w), 1181 (w), 1153 (w), 1135 (w), 1121 (w), 1080 (w), 1057 (w), 923 (w), 857 (m), 825 (w), 806 (m), 794 (m), 750 (s), 723 (m) cm^{-1}.

UV ($CHCl_3$) λ_{max}/nm (ε/dm^3 mol^{-1} cm^{-1}): 600 (6400), 430 (10710), 380 (27200), 348 (13350), 333 (sh)(7920), 296 (21650), 274 (33180).

MS (MALDI-TOF): *m/z* = 811 (M^+)

1.2.6.2.35.3. Bis(2,4,6-trichlorophenyl)(4-(*N*-ethyl)amino-2,6-dichlorophenyl) methyl radical (38)

Starting materials: **39** (0.134 g, 0.23 mmol), $LiAlH_4$ (0.0010 g, 0.24 mmol), THF (30 ml)

Eluent: $CHCl_3$/ hexane (9:1)

η = 33%

IR (KBr): 3419 (w), 3072 (w), 2956 (w), 2920 (w), 2850 (w), 1594 (s), 1554 (w), 1524 (w), 1477 (w), 1455 (w), 1369 (m), 1314 (m), 1243 (w), 1180 (w), 1136 (w), 1080 (w), 1053 (w), 970 (w), 923 (w), 858 (m), 806 (m), 793 (m), 720 (w) cm^{-1}.

UV ($CHCl_3$) λ_{max}/nm (ε/dm^3 mol^{-1} cm^{-1}): 597 (4515), 430 (7840)

MS (EI): *m/z* = 562 (M^++1)

References

[1] O. Armet, J. Veciana, C. Rovira, J. Riera, J. Castaner, E. Molins, J. Rius, C. Miravitlles, S. Olivella, J. Brichfeus, *J. Phys. Chem.* **1987**, *91*, 5608-5616.

[2] V. Gamero, D. Velasco, S. Latorre, F. López-Calahorra, E. Brillas, L. Juliá, *Tetrahedron Lett.* **2006**, *47*, 2305-2309.

[3] M. Martinez-Palau, E. Perea, F. Lopez-Calahorra, D. Velasco, *Lett. Org. Chem.* **2004**, *1*, 231-237.

[4] G. Mann, J. F. Hartwig, M. S. Driver, C. Fernandez-Rivas, *J. Am. Chem. Soc.* **1998**, *120*, 827-828.

[5] M. Watanabe, M. Nishiyama, T. Yamamoto, Y. Koie, *Tetrahedron Lett.* **2000**, *41*, 481-483.

[6] M. R. Puntí, *Preparació dels radicals lliures orgànics estables bis(3-amino-2,6-diclorofenil)(2,4,6-triclorofenil)metil i bis(2,6-diclorofenil)(2,4,6-triclorofenil)metil, integrants de nous materials orgànics amb propietats magnètiques.* **1998**, Experimental Master. Universitat de Barcelona.

[7] M. López, D. Velasco, F. López-Calahorra, L. Juliá, *Tetrahedron Lett.* **2008**, *49*, 5196-5199.

[8] D. Velasco, S. Castellanos, M. Lopez, F. Lopez-Calahorra, E. Brillas, L. Julia, *J. Org. Chem.* **2007**, *72*, 7523-7532.

[9] S. Castellanos, D. Velasco, F. Loì pez-Calahorra, E. Brillas, L. Julia, *J. Org. Chem.* **2008**, *73*, 3759-3767.

[10] P. Bauer, H. Wietasch, S. M. Lindner, M. Thelakkat, *Chem. Mater.* **2006**, *19*, 88-94.

[11] T. D. M. Bell, T. A. Smith, K. P. Ghiggino, M. G. Ranasinghe, M. J. Shephard, M. N. Paddon-Row, *Chem. Phys. Lett.* **1997**, *268*, 223-228.

[12] J.-L. Bredas, D. Beljonne, V. Coropceanu, J. Cornil, *Chem. Rev.* **2004**, *104*, 4971-5004.

[13] H. Imahori, K. Hagiwara, M. Aoki, T. Akiyama, S. Taniguchi, T. Okada, M. Shirakawa, Y. Sakata, *J. Am. Chem. Soc.* **1996**, *118*, 11771-11782.

[14] T. Konno, M. E. El-Khouly, Y. Nakamura, K. Kinoshita, Y. Araki, O. Ito, T. Yoshihara, S. Tobita, J. Nishimura, *J. Phys. Chem. C* **2008**, *112*, 1244-1249.

[15] Y. Oseki, M. Fujitsuka, D. W. Cho, A. Sugimoto, S. Tojo, T. Majima, *J. Phys. Chem. B* **2005**, *109*, 19257-19262.

[16] J. L. Segura, N. Martin, D. M. Guldi, *Chem. Soc. Rev.* **2005**, *34*, 31-47.

[17] L. Teruel, L. Viadel, J. Carilla, L. Fajari, E. Brillas, J. Sane, J. Rius, L. Julia, *J. Org. Chem.* **1996**, *61*, 6063-6066.

[18] R. F. Nystrom, W. G. Brown, *J. Am. Chem. Soc.* **1948**, *70*, 3738-3740.

[19] M. Ballester, D. Bethell, in *Adv. Phys. Org. Chem.*, Vol. Volume 25, Academic Press, **1989**, 267-445.

[20] I. Haiduc, H. Gilman, *J. Organomet. Chem.* **1968**, *12*, 394-396.

[21] S. Castellanos, F. López-Calahorra, E. Brillas, L. Juliá, D. Velasco, *Angew. Chem. Int. Ed.* **2009**, *48*, 6516-6519.

[22] C. Deibel, D. Janssen, P. Heremans, V. De Cupere, Y. Geerts, M. L. Benkhedir, G. J. Adriaenssens, *Org. Electron.* **2006**, *7*, 495-499.

[23] E. Grelet, H. Bock, *Europhys. Lett.* **2006**, *73*, 712-718.

[24] I. Hiroaki, H. Jun-ichi, J. B. Richard, M. Bijan, J. W. Benjamin, *J. Appl. Phys.* **2006**, *100*, 043716.

[25] C.-y. Liu, A. Fechtenkotter, M. D. Watson, K. Mullen, A. J. Bard, *Chem. Mater.* **2002**, *15*, 124-130.

[26] K. Marcel, L. Frederic, M. Klaus, W. Gerhard, *Appl. Phys. Lett.* **2006**, *89*, 252103.

[27] K. Tominaga, G. C. Walker, W. Jarzeba, P. F. Barbara, *J. Phys. Chem.* **1991**, *95*, 10475-10485.

1.3. Non-radical carbazole derivatives

1.3.1. Molecular glasses

In this section the synthesis and characterization of small molecules based on the *N*-phenylcarbazole unit is presented. The target products were *N*-phenylcarbazole derivatives bearing 4 and 7 methoxy groups and 1,3,5-tris(*N*-carbazolyl)benzene (TCB) derivatives bearing tricyanovinyl gropus. The aim for the first family of compounds was comparing the physical properties deriving from the amorphous state with the physical properties deriving from the liquid-crystalline state for molecules with the same aromatic core. The chosen cores were the central fragments of the discotic *N*-phenylcarbazole mesogens discussed in section 1.3.2. For the second kind of compounds it was sought the study of the variations in the properties of the well-known hole-transporting TCB by the attachment of an electron-withdrawing fragment the group was already familiar with.

1.3.1.1. Synthesis

Preparation of the carbazole fragments for the *N*-phenylcarbazole derivatives was performed through a two-steps synthesis consisting in a Suzuki coupling between the suitable nitrobenzene and a phenylboronic acid and the subsequent reductive Cadogan cyclation of the resulting biphenyl system, as shown in Scheme 1.21. All starting materials were commercially available, except for the 4-bromo-5-nitroveratrole (**42**), which was prepared by treating 3-bromoveratrole with $AcOH/HNO_3$. The nitration gave the target product in quantitative yields ought to the *o*-*p*-orienting effects of the methoxy group in position 2 and the bromide atom, as well as to the less steric hindrance of position 5 versus the other active position 3.

While the cyclation of the biphenyl bearing two methoxy groups in 3 and 3' led to a unique symmetrically substitued 2,7-dimethoxy-*N*H-carbazole (**43**), the Cadogan reaction of the 3',4,4',5-tetramethoxy-2-nitrobiphenyl (**44**) gave two isomers in a 1:1 ratio as a result of the rotational conformations of the biphenyl system, 2,3,5,6-tetramethoxy-*N*H-carbazole (**45**) and 1,2,5,6-tetramethoxy-*N*H-carbazole (**46**). The copper catalyzed Ullmann couplings between the corresponding commercially available bromobenzene and the proper synthesized *N*H-carbazole led to the two target products 2,7-dimethoxy-*N*-(3,5-dimethoxyphenyl)carbazole (**48**) and **49** (Scheme 1.22).

The preparation of 1,3,5-tris(*N*-carbazolyl)benzene (TCB) derivatives bearing tricyanovinyl groups, by a direct coupling of 3-tricyanovinyl-*N*H-carbazole with a 1,3,5-tribromobenzene was considered in advance an unviable synthetic path, since the strong electron-withdrawing character of the tricyanovinyl group might deactivate strongly the carbazole as a nucleophylic agent, both by

inductive and mesomeric effects. Hence, it was decided to prepare these compounds through the electrophilic attack of tetracyanoethylene to the aromatic system.

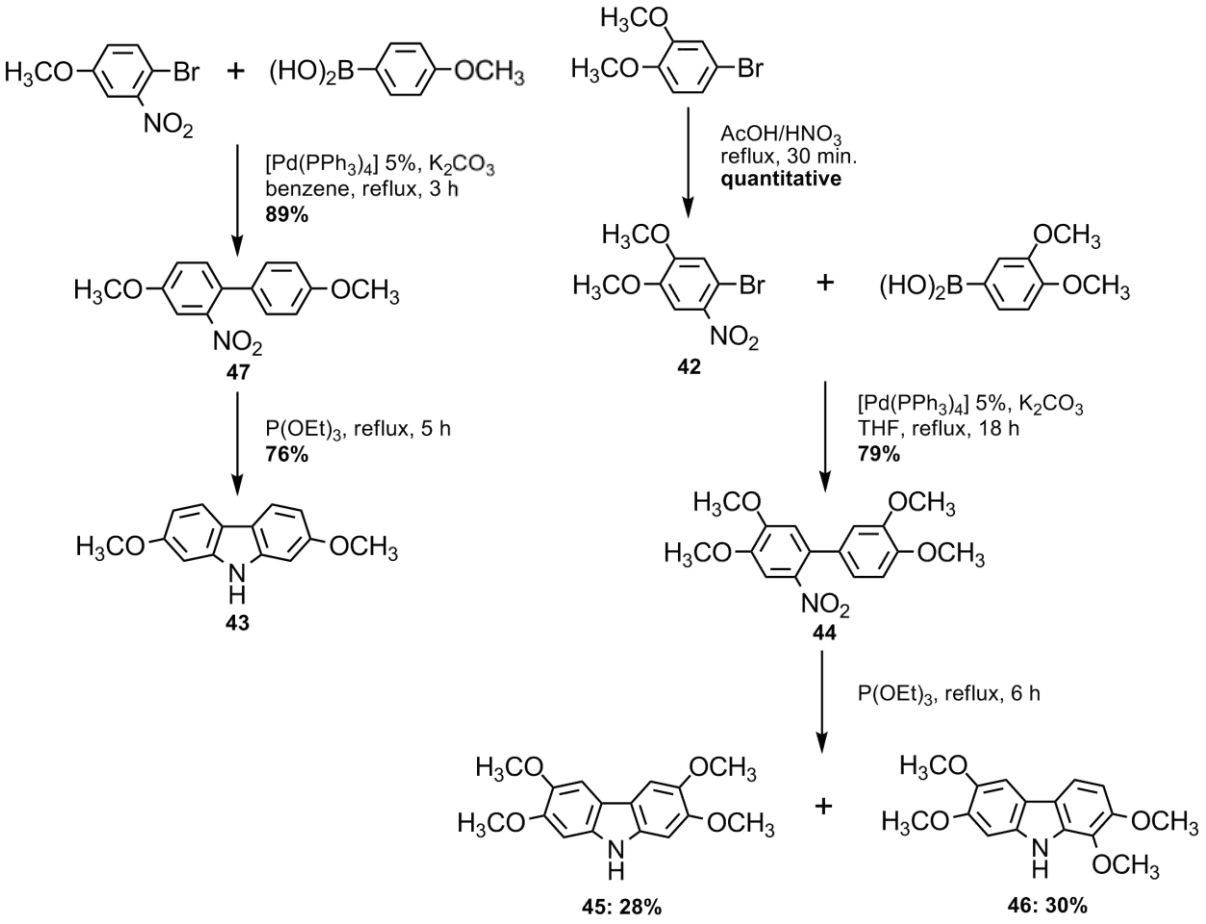

Scheme 1.21

This reaction was already known in our group for *N*H-carbazole and *N*-methylcarbazoles which underwent the electrophylic aromatic substitution (EAS) when they were treated directly with tetracyanoethylene in boiling DMF for 24h.[1] However, these reaction conditions did not led to any product in the case TCB, even after one week of reaction.

By the addition of $AlCl_3$, though, the sought reaction took place giving the three different products that resulted from the introduction of one, two or three tricyanovinyl groups, each one in the position 3 of a different fragment of carbazole (Scheme 1.23) thus giving 1,3-di(*N*-carbazolyl)-5-(3-cyanovinyl-*N*-carbazolyl)benzene(**50**), 1-(*N*-carbazolyl)-3,5-bis(3-cyanovinyl-*N*-carbazolyl)benzene (**51**) and 1,3,5-tris(3-cyanovinyl-*N*-carbazolyl)benzene (**52**), respectively. The monitoring of the reaction evolution by thin layer chromatography (TLC) revealed that short reaction times barely gave any product while lengthening of the reaction times provided moderate yields of each one with a higher proportion of **52**.

The proposed mechanism for this reaction, shown in Scheme 1.24, is analog to the Friedel-Crafts acylation mechanism. It starts with the coordination of the $AlCl_3$, a Lewis acid, with one of the cyano groups of the tretracyanoethylene molecule through the nitrogen atom thus increasing the electrophilic character of the tetracyanoethylene. Once the electrophyl attack takes place, one of the cyano groups acts as a leaving group. The reaction is completed by the loose of a proton and the regain of the aromaticity of the carbazole.

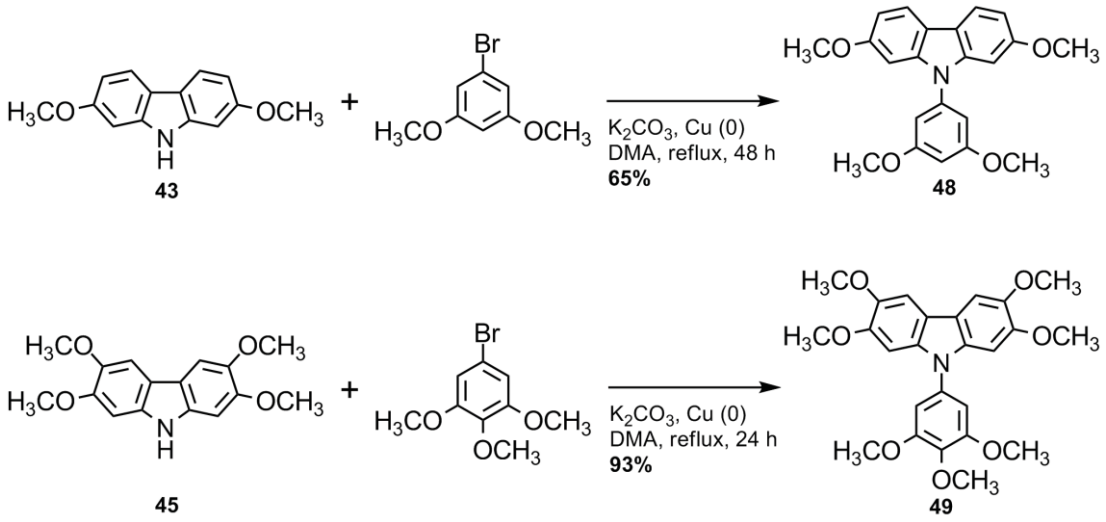

Scheme 1.22

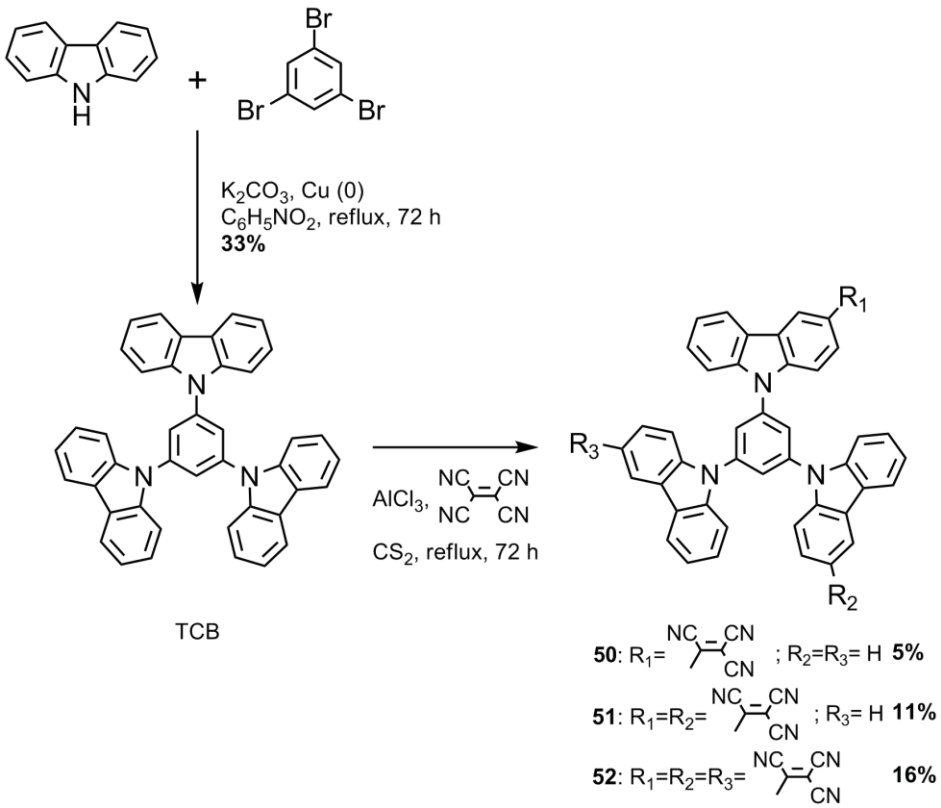

Scheme 1.23

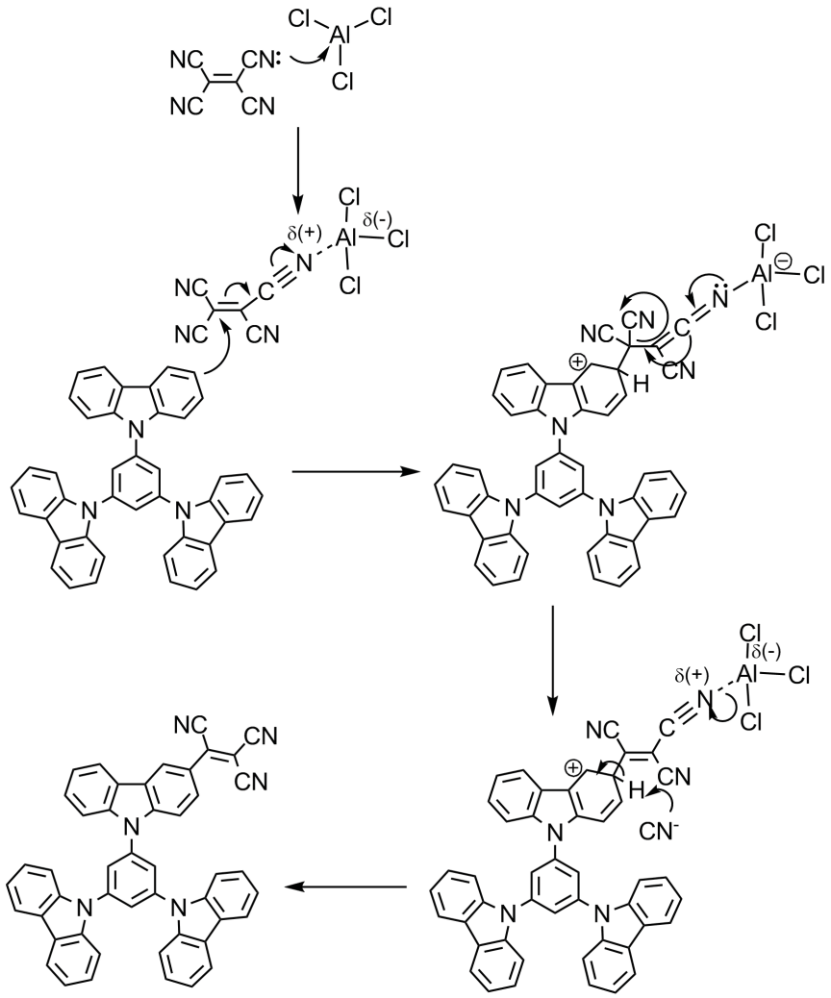

Scheme 1.24

1.3.1.2. Differential scanning calorimetry analyses

Despite the synthesized *N*-phenylcarbazoles are crystalline species, they have the capability of forming amorphous films both by applying a rapid cooling on their melted states or by spin coating or drop casting of their solutions.

It was observed by POM that **48** and **49** cooled down as vitreous transparent drops from the liquid state. The same phenomena is deduced from the DSC analyses (Figure 1.37), which present no exothermic peaks corresponding to the crystallization of the compounds when cooling from the liquid state, but an inflexion that indicates the glass transition temperature. The inverted inflexion was reproduced in the second heating curve, where no endothermic peak was detected, a feature that is in agreement with the lack of crystalline structure melting.

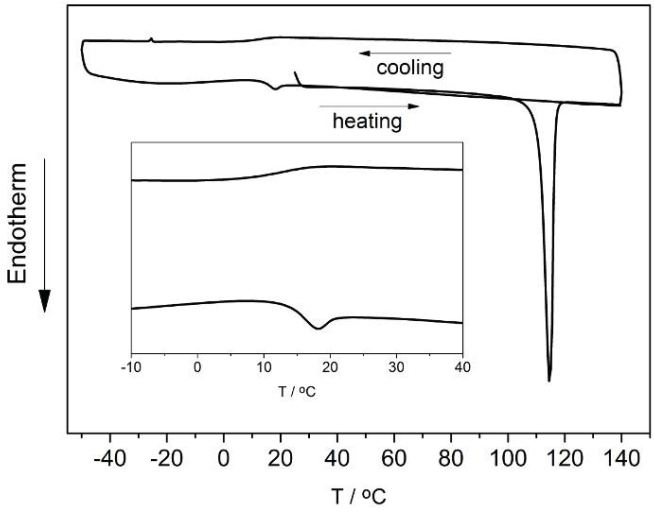

Figure 1.37. DSC of **48** (10 °C/min rate). Insert shows the zoomed area were the glass transition is detected.

Melting points and glass transition temperatures of the synthesized compounds are given in Table 1.17. It can be observed that increasing the number of methoxy groups attached to the *N*-phenylcarbazole core raises both the melting and the glass transition temperatures. The same trend is detected by the increase of tricyanovinyl groups in the TCB core in the m. p. of **50**, **51** and **52**. However, compound **52** undergoes decomposition during the melting process, as it was evidenced by thermogravimetry analyses (TGA). T_g could only be detected in the cyclic DSC experiments of compound **51**.

Table 1.17. Glass transition temperatures (T_g) and melting points (m. p.) of the prepared compounds.

	T_g / °C	m.p. / °C
48	16	114
49	60	168
50	-	190
51	167	212
52	-	239 (dec)

1.3.2. Liquid Crystals

As it was exposed in the introduction, there are not many examples of discotic liquid crystals derived from carbazole. Some of this kind of mesogens reported in the literature were prepared in our research group. From an structural point of view, two families can be distinguished: discotic mesogens based on the *N*-phenylcarbazole core[2, 3] and a dimeric system consisting in two polyalkoxyl carbazole units linked by an alkyl chain.[4] In this section it is presented the synthesis of the mentioned compounds and the study of the variation in their liquid-crystalline properties by: 1) the addition of a terminal carboxylic acid in the side chains of the *N*-phenylcarbazole derivatives, 2) the doping with an electron-acceptor molecule of the proper carbazole systems in different proportions, 3) the modification of the chain length of the linking chain in the dimeric systems.

The main goal of such modifications was the attainment of stable columnar arrangements of the carbazole derivatives, preferably at rt., showing the proper physical properties required for their potential application as semiconductors. The presence of terminal carboxylic acids in the side chains had proved to produce drastic changes in the mesophases of some compounds,[5-7] and, in addition, provide the mesogenic units with an attachment point for their introduction into larger structures, like dendrimers or polymers. The aim of doping *N*-phenylcarbazole mesogens with an electron-acceptor compound was to enhance their photoconductivity either by the stabilization of the columnar arrangement through stronger supramolecular interactions, such as charge transfer interactions, or by the generation of two independent conduction channels along columns of stacked donor and acceptor molecules.[8-15] Finally, the dimeric systems had previously shown mesomorphic characteristics but a deeper study of these compounds was needed.

1.3.2.1. Synthesis

N-phenylcarbazole derivatives bearing alkoxyl chains were obtained using the same strategy as for their methoxy counterparts presented in the previous section. The substituted carbazole moieties and the substituted bromobenzenes were prepared separately and then coupled by an Ullmann reaction catalyzed by copper powder.

2,7-dioctadecyloxycarbazole (**53**) was prepared from 2,7-dimethoxycarbazole (**43**), whose synthesis was already discussed in the previous section. Cleavage of the methoxy groups was achieved using pyridine hydrochloride. The alkylated compound was obtained by a Williamson alkylation of the resulting 2,7-dihydroxycarbazole (**54**) in moderate yields (Scheme 1.25).

Since the cleavage and alkylation of 2,3,6,7-tetramethoxycarbazole (**45**) proved to be an unsuccessful synthetic way to obtain 2,3,6,7-tetranonoxyl-*N*H-carbazole (**55**), the alternative synthetic route shown in Scheme 1.26 was used. First attempts to obtain the proper nitrobenzene consisted in cleaving the methoxy groups in the already known the 4-bromo-5-nitroveratrole (**42**) and then alkylating the resulting phenol. However the starting material degraded when it was treated with the cleaving agent, the BBr_3. Therefore, the inverse strategy was used (Scheme 1.26), that is, 2-bromo-4-hydroxyphenol (**56**) was prepared from the commercially available 4-bromoveratrole by cleaving the methoxy groups with boron tribromide and was then alkylated using Williamson alkylation conditions with 1-bromononane to give **57**. The treatment of compound **57** with an $AcOH/HNO_3$ mixture gave nitrocompound **58** in quantitative yields. Namely, the *o*-*p*-orienting effects of the alkoxyl chain at the position 3 and of the bromide plus the less steric hindrance made the position in *ortho* regarding the bromide and in *para* regarding the chain at position 3 the most active for an electrophilic substitution.

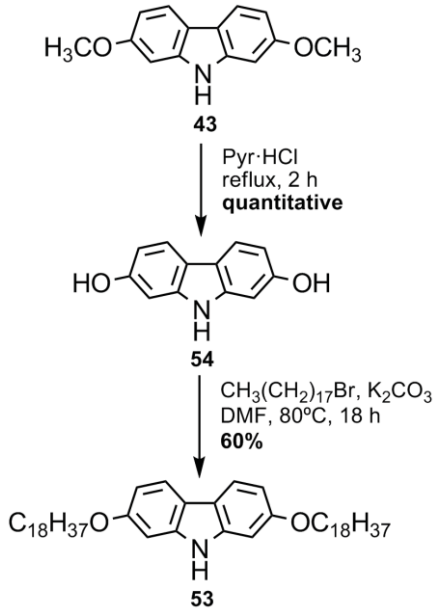

Scheme 1.25

By treating compound **57** with nBuLi, a metal-halogen exchange took place between both species so that the corresponding aromatic organolithium compound was formed. The addition of trimethylborane to the reaction produced a methyl phenylboronate that underwent hydrolysis in mild acidic conditions, thus obtaining phenylboronic acid **59**. Given that the isolation of the boronic acid by crystallization was not successful, the crude was used without further purification in the next step.

The Pd(0) Suzuki cross-coupling reaction between the mentioned compounds **58** and **59** led to biphenyl **60** in good yields. Diasteroisomers 2,3,6,7-tetranonoxyl-*N*H-carbazole (**55**) 1,2,6,7-tetranonoxyl-*N*H-carbazole (**61**) were then formed in the same yield by a Cadogan reductive cyclation of biphenyl **60** with triethylphosphite, $P(OEt)_3$.

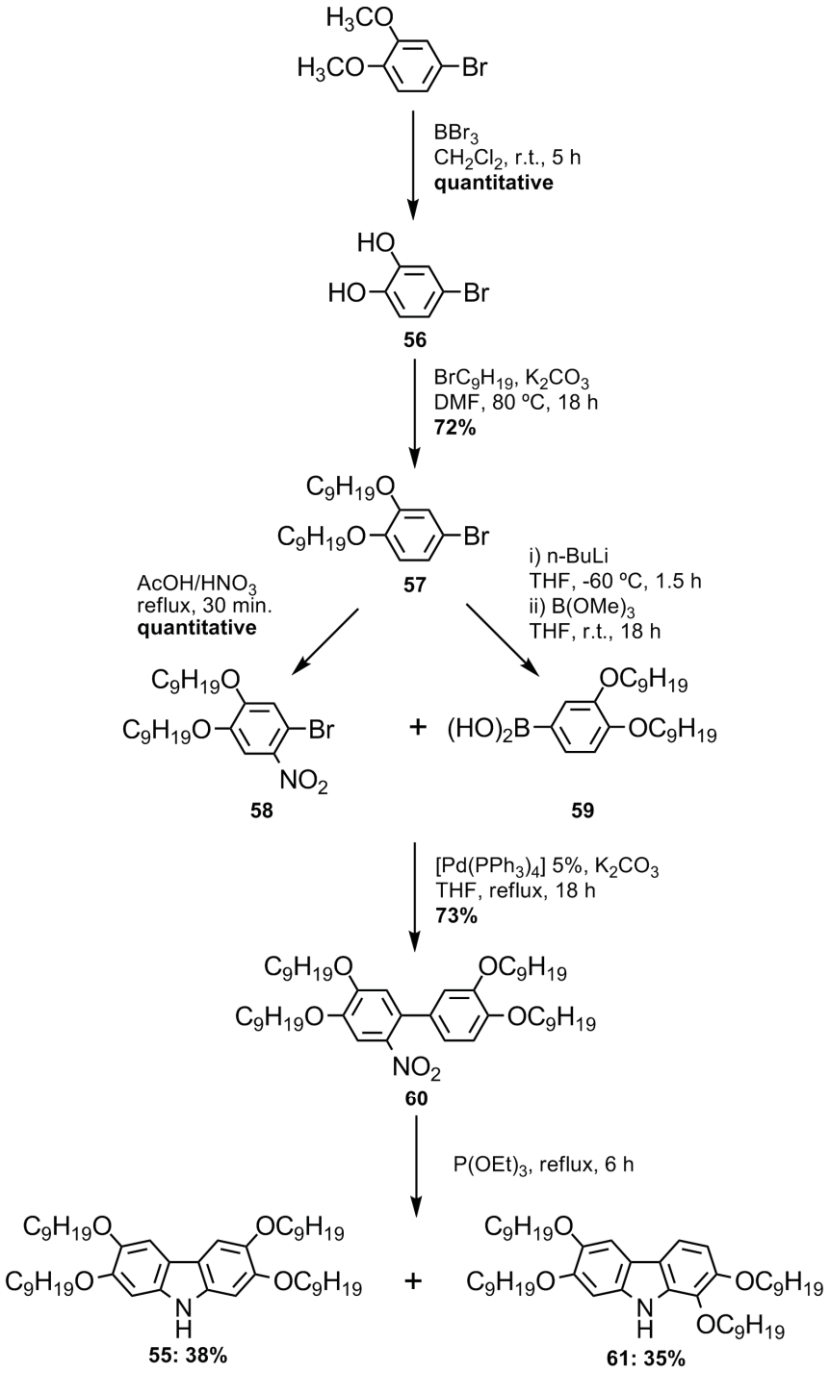

Scheme 1.26

Homoalkyl bromobenzenes **62** and **63** and **64** where prepared in good yields by a two-step synthesis consisting in the methoxy cleavage of the starting materials with boron tribromide followed by a Williamson alkylation with the suiTable bromoalkyl (Scheme 1.27).

Cleavage of a single methoxy group of 3,5-dimethoxybromobenzene to give the phenol **67** was achieved using sodium ethanethiolate as cleaving agent. The alkylation of **67** with 1-bromooctadecane gave the bromobenzene **68**, which was treated with sodium ethanethiolate for the cleavage of the remaining methoxy group leaving the long alkoxyde chain untouched. Mitsunobu reaction of previously prepared methyl 16-hydroxyhexadecanoate (**69**) with phenol **70** led to the heterosubstituted bromobenzene **71** (Scheme 1.28)

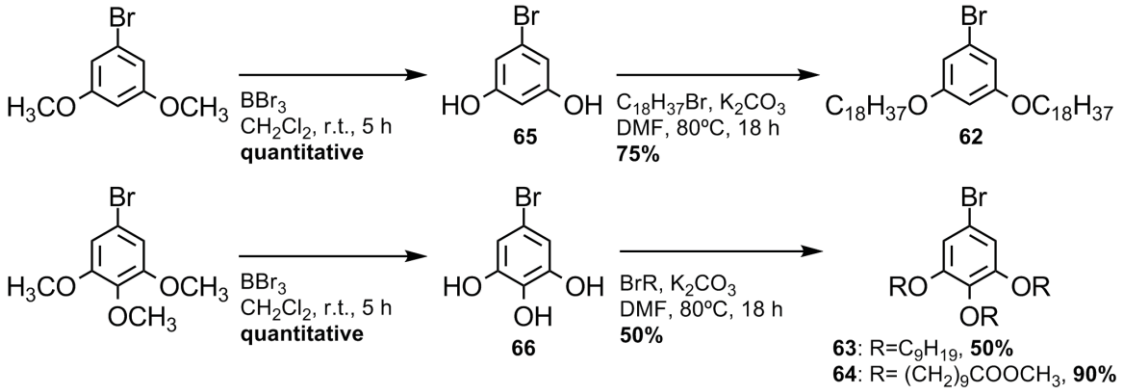

Scheme 1.27

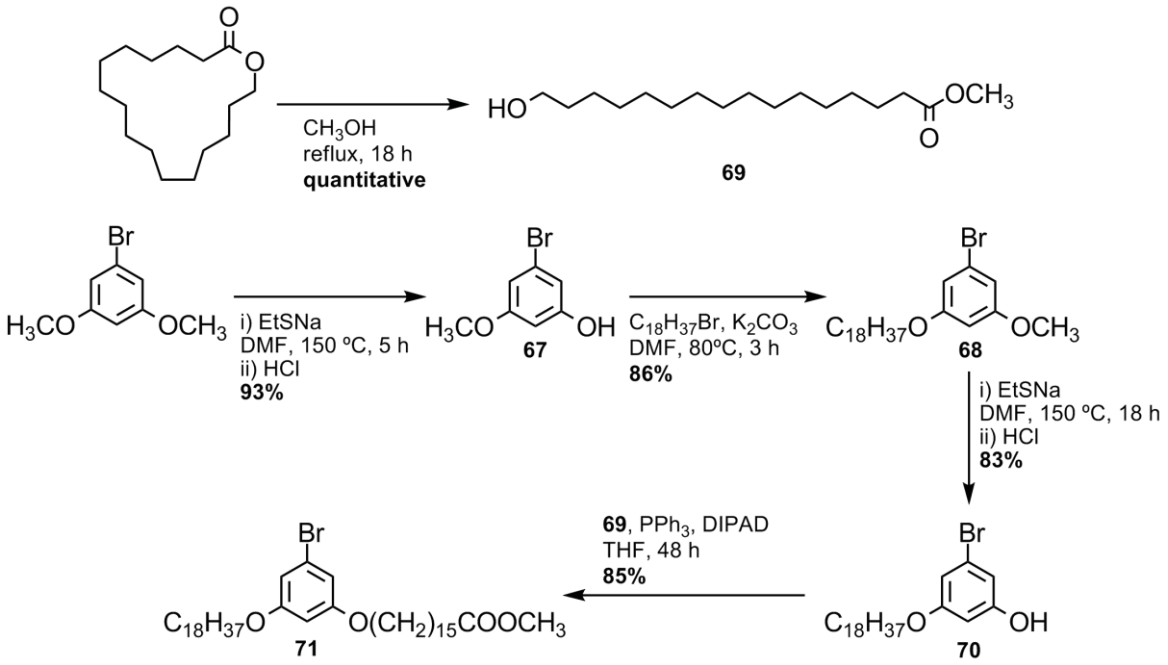

Scheme 1.28

The synthetic path for bromobenzene **72** is presented in Scheme 1.29. The protection of two adjacent hydroxyl groups with an acetal afforded the alkylation of 5-bromo-2,3-dihydroxyphenol (**66**) with two different alkylating agents. The remaining hydroxyl group in acetal **73** was alkylated with methyl 10-bromodecanoate in presence of K_2CO_3 to give **74**. The acetal opening took place under acidic conditions in which the terminal ester was hydrolyzed. Therefore, once the corresponding hydroxyphenol was obtained, esterification of the terminal acid had to be performed to obtain **75** and perform the following alkylation that led to the target compound **72**.

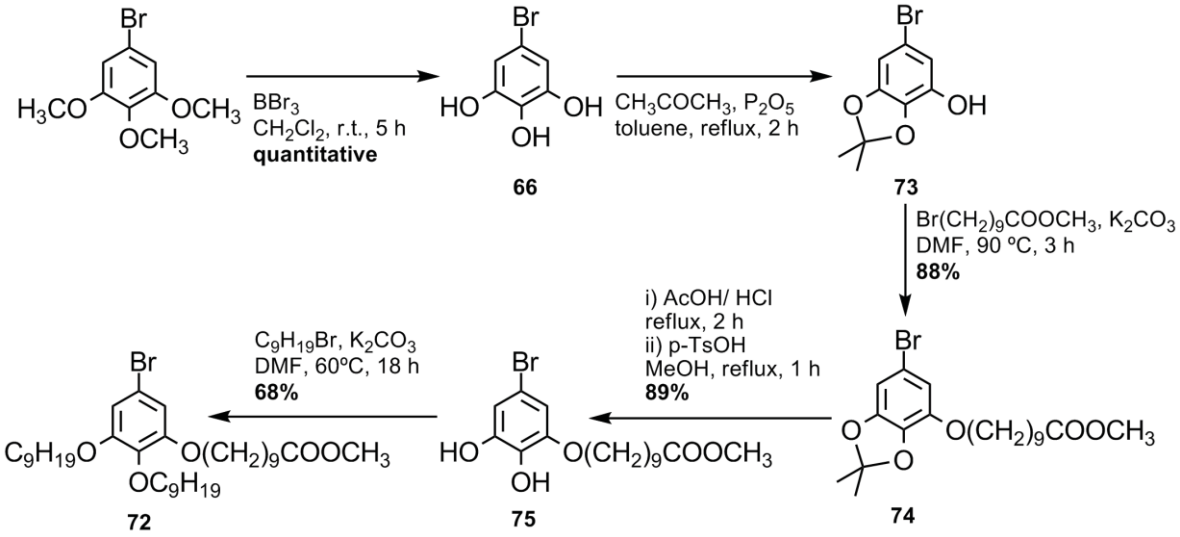

Scheme 1.29

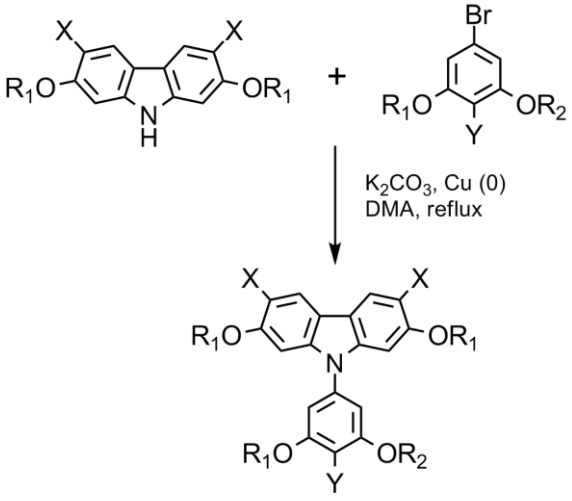

76: X=Y= H, R_1= R_2= $C_{18}H_{37}$ 48 h, **37%**
77: X=Y= H, R_1= $C_{18}H_{37}$, R_2= $(CH_2)_{15}COOCH_3$ 24 h, **80%**
79: X=Y= OC_9H_{19}, R_1= R_2= C_9H_{19} 48 h, **81%**
80: X=Y= OC_9H_{19}, R_1= C_9H_{19}, R_2= $(CH_2)_9COOCH_3$ 48 h, **58%**
82: X= OC_9H_{19}, Y= $O(CH_2)_9COOH$, R_1= R_2= $(CH_2)_9COOH$ 48 h, **50%**

Scheme 1.30

Ullmann couplings between the *N*H-carbazole **53** and the two bromobenzenes **62** and **72** worked with good yields giving 2,7-dioctadecyloxy-9-(3,5-dioctadecyloxyphenyl)carbazole (**76**) and methyl 16-[3-(2,7-dioctadecyloxy-9-carbazolyl)-5-octadecyloxyphenyloxy]hexadecanoate (**77**) (Scheme 1.30). However, all attempts of saponification of terminal ester of compound **77** by using sodium or potassium hydroxide as base failed. Therefore, the final *N*-phenylcarbazole derivative with a terminal carboxylic acid, 16-[3-(2,7-dioctadecyloxy-9-carbazolyl)-5-octadecyloxyphenyloxy] hexadecanoic acid (**78**), was obtained by the cleavage of the methoxy group with sodium ethanethiolate (Scheme 1.31).

Similarly, compounds 2,3,6,7-tetranonyloxy-9-(3,4,5-trinonyloxybenzene)carbazole (**79**) and methyl 10-[2,3-dinonyloxy-5-(2,3,6,7-tetranonyloxy-9-carbazolyl)]decanoate (**80**) were prepared in good yields by Ullmann condensation, but once again saponification of the terminal ester of **80** to give-[2,3-dinonyloxy-5-(2,3,6,7-tetranonyloxy-9-carbazolyl)phenyl]oxydecanoic acid (**81**) under the traditional conditions was not possible and the methoxy cleavage was achieved with sodium ethanethiolate, as in the case of compound **77** (Scheme 1.31). The Ullmann coupling between **64** and *N*H-carbazole **55** gave compound 10,10',10''-{5-[*N*-(2,3,6,7-tetranonyloxycarbazolyl)]benzene-1,2,3-triyl}tris(oxy)tris(decanoic acid) (**82**) instead of the expected analog with three terminal esters. The causes of the hydrolysis of the esters during the reaction were not investigated, but could be due to the presence of traces of water in the solvent.

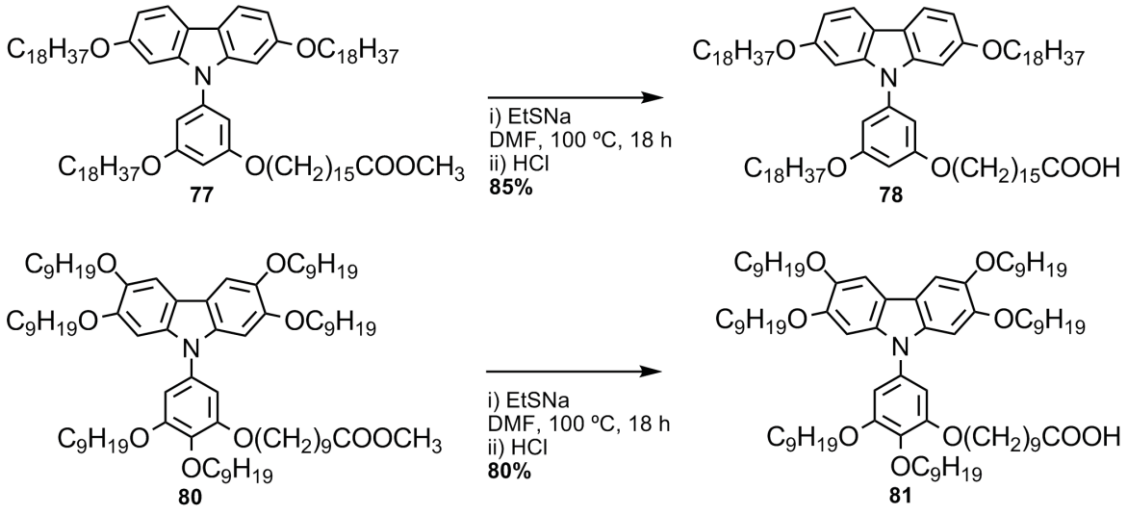

Scheme 1.31

Preparation of 1,2,3,6,7-pentaoctyloxy-N*H*-carbazole (**83**) was achieved following a similar synthetic path to that previously described for the tetraalkoxycarbazole **55** (Scheme 1.32). 4-Bromoveratrole and 1-bromo-3,4,5-trimethoxybenzene were separately treated with BBr_3 to give the corresponding bromophenols **56** and **66**. Williamson alkylation of both compounds with 1-bromooctane gave products **84** and **85** respectively in good yields.

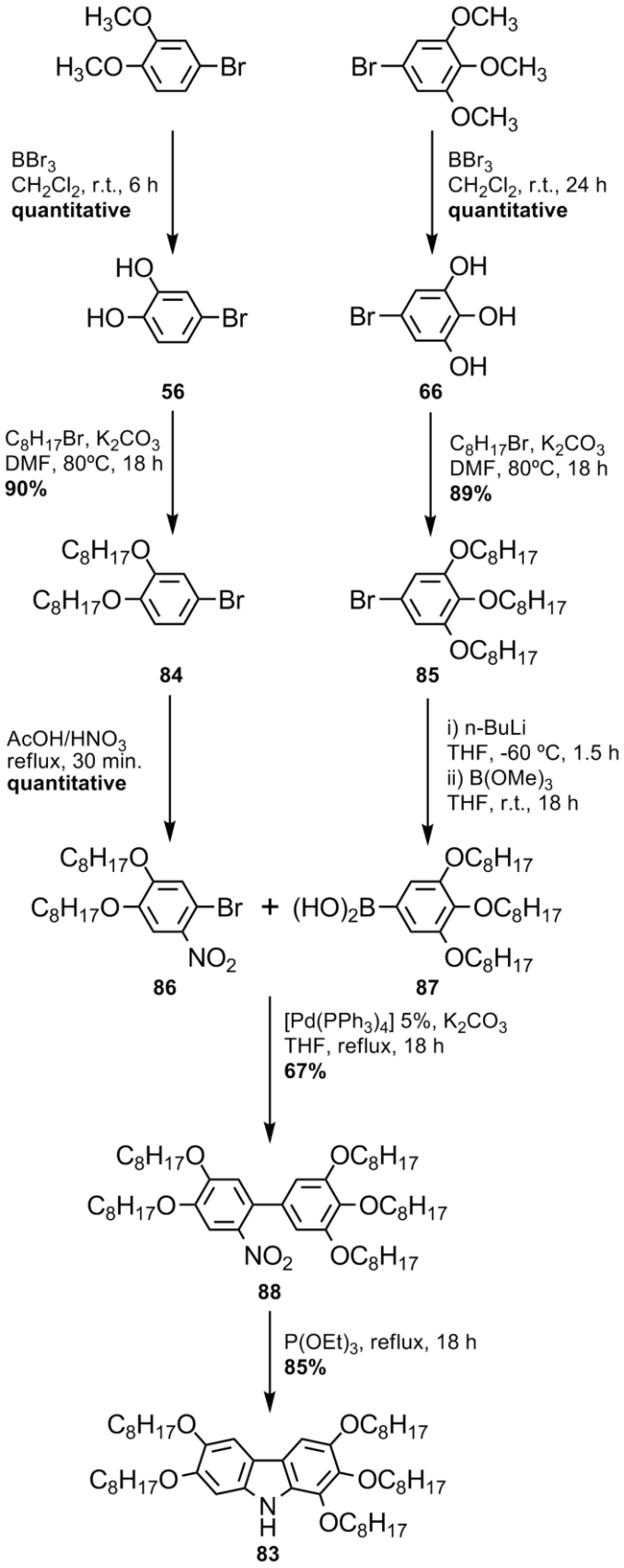
BBr3
CH2Cl2, r.t., 6 h
quantitative
BBr3
CH2Cl2, r.t., 24 h
quantitative
56
66
C8H17Br, K2CO3
DMF, 80ºC, 18 h
90%
C8H17Br, K2CO3
DMF, 80ºC, 18 h
89%
84
85
AcOH/HNO3
reflux, 30 min.
quantitative
i) n-BuLi
THF, -60 ºC, 1.5 h
ii) B(OMe)3
THF, r.t., 18 h
86
87
[Pd(PPh3)4] 5%, K2CO3
THF, reflux, 18 h
67%
88
P(OEt)3, reflux, 18 h
85%
83

Scheme 1.32

Like in the case of its 9-carbon alkoxyl chains counterpart **57** previously described, the treatment of 3,4-dioctyloxybromobenzene **84** with $AcOH/HNO_3$ produced a quantitative yields of **86** by nitration at the carbon located in the *ortho* position regarding the bromide and the *para* position regarding the alkoxyl chain at position 3 of **84**.

The synthesis of 3,4,5-trioctyloxyphenylboronic acid (**87**) involved the same steps as those previously described for the phenylboronic acid **59**: a metal-halogen exchange between bromobenzene **85** and nBuLi; the formation of a phenylboronic ester by reacting with trimethoxyboron and the hydrolysis of the boronic ester in mild acidic conditions to give the targeted boronic acid. Since compound **87** did not undergo crystallization, the crude was used in the following reaction.

Biphenyl **88** was obtained by a Pd(0) catalyzed Suzuki cross-coupling reaction of penylboronic acid **87** and nitrocompound **86**. Finally, the biphenyl underwent reductive cyclation by reacting with triethylphosphite and gave 1,2,3,6,7-pentalkoxycarbazole (**83**) in good yields.

The *N*-alkylation of *N*H-carbazole **83** with dibromoalkanes of different chain length in a 2:1 ratio was performed in the presence of NaH as a base and worked with excellent yields (Scheme 1.33) giving 1,2,3,6,7-pentaoctyloxy-[10-(1,2,3,6,7-pentaoctyloxycarbazol-9-yl)decyl]carbazole (**89**), 1,2,3,6,7-pentaoctyloxy-[12-(1,2,3,6,7-pentaoctyloxycarbazol-9-yl)dodecyl]carbazole (**90**) and 1,2,3,6,7-pentaoctyloxy-[14-(1,2,3,6,7-pentaoctyloxycarbazol-9-yl)tetradecyl]carbazole (**91**).

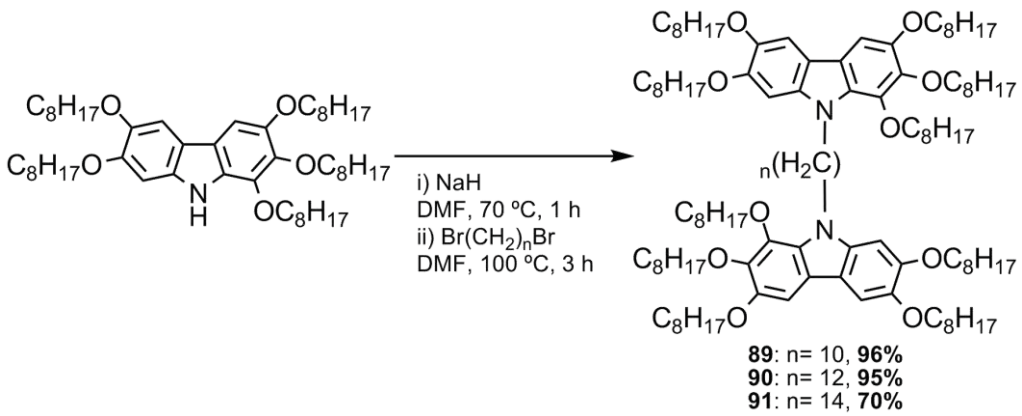

Scheme 1.33

1.3.2.2. Study of the liquid-crystalline phases

1.3.2.2.1. Differential Scanning Calorimetry analyses

1.3.2.2.1.1. Tetraalkoxyl *N*-phenylcarbazoles

The characteristics of the DSC curves of the compounds based on the tetraalcoxylated *N*-phenylcarbazole core are presented in Table 1.18. The liquid crystal phase shown by this family of compounds, identified as a lamellar mesophase by X-ray diffraction studies (section 1.3.2.2.2)[2], could only be detected in a short temperature ranges during the second heating process, that is, it has a monotropic character.

Table 1.18. Phase transition temperatures (°C) and transition enthalpies (kJ mol^{-1} in square brackets) of heptaalkoxyl *N*-phenylcarbazole derivatives observed in the second heating and in the first cooling processes by DSC analyses (2 °C min^{-1} rate).

	Heating					Cooling		
	Cr		M		I	I		Cr
76	•	64 [9]	•	79 [160]	•	•	67 [-152]	•
77	•	53 [4]	•	73 [159]	•	•	58 [-160]	•
78	•	65 [110]	• 71 [9] •	82 [48]	•	•	54 [-125]	•

Cr= crystalline phase, M= mesophase, I= isotropic phase. Negative values of the enthalpies refer to exothermic processes and *vice versa*.

The three compounds present very similar phase transitions. However, there is a shift of the mesophase to lower temperatures for **77** in comparison to **76**. Another difference is the higher enthalpy associated to the crystal to liquid crystal phase transition and the following low energetic transition for the compound bearing the terminal carboxylic acid, **78**. A small rearrangement can be associated to the latest, though no texture change was detected in the polarized light optical microscope (POM) in this range of temperatures. The higher enthalpy value for the first endothermic peak, in turn, indicates that the transition from the crystalline phase to the lamellar phase must overcome stronger intermolecular interactions for molecules bearing a terminal acid (**78**) than for the other analogues (**76** and **77**), something that may be related to the presence of hydrogen bonds in the solid phase. Nevertheless, providing the mesogen **76** with a terminal carboxylic acid does not lead to significant modifications in the mesophase stability.

1.3.2.2.1.2. Heptaalkoxyl *N*-phenylcarbazoles

The results obtained by DSC analysis of the compounds belonging to the family of heptaalkoxyl substituted compounds are summarized in Table 1.19. As it had been previously reported, the symmetrically heptanonyloxy substituted **79** showed an enantiotropic Col_r mesophase in a wide range of temperatures going from negative temperatures to temperatures above rt.[3]

The introduction of a terminal carboxylic group in one of the alcoxyl chains attached to the phenyl fragment leads to a decrease of the thermal stability of the Col_r phase in both **80** and **81**. Namely the presence of a terminal methyl carboxylate in the former and a terminal carboxylic acid in the second produces a lowering of the clearing point. Enthalpy values for the isotropization are very similar to the ones observed for the mesophase of **79**. Thus, no stronger intermolecular forces are operating in the Col_r phase of these two mesogens comparing to the ones in the Col_r phase of **79**.

Table 1.19. Transition temperatures (°C) and transition enthalpies (kJ mol^{-1} in square brackets) of heptaalkoxylated *N*-phenylcarbazole derivatives observed in the second heating and in the first cooling processes by DSC analyses (2 °C min^{-1} rate).

	Heating					Cooling				
	Cr		**M**		**I**	**I**		**M**		**Cr**
79	•	-5 [2]	•	32 [24]	•	•	29 [-18]	•	-3 [-2]	•
80	•	-10 [5]	•	16 [26]	•	•	6 [-17]	•	-18 [-7]	•
81[a]	•	51 [100]			•	•	2 [-19]	•		
81[b]			•	15 [19]	•	•	2 [-19]	•		
82	•	-13 [-18]	•	41 [53]	•	•	4 [-8]	•	-24 [-7]	•

[a]Transitions found for the stable crystal phase during the first heating. [b]Transitions found for the metastable LC phase. Cr= crystalline phase, M= mesophase, I= isotropic phase. Negative values of the enthalpies refer to exothermic processes and *vice versa*.

After the first cooling, compound **81** shows a mesophase in the second heating process with a clearing point of 15 °C. However, when the material is left at rt. in the isotropic state obtained in this second heating it evolves with time to a crystalline phase with a melting point of 51 °C, which is the transition observed in the first heating process. The broadness of the peak associated to the melting process and its higher enthalpy prove the presence of strong and complex intermolecular interactions in the crystalline phase. Neither compound **79** nor the methyl carboxylate analog **80** present this behavior. Hence, the formation of this new crystalline phase could be attributed to the formation of intermolecular H-bonds, whose kinetics is too slow to occur during the cooling process from the isotropic state at the used rates in the DSC analyses. IR spectra at rt. of compound **81** in the crystalline phase (in KBr) and of the isotropic state (in NaCl) were registered in an attempt to confirm this hypothesis. However, the O-H stretching characteristic for carboxylic acids (3500 cm^{-1}) was

present in both states and no variation of the C=O stretching frequency (1720 cm^{-1}) was detected, thus giving no evidences of H-bonding.[7] These results could mean that other supramolecular interactions are the responsible of the crystallization.

In order to determine the time required for this metastable isotropic phase to transform into the crystalline phase completely, the enthalpies of the phase transition at 51 °C were registered at different times after isotropization by DSC analyses. From this study it was determined that at least 20 hours are needed to attain the stabilized crystalline form (Figure 1.38).

An increase of the number of carboxylic terminal acids in the phenyl moiety of the *N*-phenylcarbazole core produced drastic changes in the DSC curves. Similarly to the analog compounds **79**, **80** and **81**, compound **82** presented two exothermic processes within the cooling down from the isotropic state. The first one centered at 4 °C, was assigned to a liquid-mesophase transition by POM. The low registered enthalpy value for this peak seems to indicate that week intermolecular interactions are established. The second peak, at -24 °C, corresponds to a liquid crystal-crystal phase transition.

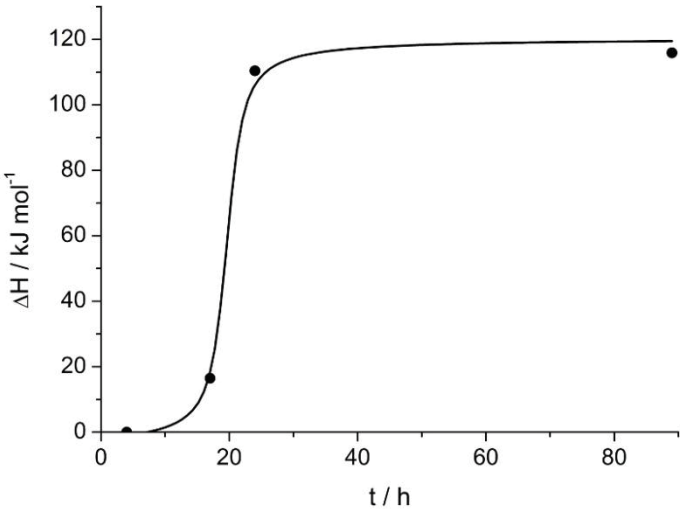

Figure 1.38. Enthalpies registered for the crystal to isotropic state phase transition of **81** at different times after isotropization.

The DSC curve for the second heating process (Figure 1.39) presented a main difference with respect to its other counterparts: an exothermic peak at -13 °C assigned to a crystal to liquid crystal phase transition by POM observations. Its exothermic nature indicates it is a favorable process. Thus, the transferred thermal energy to the system promotes the establishment of stronger intermolecular interactions. Accordingly, the isotropization of this material, assigned to the following endothermic peak, occurs at a higher temperature and has a higher associated enthalpy value in comparison with the previously discussed similar LCs. This DSC curve profile suggests that new H-bonds are formed

during the heating process and then destroyed in the melting process. In addition, the liquid crystal phase formed by **82** is not a columnar mesophase, as in the case of **79** or **81**, but a nematic mesophase, as it was evidenced by X-ray studies (see section 1.3.2.2.2).

Therefore, the DSC analyses of compounds **79**, **81** and **82** indicate that the introduction of a single terminal acid in the side chains of the heptaalkoxyl *N*-phenylcarbazole discotic mesogens produces the destabilization of the columnar mesophase, since the Col_r mesophase observed for compound **81** presents a lower clearing point than in the case of **79** and is metastable –the melted state becomes crystalline with time at rt. The presence of three terminal carboxylic acids in the phenyl moiety, in turn, confers the material higher clearing points, though it destroys the columnar arrangement (see X-ray studies, section 1.3.2.2.2).

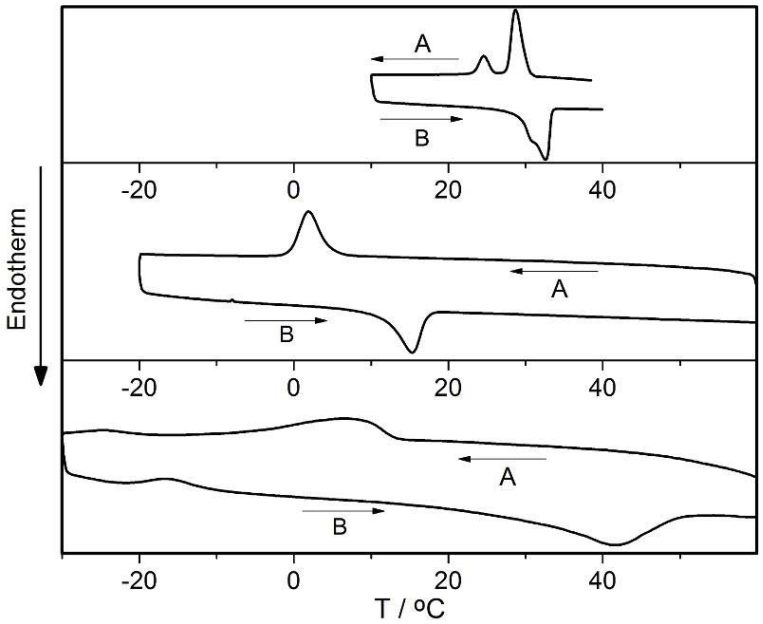

Figure 1.39. DSC curves of the cooling from the isotropic state (A) and the second heating (B) processes of mesogens **79** (top), **81** (middle) and **82** (bottom).

1.3.2.2.1.3. Doped systems

Two different molar ratios of *N*-phenylcarbazole derivative, donor (D), and 2,4,7-trinitrofluorenone (TNF), acceptor (A), 1:1 and 3:1, were chosen to study the trend of the variations of the molecular arrangement and derived properties of the different systems depending on the doping degree. While TNF proved to be non-miscible in the tetraalkoxyl substituted compounds **76** and **77**, the doping of the heptaalkoxyl substituted compounds, **79** and **81**, led to the formation of strongly colored complexes in both 1:1 and 3:1 ratios.

As in the case of other discotic mesogens found in the literature, [9-15] the addition of TNF to **79** in a 1:1 ratio broadens the temperature of the liquid crystal phase. The clearing point of the equimolecular complex is 18 °C higher than the one of the starting material. Furthermore, the **79**:TNF complex does not undergo crystallization. It must be remarked that, despite the complex formation enhance the intermolecular interactions, the values of the enthalpy associated to the clearing processes of the complex and the pure starting material are very similar. This fact indicates that many factors are contributing to the final energy of the mesophase. For intance, DD interactions might be broken by the insertion of the A into the columns, thus decreasing the enthalpy.[11]

The doping of material **79** with smaller amounts of TNF (**79**:TNF 3:1), though, shrinks the temperature range of the liquid-crystalline phase, both in the cooling and the second heating processes. Probably the amount of electron-acceptor might not be sufficient to produce the establishment of the proper intermolecular charge transfer, while the DD interactions, responsible of the columnar arrangement in pure **79**, might be destroyed. This might explain the low enthalpy values and the texture observed by POM (see section 1.3.2.2.3), which suggest that a nematic mesophase is formed instead of a columnar mesophase.

Although compound **81** presents an identical aromatic core to the one of compound **79**, and a very similar behavior could be anticipated for their TNF doped systems, arising from the resemblance of their donor nature, many differences were detected. A 25% doping of the starting material produces indeed a very effective stabilization of the liquid crystal phase. Namely, while in the pure compound **81** the mesophase has a metastable character and occurs below rt., the mesophase of the complex is perfectly stable and is present at rt. and at higher temperatures showing a clearing point of the complex increased in 45 °C regarding **81**. The liquid crystal phase did not undergo vitrification during the cooling process but a phase transition identified as crystallization by POM, involving some molecular rearrangements, evidenced by X-ray diffraction (see 1.3.2.2.2)

The equimolecular complex, in turn, does not form any liquid crystal phase and presents only a crystalline phase with a very high melting point instead. Taking into account that the only difference between compound **79** and **81** is the presence of a terminal carboxylic acid in one of the alkoxy chains, it is clear that this group is playing a main role in the intermolecular interactions. The lack of the liquid crystal character excluded the **81**:TNF 1:1 complex of the target systems to study and it was not further characterized.

Table 1.20. Transition temperatures (°C) and transition enthalpies (kJ mol^{-1} in square brackets) of heptaalkoxyl *N*-phenylcarbazole derivatives observed in the second heating and in the cooling processes by DSC analyses (2 °C min^{-1}).

	Heating						Cooling			
	Cr		M		I	I		M		Cr
79	•	-5 [2]	•	32 [24]	•	•	29 [-18]	•	-3 [-2]	•
79:TNF [3:1]	•	22 [4]	•	37 [2]	•	•	19 [-2]	•	-12 [8]	•
79:TNF [1:1]			•	50 [25]	•	•	39 [-24]	•		
81[a]			•	15 [19]	•	•	2 [-19]	•		
81:TNF [3:1]	•	9 [12]	•	59 [7]	•	•	24 [-4]	•	-7 [-10]	•
81:TNF [1:1]	•	80			•					

[a]MetasTable mesophase. Cr= crystalline phase, M= mesophase, I= isotropic phase. Negative values of the enthalpies refer to exothermic processes and vice versa.

Thus, doping with TNF the heptaalkoxyl N-phenylcarbazole derivatives with the proper molar ratios stabilizes the columnar mesophases of the starting materials. That is the mesophases formed by the **79**:TNF (1:1) and **81**:TNF (3:1) complexes present higher clearing points and wider temperature ranges than the pure materials **79** and **81**. It is remarkable that, whereas the terminal carboxylic acid of **81** has a destabilizing effect in the columnar arrangement of the pure mesogens, in the doped systems it contributes to the attainment of a stable Col mesophase with a higher clearing point than the doped material **79**, requiring lower ratios of TNF.

1.3.2.2.1.4. Dimeric systems.

Although the variation of the length of the alkyl chain linking the two polyalkyl carbazole fragments in two carbons could seem a minor one (Scheme 1.33), it proved to produce drastic changes in the thermal behavior when comparing the different compounds to each other (Table 1.21).

Taking the previously described compound with a dodecyl linking chain **90** as reference compound, the decrease of the central chain in two methylenes (**89**) leads to the loss of the mesomorphic phase. Compound **89** presents only a crystalline phase with a higher melting point than the clearing point of its 12-carbon counterpart **90**. Compound with a 14-carbon linking chain **91**, in turn, shows two different phases depending on the thermal treatment applied to the material. Thus, when the material is cooled down from the isotropic state using cooling rates of 2 °C/min or faster, the system undergoes a supercooling and forms a liquid crystal phase with a clearing point of 30 °C. This mesophase does not crystallize at lower temperatures but vitrifies. However, by applying lower cooling rates and leaving the system at rt. for long times it forms a crystalline phase with a higher melting point (49 °C). Hence, the observed liquid-crystalline phase of **91** is a metastable mesophase that is formed when the system is not allowed to establish the necessary intermolecular interactions

that lead to the thermodynamically stable crystalline phase with slower kinetics. The nature of these two found phases will be discussed in the next section.

Table 1.21. Transition temperatures (°C) and transition enthalpies (kJ mol^{-1} in square brackets) of heptaalkoxyl *N*-phenylcarbazole derivatives observed in the second heating and in the cooling processes by DSC analyses (2 °C min^{-1} rate).

	Heating						Cooling			
	Cr		M		I	I		M		Cr
89	•	63 [113]			•	•			45 [-110]	•
90	•	31 [30]	•39 [45] •	51 [21]	•	•		•	13 [-100]	•
91[a]	•	49 [140]			•	•	-2 [-100]	•		•
91[b]			•	30 [94]	•	•				

[a]Transitions found for the sTable crystal phase during the first heating. [b]Transitions found for the metasTable LC phase. Cr = crystalline phase, M = mesophase, I = isotropic phase. Negative values of the enthalpies refer to exothermic processes and *vice versa*.

Therefore, no specific trend in the thermal behavior can be deduced from the elongation of the linking alkylic chain in the studied dimers, but the decrease of the isotropization temperature when going from 10 to 14 carbons.

1.3.2.2.2. X-ray diffraction studies

1.3.2.2.2.1. Tetraalkoxyl *N*-phenylcarbazoles

Compounds **76** and **78** show similar X-ray diffraction patterns in the low-angle region, that is, sharp equidistant peaks that indicate that the molecules are arranged in layers, i.e. a lamellar mesophase (Table 1.22). However, remarkable differences can be spotted in the wide-angle region. In addition to the diffuse halo centered at 4.3 Å that corresponds to the mean distance between the alkyl chains, the mesogen **78** presents two additional sharp reflections, one at 5.3 Å and another overlapped with the broad peak at 4.3 Å.

These sharp reflections may evidence a well defined periodic arrangement of the molecules in the normal direction of the layers in a 3D crystalline fashion. However, POM observations in this temperature confirmed a clear fluidness and elasticity of the system when pressure was applied onto the sample, which leaves no doubt of the liquid-crystalline nature of the phase.

It can be deduced from these results that the terminal carboxylic acid in the tetraalkoxy *N*-phenylcarbazole derivatives do not promote many changes in the molecular arrangement.

Table 1.22. X-ray data for the lamellar liquid crystalline phase of compounds **76** and **78**.

Compound	T [°C]	d [Å]	Miller indices (hkl)
76	70	41.9	100
		20.9	200
		13.9	300
		4.3	
78	68	40.2	100
		20.3	200
		13.5	300
		10.1	400
		5.3	
		4.3	

1.3.2.2.2.2. Heptaalkoxyl *N*-phenylcarbazoles

Table 1.23 summarizes the parameters found for the mesophases of compounds **79** and **81**. The two first intense peaks in the low angle region indicated a rectangular arrangement of the columns in the 2D lattice for both compounds. The indexation of the following less intense diffraction peaks could suggest a C2/m lattice structure for compound **79**, since the Miller indices of the planes corresponding to the observed distances fit the diffraction condition h+k = 2n, where n is an integer number. However, the weak peak at 11.7 Å assigned to the (120) plane violates this selection rule, what leads to a $P2_1/a$ symmetry.

Table 1.23. X-ray data of the ordered rectangular columnar mesophase of **79** and **81**.

Compound	T [°C]	d [Å]	Miller indices (hkl)	latice parameters [Å]
79	28	25.6	200	a = 51.2
		21.5	110	b = 23.6
		13.6	310	c = 3.5
		11.7	120	
		10.8	220	
		7.0		
		4.3		
		3.5	001	
81	5	26.4	200	a = 52.8
		20.8	110	b = 22.6
		14.3	310	c =3.5
		7.1		
		4.3		
		3.5	001	

Although the diffractograms of compound **81** did not present so many peaks and an unambiguous determination of the space group is not possible, it could be assumed from the structural resemblance to the analog compound **79** that the Col_r of this compound might most likely present a $P2_1/a$ symmetry.

Wide angle diffraction peaks correspond to the intermolecular distances within the columns. The wide peak centered at 4.3 Å shows the mean distance between the alkoxyl chains while the sharper peak at 3.5 Å is the Bragg distance between the aromatic cores of the piled molecules. Such a small intermolecular distance evidences a π-π interaction along the column, and gives rise to what is known as an ordered columnar mesophase.

A third broad peak is observed in this region of the diffractograms of both materials corresponding to a distance of 7 Å. This value fits the double of the core-core distance, what suggests the presence of an alternating element along the columns. This feature could be attributed to the head to tail stacking of the *N*-phenylcarbazole units like the one shown in Figure 1.40.

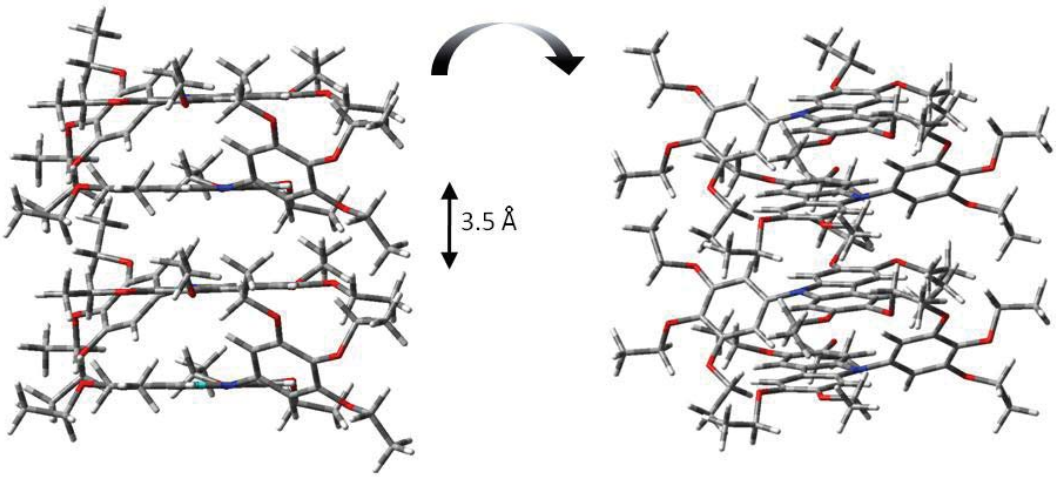

Figure 1.40. Scheme of the piling of the heptaalkoxyl *N*-phenylcarbazole (**79**) in a head-to-tail fashion.

Material **82** was studied by X-ray diffraction at different temperatures in order to detect the structural changes associated to the endothermic and exothermic processes detected by the previous DSC analyses (section 1.3.2.2.1.2). All diffractograms show the same profile consisting in a intense broad peak at wide angles centered at around 4.3 Å and two weaker and not well defined reflections at low angles centered at 25.6 and 17.3 Å (Figure 1.41). Hence, some periodical distance in the normal direction to the disks due to the interactions between the disordered chains is observed but no bidimensional order. That is, no columnar staking takes places but a nematic

mesophase is formed and no molecular rearrangements are associated to the peaks detected in the DSC curves.

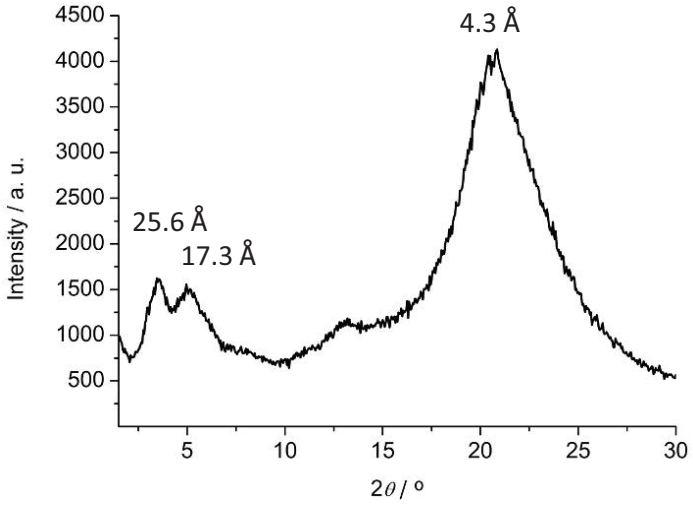

Figure 1.41. X-Ray diffractogram of **82** at -10, -50 and 20 °C.

Hence, whereas the presence of a single terminal carboxylic acid produces a destabilization of the columnar mesofase from a thermal point of view, it does not produce changes in the molecular arrangement. The presence of three terminal carboxylic acids, though, avoids the formation of the columnar mesophase. Taking into account the DSC curves registered for this material, this drastic change in the molecules disposition when the number of carboxylic groups increases might be related to the establishment of H-bonds.

That is, the molecular arrangement is a result of the sum of the intermolecular interactions acting in the different systems. In the case of compound **79**, the π-π interactions between aromatic cores are responsible for the piling of the discotic molecules. However, in the case of compound **82**, the formation of H-bonds might govern over the intercore interactions. Given the freedom of movement of the alkoxyl chains bearing the carboxylic acids and the multiple possible combinations of molecules that can occur when three terminal carboxylic groups are present in each molecule, the intermolecular H-bonds promote a quite disordered mesophase –a nematic mesophase. Thus, in the case of compound **81**, which bears a single terminal carboxylic acid, shows a behavior in between these two extremes.

1.3.2.2.2.3. Doped systems

The two TNF doped heptaalkoxyl *N*-phenylcarbazoles presenting the most stable liquid-crystalline phases were studied by X-ray diffraction technique. The incorporation of the electron acceptor into the materials **79** and **81** produced important structural changes in the columnar arrangement of the starting materials.

The X-ray diffractogram of the equimolecular **79**:TNF complex showed several new reflections in comparison to the pure material **79** (Figure 1.42). The first diffraction peak at low angles revealed that the complexation keeps the intercolumnar distance corresponding to the (200) plane. However, the (110) reflection varies drastically so that the observed distance moves closer to the value expected for a hexagonal lattice. Accordingly, the new arrangement could be considered a deformed columnar hexagonal mesophase, although in a rigorous way it must be treated as a columnar rectangular mesophase, and so were indexed the observed peaks.

Assigning the reflections in the wide angle region is not a trivial task, since it is not completely clear if they are due to intercolumnar or to intracolumnar distances. In the assignation proposed here all reflections in this region are attributed to the 2D lattice formed by the columns except for the broad peak centered around 4.3 Å and the peak centered at 3.3 Å, which derive from the distances between the disordered alkoxyl chains and between the aromatic cores along the columns respectively. Taking into account that there is the same amount of donor and acceptor molecules, the formed columns may contain both types of molecules in an alternating fashion, a feature that is responsible of the decrease of the intracolumnar distance respect to the starting material as a consequence of the intermolecular charge transfer.

Even thought the X-ray diffractogram of the complex formed by **81** and TNF in a 3:1 rate had a much simpler profile, a similar arrangement for this system in the liquid-crystalline phase can be deduced from it (Figure 1.43). A first Bragg distance around 25 Å was detected, like in the pure materials **79** and **81**. But in this case it was followed by a peak at 14.7 Å that holds a $1/\sqrt{3}$ ratio with the first reflection, thus evidencing a columnar hexagonal mesophase instead of a rectangular columnar phase, like in the systems studied so far. In addition, the core-core distance in this Col_h mesophase presented a slightly lower value comparing to the starting material as a result of the charge transfer interaction generated by the introduction of the TNF.

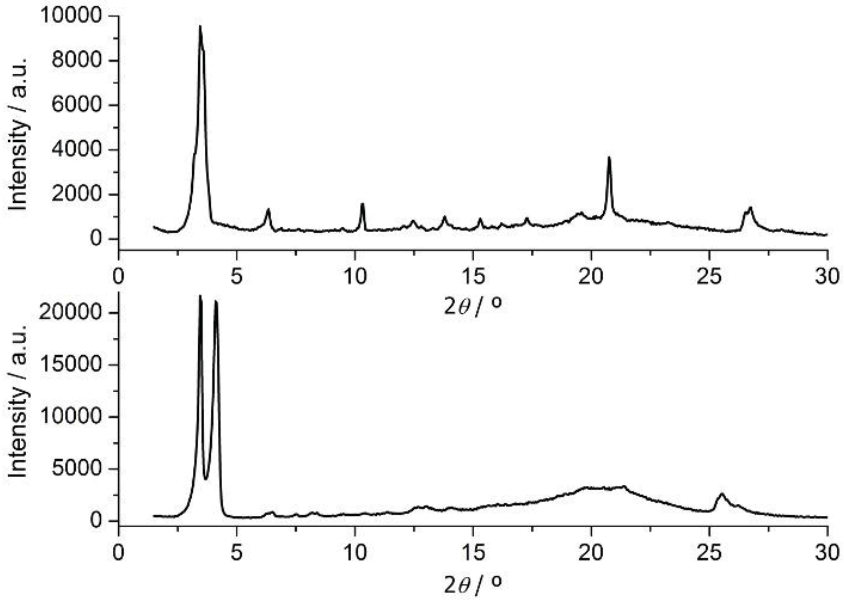

Figure 1.42. X-ray diffractograms of **79**:TNF 1:1 complex (top) and of **79** (bottom) at 25 and 10 °C respectively.

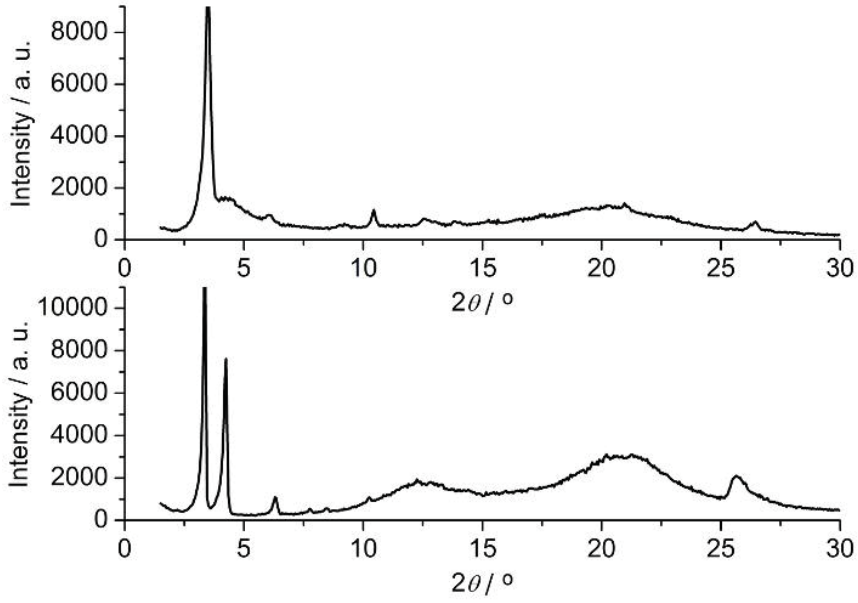

Figure 1.43. X-ray diffractograms of **81**:TNF 3:1 complex (top) and of **81** (bottom) at 30 and 5 °C respectively.

X-ray diffraction of this system at lower temperatures reveals that the phase transition observed in the DSC analyses in the cooling process involves a rearrangement of the columns to a rectangular lattice presenting similar distances for the (200) and (110) planes as those observed for the *N*-phenylcarbazole pure mesogens **79** and **81**. However, the lack of fluidness of this phase indicates that it is a glassy columnar phase instead of a liquid crystalline phase.

Table 1.24. List of reflections detected by X-ray diffraction for the complexes **79**:TNF 1:1 and **81**:TNF 3:1 at given temperatures and proposed indexation and lattice parameters.

Compound	T [°C]	Type	d [Å]	Miller indices (hkl)	Lattice parameters [Å]
79:TNF 1:1	25	Col_{ro}	25.6	200	a= 51.2
			13.9	110	b= 14.4
			8.6	600	c= 3.3
			7.1	120	
			6.4	800	
			5.8	520	
			5.1	720	
			4.3	530	
			4.4		
			3.3	001	
81:TNF 3:1	30	Col_{ho}	25.2	100	a= 25.2
			14.7	110	c= 3.4
			9.6	210	
			8.5	300	
			7.0		
			3.4	001	
	-20	$GCol_{ro}$	25.2	100	a= 50.4
			21.3	110	b= 21.3
			14.3*	110’	c= 3.4
			8.3	300	
			6.9		
			3.5*	001	
			3.4	001’	

*Remaining reflections from the Col_{ho} mesophase.

In an attempt to understand how the TNF molecules were inserted into the columns of the mesophase, a concentrated solution of the heptamethoxy substituted *N*-phenylcarbazole **49** and TNF in a 1:1 ratio was prepared and its ^{1}H NMR spectrum was studied and compared to the spectra of the two separated species. The aim was detecting the protons of the heptaalkoxyl *N*-phenylcarbazole that undergo a variation of their chemical shift by forming a complex with the TNF, so that some information about how the TNF and the mesogen are disposed in the column could be obtained. Compound **49** was chosen for this analysis because it shares the electron donor nature with the 9-carbon alkoxyl chain analog **79**, while presenting a simpler ^{1}H NMR spectrum and requiring less material for a concentrated solution.

Figure 1.44 shows the chemical shift of both species as pure materials and when forming a complex. It might be expected that some aromatic protons of the electron donor present higher chemical shifts in the complex than in the pure material as a result of the loss of electron density and, therefore, the opposite phenomena would be expected for the electron acceptor molecule TNF.

However, a decrease of the chemical shift was observed for both species, that is, an increase of the shielding on both molecules. An explanation for this could be that, since the complex involves an overlap of the two π systems and thus a closeness of both molecules, the protons that belong to the moieties participating in the charge transfer are more shielded than in the free species. Considering this, the TNF might be located over the carbazole fragment and not in the trialkoxyphenyl moiety in the concentrated solution and most probably also in the condensed state, in agreement to the more electron donor character of the heterocycle within the whole molecule.

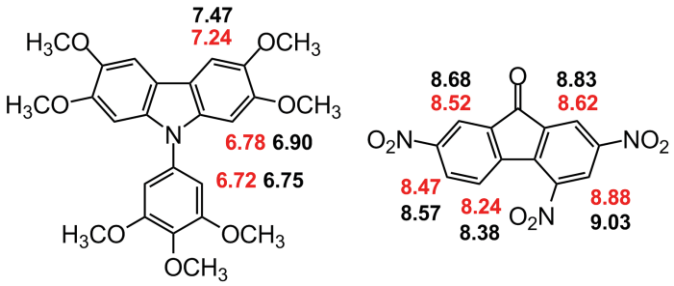

Figure 1.44. Chemical shifts in ppm of the aromatic protons of the pure materials (black) and in the 1:1 complex (red).

Summarizing, the X-ray studies of the complexes **79**:TNF (1:1) and **81**:TNF (3:1) indicate that doping the heptaalkoxyl *N*-phenylcarbazole discotic molecules with the electron-acceptor TNF not only stabilizes the columnar mesophases, as it had been evidenced by the DSC studies, but also modifies the intercolumnar and intracolumnar distances of the liquid crystal phase, so that hexagonal lattices rather than rectangular lattices are observed. Most probably the TNF molecules are inserted in between the carbazole fragments of the *N*-phenylcarbazole cores.

1.3.2.2.2.4. Dimeric systems

The Bragg distances observed in the X-ray diffractogrames of the mesophases presented by the dimeric system **90** are listed in Table 1.25.

Despite the distance ratios of the diffraction peaks at 20.8, 10.5 and 7.0 Å follow the typical pattern of a lamellar mesophase, the reflection at 13.9 Å does not fit this profile. Thus a columnar rectangular arrangement is deduced from the diffractogram, although more peaks are needed to determine the space group of the lattice. Moreover, it is also not possible to confirm if the two discotic units of the dimers are piled in the same column or if each disk belongs to a different adjacent column. Certainly, 13.9 Å could fit the second possibility, since the length of the chain is estimated to be of 16.2 Å in the all-anti conformation in the gas phase according to the semi-empirical calculations (AM1), but concluding evidences are missing.

Table 1.25. List of reflections detected by X-ray diffraction for compound **90** at the given temperature range and proposed indexation and lattice parameters.

T [°C]	d [Å]	Miller indices (hkl)	Lattice parameters [Å]
25-45	20.8	200	a = 41.6
	13.9	110	b = 14.7
	10.5	400	
	7.0	600	
	4.3		
	3.7	001	

The molecular arrangement in the mesophase obtained by a fast cooling from the isotropic state of compound **91** proved to be a complex one. Figure 1.45 shows the X-ray diffractogram of this observed mesophase. It does not present well defined reflections, but big overlaps of diffraction peaks thus giving rise to broad bands centered at around 20, 7 and 4.4 Å. This suggests that the molecules are randomly disposed, only keeping a mean distance close to their disk dimensions, while the Van der Waals forces created between the alkyl chains induce some periodicity along a normal direction to the disks, like in the case of compound **82**. In other words, the molecules in this phase do not present positional order but do present orientational order, what is defined as a nematic liquid crystal phase.

Contrarily, the thermodynamically favored crystalline phase presented the same diffraction peaks in the low angles (20.3, 13.9, 9.8, 6.9 Å) as those found in the mesophase of the dimeric system **90**. Thus, the increase of the chainlength leads to stronger intermolecular interactions that suppress the fluidness of the lamellar phase.

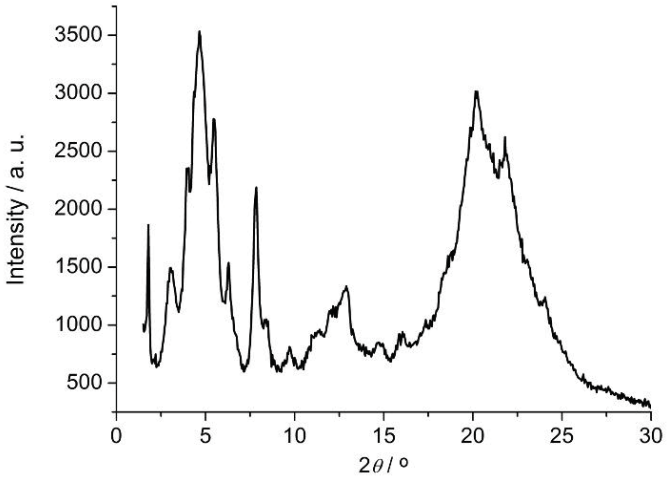

Figure 1.45. X-Ray diffractogram of **91** at 20 °C

1.3.2.2.3. Polarized Optical Microscopy observations

Figure 1.46 summarizes the phases of each prepared system, deduced from the DSC analyses, the X-ray studies and the POM observations. The letter in brackets indicates the picture of the texture observed in the polarized optical microscope for the corresponding phase, shown in Figure 1.47.

The three tetraalkoxy *N*-phenylcarbazoles, **76**, **77** and **78** present a broken fan texture (see A, B and D) typical for a lamellar arrangement in the range of temperatures in which the mesophase takes place. In the case of **78** the transition from the crystalline phase (C) to the mesophase (D) is detectable not only by the appearance of fluidness but also by a clear change in the texture.

The textures found for the mesophases of the compounds bearing seven chains in the *N*-phenylcarbazole core were very different from one another. While material **79** presented a focal conic texture (E), **80** formed granular textures (F) and **81** a needle-like texture (H). The first texture is common for columnar liquid-crystalline phases. The needle-like texture could be indicative of an edge-on disposition of the columns of **81** sandwiched between the glasses, which could be promoted by the interaction of the glass surfaces with the carboxylic groups at the end of the chains. Compound **82**, to which a nematic mesophase had been assigned from the X-ray studies, did not present a well-defined texture (I).

By doping compound **79** with TNF in a 3:1 ratio the focal conic texture became a granular one (J), and by increasing the proportion of TNF to a equimolecular ratio, big crossed bow-ties figures were obtained (K). This texture was also observed in complex **81**:TNF 3:1 mesophase (L) and resembles the fan-like textures, common in columnar mesophases.

The two different textures formed **90** and **91** are in agreement with their different molecular arrangment. The Col_r mesophase of **90** presented a spherulitic-like texture with maltese crosses (N), while the nematic mesophase of **91** gave a granular texture (P).

Taking into account all the characterization studies performed on the prepared carbazole derivatives, the most interesting compounds for their application as semiconductor materials are, from a mesomorphic point of view, are compound **79** and the doped systems **79**:TNF (1:1) and **81**:TNF (3:1), since they present stable ordered columnar mesophases at rt.

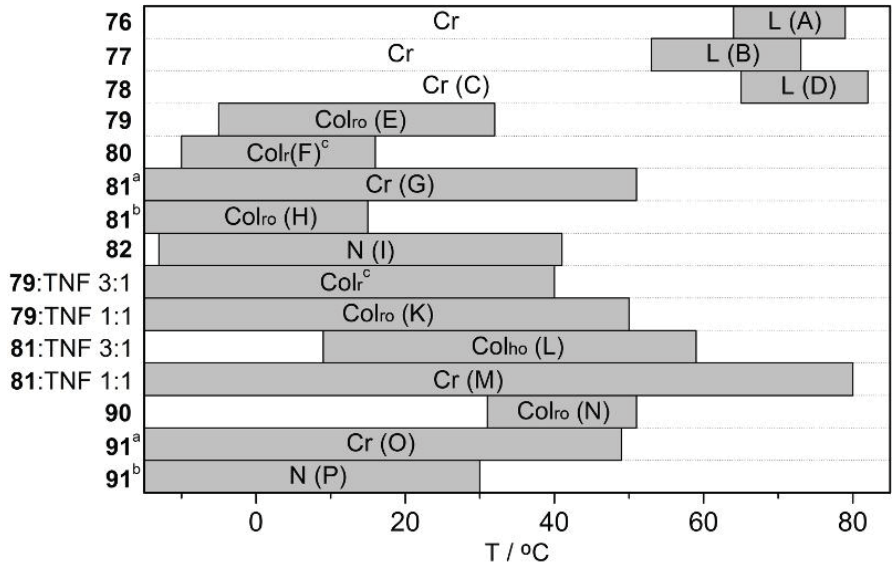

Figure 1.46. Temperature ranges of the mesophases found for the different compounds. Cr = crystalline phase, Col_{ho} = ordered hexagonal columnar mesophase, Col_{ro} = ordered rectangular columnar mesophase, L = lamellar mesophase, N = nematic mesophase. [a]Phases detected in the first heating. [b]Phases detected in the second heating process. [c]Confirmation by X-ray studies missing.

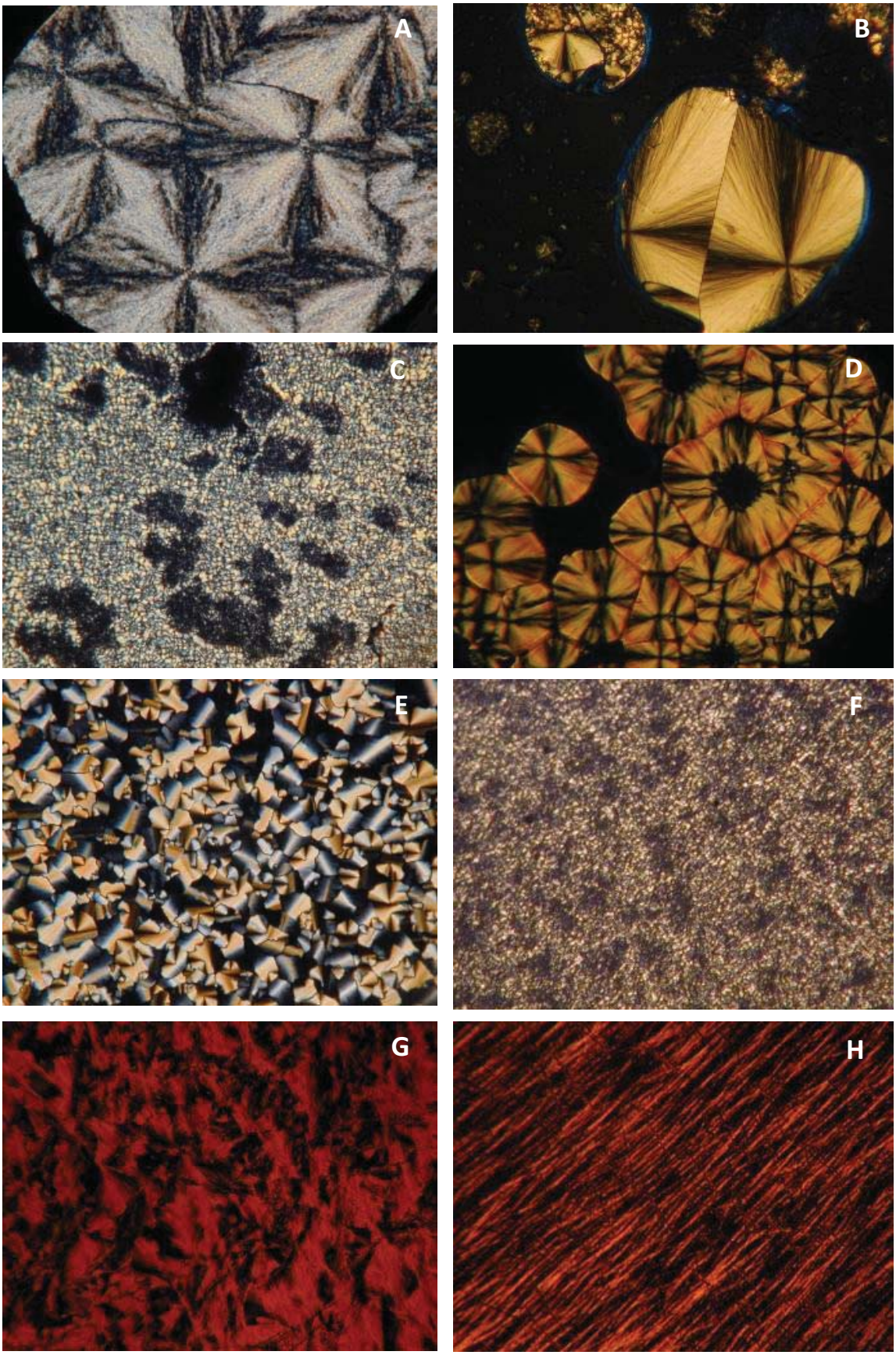
A
B
C
D
E
F
G
H

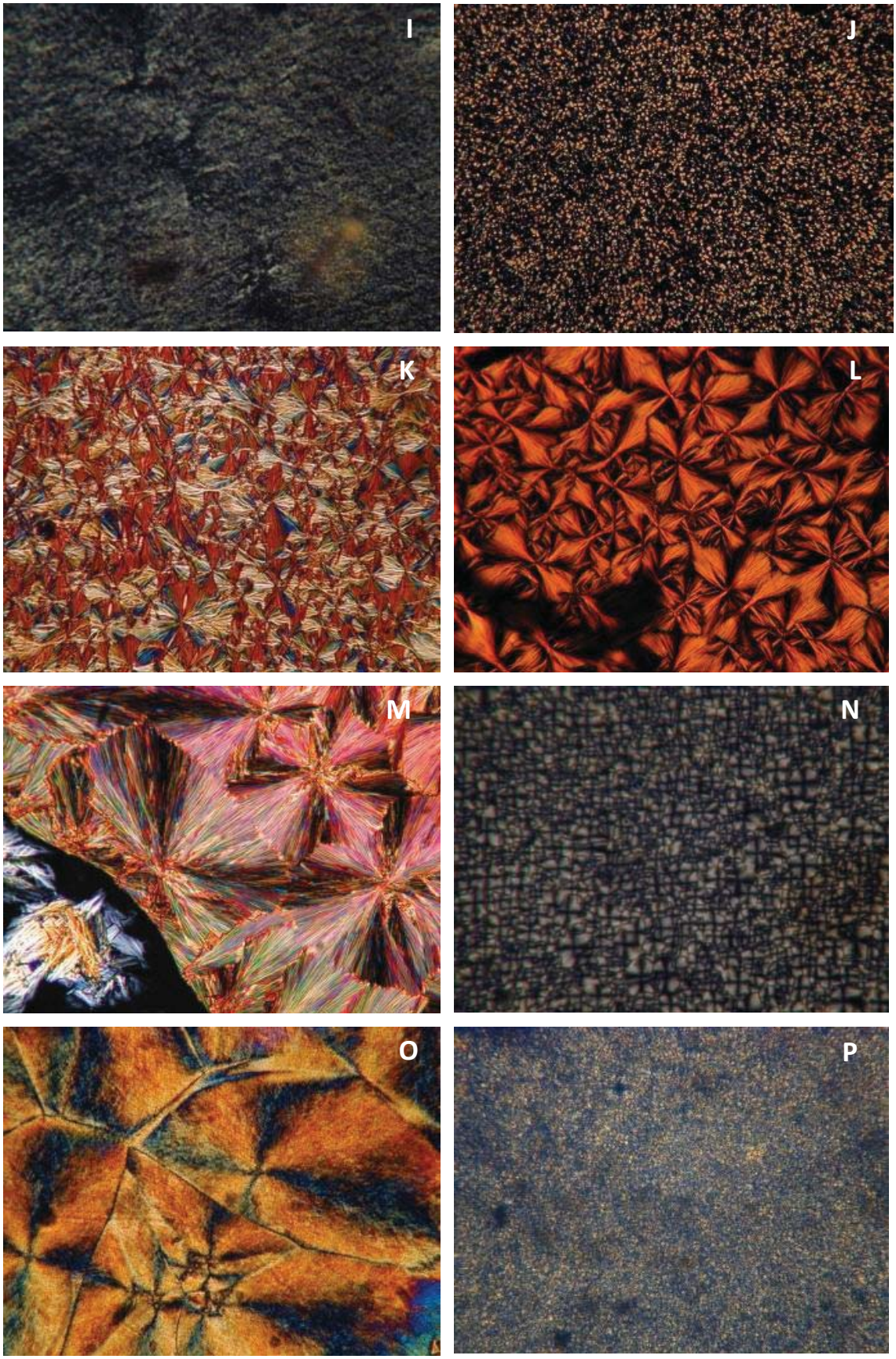

Figure 1.47. Textures observed for the phases presented by the different compounds. For the assignment of the pictures see Figure 1.46.

1.3.3. Absorption and photoluminescence studies

The absorption spectra in CH_2Cl_2 solution at room temperature of the *N*-phenylcarbazole derivatives and the dimeric carbarzole systems presented in the previous sections are shown in Figure 1.48.

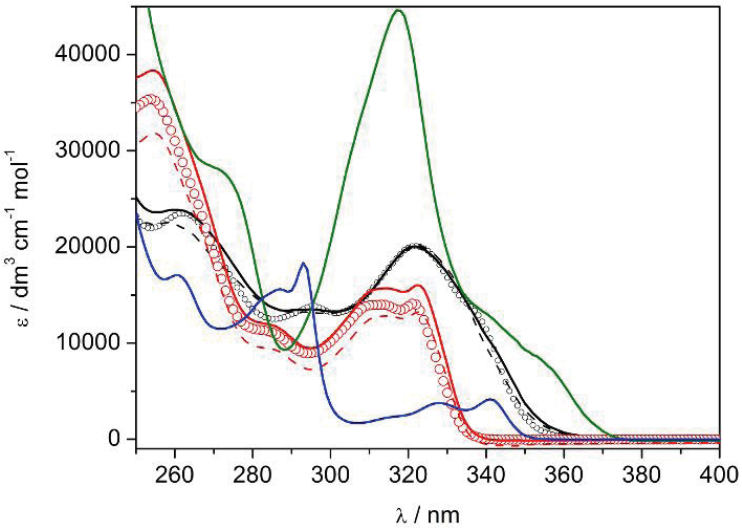

Figure 1.48. Absorption spectra of *N*-phenylcarbazole (blue) and its tetraalkoxyl (red) and heptaalkoxyl (black) derivatives with long chains (solid), methoxy groups (circle) and terminal carboxylic acids (dashed). In green, absorption spectrum of **90**.

It can be observed that the absorption profiles depend only on the core structure but not on the chainlength. The *N*-phenylcarbazole derivatives present two overlapped absorption bands within the 280-360 nm range attributed to the $S_0 \rightarrow S_1$ (around 320 nm) and to the $S_0 \rightarrow S_2$ (around 290 nm) transitions, both of π,π^* nature, by analogy with *N*-phenylcarbazole absorption spectrum.[16] The less energetic band in the tetraalkoxyl compounds **48**, **76** and **78** shows some fine structure with maxima at 314 and 322 nm, while in heptaalkoxyl compounds **49**, **79** and **81**, the λ_{max} for this band is 322 nm.

Given that the transition to the first excited state ($S_0 \rightarrow S_1$) can be assigned to the promotion of an electron from the HOMO to the LUMO, the onset of the absorption of this band can be used to estimate the HOMO-LUMO gap. This value presents a bathochromic shift when going from the tetraalkoxyl carbazole derivatives **48**, **76** and **78** to the heptaalkoxyl carbazole derivatives **49**, **79** and **81**. The observed shift means a decrease in the HOMO-LUMO gap, which is most probably due to a higher destabilization of the HOMO with the increase of the electron-donor groups.

From an inductive point of view it might be expected that the absorption onset value of the *N*-phenylcarbazole would be located at lower wavelength than the alkoxyl counterparts. However, the dihedral angle in the alkoxyl compounds might be higher than in the bare *N*-phenylcarbazole due to

the presence of the chains in the 2 and 7 positions of the carbazole fragment, thus reducing the conjugation and adding a factor that makes the HOMO-LUMO energy gap rise.

Compound **90** presents a band at 317 nm in its absorption spectra assigned to the $S_0 \rightarrow S_1$ transition. Despite this compound bears a higher number of alkoxyl chains in the carbazole fragment, this transition occurs at a slightly blue shifted wavelength comparing to the tetraalkoxyl carbazole derivatives. However, once more it must be taken into account the role of the phenyl ring in the *N*-phenylcarbazole core. Namely, even though it forms a dihedral angle bigger than 40° with the heterocycle, it participates to some extent in the aromatic conjugation, thus reducing the HOMO-LUMO gap. Moreover, the higher absorption molar coefficient of this band is due to the presence of two carbazole moieties in each molecule.

An overlapped band is also observed at longer wavelengths, which seems to indicate that excimers between two carbazole fragments belonging to the same molecule are formed in the solution. Thus, the HOMO-LUMO gap of **90** was estimated by the interception of the line that results of extrapolating the lineal range of the band with the axis of abscissas.

Emission spectra of all materials were registered in the same solvent at rt. both in air saturated and nitrogen saturated solutions. Excitation and emission maxima wavelengths and quantum yields relative to naphtalene in each media are reported in Table 1.26.

Table 1.26. Emission parameters of the synthesized polyalkolxyl carbazole derivatives.

	λ_{abs} / nm	λ_{exc} / nm	λ_{em} / nm	Φ_f (air)	Φ_f (N_2)
***N*-phenylcarbazole**	318, 341	285	348, 361	0.28[a]	0.34
48	314, 322	285	336, 349	0.17	0.22
76	314, 322	285	336, 349	0.13	0.15
78	314, 322	285	336, 349	0.14	0.16
49	322	266	372	0.09	0.11
79	322	266	374, 381	0.07	0.08
81	322	266	374, 382	0.08	0.10
90	317	275	375, 391	0.11	0.14

[a] In agreement with the results reported in reference [16].

All compounds emit in the UV region. The fine structure of their emission bands (double peak) was detected in all spectra except in the case of **49**. While the tetraalkoxyl *N*-phenylcarbazoles **48**, **76** and **78** derivatives emit blue-shifted regarding *N*-phenylcarbazole, the heptaalkoxyl **49**, **79** and **81** emit at longer wavelengths, 30 nm red-shifted to the non-alkoxyl analog. The quantum yields tended to decrease with the addition of more alkoxyl chains to the *N*-phenylcarbazole core. It could be also observed that compounds with methoxy groups had slightly higher fluorescence efficiencies than

their long-chain counterparts. Quantum yields in nitrogen saturated solvent proved to be higher than in air saturated solvents in all cases, as a result of the oxygen triplet quenching of the excited state that favors the intersystem crossing.[16]

The attachment of a strong electron-withdrawing group such as the tricyanovinyl in the carbazole fragment of the 1,3,5-tris(*N*-carbazolyl)benzene (TCB) results in the appearance of a new band in the visible region of the absorption spectra. Dichloromethane solutions of **50**, **51** and **52** at rt. (Figure 1.49) present absorption bands at 479, 475 and 473 nm, respectively, which are attributed to a π,π^* intramolecular charge transfer (ICT) from the carbazole to the side chain tricyanovinyl chromophore,[17] as a consequence of the donor (D) and acceptor (A) nature of these two fragments. Namely, previous X-ray studies of the crystalline phase of the 3-tricyanovinylcarbazole core proved that it presents a nearly planar structure bearing a small angle of rotation of the tricyanovinyl fragment with respect to the carbazole moiety, thus allowing the conjugation between D and A fragments and favoring the ICT.[18] The 1:2:3 ratio of the intensity of this ICT band for **50**, **51** and **52** is accordingly attributed to the ratio of probability of the ICT to happen, since these compounds bear one, two and three D-A units in their structure, respectively.

Two more absorption bands within the UV region with maxima at 335 nm and 298 nm are present in the spectra, sharing the absorption profile of the *N*-phenylcarbazole and the TCB. These two bands are therefore assigned to π,π^* transitions involving the *N*-phenylcarbazole core, so that the absorption spectra are the result of the overlapping of two electronic transitions: the $S_0 \rightarrow$LE (LE = locally excited) transition and the $S_0 \rightarrow$CT transition.[19] The estimation of the HOMO-LUMO gap from the absorption spectra for these materials will be discussed in section 1.3.4.

Emission spectra of **50**, **51** and **52** in solvents of different polarity were registered at room temperature. It was observed that all compounds presented dual fluorescence in 1,4-dioxane (Figure 1.50), although the intensity of the band at shorter wavelengths was of very low intensity for **51** and **52**. The phenomenon of dual fluorescence in D-A compounds is attributed to the emission from the localized excited state (D-A*) and from the product of the ICT state, a zwitterionic species (D^+-A^-).[20] Hence, emission bands in the UV region are attributed to the radiative relaxation of the LE states of these compounds, by analogy with the *N*-phenylcarbazole and the TCB fluorescence.

The emission in the visible region of **50** and **51** was quenched in dichloromethane, unlike in the case of **52**, for which a strong bathochromic shift for this emission band was detected in this solvent regarding the more apolar solvent 1,4-dioxane. The increase in the Stokes shift with the increase of the polarity is an indicator of the polar character of the ICT state, which is better stabilized by polar media, thus decreasing its energy and leading to longer emission wavelengths.

A total lack of emission bands in the visible region was detected in CH_3CN solutions of this family of compounds. However, the non-radiative de-excitation processes that the compounds could undergo in the different media are not the object of this photoluminescence study, which is only aimed to understand the electronic transitions that take place in these systems.

Table 1.27. Emission parameters of **50**, **51** and **52** in different solvents.

	Solvent	λ_{exc} / nm	λ_{em} / nm	Φ_f [a]	Stokes shift / cm^{-1}
TCB	1,4-dioxane	280	343, 357	0.46	519
	CH_2Cl_2	285	342, 358	0.33	346
	CH_3CN	285	342, 357	0.47	610
50	1,4-dioxane	280	343, 357	0.02	865
		430	575	0.02	4347
	CH_2Cl_2	260	345, 357	0.01	776
	CH_3CN	285	345, 355	0.01	776
51	1,4-dioxane	420	565	0.02	4230
52	1,4-dioxane	420	555	0.02	4209
	CH_2Cl_2	445	595	0.02	4380

[a]Quantum yields of the bands relative to naphtalene for emission in the UV region and relative to $Ru(bipy)_3 \cdot 6H_2O$ for emission in the visible region.

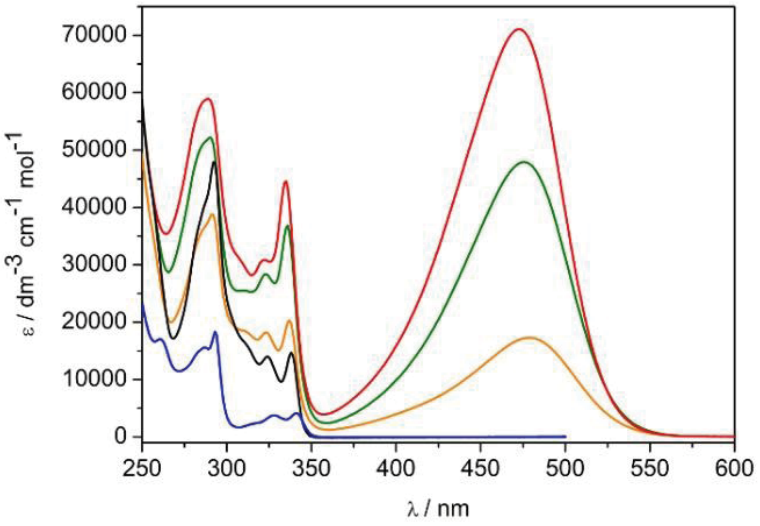

Figure 1.49. Absorption and of compounds *N*-phenylcarbazole (blue), TCB (black), **50** (orange), **51** (green) and **52** (red) in CH_2Cl_2.

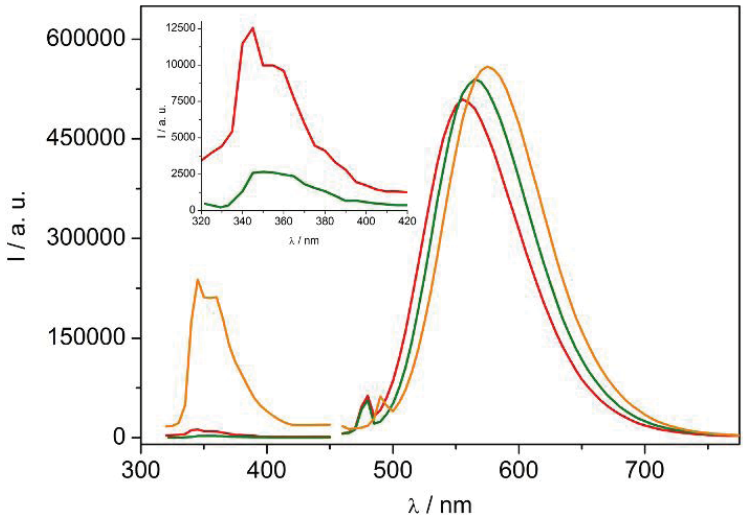

Figure 1.50. Emission spectra of **50** (orange), **51** (green) and **52** (red) in 1,4-dioxane. The insert shows the rescaled bans in the UV region of **51** and **52**.

1.3.4. Electrochemical studies

Electrochemical properties of the prepared systems were studied using two techniques: cyclic voltammetry and photo-emission in air. The experiments using the second technique were performed during an intership in the Solid State Electronics Department of the Vilnius University (Lithuania) under Prof. Gaidelis' supervision. Table 1.28 summarizes the parameters measured with both methods of the carbazole derivatives presenting alkoxyl chains.

Table 1.28. Electrochemical characteristics of the prepared carbazole derivatives bearing alkoxyl chains.

	E^0_{ox}/ V[a]	E^{onset}/ V	IP/ eV[b]	IP[c]/ eV	E_{gap}/ eV[d]
48	-	0.91	5.52	5.65	3.70
76	-	0.91	5.52	5.65	3.70
78	-	0.91	5.52	-	3.70
49	0.90	0.83	5.44	5.44	3.51
79	0.85	0.77	5.38	5.18	3.51
81	0.85	0.77	5.39	-	3.51
90	0.81	0.74	5.35	5.23	3.37

[a]Only for reversible oxidation processes. [b]Calculated according to the formula IP = E^{onset}-$E^0(Fc/Fc^+)$+4.8 where E^{onset} is the onset oxidation value, $E^0(Fc/Fc^+)$ = 0.19 V is the standard reduction potential of ferrocene vs. Ag/AgCl (3M) reference electrode and 4.8 is the reference energy level of ferrocene in eV. [c]Calculated from the photo-emission of the corresponding amorphous film. [d]Calculated from the λ_{onset} determined from the absorption spectrum.

As it could be foreseen from the electron-donor nature of these systems, only oxidation processes were observed in the cyclic voltammetries of all the compounds, since they are based on an electron-rich fragment, the carbazole, and in addition they bear electron-donor alkoxyl chains. However, many differences are detected in their redox properties.

On the one hand, the cathodic peaks in the CVs of all compounds based on tetraalkoxyl *N*-phenylcarbazole, **48**, **76** and **78**, is much less intense than the anodic peak (Figure 1.51 left). This marked asymmetry in the redox couple indicates that these species undergo irreversible oxidation, unlike the heptaalkoxyl *N*-phenylcarbazole systems, **49**, **79** and **81**, which show perfectly symmetric curves and thus reversible oxidations (Figure 1.51 right). It is also remarkable that the current density registered in the CV of the dimeric system **90** doubled the current densities of the other systems in the same conditions (concentration, scanning rate and electrode area). Namely, the two carbazole units in **90** may behave as two independent fragments so that for every mol of **90** that is oxidized two moles of electrons are collected in the working electrode.

On the other hand, the onset oxidation values present a clear trend of decrease when going from two to five alkoxyl gropus attached to the carbazole moiety. This trend is in agreement with the enhancement of the electron-donor character of the materials and the better stabilization of radical cation formed in the oxidation, which locates the positive charge on mainly on the nitrogen atom, with the increase of number of electron-donors.

It is interesting that a variation in the length of the alkoxyl chain could affect the redox properties in the case of the heptaalkoxyl *N*-phenylcarbazole compounds **49**, **79** and **81**. The lower E^0_{ox} and E^{onset} values of **79** and **81** in front of **49** could be attributed to a less conjugation degree over the *N*-phenylcarbazole core due to some distortions in the aromatic structure as a result of the repulsions between the adjacent alkoxyl groups, which are more important in the 9-carbon chain than in the methoxy fragments. Thus, a destabilization of the HOMO levels of **79** and **81** is produced, rising their energy levels and decreasing their ionization potentials.

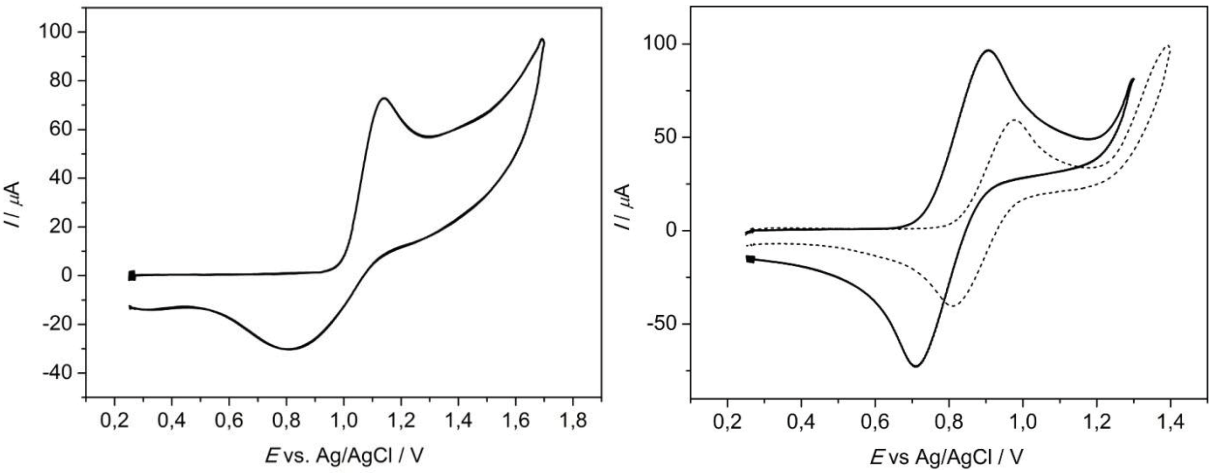

Figure 1.51. a) Cyclic voltammetry of **76** in dichloromethane solution at rt. b) Cyclic voltammetry of **49** (dashed line) and of **90** in dichloromethane at rt.

Despite the ionization potentials obtained for the thin layers of the studied compounds are higher than those approximated from the CVs in almost all the cases, the same trends discussed above are observed in this set of values. It should be noticed that the only materials that show lower IP values in the condensed state than in solution are **79** and **90**, which are the only ones that present a liquid crystalline phase at rt. where π-π intermolecular interactions take place (section 1.3.2.2). It had been shown that HOMO-LUMO gaps correlate with crystal packing parameters[21] and, more precisely, intermolecular interactions through π-π coupling can lead to lower HOMO-LUMO gaps than in the isolated molecule.[22] Therefore, a possible explanation for the lower IP values for the LC phase than for the molecule in solution could be the columnar stacking. An example of the plot obtained from an

experiment of photo-emission in air is shown in Figure 1.52. In the graphic the linear dependence of the current intensity on the energy of the incident photons, $f(h\upsilon) = I^{0.5}$, can be observed.

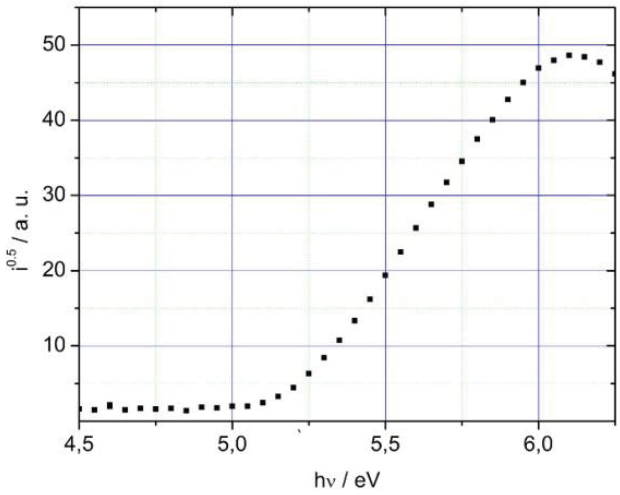

Figure 1.52. Photocurrent vs. incident light energy curve registered for compound **79**.

The addition of tricyanovinyl groups to the 1,3,5-tris(*N*-carbazolyl)benzene aromatic core (TCB) resulted in a very different electrochemical behavior from the pure electron-donor discussed above. Namely, compounds **50**, **51** and **52** undergo reversible reduction (Figure 1.53) instead of oxidation, unlike the corresponding precursor TCB.[23] Bipolar-transporting –an evidence of reversible reduction capabilities- had been reported for the compounds that result from substituting the central benzene of TCB by pyrimidine and triazine[24]. However, no reversible reduction for TCB derivatives conserving this central aromatic core had been described until now in the literature.

The standard reduction potentials show a slight decreasing trend from the trisubstituted compound **52** to the monosubstituted compound **50**. This behavior is agreement with the inductive effects produced by the electron-withdrawing groups. In other words, adding an electron should cost less energy in a molecule bearing more electron-withdrawing substituents, thus leading to higher EAs. However, the fact that reduction potentials have almost an identical value in the three compounds suggests that the tricyanovinyl group plays the main role in the gain of a single electron, in other words, the LUMO is mainly centered in the tricyanovinyl group. Thus it could be considered that the ICT absorption band corresponds to the promotion of an electron from the HOMO to the LUMO. However, theoretical calculations should be performed to confirm this hypothesis.

Table 1.29. Electrochemical characteristics of tris(*N*-carbazolyl)benzene systems bearing one (**50**) two (**51**) and three (**52**) tricyanovinyl fragments.

	E^0_{red} / V	E^{onset} / V	E^{onset} (ox) / V	EA / eV [a]	E_{gap} [b] / eV
50	-0.41	-0.50	0.98	4.11	2.33
51	-0.40	-0.49	0.93	4.12	2.35
52	-0.39	-0.48	0.83	4.13	2.38

[a]Values calculated using the formula E^{onset}-$E^0(Fc/Fc^+)$+4.8, where $E^0(Fc/Fc^+)$ = 0.19 V is the standard oxidation potential of ferrocene vs. Ag/AgCl electrode; [b]Estimated from the edge of the absorption spectra.

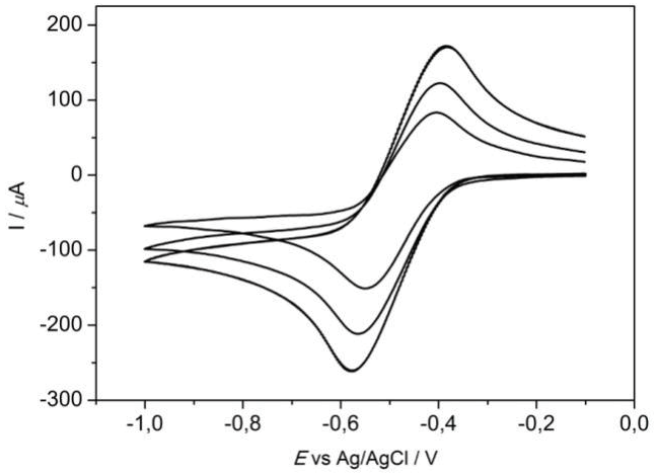

Figure 1.53. Reversible reduction of **50**. Scanning rates going from the curve showing the less intense to the curve with more intense peaks are 0.05, 0.1 and 0.2 V/s respectively.

The HOMO and LUMO energies of all the prepared compounds (Figure 1.54) were calculated according to IP= $-E_{HOMO}$ and EA= $-E_{LUMO}$ in eV. Thus, by adding to the E_{HOMO} value or extracting to the E_{LUMO} value the HOMO-LUMO gap estimated from the absorption spectra, the E_{LUMO} and E_{HOMO} could be calculated respectively.

Mesogens **76**, **78**, **79**, **81** and **90** present similar HOMO and LUMO energy values, the first ones within the [-5.52, -5.35] eV range and the second ones within the [-1.98,-1.82] eV range respectively. However, a slight trend of decrease in the E_{gap} by increasing the number of alkoxyl chains is noticeable. Like in the case of the oxidation potentials, this effect is a result of the higher electron-donor character of the molecules bearing more alkoxyl groups.

The same energy levels were found for the two glassy molecules **48** and **49**, which share the aromatic *N*-phenylcarbazole core with the disk-like mesogens mentioned above, but not for the star shaped compounds bearing tricyanovinyl moieties **50**, **51** and **52**. LUMO energies of this family of compounds were calculated from the onset reduction potentials and have much lower values than

for the alkoxyl systems (~4.1 eV) , due to the strong electron-withdrawing character of the tricyanovinyl groups, as it was already discussed.

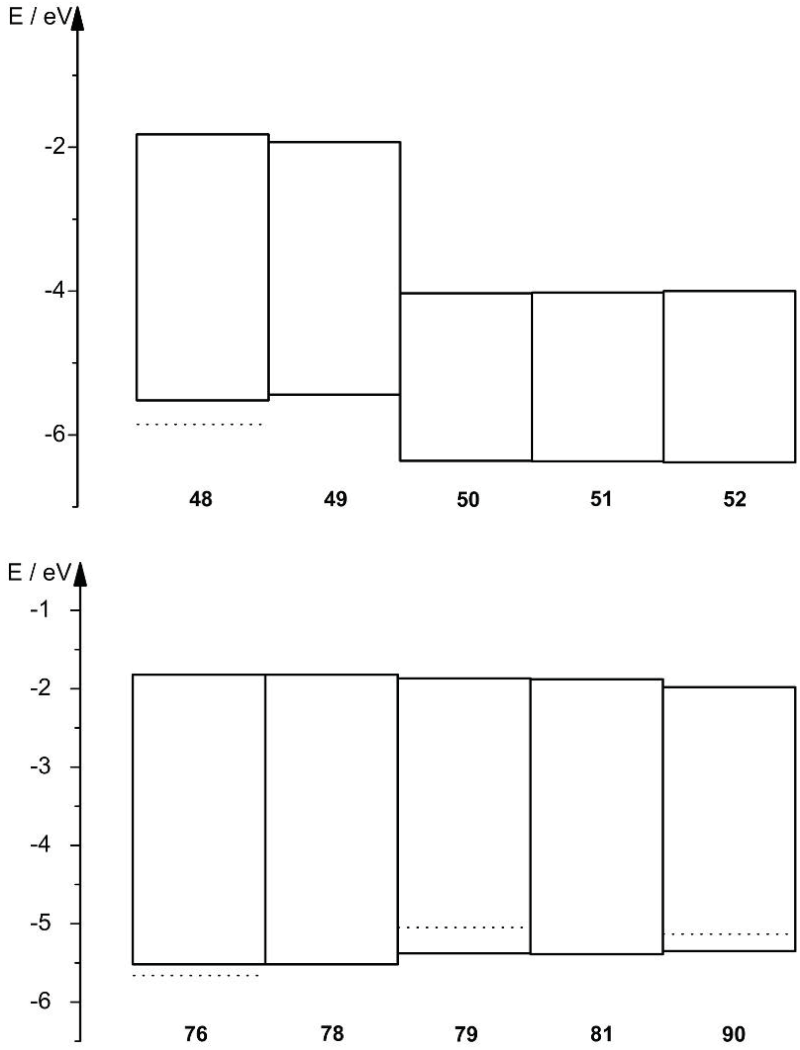

Figure 1.54. Bottoms and tops of the rectangles give the estimated HOMO and LUMO levels for each compound. Dashed lines represent the HOMO levels according to the obtained IP values by electron photoemission.

It is noteworthy that HOMO values of all akoxyl carbazole derivatives are comparable to those shown by many hole-transporting materials with similar aromatic cores in the bibliography, such as the tetraphenyldiphenylamine (TPD), the triphenylamine (TPA) and the naphtylamine (NPA) derivatives,[23] while the LUMOs of the tricyanovinyl substitued carbazole derivatives show lower energies than the usual electron-transporting materials.[23, 25] Thus, from an electrochemical point of view, the synthesized materials seem promising for hole-transporting and electron-transporting applications, in each case.

1.3.5 Summary

The attachment of seven alkoxyl side chains to the *N*-phenylcarbazole core affords the attainment of systems with better characteristics for their application as hole-transporting materials than the attachment of four alkoxyl groups. On the one hand, in the case of molecular glasses -attained by inserting mehtoxy groups in the *N*-phenylcarbazole core- the heptamethoxy derivative **49** presents higher T_g and m.p. than the tetramethoxy derivative **48**, which are favoring mechanical properties for organic electronic devices. On the other hand, presence of only 4 docecyloxy chains in the *N*-phenylcarbazole core leads to lamellar arrangments in mesogens **76**, **77** and **78**, whereas the presence of seven nonyloxy chains sorrounding the aromatic core promotes columnar arrangements at rt. for the discotic mesogen **79**. From an electrochemical point of view, compounds belonging to the seven alkoxyl *N*-phenylcarbazole family **49**, **79** and **81** show slightly lower IP values than their four alkoxyl counterparts **48**, **76** and **78**

Doping of the compounds bearing seven alkoxyl chains **79** and **81** with the proper ratio of electron-acceptor TNF not only stabilizes the Col_{ro} of the starting materials by intermolecular charge transfer but even promotes the formation of Col_{ho} with shorter intercore distances than in the non-doped materials. However, providing these discotic systems with terminal carboxylic acids destabilizes the columnar mesophases, in the case of **81**, and leads to a nematic mesophase for **82**.

The optimal chainlength for the alkyl spacer of the dimeric carbazolic systems to attain columnar arrangement is twelve carbons, compound **90**. The presence of 5 alkoxyl chains in the carbazole fragments confers reversible oxidation at lower potentials than in the previous carbazole derivatives to this compounds due to the better stabilizing effect of the donor chains on the cation radical of the carbazole moiety.

A set of compounds with high electron-affinity values and showing reversible reduction and high stability can be obtained from the 1,3,5-tris(*N*-carbazolyl)benzene by the attachment of tricyanovinyl fragments to its carbazolic moieties. The electron-withdrawing nature of the tricyanovinyl group leads to low reduction potentials and gives rise to an intramolecular charge transfer that provides materials with **50**, **51** and **52** intense light absorption in the visible region of the light spectrum.

Photoluminescence studies revealed that all synthesized carbazole derivatives present emission bands in the UV region with quantum yields (Φ_f) between 0.10-0.20, except for compounds with donor-acceptor (D-A) structure, **50**, **51** and **52**, which show emission bands with $\Phi_f \sim 0.02$ in the visible range.

1.3.6. Experimental section

1.3.6.1. Materials and methods.

^{1}H spectra were recorded in Varian Geminy (300 MHz), Varian Inova (300 MHz), Varian Unity (300 MHz) and Varian Mercury (400 MHz) spectrometers. Signals were noted as singlet (s), doublet (d), triplet (t) and multiplet (m).

Mass spectra were recorded by the Mass spectrometry service at the Chemistry faculty of the Universitat de Barcelona using the techniques: chemical ionization (CI) with a ThermoFinniganTRACE DSQ spectrometer using NH_3 as reagent gas and; electronic impact (EI) and MALDI-TOF with a Voyager-DE RP spectrometer.

UV-vis. absorption spectra were recorded in two Varian spectrometers, models Cary 300-Bio and Cary 500. Emission and excitation spectra were recorded in a PTI fluorimeter equipped with a 220B lamp power supply, an 815 photomultiplier detection system and a Felix 32 software. Quartz cuvettes of 1 cm optical path were used.

Cyclic voltammetries were registerd using an Autolab PGSTAT30 potentiostat-galvanostat. The working electrode was a platinum wire, the contraelectrode was a platinum spiral and the reference electrode was an Ag/AgCl KCl (3 M) electrode. The studied compounds were dissolved in distilled CH_2Cl_2 (~10^{-3} M) with *tert*-buthylamonium perchlorate, TBAP, (~0.1 M) as supporting electrolite at rt.

DSC diagrams were registered by the Thermal Analysis service at the Institut de Química Avançada de Catalunya (IQAC-CSIC) with a Mettler-Toledo DSC821 apparatus.

X-ray diffractograms were registered by the Serveis Cientificotècnics of the Universitat de Barcelona using a CPS-120 Debye-Scherrer diffractometer and a Siemens D-500 diffractometer with a Bragg-Bentano geometry theta/2theta, both apparatus equipped with temperature control devices.

1.3.6.2. Experimental

1.3.6.2.1. 2-nitro-4,4'-dimethoxybiphenyl (47)

To a solution of 2-bromonitroanisole (2.5 g, 10.8 mmol), 4-methoxyphenylboronic acid (1.8 g, 11.1 mmol) and tetrakistriphenylphosphine palladium (0) (127 mg, 0.12 mmol), in benzene (18 ml) was added K_2CO_3 (2 M) (13 ml, 26 mmol), previously purged with N_2. The mixture refluxed (3 h) and poured over ice/water. The aqueous layer was extracted with chloroform. The organic layer was

washed with water, dried over Na_2SO_4 and evaporated to dryness. The residue was chromatographied on silica gel using hexane:AcOEt 4:1 as eluent to give **47** (2.5 g, 89%).

m.p. (POM): 136-137 °C

^{1}H NMR (300 MHz, $CDCl_3$) δ: 7.32 (d, *J* = 8.4 Hz,1H, $H_{(6)}$); 7.32 (d, *J* = 2.7 Hz, 1H, $H_{(3)}$); 7.23-7.19 (m, 2H, $H_{(2',6')}$); 7.13 (dd, *J* = 8.7 Hz, *J* = 2.7 Hz, $H_{(6)}$); 6.96-6.91 (m, 2H, $H_{(3',5')}$); 3.89 (s, 3H, OCH_3); 3.84 (s, 3H, OCH_3) ppm.

1.3.6.2.2. 2,7-dimethoxycarbazole (43)

A suspensión of **47** (2.53 g, 9.7 mmol) in triethylphosphite (10 ml) was heated and kept boiling with reflux for 5 hours. The crude was left to attemperate and **43** (1.68 g, 76%) was collected by filtrating and washing the filtrate with cold methanol.

m.p. (POM): 172-174 °C

^{1}H NMR (300 MHz, DMSO-d_6) δ: 10.92 (s, 1H, NH); 7.83 (d, *J* = 8.7 Hz, 2H, $H_{(4,5)}$); 6.93 (d, *J* = 2.1 Hz, 2H, $H_{(1,8)}$); 6.72 (dd, *J* = 8.4 Hz, *J* = 2.1 Hz, 2H, $H_{(3,6)}$); 3.82 (s, 6H, OCH_3) ppm.

1.3.6.2.3. 2,7-dihydroxycarbazole (54)

43 (1 g, 4.4 mmol) and pyridine hydrochloride (5 g, 44 mmol) were heated at 150 °C (2 h). The system was left to atemperate and the solid crude was dissolved with water and AcOEt. The organic layer was washed with water, dried over $MgSO_4$ and evaporated to dryness to give **54** (870 mg, quantitative). The product was used in next step without further purification.

^{1}H NMR (300 MHz, acetone-d_6) δ: 8.10 (s, 1H, NH); 7.72 (d, *J* = 8.4 Hz, 2H, $H_{(4,5)}$); 6.85 (d, *J* = 2.4 Hz, 2H, $H_{(1,8)}$); 6.67 (dd, *J* = 8.4 Hz, *J* =2.1 Hz, $H_{(3,6)}$) ppm.

1.3.6.2.4. 2,7-dioctadecyloxycarbazole (53)

To a solution of **54** (875 mg, 4.4 mmol) and octadecylbromide (3.7 g, 11 mmol) in anhydrous DMF (8 ml) K_2CO_3 was added until basic pH starting with 3 g. Reaction was kept at 80 °C (18 h) and then left to attemperate. The resulting precipitate was collected by filtration and was digested in methanol to give **53** (1.86 g, 60%).

m.p. (POM): 177-179 °C

^{1}H NMR (300 MHz, $CDCl_3$) δ: 7.83 (d, *J* = 8.4Hz, 2H, $H^{4,5}$); 6.83-6.79 (m, 4H, $H^{1,3,6,8}$); 4.07 (t, *J* = 6.6Hz, 4H, OCH_2); 1.89-1.79 (m, 60H, chain CH_2); 0.88 (q, *J* = 6.3Hz, 6H, CH_3) ppm.

MS (CI): *m/z* = 703.5 (M^+)

1.3.6.2.5. 3-bromo-5-methoxyphenol (67)

To a suspension of NaH in oil (60%) (2.21 g, 55.3 mmol) in anhydrous DMF (30 ml) under N_2 atmosphere at 0 °C EtSH (4.14 ml, 55.3 mmol) was added. The reaction was kept at rt. (1 h) and then a solution of 1-bromo-3,5-dimethoxybenzene (1 g, 4.6 mmol) in anhydrous DMF (5 ml) was canulated. Temperature was raised and the reaction was kept at 150 °C (5 h) and then poured over water. The aqueous layer was neutralised with HCl (2 M) and extracted with AcOEt. The organic layer was washed with abundant water and dried over $MgSO_4$. The solvent was evaporated under vacuum and the resultant crude was chromatographed on silica gel eluating with hexane:AcOEt 7:3 to give compound **67** (872 mg, 93 %).

^{1}H NMR (300 MHz, $CDCl_3$) δ: 6.65 (dd, *J* = 1.5 Hz, *J* = 2.4 Hz, 1H, $H_{(4)}$); 6.61 (dd, *J* = 1.5 Hz, *J* = 2.4 Hz, 1H, $H_{(2)}$); 6.33 (t, *J* = 2.4Hz, 1H, $H_{(6)}$); 4.87 (s, 1H, OH); 3.77 (s, 3H, OCH_3) ppm.

1.3.6.2.6. 1-bromo-5-methoxy-3-octodecyloxybenzene (68)

Using NaH as base

Compound **67** (440 mg, 2,2 mmol) and NaH in oil (60%) (190 mg, 4.8 mmol) were dissolved in anhydrous DMF (10 ml) at 0 °C and under nitrogen atmosphere and the solution was heated at 60 °C for 1 h. Octodecylbromide (1.09 g, 3.3 mmol) in DMF (3 ml) was added and temperature was kept at 60 °C (4.5 h). Reaction was left to attemperate and was poured over ice/water and neutralised with HCl (5%). The aqueous layer was extracted with AcOEt and the organic layer was washed with abundant water and dried over $MgSO_4$. The solvent was evaporated under vacuum and the crude was chromatographied with a flash silica gel column eluating with hexane:AcOEt 9:1 to isolate **68** (711 mg, 72%).

Using K_2CO_3 as base

A suspension of **67** (870 mg, 4.4 mmol), octadecylbromide (2.2 g, 6.6 mmol) and K_2CO_3 (1.2 g, 8.8 mmol) in anhydrous DMF (15 ml) was kept at 100 °C under nitrogen atmosphere (3 h) and then poured over water. The aqueous layer was extracted with CH_2Cl_2 and the organic layer was washed with water and dried over $MgSO_4$. The solvent was evaporated to dryness. Product **68** (1.73 g, 86%) by chromatography of the crude on silica gel eluating with hexane:AcOEt 9:1.

m. p. (POM): 54-56 °C

^{1}H NMR (300 MHz, $CDCl_3$) δ: 6.66-6.64 (m, 2H, $H_{(2,6)}$); 6.37 (t, *J* = 2.1 Hz, 1H, $H_{(4)}$); 3.92 (t, *J* = 6.3 Hz, 2H, $CH_{2(\alpha)}$); 3.76 (s, 3H, OCH_3); 1.80-1.71 (m, 2H, $CH_{2(\beta)}$); 1.48-1.26 (m, 30H, CH_2 x 15), 0.88 (t, *J* = 6.6 Hz, 3H, CH_3) ppm.

1.3.6.2.7. 3-bromo-5-octadecyloxyphenol (70)

To a suspension of NaH in oil (60%) (686 mg, 17.2 mmol) in anhydrous DMF (18 ml) under N_2 atmosphere at 0 °C was added EtSH (1.28 ml, 17.2 mmol). Reaction was kept at rt. (1 h) and then a solution of **67** (625 mg, 1.35 mmol) in anhydrous DMF (20 ml) was added. Reaction was kept overnight at 150 °C and then poured over water. The aqueous layer was neutralised with HCl (2 M) and extracted with AcOEt. The organic layer was washed with abundant water to eliminate DMF and dried over $MgSO_4$. The solvent was evaporated to dryness and the resultant crude was chromatographied in a flash silica-gel column eluating with hexane:AcOEt 7:3 to give compound **70** (500 mg, 83%).

m.p. (POM): 64-66 °C

^{1}H NMR (300 MHz, $CDCl_3$) δ: 6.64 (dd, *J* = 1.8 Hz, *J* = 2.1 Hz, 1H, $H_{(4)}$); 6.58 (dd, *J* = 1.8Hz, *J* = 2.1 Hz, 1H, $H_{(2)}$); 6.32 (t, *J* = 2.1 Hz, 1H, $H_{(6)}$); 4.84 (s, 1H, OH); 3.89 (t, *J* =6.6 Hz, 2H, OCH_2); 1.79-1.70 (m, 2H, $CH_{2(\beta)}$); 1.44-1.26 (m, 30H, CH_2 x 15); 0.88 (t, *J* = 6.6 Hz, 3H, CH_3) ppm

1.3.6.2.8. Methyl 16-hydroxyhexadecanoate (69)

A solution of hexadecanolide (1 g, 3.9 mmol) and *p*-toluensulfonic acid (100 mg, 0.58 mmol) in methanol (15 ml) was refluxed overnight. The solvent was removed under vacuum and the crude was dissolved in dichloromethane and washed with saturated $NaHCO_3$ (aq) and water. The organic layer dried over $MgSO_4$ and evaporated to dryness to give the methyl ester **69** (1.11 g, quantitative)

m.p. (POM): 53-55 °C

^{1}H NMR (300 MHz, $CDCl_3$) δ: 3.67 (s, 3H, CH_3), 3.64 (t, *J* = 6.6 Hz, 2H, $HOCH_2$), 2.30 (t, *J* = 7.5 Hz, 2H, CH_2COO), 1.64-1.26 (m, 26H, CH_2 x 13) ppm.

1.3.6.2.9. Methyl 16-(3-bromo-5-octadecyloxyphenoxy)-hexadecanoate (71)

A solution of phenol **70** (1.2 g, 2.80 mmol) and triphenylphosphine (808 mg, 3.08 mmol) in THF (15 ml) was stirred at rt. (40 min.) under N_2 atmosphere. Methyl 16-hydroxyhexadecanoate (**69**) (962 mg, 3.36 mmol) and DIPAD (0.66 ml, 3.36 mmol) in THF (8 ml) were then added. After 48 h of reaction at rt., the solvent was removed under vacuum and the residue was chromatographied on silica gel using hexane:AcOEt 95:5 to give **71** (1.7 g, 85%).

m. p. (POM): 58-60 °C

^{1}H NMR (300 MHz, $CDCl_3$) δ: 6.63 (d, *J* = 2.4 Hz, 2H, $H_{(2,4)}$); 6.36 (t, *J* = 2.4 Hz, 1H, $H_{(6)}$); 3.89 (t, *J* = 6.6 Hz, 4H, OCH_2); 3.66 (s, 3H, $COOCH_3$); 2.30 (t, *J* = 7.5 Hz, 2H, CH_2COO); 1.79-1.70 (m, 4H, OCH_2CH_2); 1.66-1.57 (m, 2H, CH_2CH_2COO); 1.47-1.26 (m, 52H, CH_2 x 26); 0.88 (t, *J* = 6.6 Hz, 3H, CH_3) ppm.

1.3.6.2.10. Methyl 16-(3-(2,7-dioctadecyloxy-9-carbazolyl)-5-octadecyloxyphenyloxy)(oxy) hexadecanoate (77).

A suspension of *N*H-carbazole **53** (500 mg, 0.71 mmol), **71** (1.5g, 2.13mmol), anhydrous K_2CO_3 (500 mg, 3.62 mmol) and copper powder (45 mg, 0.71 mmol) in anhydrous DMA (4 ml) was refluxed at (24 h) under N_2 atmosphere. The reaction was poured over water and the aqueous layer was extracted with CH_2Cl_2. The combined organic layer was washed with abundant water and dried over $MgSO_4$. The solvent was removed under vacuum and compound **77** (750 mg, 80%) was isolated by silica-gel column chromatography of the crude using hexane:CH_2Cl_2 7:3 as eluent.

m. p. (DSC): 73 °C

^{1}H NMR (300 MHz, $CDCl_3$) δ: 7.85 (d, *J* = 8.4 Hz, 2H, $H_{(4,5)}$ cz); 6.86 (d, *J* = 2.1 Hz, 2H, $H_{(1,8)}$ cz); 6.84 (dd, *J* = 8.4Hz, *J* = 2.1 Hz, 2H, $H_{(3,6)}$ cz); 6.64 (d, *J* = 2.4 Hz, 2H, $CH_{(2,6)}$ ph); 6.55 (t, *J* = 2.4 Hz, 1H, $CH_{(4)}$ ph); 3.99-3.94 (m, 8H, OCH_2); 3.66 (s, 3H, $COOCH_3$); 2.29 (t, 2H, *J* = 7.5 Hz, CH_2COO); 1.82-1.74 (m, 8H, OCH_2CH_2); 1.66-1.57 (m, 2H, CH_2CH_2COO); 1.50-1-26 (m, 112H, CH_2 x 56); 0.88 (t, 6.6 Hz, 9H, CH_3 x 3) ppm

MS (MALDI-TOF): *m/z* = 1332.3 (M^+)

1.3.6.2.11. 16-[3-(2,7-dioctadecyloxy-9-carbazolyl)-5-octadecyloxyphenyloxy](oxy)hexadecanoic acid (78)

To a suspension of NaH in oil (60%) (216 mg, 5.4 mmol) in anhydrous DMF (20 ml) under N_2 atmosphere at 0 °C EtSH (0.40 ml, 5.4 mmol) was added. After 2 h of reaction at rt. a solution of **77** (600 mg, 0.45 mmol) in anhydrous THF (14 ml) was added. Reaction was kept overnight at 100 °C, cooled down to rt. and poured over water. The aqueous layer was neutralised with HCl (2 M), extracted with $CHCl_3$ and the organic layer was washed with abundant water and dried over $MgSO_4$. The solvent was removed under vacuum and the resultant crude was chromatographied on silica gel eluating with hexane:AcOEt 9:1 to isolate compound **78** (507 mg, 85%).

m. p. (DSC): 82 °C

^{1}H NMR (300 MHz, $CDCl_3$) δ: 7.85 (d, *J* = 8.1 Hz, 2H, $CH_{(4,5)}$ cz); 6.86 (d, *J* = 2.1 Hz, 2H, $CH_{(1,8)}$ cz); 6.84 (dd, *J* = 8.4Hz, *J* = 2.1Hz, 2H, $CH_{(3,6)}$ cz); 6.64 (d, *J* = 2.4 Hz, 2H, $CH_{(2,6)}$ ph); 6.55 (t, *J* = 2.4 Hz, 1H, $CH_{(4)}$

ph); 3.99-3.94 (m, 8H, OCH_2); 2.34 (t, 2H, *J* = 7.5 Hz, CH_2COO); 1.84-1.73 (m, 8H, OCH_2CH_2); 1.67-1.26 (m, 114H, CH_2 x 57); 0.88 (t, *J* = 6.6 Hz, 9H, CH_3 x 3) ppm

^{13}C NMR (400 MHz, $CDCl_3$) δ: 178.79, 161.41, 157.95, 142.43, 139.39, 120.14, 117.48, 108.77, 105.78, 95.56, 68.74, 68.61, 68.18, 34.07, 32.16, 29.92, 29.92, 29.90, 29.88, 29.86, 29.84, 29.83, 29.70, 29.68, 29.66, 29.60, 29.58, 29.47, 29.44, 29.31, 29.16, 26.36, 26.29, 24.94, 22.92, 14.36 ppm.

UV (CH_2Cl_2) λ_{max}/nm (ε/dm^3 mol^{-1} cm^{-1}): 322 (13200), 314 (12800), 286 (sh) (9260), 255 (31800).

MS (MALDI-TOF): *m/z* = 1319.1 (M^+)

1.3.6.2.12. 2,7-dimethoxy-9-(3,5-dimethoxyphenyl)carbazole (48)

A suspension of **43** (840 mg, 3.7 mmol), 1-bromo-3,5-dimethoxybenzene (1.6 g, 7.4 mmol), anhydrous K_2CO_3 (5 g, 37 mmol) and copper powder (233 mg, 3.7 mmol) in anhydrous DMA (7 ml) was heated at boiling temperature under nitrogen atmosphere. After 24 h the reaction was left to attemperate and poured over water. Aqueous layer was extracted with CH_2Cl_2 and the combined organic layer was washed with abundant water and dried over $MgSO_4$. The solvent was removed under vacuum and the product (1.25 g, 93%) and the residue was chromatographied on silica gel using a mixture of hexane:CH_2Cl_2 increasing polarity from 7:3 to 9:1 as eluent.

m. p. (DSC): 114 °C

^1H NMR (300 MHz, $CDCl_3$) δ: 7.88 (d, *J* = 6.3 Hz, 2H, $CH_{(4,5)}$ cz); 6.89 (d, *J* =1.5 Hz, 2H, $CH_{(1,8)}$ cz); 6.86 (dd, *J* = 6.3 Hz, *J* = 1.8 Hz, 2H, $CH_{(3,6)}$ cz); 6.69 (d, *J* =1.8 Hz, 2H, $CH_{(2,6)}$ ph); 6.57 (t, *J* = 1.8 Hz, 1H, $CH_{(4)}$ ph); 3.85 (s, 12H, CH_3 x 4) ppm

UV (CH_2Cl_2) λ_{max}/nm (ε/dm^3 mol^{-1} cm^{-1}): 322 (14000), 312 (13970), 286 (sh) (10900), 255 (35400).

1.3.6.2.13. General procedure for the cleavage of methoxy groups in bromopolymethoxybenzenes with BBr_3

BBr_3 in CH_2Cl_2 (1M) was added slowly to the suitable bromopolymethoxybenzene under nitrogen atmosphere at -78 °C. After 24 -48 h of stirring at rt. the solution was poured over ice/water. The aqueous layer was extracted with AcOEt and the organic layer was washed with abundant water, dried over $MgSO_4$and evaporated to dryness to give the corresponding bromohydroxyphenol in quantitative yield. The phenol was used in next step without further purification.

1.3.6.2.13.1. 4-bromo-2-hydroxyphenol (56)

Starting materials: 1-bromo-3,4-dimethoxybenzene (2.07g, 9.5mmol), BBr_3 (57 ml, 57 mmol)

Reaction time: 6 h.

^{1}H NMR (300 MHz, $CDCl_3$) δ: 6.86 (d, *J* =2.4 Hz, 1H, $H_{(3)}$); 6.73 (dd, *J* = 8.4 Hz, *J* = 2.4 Hz, 1H, $CH_{(5)}$), 6.65 (d, *J* = 8.4Hz, 1H, $H_{(6)}$) ppm.

1.3.6.2.13.2. 5-bromo-3-hydroxyphenol (65)

Starting materials: 1-bromo-3,5-dimethoxybenzene (1.73 g, 7.97 mmol), BBr_3 (24 ml, 24 mmol)

Reaction time: 24 h.

^{1}H NMR (300 MHz, $CDCl_3$) δ: 8.60 (s, 2H, OH); 6.53 (d, *J* = 2.1 Hz, 2H, $H_{(4,6)}$); 6.34 (t, *J* = 2.1 Hz, 1H, $H_{(2)}$) ppm.

1.3.6.2.13.3. 5-bromo-2,3-dihydroxyphenol (66)

Starting materials: 1-bromo-3,4,5-trimethoxybenzene (1.5 g, 6.1 mmol), BBr_3 (24 ml, 24 mmol)

Reaction time: 24 h.

^{1}H NMR (300 MHz, acetone-d_6) δ: 8.22-8.21 (m, 2H, $H_{(4,6)}$); 7.49 (s, 1H, $OH_{(p)}$), 6.56 (s, 2H, $OH_{(m)}$)ppm.

1.3.6.2.14. General procedure for the alkylation of bromohydroxyphenols

A solution of the suitable phenol and alkylbromide in anhydrous DMF (15 ml) was stirred overnight at 80 °C in the presence of K_2CO_3 under nitrogen atmosphere and then left to attemperate, poured over water and extracted with CH_2Cl_2. The organic layer was washed with water and dried over $MgSO_4$ and solvent was evaporated until dryness. The final product was obtained by silica gel column chromatography of the crude.

1.3.6.2.14.1. 1-bromo-3,4-dinonyloxybenzene (57)

Starting materials: **56** (1.80 g, 9.5 mmol), K_2CO_3 (3.93 g, 28.5 mmol), nonylbromide (4.5 ml, 23.8 mmol), DMF (15 ml)

η = 72%

m. p. (POM): 34-36 °C

^{1}H NMR (300 MHz, $CDCl_3$) δ: 6.98 (dd, *J* = 9.0 Hz, *J* = 2.1 Hz, 1H, $H_{(6)}$); 6.97 (dd, *J* = 2.1 Hz, 1H, $H_{(2)}$); 6.74 (d, *J* = 9 Hz, 1H, $H_{(5)}$); 3.96 (t, *J* = 6.6 Hz, 2H, OCH_2); 3.95 (t, *J* = 6.6 Hz, 2H, OCH_2); 1.85-1.81 (m, 4H, OCH_2CH_2); 1.48-1.26 (m, 24H, CH_2 x 12); 0.88 (t, *J* = 6.6 Hz, 6H, CH_3 x 2) ppm

1.3.6.2.14.2. 1-bromo-3,5-dioctadecyloxybenzene (62)

Starting materials: **65** (530 mg; 2.8 mmol), octadecylbromide (2.3 mg; 7.0 mmol), K_2CO_3 (1.2 g, 8.8 mmol), DMF (15 ml).

Eluent: hexane/AcOEt (9:1)

η = 75%

m. p. (POM): 59-61 °C

^{1}H NMR (300 MHz, $CDCl_3$) δ: 6.63 (d, *J* = 2.1 Hz, 2H, $H_{(2,6)}$); 6.36 (t, *J* = 2.1 Hz, 1H, $H_{(4)}$); 3.89 (t, *J* = 6.6 Hz, 4H, OCH_2 x 2); 1.75 (m, *J* = 6.6 Hz, 4H, OCH_2CH_2 x 2); 1.48-1.26 (m, 60H, CH_2 x 30); 0.88 (t, *J* =6.6 Hz, 6H, CH_3 x 2) ppm.

1.3.6.2.14.3. 1-bromo-3,4,5-trinonyloxybenzene (63)

Starting materials: **66** (680 mg, 2.72 mmol), nonylbromide (1.82 ml, 9.52 mmol), K_2CO_3 (1.5 g, 10.88 mmol), DMF (10 ml)

η = 50%

^{1}H NMR (300 MHz, $CDCl_3$) δ: 6.67 (s, 2H, $H_{(2,6)}$); 3.95-3.88 (m, 6H, OCH_2); 1.83-1.66 (m, 6H, OCH_2CH_2); 1.50-1.28 (m, 36H, CH_2 x 18); 0.88 (t, *J* = 6.6 Hz, 9H, CH_3 x 3) ppm

1.3.6.2.14.4. Trimethyl 10,10',10''-(5-bromobenzene-1,2,3-triyl)tris(oxy)tris(decanoate) (64)

Starting materials: **66** (222 mg, 1.09 mmol), methyl 10-bromodecanoate (1 g, 3.8 mmol), K_2CO_3 (602 mg, 4.4 mmol), DMF (15 ml)

η = 90%

^{1}H NMR (300 MHz, $CDCl_3$) δ: 6.67 (s, 2H, $H_{(2,6)}$); 3.95-3.88 (m, 6H, OCH_2); 1.83-1.66 (m, 6H, OCH_2CH_2); 1.50-1.28 (m, 36H, CH_2 x 18); 0.88 (t, *J* = 6.6 Hz, 9H, CH_3 x 3) ppm

1.3.6.2.14.5. 1-bromo-3,4-dioctyloxybenzene (84)

Starting materials: **56** (1.80 g, 9.5 mmol), K_2CO_3 (3.93 g, 28.5 mmol), octylbromide (4.92 ml, 28.5 mmol), DMF (15 ml)

η = 90%

^{1}H NMR (300MHz, $CDCl_3$) δ: 6.98 (dd, *J* =9.0Hz, *J* =2.1Hz, 1H, H^6); 6.97 (dd, *J* =2.1Hz, 1H, H^2); 6.74 (d, *J* = 9Hz, 1H, H^5); 3.96 (t, *J* = 6.6Hz, 2H, OCH_2); 3.95 (t, *J* = 6.6Hz, 2H, OCH_2); 1.85-1.81 (m, 4H, OCH_2CH_2); 1.48-1.26 (m, 20H, chain CH_2); 0.88 (t, *J* =6.6Hz, CH_3) ppm

1.3.6.2.14.6. 1-bromo-3,4,5-trioctyloxybenzene (85)

Starting materials: **66** (1.34 g, 6.54 mmol), octylbromide (4.5 ml, 26 mmol), K_2CO_3 (3.6 g, 26 mmol), DMF (17 ml).

η = 89%

^{1}H NMR (300 MHz, $CDCl_3$) δ: 6.67 (s, 2H, $H_{(2,6)}$); 3.95-3.88 (m, 6H, OCH_2 x 3); 1.83-1.66 (m, 6H, OCH_2CH_2 x 3); 1.50-1.28 (m, 30H, CH_2 x 15); 0.88 (t, *J* = 6.6 Hz, 9H, CH_3 x 3) ppm

1.3.6.2.15. 2,7-dioctadecyloxy-9-(3,5-dioctadecyloxyphenyl)carbazole (76)

*N*H-carbazole **53** (665 mg, 0.94 mmol), **62** (1.5 g, 2.1 mmol), anhydrous K_2CO_3 (1.3 mg, 9.4 mmol) and copper powder (56 mg, 0.94 mmol) in anhydrous DMA (5 ml) were stirred at boiling temperature for 24 h under nitrogen atmosphere. The reaction was left to attemperate and poured over water. The aqueous layer was extracted with CH_2Cl_2 and combined organic layer was washed with abundant water and dried over $MgSO_4$. The solvent was removed under vacuum the target product **76** (740 mg, 60%) was obtained by silica gel column chromatrography of the residue using hexane/CH_2Cl_2 8:2 as eluent.

m. p. (POM): 74-76 °C

^{1}H NMR (300 MHz, $CDCl_3$) δ: 7.86 (d, *J* = 8.1 Hz, 2H, $H_{(4,5)}$ cz); 6.87 (d, *J* = 2.1 Hz, 2H, $H_{(1,8)}$ cz); 6.84 (dd, *J* = 8.4 Hz, *J* = 2.1 Hz, 2H, $H_{(3,6)}$ cz); 6.65 (d, *J* = 2.1 Hz, 2H, $H_{(2,6)}$ ph); 6.56 (t, *J* = 2.4 Hz, 1H, $H_{(4)}$ ph); 3.99-3.94 (m, 8H, OCH_2 x 4); 1.84-1.73 (m, 8H, OCH_2CH_2 x 4); 1.67-1.26 (m, 120H, CH_2 x 60); 0.88 (t, *J* = 6.6 Hz, 12H, CH_3 x 4) ppm

UV (CH_2Cl_2) λ_{max}/nm (ε/dm^3 mol^{-1} cm^{-1}): 322 (16000), 314 (15700), 286 (sh) (11700), 255 (38370).

1.3.6.2.16. General procedure for the nitration of 3,4-dialkoxybromobenzenes

To a suspension of the 3,4-dialkyloxybromobenzene in acetic acid at rt. was added nitric acid. Afte 30 min. of reflux the reaction was left to attemperate, poured over water and extracted with AcOEt. The organic layer was washed subsequently with water, saturated. $NaHCO_3$ (aq) and water and dried over $MgSO_4$. The solvent was removed under vacuum and the corresponding nitrocompound was obtained in quantitative yield.

1.3.6.2.16.1. 2-bromo-1-nitro-4,5-dimethoxybenzene (42)

Starting materials: 3,4-dimethoxy-1-bromobenzene (2 g, 9.2 mmol), AcOH (10 ml), HNO_3 (3.5 ml, 46.0 mmol).

m. p. (POM): 120-124 °C

^{1}H NMR (300 MHz, $CDCl_3$) δ: 7.58 (s, 1H, $H_{(6)}$); 7.09 (s, 1H, $H_{(3)}$), 3.97 (s, 3H, OCH_3), 3.94 (s, 3H, OCH_3) ppm.

1.3.6.2.16.2. 2-bromo-1-nitro-4,5-dinonyloxybenzene (58)

Starting materials: **57** (1 g, 4.2 mmol), AcOH (8 ml), HNO_3 (0.87 ml, 11.3 mmol)

m. p. (POM): 40-42 °C

^{1}H NMR (300 MHz, $CDCl_3$) δ: 7.55 (s, 1H, $H_{(6)}$); 7.08 (s, 1H, $H_{(3)}$); 4.05 (t, 2H, OCH_2 *p*-NO_2); 4.03 (t, 2H, OCH_2 *m*-NO_2); 1.88-1.81 (m, 4H, OCH_2CH_2); 1.60-1.26 (m, 24H, CH_2 x 12), 0.88 (t, *J* = 6.6 Hz, 6H CH_3 x 2) ppm

1.3.6.2.16.3. 2-bromo-1-nitro-4,5-dioctyloxybenzene (86)

Starting materials: **84** (1.8 g, 4.4 mmol), AcOH (10ml), HNO_3 (1.7 ml, 22.2 mmol)

m. p. (POM): 33-35 °C

^{1}H NMR (300 MHz, $CDCl_3$) δ: 7.55 (s, 1H, $H_{(6)}$); 7.80 (s, 1H, $H_{(3)}$); 4.05 (t, *J* = 6.6 Hz, 2H, OCH_2 *p*-NO_2); 4.03 (t, 2H, OCH_2 *m*-NO_2); 1.88-1.81 (m, 4H, OCH_2CH_2); 1.60-1.26 (m, 20H, CH_2 x 10), 0.88 (t, *J* = 6.6 Hz, CH_3) ppm

1.3.6.2.17. 3,4-dinonyloxyphenylboronic acid (59)

To a solution of **57** (3 g, 6.8 mmol) in anhydrous THF (18 ml) under nitrogen atmosphere was added n-BuLi in CH_2Cl_2 (1.6 M) (7.2 ml, 11.6 mmol) dropwise at -60 °C. After 1.5 h of stirring -60 °C $B(OMe)_3$ (1.9 ml, 17 mmol) was added. The reaction was allowed to attemperate and left stirring overnight. The resulting suspension was poured into saturated NH_4Cl (aq), extracted with CH_2Cl_2 and dried over $MgSO_4$. The solvent was evaporated to dryness and the resulting crude was kept colf and under inert atmosphere and used in next step without further purification.

1.3.6.2.18. 3',4,4',5-tetraalkyloxy-2-nitrobiphenyl general procedure

The suitable phenylboronic acid nitrocompound and catalyst tetrakis(triphenylphosphine)palladium under N_2 atmosphere were dissolved in THF previously flushed with nitrogen. K_2CO_3 (1M) flushed with nitrogen was added and the reaction was heated to boiling temperature and stirred overnight. THF was evaporated and the resulting crude was dissolved in dichloromethane, washed with water and dried over $MgSO_4$. The product was isolated by silica gel column chromatography of the crude.

1.3.6.2.18.1. 3',4,4',5-tetramethoxy-2-nitrobiphenyl (44)

Starting materials: 3,4-dimethoxyphenylboronic acid (1.5 g, 9.9 mmol), **42** (2.3 g, 8.8 mmol), $[Pd(PPh_3)_4]$ (224 mg, 0.19 mmol), K_2CO_3 (26.4 ml, 26.4 mmol), THF (40 ml)

Eluent: CH_2Cl_2

η = 79%

^{1}H NMR (300 MHz, $CDCl_3$) δ: 7.51 (s, 1H, $H_{(3)}$); 6.92 (d, *J* = 6 Hz, 1H, $H_{(5')}$); 6.86 (dd, *J* = 6 Hz, *J* = 1.5 Hz, 1H, $H_{(6')}$), 6.95 (s, 1H, $H_{(6)}$), 6.97 (d, *J* =1.5 Hz, 1H, $H_{(2')}$), 3.98 (s, 3H, OCH_3), 3.96 (s, 3H, OCH_3), 3.92 (s, 3H, OCH_3), 3.88 (s, 3H, OCH_3) ppm

1.3.6.2.18.2. 2-nitro-3',4,4',5-tetranonyloxybiphenyl (60)

Starting materials: **59** (2.76 g, 6.8 mmol), **58** (2.45 g, 5.0 mmol), [$Pd(PPh_3)_4$] (350 mg, 0.34 mmol), K_2CO_3 (13.6 ml, 13.6 mmol), THF (30 ml).

Eluent: hexane/CH_2Cl_2 (7:3)

η = 73%

m. p. (POM): 94-95 °C

^{1}H NMR (300 MHz, $CDCl_3$) δ: 7.47 (s, 1H, $H_{(3)}$); 6.89 (d, *J* = 8.7 Hz, 1H, $H_{(5')}$); 6.81-6.76 (m, 3H, $H_{(2',4,6')}$); 4.08-3.95 (m, 8H, OCH_2 x 4); 1.90-1.75 (m, 8H, OCH_2CH_2 x 4); 1.50-1.29 (m, 48H, CH_2 x 24) ppm.

1.3.6.2.19. 2,3,6,7-tetramethoxycarbazole (45)

44 (2.2 g, 6.89 mmol) and $P(OEt)_3$ (6.6 ml, 38.3 mmol) were heated to boiling temperature of the phosphite (6 h). The reaction was left to cool down to rt. and the resulting precipitate was filtered and washed with methanol. The mother liquor was treated with HCl (2 M) and extracted with $CHCl_3$. The chloroform layer was washed with water, dried over $MgSO_4$ and the solvent was removed under vacuum evaporation. The precipitate and the crude from the extractions were combined and chromatographied in a silica gel column using CH_2Cl_2/AcOEt (4:1) to obtain the symmetric carbazole **45** (555 mg, 28%).

m. p. (POM): 213-215 °C

^{1}H NMR (300 MHz, DMSO-d_6) δ: 10.61 (s, 1H, NH); 7.55 (s, 2H, $H_{(4,5)}$); 6.97 (s, 2H, $H_{(1,8)}$); 3.82 (s, 12H, OCH_3) ppm.

1.3.6.2.20. 2,3,6,7-tetranonyloxycarbazole (55)

60 (2.8 g, 3.60 mmol) and $P(OEt)_3$ (6.0 ml, 36 mmol) were heated to boiling temperature of the phosphite for 6 h. The reaction was left to cool down to rt. and was treated with HCl (2 M) and extracted with $CHCl_3$. The chloroform layer was washed with water, dried over $MgSO_4$ and the solvent was removed under vacuum. The crude was chromatographied in a silica-gel column eluating with hexane/CH_2Cl_2 going from 6:4 to 7:3 to give *N*H-carbazole **60** (1.01 g, 38%)

m. p. (POM): 70-72 °C

^{1}H NMR (300 MHz, CDCl3) δ: 7.64 (s, 1H, NH), 7.41 (s, 2H, H(4,5)), 6.84 (s, 2H, H(1,8)), 4.08-4.02 (m, 8H, OCH_2 x 4), 1.93-1.75 (m, 8H, OCH_2CH_2 x 4), 1.54-1.10 (m, 48H, CH_2 x 24), 0.88 (t, *J* = 6.6 Hz, 12H, CH_3 x4) ppm.

MS(CI): *m/z* = 734.9 (M^+-1)

1.3.6.2.21. 6-bromo-2,2-dimethyl-1,3-benzodioxol-4-ol (73)

A solution of hydroxyphenol **66** (1.87 g, 9.12 mmol) in toluene (25 ml) containing P_2O_5 (1.55 mg, 10.94 mmol) was heated to 75 °C under nitrogen atmosphere. Acetone (1.34 ml, 18.24 mmol) was added and after 2 h of reaction it was left to attemperate and decantated. The organic layer was washed with NaOH (aq). The aqueous layer was then carefully neutralised with HCl (2 M) and extracted with AcOEt. The organic layer was dried over $MgSO_4$ and the solvent was removed under vacuum to give acetal **73** (1.28 g, 57%).

^{1}H NMR (300 MHz, $CDCl_3$) δ: 6.63 (d, *J* =1.8 Hz, 1H, $H_{(7)}$); 6.53 (d, *J* = 1.8 Hz, 1H, $H_{(5)}$); 1.68 (s, 6H, CH_3 x 2) ppm.

1.3.6.2.22. 5-bromo-7-(10-methoxycarboxydecyloxy)-2,2-dimethyl-1,3-benzodioxole (74)

A solution of acetal **73** (1.20 g, 4.9 mmol), K_2CO_3 (1.46 g, 10.6 mmol) and methyl 10-bromohexadecanoate (1.6 g, 5.9 mmol) in anhydrous DMF (15 ml) was stirred at 90 °C. After 3 h the reaction was left to cool down to rt., poured over water and extracted with Et_2O. The organic layer was washed with sat. NaCl, dried over $MgSO_4$ and the solvent was evaporated to dryness. The resulting crude was chromatographied on neutralised silica gel using hexane/AcOEt 9:1 as eluent to give **74** (1.85 g, 88%).

m.p. (POM): 117-121 °C

^{1}H NMR (300 MHz, $CDCl_3$): 6.62 (d, *J* = 1.8 Hz, 1H, H *o*-Br); 6.57 (d, *J*= 1.8 Hz, 1H, *o*-Br); 4.01 (t, *J* = 6.6 Hz, 2H, OCH_2); 3.67 (s, 3H, $COOCH_3$); 2.30 (t, *J* = 7.2 Hz, 2H, CH_2COO); 1.82-1.71 (m, OCH_2CH_2); 1.68 (s, 6H, CH_3); 1.64-1.59 (m, 2H, CH_2CH_2COO); 1.49-1.30 (m, 10H, CH_2 x 5) ppm.

1.3.6.2.23. Methyl 10-(5-bromo-2,3-dihydroxyphenoxy)decanoate (75)

Compound **74** (1.78 g, 4.16 mmol) was dissolved in a mixture of AcOH/H_2O/HCl(6M) 20:7:2.5 and heated to boiling temperature. After 2 h of stirring the reaction was left to attemperate, and the solvent mixture was removed under vacuum. The crude was dissolved in Et_2O, washed with abundant water, dried over $MgSO_4$. Evaporation of the organic solvent gives 10-(5-bromo-2,3-

dihydroxyphenoxy)decanoic acid (1.38 g, 89 %). The acid was dissolved in MeOH (35 ml) in the presence of p-TsOH (150 mg) and heated to boiling temperature for 1 h. The solvent was removed under vacuum and the crude was dissolved in chloroform and washed with water. The organic layer was dried over $MgSO_4$ and evaporated to dryness to give compound 75 in quantitative yield.

10-(5-bromo-2,3-dihydroxyphenoxy)decanoic acid

^{1}H NMR (300 MHz, $CDCl_3$) δ: 6.65 (s, 2H, $H_{(4,5)}$); 4.01 (t, *J* = 6.6 Hz, 2H, OCH_2); 2.28 (t, *J* = 7.5 Hz, 3H, CH_2COO); 1.81-1.72 (m, 2H, OCH_2CH_2); 1.64-1.34 (m, 12H, CH_2 x 6) ppm

Methyl 10-(5-bromo-2,3-dihydroxyphenoxy)decanoate (75)

^{1}H NMR (300 MHz, $CDCl_3$) δ: 6.65 (s, 2H, $H_{(4,5)}$); 4.02 (t, *J* = 6.6 Hz, 2H, OCH_2); 3.60 (s, 3H, $COOCH_3$); 2.28 (t, *J* = 7.5 Hz, 3H, CH_2COO); 1.81-1.72 (m, 2H, OCH_2CH_2); 1.64-1.33 (m, 12H, CH_2 x 6) ppm

1.3.6.2.24. Methyl 10-(5-bromo-2,3-dinonoxyphenoxy)decanoate (72)

A solution of **75** (1.30 g, 3.46 mmol), anhydrous K_2CO_3 (1.43 g, 10.38 mmol) and nonylbromide (1.66 ml, 8.66 mmol) in anhydrous DMF (17 ml) was stirred overnight at 60 °C under nitrogen atmosphere. Reaction was left to attemperate, poured over water and extracted with AcOEt. The organic layer was washed with sat. NaCl and dried over $MgSO_4$. The solvent was evaporated to dryness and the crude was chromatographied on silica gel to isolate **72** (1.52 g, 68%) using hexane/CH_2Cl_2 (from 7:3 to 2:8) as eluent.

^{1}H NMR (300 MHz, $CDCl_3$) δ: 6.67 (s, 2H, $H_{(4,5)}$); 3.95-3.88 (m, 6H, OCH_2); 2.30 (t, *J* = 7.5 Hz, 2H, CH_2COO); 1.81-1.28 (m, 42H, CH_2 x 21); 0.88 (t, *J* = 6.6 Hz, 6H, CH_3 x 2) ppm

1.3.6.2.25. General procedure for the coupling of 2,3,6,7-tetraalkoxy-*N*H-carbazoles and 3,4,5-trialkoxybromobenzenes.

A suspension of 2,3,6,7-tetraalkoxy-*N*H-carbazole, 3,4,5-trialkoxybenzene, anhydrous K_2CO_3 and copper powder in anhydrous DMA was refluxed (48 h) under nitrogen atmosphere. Reaction was left to attemperate and poured over water. Aqueous layer was extracted with $CHCl_3$. The organic layer was washed with abundant water and dried over $MgSO_4$. The solvent was removed under vacuum and the product was purified by silica gel column chromatrography.

1.3.6.2.25.1. 2,3,6,7-tetramethoxy-9-(3,4,5-trimethoxyphenyl)carbazole (49)

Starting materials: **45** (362 mg, 1.26 mmol), 1-bromo-3,4,5-trimethoxybenzene (778 mg, 3.15 mmol), K_2CO_3 (1.74 g, 12.6 mmol), copper powder (80 mg, 1.27 mmol), DMA (3 ml)

Eluent: CH_2Cl_2/AcOEt from 95:5 to 9:1

η = 65%

^{1}H NMR (300 MHz, $CDCl_3$) δ: 7.47 (s, 2H, $H_{(4,5)}$ cz); 6.90 (s, 2H, $H_{(1,8)}$ cz); 6.76 (s, 2H, $H_{(2,6)}$ ph), 4.03 (s, 6H, OCH_3 x 2); 3.99 (s, 3H, OCH_3); 3.88 (s, 12H, OCH_3 x 4) ppm

UV (CH_2Cl_2) λ_{max}/nm (ε/dm^3 mol^{-1} cm^{-1}): 322 (20200), 296 (13840), 262 (23500)

1.3.6.2.25.2. 2,3,6,7-tetranonyloxy-9-(3,4,5-trinonyloxyphenyl)carbazole (79)

Starting materials: **55** (400 mg, 0.54 mmol), **63** (800 mg, 1.37 mmol), K_2CO_3 (745 g, 5.4 mmol), Cu (34 mg, 63 mmol), DMA (3 ml)

Eluent: hexane/AcOEt 95:5

η = 81%

m. p. (DSC): 159 °C

MS (MALDI-TOF): *m/z* = 1238.2 (M^+)

^{1}H NMR (400 MHz, $CDCl_3$) δ: 7.46 (s, 2H, $H_{(4,5)}$ cz); 6.88 (s, 2H, $H_{(1,8)}$ cz); 6.68 (s, 2H, $H_{(2,6)}$ ph), 4.10-4.06 (m, 6H, OCH_2 x 3); 3.95 (t, *J*= 6.4 Hz, 8H, OCH_2 x 4); 1.90-1.78 (m, 14H, OCH_2CH_2); 1.55-1.28 (m, 84H, CH_2 x 42); 0.90-0.86 (m, 21H, CH_3 x 7) ppm

UV (CH_2Cl_2) λ_{max}/nm (ε/dm^3 mol^{-1} cm^{-1}): 322 (20200), 295 (sh) (13500), 262 (23500)

1.3.6.2.25.3. Methyl 10-[2,3-dinonyloxy-5-(2,3,6,7-tetranonyloxy-9-carbazolyl)]decanoate (80)

Starting materials: **55** (510 mg, 0.69 mmol), **72** (1.08 mg, 1.68 mmol), K_2CO_3: (475 g, 3.5 mmol), Cu (44 mg, 0.7 mmol), DMA (3 ml)

Eluent: hexane/Et_2O from 95:5 to 90:10

η = 58%

m. p. (DSC): 16 °C

MS (MALDI-TOF): *m/z* = 1296.3 (M+)

^{1}H NMR (300 MHz, $CDCl_3$) δ: 7.46 (s, 2H, $H_{(4,5)}$ cz); 6.87 (s, 2H, $H_{(1,8)}$ cz); 6.68 (s, 2H, $H_{(2,6)}$ ph), 4.11-4.05 (m, 6H, OCH_2 x 3); 3.95 (t, *J* = 6.6 Hz, 8H, OCH_2 x 4); 3.66 (s, 3H, $COOCH_3$); 2.29 (t, *J* = 7.5 Hz, 2H, CH_2COO); 1.91-1.76 (m, 14H, OCH_2CH_2 x 7); 1.55-1.28 (m, 84H, CH_2 x 42); 0.90-0.86 (m, 21H, CH_3 x 7) ppm

1.3.6.2.25.4. 10,10',10''-(5-(*N*-(2,3,6,7-tetranonyloxycarbazolyl))benzene-1,2,3-triyl)tris(oxy)tris(decanoic acid) (82)

Starting materials: **55** (350 mg, 0.48 mmol), **64** (720 mg, 0.95 mmol), K_2CO_3: (330 mg, 2.4 mmol), Cu (30 mg, 0.5 mmol), DMA (10 ml)

η = 50%

m. p. (DSC): 41 °C

MS (MALDI-TOF): *m/z* = 1370.8 (M^+)

^{1}H NMR (300 MHz, $CDCl_3$) δ: 7.46 (s, 2H, $H_{(4,5)}$ cz), 6.87 (s, 2H, $H_{(1,8)}$ cz), 6.68 (s, 2H, $H_{(2,6)}$ ph), 4.11-4.05 (m, 6H, OCH_2 x 3); 3.98-3.91 (m, 8H, OCH_2 x 4), 2.33 (m, 6H, CH_2COO), 1.91-1.28 (m, 98H, CH_2 x 49), 0.90-0.86 (m, 12H, CH_3 x 4) ppm.

1.3.6.2.26. 10-(2,3-Dinonyloxy-5-(*N*-(2,3,6,7-tetranonyloxycarbazolyl)phenyl)oxydecanoic acid (81)

To a suspension of NaH in oil (60%) (188 mg, 4.7 mmol) in anhydrous DMF (20 ml) under N_2 atmosphere at 0 °C EtSH (0.35 ml, 4.7 mmol) was added. After 2 h of reaction at rt. a solution of **80** (510 mg, 0.39 mmol) in anhydrous THF (20 ml) was added. Reaction was kept at 60-70 °C (4.5 h), cooled down to rt. and poured over water. The aqueous layer was neutralised with HCl (2 M), extracted with Et_2O and the organic layer was washed with abundant water and dried over $MgSO_4$. The solvent was evaporated under vacuum and the resultant crude was chromatographied on silica gel eluating with hexane/AcOEt 85:15 to isolate compound **81** (400 mg, 80%).

m. p. (DSC)= 51 °C

MS (MALDI-TOF): *m/z* = 1282.0 (M^+)

^{1}H NMR (300 MHz, $CDCl_3$) δ: 7.46 (s, 2H, $H_{(4,5)}$ cz), 6.87 (s, 2H, $H_{(1,8)}$ cz), 6.68 (s, 2H, $H_{(2,6)}$ ph), 4.11-4.05 (m, 6H, OCH_2 x 3); 3.95 (t, *J* = 6.6 Hz, 8H, OCH_2 x 4), 2.33 (t, *J* = 7.5 Hz, 2H, CH_2COO), 1.91-1.76 (m, 14H, OCH_2 x 7); 1.55-1.28 (m, 84H, CH_2 x 42); 0.90-0.86 (m, 21H, CH_3 x 7) ppm.

^{13}C NMR (300 MHz, $CDCl_3$) δ: 178.73, 153.84, 153.82, 148.71, 144.40, 137.05, 136.06, 133.26, 115.92, 105.71, 105.37, 96.09, 73.56, 70.84, 70.82, 69.72, 69.23, 60.70, 33.82, 31.96, 31.92, 31.91, 31.89, 30.44, 29.72, 29.64, 29.60, 29.52, 29.50, 29.42, 29.40, 29.39, 29.32, 29.30, 29.28, 29.18, 29.04, 26.17, 26.14, 16.11, 26.07, 24.67, 22.69, 22.67, 14.10, 14.09, 14.07 ppm

UV (CH_2Cl_2) λ_{max}/nm (ε/dm^3 mol^{-1} cm^{-1}): 322 (20200), 294 (13200), 262 (23500)

1.3.6.2.27. 3,4,5-trioctyloxyphenylboronic acid (87)

To a solution of **86** (3 g, 5.54 mmol) in anhydrous THF (15 ml) n-BuLi in CH_2Cl_2 (1.6 M) (6.9 ml, 11.1 mmol) was added at -60 °C under nitrogen atmosphere. After 2 h of stirring at -60 °C $B(OMe)_3$ (1.55 ml, 13.9 mmol) was added. The reaction was left to attemperate and was stirred overnight. The resulting suspension was poured into sat. NH_4Cl, extracted with CH_2Cl_2 and dried over $MgSO_4$. The solvent was evaporated to dryness and the resulting crude was kept cold with inert atmosphere and used in next step without further purification.

1.3.6.2.28. 2-nitro-3',4,4',5,5'-pentaoctyloxybiphenyl (88)

Phenylboronic acid **87** (2.8 g, 5.4 mmol), **86** (2.25 g, 4.9 mmol) and catalyst $[Pd(PPh_3)_4]$ (300 mg, 0.26 mmol) under N_2 atmosphere were dissolved in THF previously flushed with nitrogen. K_2CO_3 (1 M) (9 ml, 9 mmol) also flushed with nitrogen was added and reaction was heated to reflux. After 18 h THF was removed under vacuum. The resulting crude was dissolved in dichloromethane, washed with water and dried over $MgSO_4$. Biphenyl **88** (2.77 g, 67%) was chromatographied on silica gel of the crude using a mixture of hexane/CH_2Cl_2 (from 7:3 to 3:7).

^{1}H NMR (300 MHz, $CDCl_3$) δ: 7.46 (s, 1H, $H_{(3)}$); 6.77 (s, 1H, $H_{(6)}$); 6.43 (s, 2H, $H_{(2',6')}$); 4.09-4.03 (m, 4H, OCH_2 *m*, *p*-NO_2 x 2); 4.01-3.92 (m, 6H, OCH_2 x 3); 1.91-1.72 (m, 10H, OCH_2CH_2 x 5); 1.52-1.28 (m, 50H, CH_2 x 25); 0.90-0.86 (m, 15H, CH_3 x 5) ppm.

1.3.6.2.29. 1,2,3,6,7-pentaoctyloxy-*N*H-carbazole (83)

Biphenyl **88** (2.72 g, 3.24 mmol) and $P(OEt)_3$ (5.6 ml, 32.6 mmol) were heated at boiling temperature of the phosphite overnight. The reaction was left to cool down to rt. and then was treated with HCl (2 M) and extracted with CH_2Cl_2. The organic layer was washed with water, dried over $MgSO_4$ and the solvent was removed under vacuum. The resulting crude was chromatographied on a silica gel using hexane/Et_2O increasing polarity from 99:1 to 94:6 to give **83** (2.22 g, 85%).

^{1}H NMR (300 MHz, $CDCl_3$) δ: 7.74 (s, 1H, NH); 7.41 (s, 1H, $H_{(5)}$); 7.13 (s, 1H, $H_{(8)}$); 6.93 (s, 1H, $H_{(4)}$); 4.24 (t, *J* = 6.6 Hz, 2H, OCH_2 *o*-NH); 4.08-4.02 (m, 8H, OCH_2 x 4); 1.93-1.75 (m, 10H, OCH_2CH_2 x 5); 1.54-1.30 (m, 50H, CH_2 x25); 0.89 (t, *J* = 6.6 Hz, 15H, CH_3 x 5) ppm.

1.3.6.2.30. 9-[n-(1,2,3,6,7-pentaoctyloxycarbazol-9-yl)alkyl]-1,2,3,6,7-pentaoctyloxy-carbazole general procedure

83 and NaH in oil (60%) in DMF were heated at 70 °C (1 h). The proper dibromoalkane was added and temperature was raised to 100 °C. The reaction was left to attemperate and was neutralised with HCl

(2 M). Aqueous layer was extracted with AcOEt and the organic layer was washed with water and dried over $MgSO_4$. The solvent was evaporated and the product was isolated by silica-gel column chromatography.

1.3.6.2.30.1. 1,2,3,6,7-pentaoctyloxy-[10-(1,2,3,6,7-pentaoctyloxy-*N*-carbazolyl)decyl]carbazole (89)

Starting materials: **83** (150 mg, 0.19 mmol), 1,10-dibromodecane (28 mg, 0.09 mmol), NaH (9 mg, 0.22 mmol)

Reaction time: 3 h

Eluent: hexane/CH_2Cl_2 from 7:3 to 1:1

η = 96%

m.p. (DSC): 62 °C

^{1}H NMR (300 MHz, $CDCl_3$) δ: 7.41 (s, 2H, $H_{(5)}$); 7.14 (s, 2H, $H_{(8)}$); 6.82 (s, 2H, $H_{(4)}$); 4.42 (t, *J* = 6.6 Hz, 4H, NCH_2 x 2); 4.19 (t, *J* = 6.6 Hz, 4H, OCH_2 *o*-NH x 2); 4.10-4.00 (m, 16H, OCH_2 x 8); 1.93-1.75 (m, 24H, OCH2C*H*2 x 10 + NCH_2C*H*_2 x 2); 1.54-1.30 (m, 116H, CH_2 x 58); 0.91-0.86 (m, 30H, CH_3 x 10) ppm.

MS (MALDI-TOF): *m/z* = 1754.5 (M^+-1)

1.3.6.2.30.2 1,2,3,6,7-pentaoctyloxy-[12-(1,2,3,6,7-pentaoctyloxy-*N*-carbazolyl)dodecyl]carbazole (90)

Starting materials: **83** (150 mg, 0.19 mmol), 1,12-dibromododecane (30 mg, 0.09 mmol), NaH (10 mg, 0.23 mmol)

Reaction time: 3 h

Eluent: hexane/AcOEt 95:5

η = 95%

m.p. (DSC): 54 °C

^{1}H NMR (300 MHz, $CDCl_3$) δ: 7.41 (s, 2H, $H_{(5)}$); 7.14 (s, 2H, $H_{(8)}$); 6.82 (s, 2H, $H_{(4)}$); 4.42 (t, *J* = 6.6 Hz, 4H, NCH_2); 4.19 (t, *J* = 6.6 Hz, 4H, OCH_2 *o*-NH x 2); 4.10-4.00 (m, 16H, OCH_2 x 8); 1.93-1.75 (m, 24H, OCH_2C*H*_2 x 10 + NCH_2C*H*_2 x 2); 1.54-1.30 (m, 120H, CH_2 x 60); 0.91-0.86 (m, 30H, CH_3 x 10) ppm.

MS (MALDI-TOF): *m/z* = 1782.5 (M^+)

UV (CH_2Cl_2) λ_{max}/nm (ε/dm^3 mol^{-1} cm^{-1}): 317 (44600), 273 (27600)

1.3.6.2.30.3. 1,2,3,6,7-pentaoctyloxy-[14-(1,2,3,6,7-pentaoctyloxy-*N*-carbazolyl)tetradecyl] carbazole (91)

Starting material: **83** (355 mg, 0.44 mmol), 1,14-dibromotetradecane (80 mg, 0.22 mmol), NaH (21 mg, 0.53 mmol)

Reaction time: 14 h

Eluent: hexane/AcOEt 95:5

η = 70%

m.p. (DSC): 49 °C

MS (MALDI-TOF): *m/z* = 1810.6 (M^+)

^{1}H NMR (300 MHz, $CDCl_3$) δ: 7.41 (s, 2H, $H_{(5)}$); 7.14 (s, 2H, $H_{(8)}$); 6.82 (s, 2H, $H_{(4)}$); 4.42 (t, *J* = 6.6 Hz, 4H, NCH_2); 4.19 (t, *J* = 6.6Hz, 4H, OCH_2 *o*-NH x 2); 4.10-4.00 (m, 16H, OCH_2 x 8); 1.93-1.75 (m, 24H, OCH_2CH_2 x 10 + NCH_2CH_2 x 2); 1.54-1.30 (m, 124H, CH_2 x 62); 0.91-0.86 (m, 30H, CH_3 x 10) ppm.

^{13}C NMR (400 MHz, $CDCl_3$) δ: 149.13, 147.46, 143.75, 140.21, 139.27, 136.52, 127.74, 119.11, 115.72, 105.79, 98.16, 95.30, 74.36, 74.08, 70.72, 69.88, 69.39, 44.79, 31.91, 31.90, 31.89, 31.85, 30.46, 30.36, 30.04, 29.81, 29.78, 29.70, 29.63, 29.48, 29.46, 29.39, 29.36, 29.33, 27.20, 26.28, 26.18, 22.69, 14.10 ppm.

1.3.6.2.31. 1,3,5-tris(*N*-carbazolyl)benzene (TCB)

A mixture of 1,3,5 tribromobenzene (1.02 g, 3.2 mmol), K_2CO_3 (2.76 g, 20 mmol), *N*H-carbazole (1.74 g, 1.0 mmol), and Cu powder (630 mg, 10 mmol) in nitrobenzene (40 ml) was refluxed under nitrogen atmosphere (3 days). The hot solution was vacuum filtered and the solid was washed with MeOH. The precipitate was dissolved in CH_2Cl_2, evaporated to dryness and chromatographied on silica gel column eluating with hexane/CH_2Cl_2 65:35. TCB was obtained as a precipitate (570 mg, 33%).

^{1}H NMR (300 MHz, $CDCl_3$) δ: 8.19 (d, *J* = 7.8 Hz, 6H, $H_{(4,5)}$ x 3), 7.97 (s, 3H, bnz), 7.68 (d, *J* = 7.8 Hz, 6H, $H_{(1,8)}$ x 3), 7.48 (t, *J* = 7.8 Hz, 6H, $H_{(3,6)}$ x 3), 7.34 (t, *J* = 7.8 Hz, 6H, $H_{(2,7)}$ x 3) ppm

MS (CI): *m/z* = 574.3 (M^++1)

UV (CH_2Cl_2) λ_{max}/nm (ε/dm^3 mol^{-1} cm^{-1}): 292 (47900), 311 (sh) (16300), 324 (14040), 328 (14700).

1.3.6.2.32. Attachment of tricyanovinyl groups to the TCB core

To a boiling solution of TCB (480 mg, 0.84 mmol) in CS_2 (25 ml) containing $AlCl_3$ (355 mg, 2.67 mmol) under anhydrous atmosphere (P_2O_5) was added tetracyanoethylene (355 mg, 2.77 mmol) in small

portions of around 100 mg every hour. After 3 days of reaction the solvent was removed under vacuum and the crude was treated with H_2O. The aqueous layer was extracted with $CHCl_3$, the organic layer was dried over $MgSO_4$ and the resulting crude was chromatographied in a silica-gel column eluating with to isolate compounds **50** (25 mg, 5%), **51** (71 mg, 11%) and **52** (120 mg, 16%).

1,3-bis(*N*-carbazolyl)-5-(3-cyanovinyl-*N*-carbazolyl)benzene(50)

^{1}H NMR (300 MHz, $CDCl_3$) δ: 8.91 (d, *J* = 1.8 Hz, 1H, $H_{(4)}$), 8.26 (d, *J* = 7.8 Hz, 1H, $H_{(5)}$), 8.25 (dd, *J* = 9.0 Hz, *J* = 1.8 Hz, 1H, $H_{(2)}$), 8.18 (d, *J* = 7.8 Hz, 4H, $H_{(4',5')}$ x 2), 8.11 (t, *J* = 1.8 Hz, 1H, bnz $H_{(4)}$), 7.92 (d, *J* = 1.8 Hz, 2H, bnz $H_{(2,6)}$), 7.75 (d, *J* = 9.0 Hz, 1H, $H_{(1)}$), 7.70-7.61 (m, 3H, $H_{(6,7,8)}$), 7.65 (d, *J* = 7.8 Hz, 4H, $H_{(1',8')}$ x 2), 7.49 (t, *J* = 7.8 Hz, 4H, $H_{(2',7')}$ x 2), 7.36 (t, *J* = 7.8 Hz, 4H, $H_{(3',6')}$ x 2) ppm.

^{13}C NMR (400 MHz, $CDCl_3$) δ: 141.89, 141.61, 141.13, 140.27, 138.87, 128.84, 127.99, 126.67, 125.21, 124.16, 124.14, 123.48, 123.20, 123.00, 121.62, 121.25, 120.92, 114.42, 112.36, 111.38, 110.94, 109.58, 29.85 ppm

UV (CH_2Cl_2) λ_{max}/nm (ε/dm^3 mol^{-1} cm^{-1}): 478 (17290), 337 (20300), 323 (18250), 312 (sh) (18250), 292 (38700)

MS (CI): *m/z* = 692.8 (M^++NH_3+1)

1-(*N*-carbazolyl)-3,5-bis(3-cyanovinyl-*N*-carbazolyl)benzene (51)

^{1}H NMR (300 MHz, DMSO-d_6) δ: 8.92 (d, *J* = 1.7 Hz, 2H, cz $H_{(4)}$ x 2), 8.43 (d, *J* = 7.5 Hz, 2H, cz $H_{(1)}$ x 2), 8.27 (d, *J* = 7.5 Hz, 2H, cz $H_{(4',5')}$), 8.25 (s, 3H, bnz), 8.17 (dd, *J* = 8.7 Hz, *J* = 2.1 Hz, 2H, cz $H_{(2)}$ x 2), 8.02 (d, *J* = 8.7 Hz, cz $H_{(5)}$ x 2), 7.85-7.78 (m, 4H, cz $H_{(8)}$ x 2 + cz $H_{(1',8')}$), 7.66 (t, *J* = 7.5 Hz, cz $H_{(7)}$ x 2), 7.54-7.45 (m, 4H, cz $H_{(2',3',6',7')}$), 7.34 (t, *J* = 7.5 Hz, cz $H_{(6)}$ x 2) ppm.

^{13}C NMR (400 MHz, DMSO-d_6) δ: 143.76, 141.49, 140.61, 140.23, 139.85, 138.59, 128.19, 128.53, 126.40, 125.61, 123.74, 123.52, 123.06, 122.24, 121.26, 121.14, 120.57, 120.49, 114.85, 113.02, 114.84, 113.02, 112.79, 111.89, 111.15, 110.07, 88.93

UV (CH_2Cl_2) λ_{max}/nm (ε/dm^3 mol^{-1} cm^{-1}): 476 (47900), 337 (36500), 323 (28400), 310 (sh) (25530), 289 (52010)

MS (CI): *m/z* = 793.8 (M^++NH_3+1)

1,3,5-tris(3-cyanovinyl-*N*-carbazolyl)benzene (52)

^{1}H NMR (300 MHz, DMSO-d_6) δ: 8.92 (d, *J* = 1.8 Hz, 3H, cz $H_{(4)}$ x 3), 8.44 (d, *J* = 7.8 Hz, 3H, cz $H_{(1)}$), 8.36 (s, 3H, bnz), 8.16 (dd, *J* = 8.7 Hz, *J* = 2.1 Hz, cz $H_{(2)}$ x 3), 8.03 (d, *J* = 8.7 Hz, 3H, cz $H_{(5)}$ x 3), 7.85 (d, *J* = 8.7 Hz, cz $H_{(8)}$ x 3), 7.65 (t, *J* = 7.5 Hz, 3H, cz $H_{(7)}$ x 3), 7.48 (t, *J* = 7.5 Hz, 3H, cz $H_{(6)}$ x 3) ppm.

^{13}C NMR (400 MHz, DMSO-d_6) δ: 143.65, 141.39, 140.59, 138.72, 128.16, 127.46, 126.12, 123.74, 123.51, 122.23, 121.24, 114.83, 112.99, 112.76, 111.93, 111.24, 88.05 ppm.

UV (CH_2Cl_2) λ_{max}/nm (ε/dm^3 mol^{-1} cm^{-1}): 473 (71070), 335 (44560), 321 (sh) (30760), 308 (30860), 289 (58940)

MS (CI): *m/z* = 793.8 (M^++NH_3+1)

References

[1] J. L. Diaz, A. Dobarro, B. Villacampa, D. Velasco, *Chem. Mater.* **2001**, *13*, 2528-2536.
[2] E. Perea, F. Lopez-Calahorra, D. Velasco, *Liq. Cryst.* **2002**, *29*, 421-428.
[3] E. Perea, F. López-Calahorra, D. Velasco, H. Finkelmann, *Mol. Crys. Liq. Cryst.* **2001**, *365*, 695 - 702.
[4] E. Perea, *Síntesi de 9-fenilcarbazoles polisubstituïts i altres derivats carbazòlics relacionats. Estudi del seu comportament mesomòrfic.* **2001**, Doctoral Thesis. Facultat de Química. Universitat de Barcelona.
[5] M. P. Constantinos, T. Dimitris, *Angew. Chem. Int. Ed.* **1995**, *34*, 1696-1711.
[6] K. Takashi, M. Norihiro, K. Kiyoshi, *Macromol. Rapid Commun.* **2001**, *22*, 797-814.
[7] C. Lavigueur, E. J. Foster, V. E. Williams, *J. Am. Chem. Soc.* **2008**, *130*, 11791-11800.
[8] K. J. Donovan, K. Scott, M. Somerton, J. Preece, M. Manickam, *Chem. Phys.* **2006**, *322*, 471-476.
[9] R. Helmut, B. Holger, K. Olaf, W. Renate, E. Martina, H. W. Joachim, K. Bernd, P. Klaus, *Adv. Mater.* **1990**, *2*, 141-144.
[10] P. H. J. Kouwer, W. F. Jager, W. J. Mijs, S. J. Picken, *Macromol.* **2002**, *35*, 4322-4329.
[11] P. H. J. Kouwer, W. F. Jager, W. J. Mijs, S. J. Picken, *J. Mater. Chem.* **2003**, *13*, 458-469.
[12] P. H. J. Kouwer, O. van den Berg, W. F. Jager, W. J. Mijs, S. J. Picken, *Macromol.* **2002**, *35*, 2576-2582.
[13] M. Manickam, M. Belloni, S. Kumar, S. K. Varshney, D. S. S. Rao, P. R. Ashton, J. A. Preece, N. Spencer, *J. Mater. Chem.* **2001**, *11*, 2790-2800.
[14] M. Manickam, G. Cooke, S. Kumar, P. R. Ashton, J. A. Preece, N. Spencer, *Mol. Cryst. Liq. Cryst.* **2003**, *397*, 1-1.
[15] M. Manickam, S. Kumar, J. A. Preece, N. Spencer, *Liq. Cryst.* **2000**, *27*, 703-706.
[16] S. M. Bonesi, R. Erra-Balsells, *J. Lumin.* **2001**, *93*, 51-74.
[17] K. R. Yoon, N. M. Byun, H. Lee, *Syn. Met.* **2007**, *157*, 603-610.
[18] L. Chetkina, V. Bel'skii, *Crystallogr. Rep.* **2002**, *47*, 581-602.
[19] K. Tominaga, G. C. Walker, W. Jarzeba, P. F. Barbara, *J. Phys. Chem.* **1991**, *95*, 10475-10485.
[20] A. Kapturkiewicz, J. Herbich, J. Karpiuk, J. Nowacki, *J. Phys. Chem. A* **1997**, *101*, 2332-2344.
[21] D. E. Janzen, M. W. Burand, P. C. Ewbank, T. M. Pappenfus, H. Higuchi, D. A. da Silva Filho, V. G. Young, J.-L. Bredas, K. R. Mann, *J. Am. Chem. Soc.* **2004**, *126*, 15295-15308.
[22] W. T. Geng, M. Oda, J. Nara, H. Kondo, T. Ohno, *J. Phys. Chem. B* **2008**, *112*, 2795-2800.
[23] Y. Shirota, H. Kageyama, *Chem. Rev.* **2007**, *107*, 953-1010.
[24] K. S. Son, M. Yahiro, T. Imai, H. Yoshizaki, C. Adachi, *Chem. Mater.* **2008**, *20*, 4439-4446.
[25] J. Zaumseil, H. Sirringhaus, *Chem. Rev.* **2007**, *107*, 1296-1323.

2. Charge transport properties

2.1. Theoretical basis

The time-of-flight (TOF) experiment has proven to be very successful in the determination of charge mobility in materials such as organic or amorphous semiconductors.[1-4] A schematic of a typical time-of-flight arrangement is illustrated in Figure 2.1.

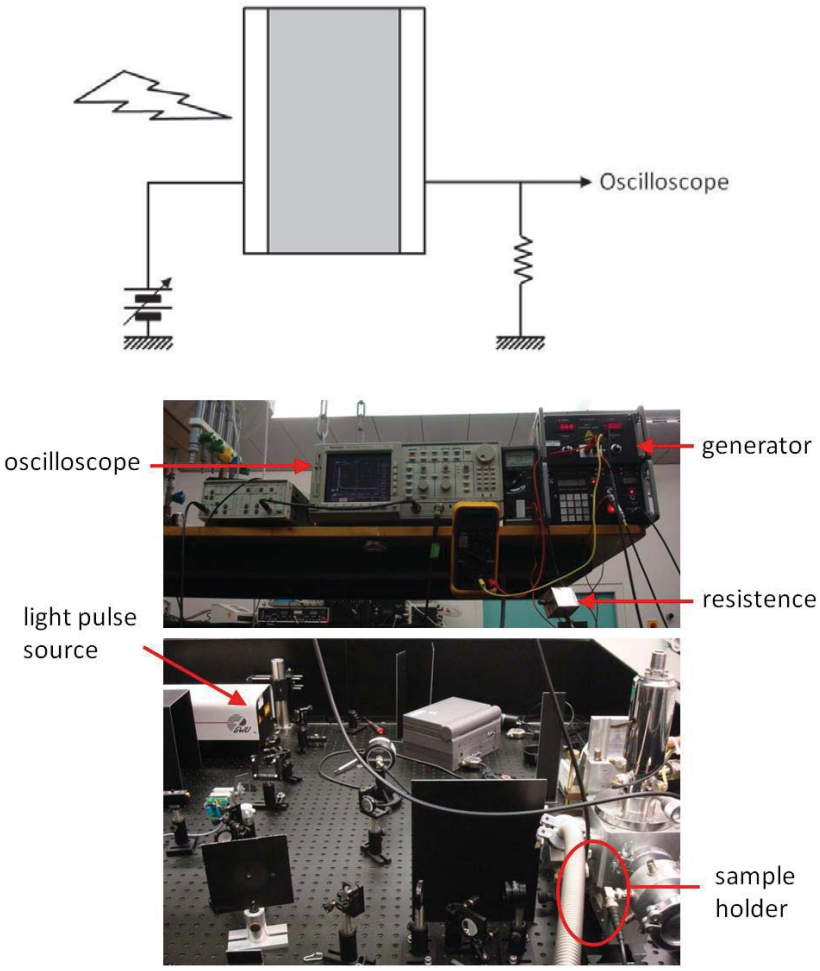

Figure 2.1. Schematic TOF apparatus (top). The grey area represents the organic layer sandwitched between the two electrodes. TOF equipment (bottom).

A sample, up to tens of microns, is placed between two electrodes, at least one of which must be semi-transparent and a potential difference is applied to the electrodes. A sheet of electron-hole pairs is created near one surface by a strongly absorbed exposure of short duration. The wavelength of the exposure is selected such that the absorption depth is much less than the thickness. Under the influence of the field, a fraction of the pairs dissociate and are displaced to the appropriate electrodes. Either electrons or holes are neutralized immediately by reaching the exposed electrode, but the opposite carriers have to migrate

across the sample to reach the opposite electrode. As the carriers migrate across the sample, they generate a displacement current which can be detected in an external circuit (Figure 2.2).

A variant of the time-of-flight technique to measure charge mobility is the time-of-flight potential discharge technique XTOF, that is, xerographic time-of-flight technique. By this method, the free surface is charged by a corona discharge and then exposed by a flash of radiation with a duration that is short compared to the transient time. The exposure creates a sheet of carriers that are injected into the sample. As the charge drifts across the sample, the surface potential decreases. From the time dependence of the rate of change of the surface potential, the mobility can be determined in an analog way to the photocurrent vs. time curves registered in the TOF technique. A photoinduced discharge apparatus is schematically illustrated in Figure 2.3. It includes a corona charging unit, an exposure system and a non-contacting voltimeter. Relative to conventional TOF technique, the advantages of the XTOF method are that higher fields can be sustained without dielectric breakdown and experimental simplicity. The main drawback, though, is that measurements are performed in air.

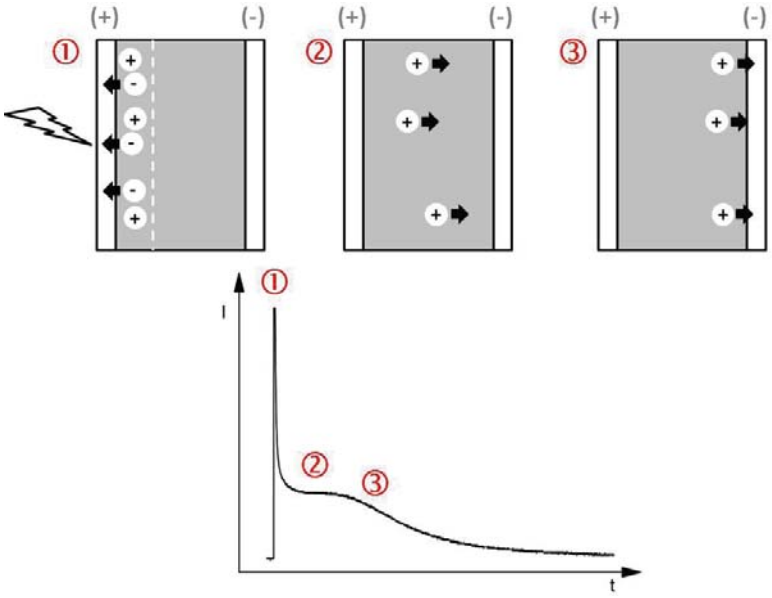

Figure 2.2. Scheme of non-dispersive hole transport in a TOF device.

Information concerning the interaction of the migrating carriers with traps or recombination centers can be derived from an analysis of the temporal features of the photocurrent and surface potential transients, which show: 1) an initial spike of short duration; 2) a plateau of variable duration and; 3) a long tail (Figure 2.2). The initial spike is due to the rapid recombination of the charges with the exposed electrode. The plateau indicates the displacement of a packet of carriers with a constant velocity in a *non-dispersive* charge transport. Provided the time constant associated with the sample resistor *R* and the capacitance *C* is much less than the transit time, t_t, the signal will be proportional to the photocurrent due to the carrier

displacement. For $RC < t_t$, the voltage across R is proportional to the current flowing in the sample. When the carriers exit the sample at the collecting electrode, a sharp decrease in the current occurs. The shape of the tail that follows the drop of current reflects the broadening of the charge carrier package during its migration through the bulk, which can be caused by the inherent diffusion of carriers or shallow traps that are present in the bulk.

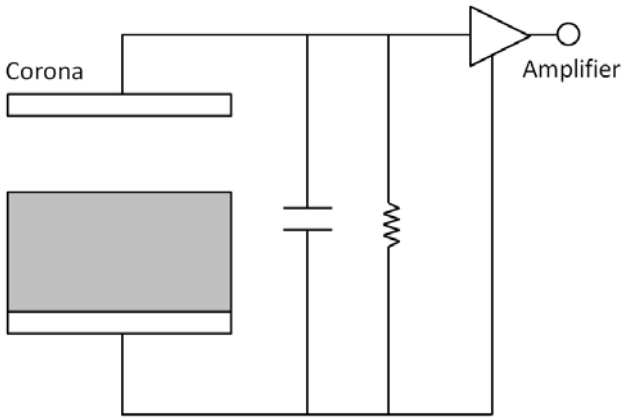

Figure 2.3. Schematic XTOF apparatus. The grey area represents the organic layer contacting an electrode at the bottom.

The time corresponding to the onset of the decrease in current, t_t, is usually determined from the intersection of the asymptotes to the plateau and trailing edge of the photocurrent (Figure 2.4 left). This technique, which is widely used in the analysis of time-of-flight transients, differs from those used in most theories of charge transport, where the t_t is defined as the mean arrival time. The ratio of the thickness to the transit time gives the velocity and the ratio of the velocity to the field then gives the mobility. The mobility, μ, is defined as

$$\mu = \frac{d}{t_t \times E} \tag{2.1}$$

where d is the thickness and E the field, which is calculated

$$E = \frac{V}{d} \tag{2.2}$$

Plots that show the absence of a plateau or the anomalous broadening of the tail are frequently described as *dispersive*. Dispersive regimes are those in which a dynamic equilibrium of the hopping is not attained within the transient time. Such regime occurs when the charge carriers occupy the so-called *deep traps*, i. e. states from which their jumps are still unlikely at a shorter time than t_t. Plots for this kind of transport are

exponential rather than Gaussian. Transient times can, though, be determined from the double logarithmic plots in some cases (Figure. 2.4 right).

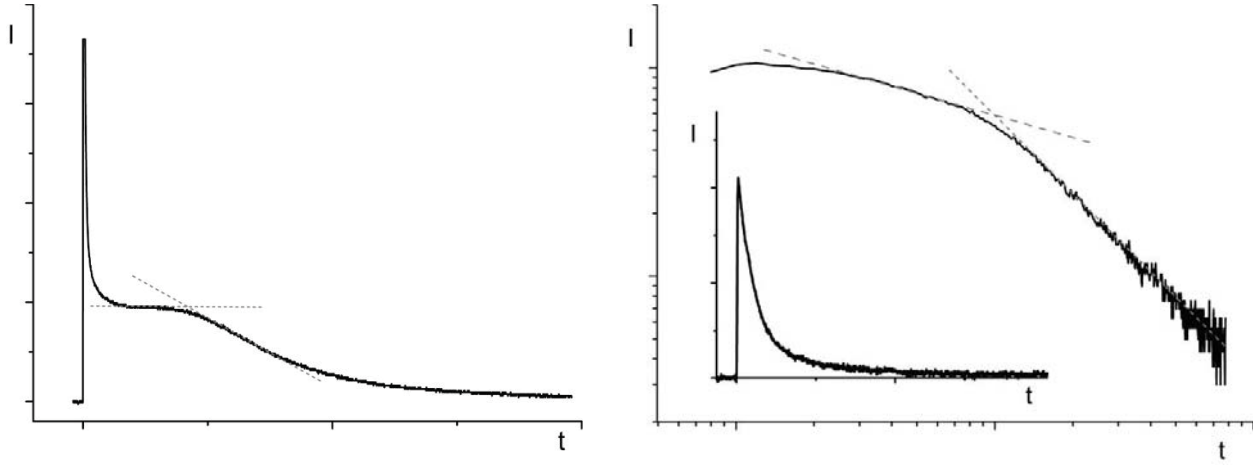

Figure 2.4. Temporal features of the photocurrent for a TOF experiment. On the left a typical plot in the linear scale for non-dispersive charge transport. On the right, a log-log plot of a dispersive (right) charge transport with an insert of the photocurrent linear scale.

Predictions of the disorder formalism have been largely developed by Monte-Carlo simulations, which use the expression

$$\mu(\sigma,\Sigma,T,E) = \mu_0 \times \exp\left[-\left(\frac{2\sigma}{3kT}\right)^2\right] \times \exp\left\{C\left[\left(\frac{\sigma}{kT}\right)^2 - \Sigma^2\right]\sqrt{E}\right\} \qquad (2.3)$$

Without going into much details, which can be found in the literature, it should be mentioned that within the frame-work of this model the following experimental observations are predicted: (1) strong temperature dependence of the mobility; (2) Poole-Frenkel-type field-dependence $\mu \alpha \beta E^{1/2}$.

The degree of energetic disorder is specified by the parameter σ/kT since energetic disorder has been accounted for by selecting site energies from a Gaussian distribution of width σ. The parameter Σ measures the relative variation of electronic intersite coupling due to variation of nearest-neighbor intersite distances, or the wavefunction overlap resulting from variable mutual orientation of nonspherical molecules. $\Sigma = 0$ indicates a pure positional disorder. Disorder gives rise to a spatial spreading of the carrier packet in the field direction that exceeds the spreading caused by diffusion. This is due to the retardation of carriers temporarily residing in energetically deep states of the DOS, i. e. traps. For low to moderate disorder, $\sigma \leq 3.0$, the migrating carriers achieve dynamic equilibrium and the transport is of Gaussian type, that is, non-dispersive. For large disorder, $\sigma \geq 5.0$, energetic relaxation of carriers within the DOS is not

completed within a transient time, giving place to dispersive transport. σ can be determined from the temperature dependence of the zero-field mobility from the relationship $\log\mu \propto -(T/T_0)^2$ where $T_0 = 2\sigma/3k$.

2.2. Results and discussion

In this section the most representative synthesized compounds are evaluated as semiconductors. The techniques used were the xerographic time-of-flight (XTOF) technique, for compounds that presented glassy states, and the time-of-flight (TOF) technique, for compounds that presented columnar mesophases.

2.2.1. XTOF measurements of molecular glasses

Charge transport properties of the most representative molecular glasses were studied by XTOF technique during an internship in the Solid State Electronics Department of the Vilnius University (Lithuania), under the supervision of Prof. Gaidelis and Prof. Grazulevicius (Kaunas University of Technology). XTOF measurements of the samples were performed by Dr. Jankauskas. Amorphous layers of the different compounds were attained by casting of the THF solution (Figure. 2.5) of the pure materials or of their blend with bisphenol Z polycarbonate (1:1). Namely, embedding the small molecules in the polymeric matrix conferred the layers mechanical stability thus avoiding crystallization.

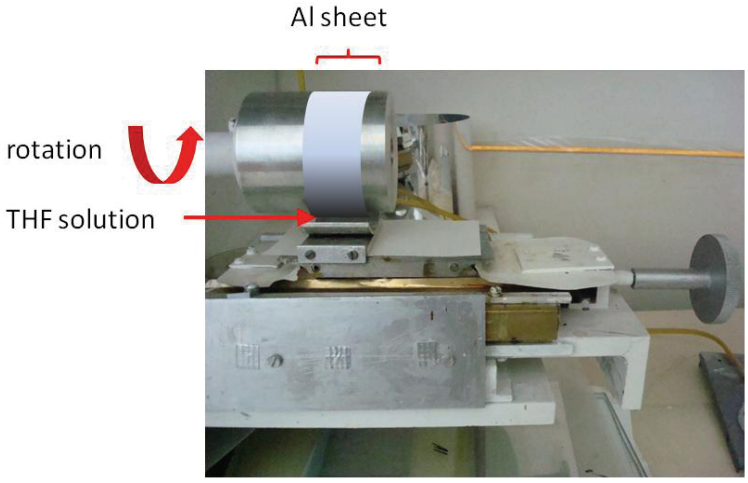

Figure 2.5. Equipment for the deposition of layers on Al films by casting of the solution of the corresponding material.

2.2.1.1. Radical derivatives

The starting point of the charge transport studies on radical molecular glasses was the study of the behavior of radical adducts **1** and **11**. XTOF experiments proved that the amorphous layers of the pure compounds presented bipolar charge transport, that is, they showed the capability of

transporting both holes and electrons. Bipolar charge transport was also observed in the doped polymeric layers for both radicals **1** and **11**, but the calculated mobility values were up to two orders of magnitude lower than those for pure **1** and **11**. Charge transport took place in dispersive regime in all cases, except in the case of **1**:PCZ blend. Figure 2.6 shows the dU/dt curves registered for material **1** as a layer of pure material and as a layer of **1**:PCZ blend. The obtained charge mobility values for both electron and hole-transport and the field dependences of the mobilities are presented in Table 2.1.

Table 2.1. Zero-field mobilities (μ_0), mobilities (μ) at an electric field of 6.4×10^5 V cm^{-1}, in cm^2 V^{-1} s^{-1}, and field dependences (β) of holes and electrons in amorphous layers of **1** and **11** and in the blends of **1**, **11**, **12** and **TTM** with polycarbonate (PCZ).

	thickness (μm)	Holes			Electrons		
		μ_0	μ	β	μ_0	μ	β
1	1.5	8.0×10^{-5}	4.6×10^{-4}	0.0023	7.5×10^{-4}	4.7×10^{-3}	0.0025
1:PCZ	7	3.0×10^{-7}	1.7×10^{-6}	0.0022	1.6×10^{-5}	6.5×10^{-5}	0.0017
11	2.1	1.4×10^{-4}	7.2×10^{-4}	0.0021	2.0×10^{-3}	7.8×10^{-3}	0.0017
11:PCZ	4.8	2.2×10^{-7}	1.6×10^{-6}	0.0025	2.2×10^{-4}	2.6×10^{-4}	0.0005
12:PCZ	6	5.4×10^{-7}	4.8×10^{-6}	0.0027	-	-	-
TTM:PCZ	6	3.3×10^{-7}	2.9×10^{-6}	0.0027	-	-	-

It is noteworthy that the measured electron-transport mobility values of pure materials **1** and **11** are among the highest reported values for low molar mass amorphous materials,[2, 5, 6] and that their hole-transport mobility values are comparable to those observed for molecular glasses based on carbazole.[4, 7] These results range them among the most efficient bipolar molecular glasses reported in the literature so far.[8]

A drop in the mobility values is normally associated with the increase of the energetic disorder, σ, thus leading to a more dispersive regime (see section 2.1). However, embedding materials **1** and **11** in a polymeric matrix did not produce changes in the shape of the dU/dt curves. In fact, **1**:PZC presents a clear Gaussian-type hole transport. A similar behavior was observed in polymers doped with hole-transporting small molecules reported by Borsenberger et al., who attributed these results to a trap-controlled mobility phenomenon.[9] According to Borsenberger, for certain concentrations of the hole transporting material in the polymeric blends, all carriers experience multiple trapping events during their transit, so that a dynamic equilibrium is still attained but the dispersion of transit times is substantially decreased leading to longer but well-defined transient times.

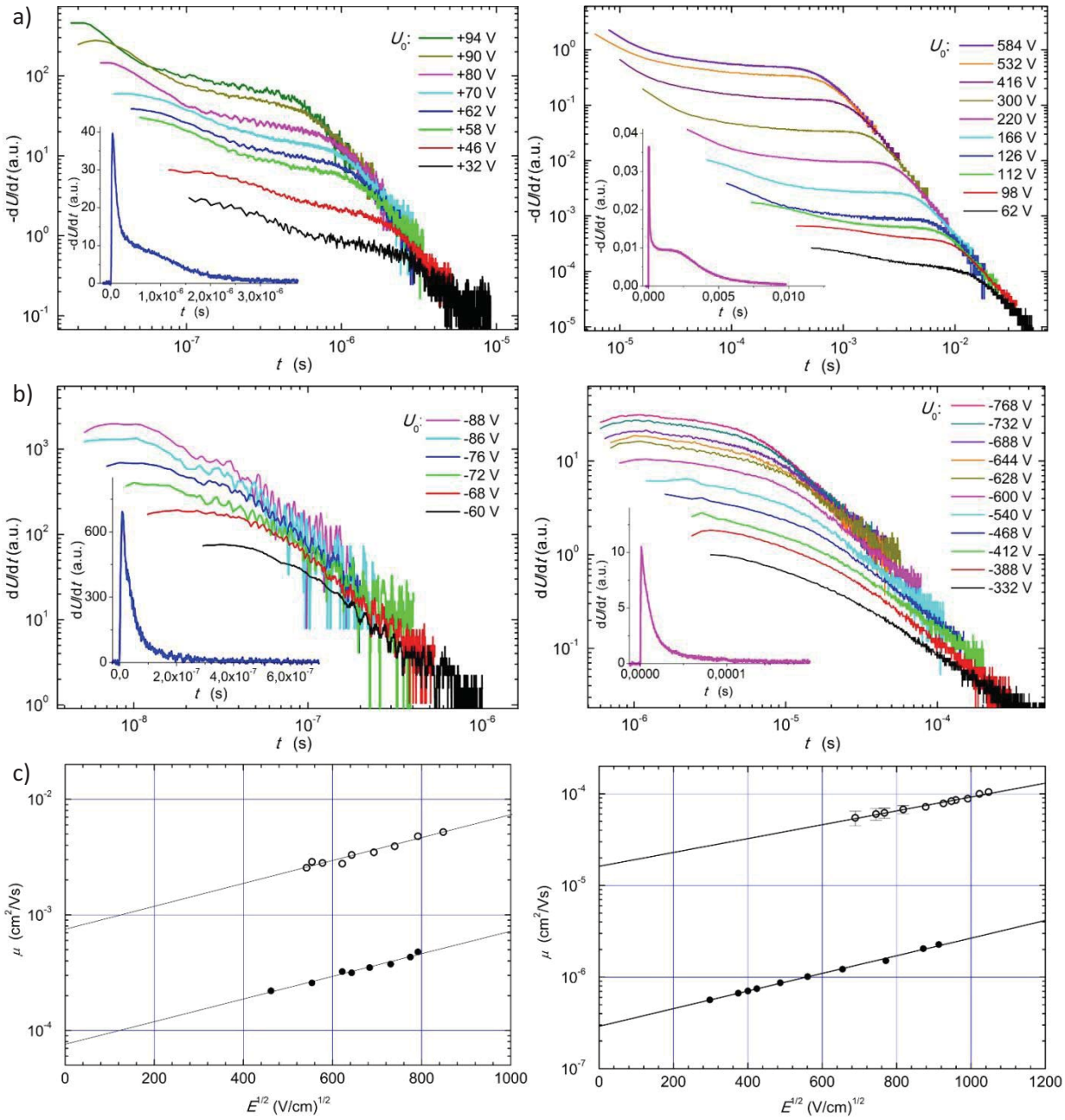

Figure 2.6. dU/dt curves in double logarithmic scale of a layer for positive (a) and negative (b) corona charge, inserts show the surface potential decay in the linear scale; charge drift mobilities as a function of the applied field (c) of holes (white circles) and electrons (black circles) for a layer of 1.5 μm of pure material **1** (left) and for a layer of 7 μm of **1**:PZC blend.

The relevance of the radical character in the semiconducting properties of the studied compounds is given by the study of the electrochemical and electronic behavior of the non-radical precursor of **1**, the compound **1H**. Cyclic voltammetries of **1H** showed a non-reversible oxidation peak and no peaks in the reduction site of the plot. Accordingly, no charge drift mobility was observable in the XTOF

experiments performed on this material. These results prove that the ambipolar charge transport of the radical adducts can be unequivocally assigned to their open-shell electronic configuration.

XTOF measurements were performed on radicals **TTM**, **2** and **12** in order to study the role of the heterocycle moieties in the transport properties of *N*-carbazolylTTM and *N*-indolylTTM derivatives. Charge transport properties of **TTM** in the amorphous state could only be evaluated in **TTM**:PCZ blend layers, since thin films of the pure material crystallized almost immediately. **TTM**:PCZ blend presented similar hole mobility values to those registered for **1**:PCZ or **11**:PCZ blends, although it proved to have a much more dispersive character (Figure 2.7). Surface potential decay for negative corona charging presented an exponential decay and no electron-transport transient time could be detected in the log-log plot. Despite comparative studies on the radical bearing two carbazole fragments could not be performed due to solubility reasons,* polycarbonate layers doped with radical **12** presented easily detectable t_t for hole-transport (Figure 2.8), but presented a too dispersive nature to determine t_t for electron transport.

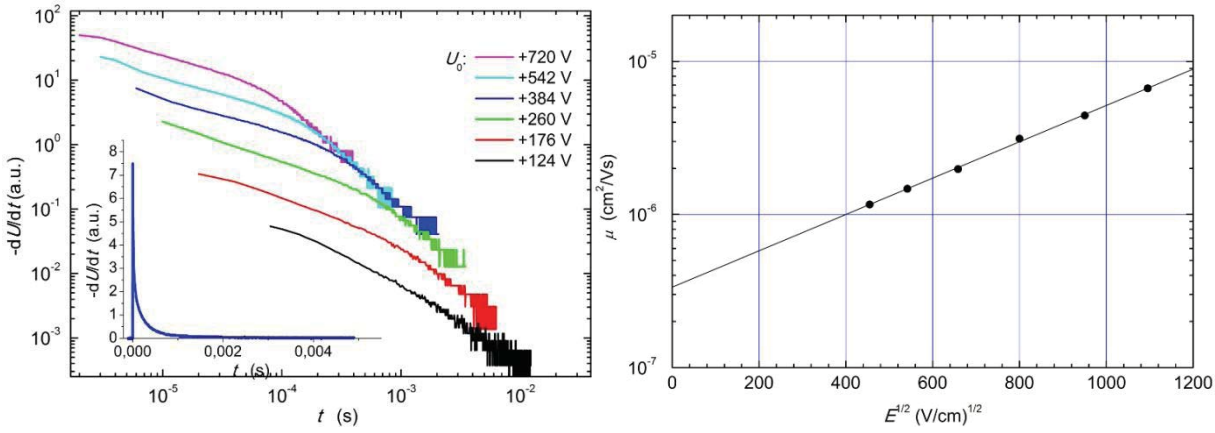

Figure 2.7. dU/dt curves for positive corona charge of a layer of 6 μm of **TTM**:PZC blend (left) and hole drifts mobilities as a function of the applied field (right).

It is tempting to associate the deep trapping, responsible of the more dispersive regime of the hole-transport in the **TTM**:PCZ blend to the less accessibility of the holes in the hopping process, since they must be strongly located in the trivalent carbon. Moreover, the delocalization of the positive charge over the heterocycle fragments in the cationic species derived from radical adducts **1** and **11** may imply a mayor participation of a molecular orbital with a π nature into the hopping process than in the case of the cation derived from **TTM**. This hypothesis would also be in agreement with the non-dispersive hole transport observed in the polymeric layer doped with radical **12**, which bears two heterocycles.

* Radical **2** could not be dissolved in the proper concentration to obtain **2**:PCZ 1:1 layers.

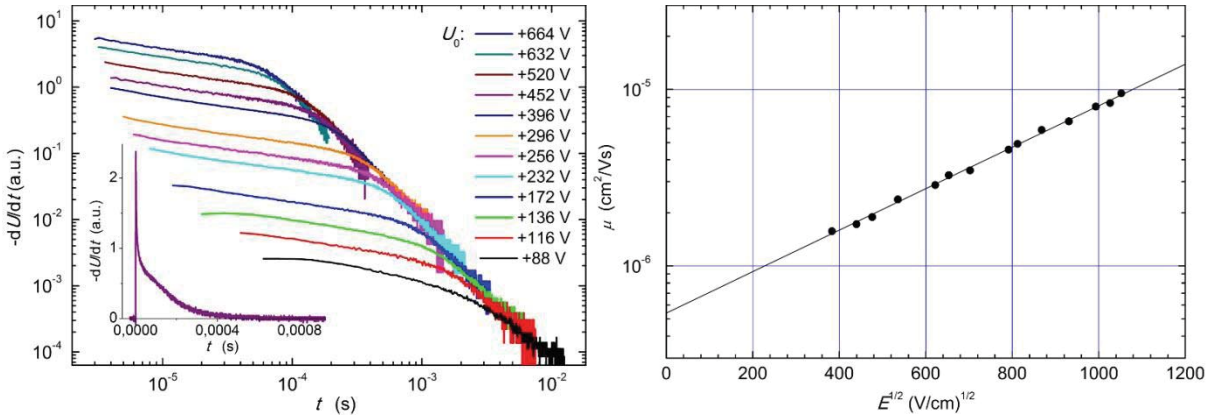

Figure 2.8. dU/dt curves for positive corona charge of a layer of 6 μm of **12**:PZC blend (left) and hole drifts mobilities as a function of the applied field (right).

However, no equivalent reasoning could be used to explain the highly dispersive regime of the electron-transport in the **TTM**:PCZ and the **12**:PCZ blends, taking into account that the electron-affinity (EA) values for the four radicals, **1**, **2**, **TTM** and **12**, vary only slightly (see section 1.2.4). This constancy in the EA values indicates that the negative charge must be mainly located in the central carbon in all reduced compounds and that the attachment of the heterocyclic moieties is not contributing to the destabilization of the anionic species. Hence, the reasons for the different electron transport characteristics remain unclear and are subject of further studies.

Charge transport in these organic compounds bearing an unpaired electron may differ from charge transport in the usual organic semiconductors with an even number of electrons. For conventional organic molecules with closed-shell electronic configuration, the molecular orbitals involved in the hole and electron transport are the HOMO and the LUMO, respectively, since these are the molecular orbitals that can lose or gain an electron. Usually the HOMO is of π nature and the LUMO of π* nature, given that organic semiconductors are based on extended aromatic cores. However, in the case of triphenylmethyl based organic radicals, oxidation and reduction processes are attributed to their capability of losing the single electron from the semioccupied molecular orbital (SOMO) or of gaining a single electron into the SOMO, in order to lead the whole system to a closed-shell electronic configuration. Assuming from previous EPR studies on radicals of the TTM series that the single electron is mainly located on the p orbital of the trivalent carbon atom,[10-12] the SOMO in **1** and **11** is considered to have a non-bonding (n.b.) nature.

Furthermore, XTOF technique may have different effects in open-shell systems and in closed-shell systems. As it was explained in the theoretical basis of the XTOF technique, when the light pulse hits the surface of the amorphous layer, the molecules that absorb the light become excitons, that is, one

of the electrons in the HOMO is promoted to the LUMO or to a more energetic MO, depending on the wavelength of the light and the absorption profile of the material. The electronic configuration of the resulting excited state makes it easier to inject a hole -extract the electron at the higher level- or to inject an electron into the HOMO (Figure 2.9). Once the cationic or the anionic species are formed, the hole or the electron transport occurs through the HOMO or the LUMO, respectively.

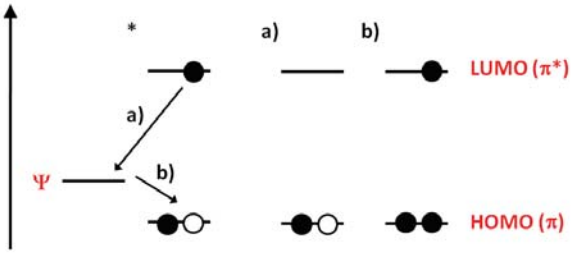

Figure 2.9. Scheme of the electronic configuration of a closed-shell configuration molecule after (a) injecting a hole (○), (b) injecting an electron (●) into the excited state (*) from the electrode (Ψ).

Considering the proposed assignation of the absorption bands of the radicals bearing a TTM fragment, by applying a pulse of 337 nm the electronic transition that could be expected is the SOMO→LUMO transition, in the case of the **TTM**, or the SOMO→$LUMO_2$ transition in the case of radicals **1**, **2** and **12**. Thus, the hole might be injected in the SOMO orbital. However, the injection of an electron when the molecule is in this excited state might take place in the lowest energetic level available (Figure 2.10). That might lead to an excited triplet state of the anion that could be involved in the charge transport or that could undergo relaxation and, therefore, the electron transport could occur through a π* MO or through the n.b. MO, respectively.

The attachment of carbonyl chains to the *N*-carbazolylTTM radical core proved to be an effective synthetic strategy to provide this kind of radicals with the capability of forming stable amorphous layers. This mechanical property, which is a most advantageous feature for a molecular material, prompted us to evaluate the charge transport properties of radical adduct **18**. However, the obtained dU/dt curves for both negative and positive corona charging revealed that this material presented highly dispersive electron and hole-transport. Thus, the addition of the chains is in detrimental of the hopping mechanism, despite favoring the amorphous state. For this reason, the more complex structures bearing carbonyl moieties were excluded from further studies with the XTOF technique.

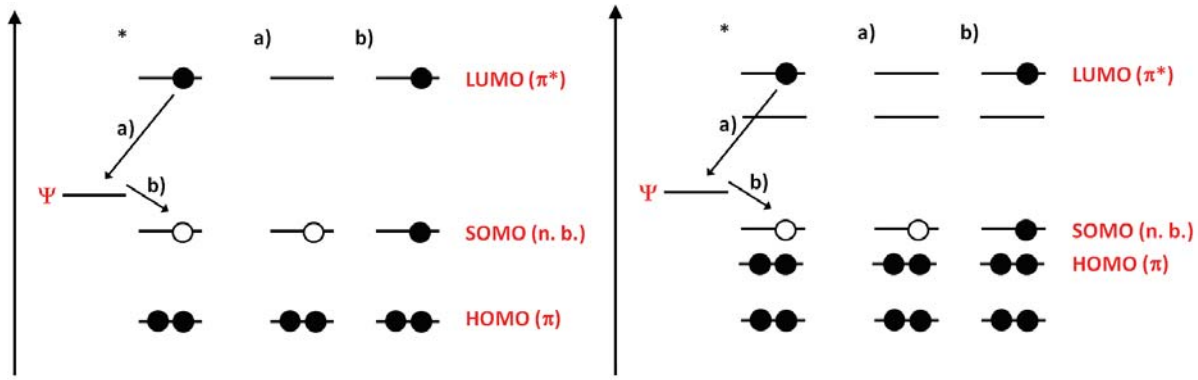

Figure 2.10. Scheme of the proposed electronic configuration of radicals TTM (left) and of radicals **1**, **11** and **12** (right) after injecting (a) injecting a hole (○), (b) injecting an electron (●) to the excited molecule (*) from the electrode (Ψ).

2.2.1.2. Non-radical derivatives

XTOF measurements were performed on three different molecular glasses based on compounds with the *N*-phenylcarbazole core: **48**, **49** and **52**. Given their electrochemical characteristics (see section 1.3.4) the two first compounds were expected to be hole-transporting materials while the third compound was expected to be an electron-transporting molecular material.

The surface potential decay curves in the log-log scaled plots indicate that hole transport takes place in materials **48** and **49**, though in a very dispersive regime. In the case of **49**, the kink in the curves could only be detected at high electric fields (Figure 2.11). Hole mobility values measured for the amorphous layers and their field dependences are given in table 2.2.

Table 2.2. Zero-field mobilities (μ_0), mobilities (μ) at an electric field of 6.4×10^5 V cm^{-1} in cm^2 V^{-1} s^{-1} and field dependences (β) of holes and electrons in amorphous layers of **48** and **49**.

	thickness / μm	μ_0	μ	β
48	5	1.2×10^{-7}	1.7×10^{-6}	0.0033
49	3.4	1.10×10^{-7}	5.92×10^{-6}	~0.0022

The logarithm of the surface potential decay vs. time of a sample of pure material **52** did not present any observable kink, thus not allowing the detection of the electron transport. The low solubility of this compound in most of the organic solvents did not allow the preparation of a blend of this material with polycarbonate and therefore the charge transport in the doped polymer could not be studied.

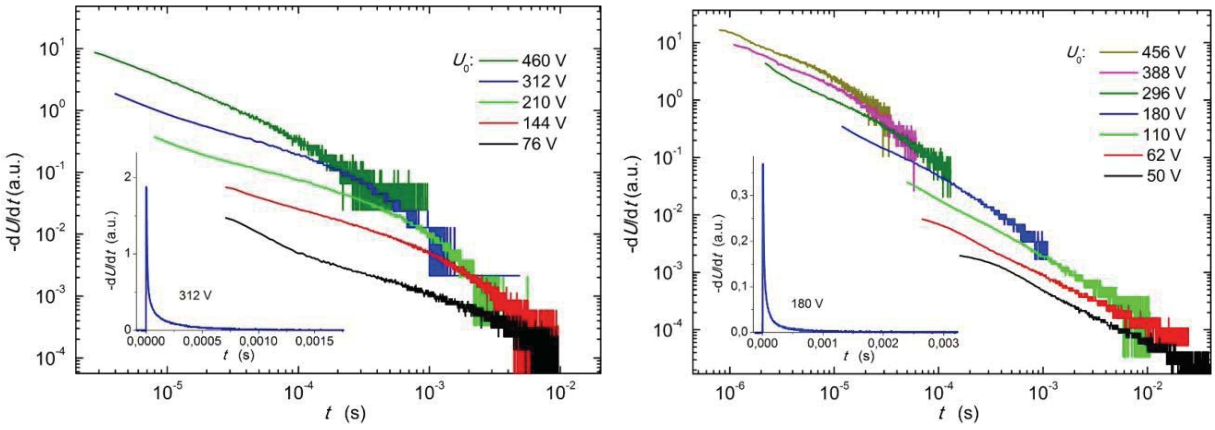

Figure 2.11. dU/dt curves in the double logarithmic scale for positive corona charge of layer of 6 μm of materials **48** and **49**. Inserts show the surface potential decay in the linear scale.

2.2.2. TOF measurements of liquid crystals

Charge transport studies of some of the synthesized mesogens by the TOF technique were performed during an internship at the Max Planck Institute for Polymer Research (Germany), under the supervision of Dr. Laquai. The TOF measurements were performed on the compounds that presented the most stable columnar mesophases, that is, compound **79**, the equimolar **79**:TNF complex and radical adduct **40**.

First attempts of measuring charge transport of these materials were performed using home-made measuring cells. These cells were built by gluing two ITO/glass electrodes parallel to each other. Control on the gap between the electrodes was achieved by adding glass spheres to the epoxy used as the glue or sandwitching polyethylene [13] strips between the electrodes (Figure 2.12). The exact thickness and uniformity of the cell gap is measured using thin film interference spectra (Figure 2.13).

Textures observed with polarized optical microscopy (POM) in all home-made cells filled with the mentioned materials revealed the presence of many defects in the liquid-crystalline phase for both slow and rapid cooling rates applied to the melted materials and no electric signal was observed in any of the experiments performed on these samples. These results were attributed to the lack of contact between the materials and the ITO electrodes. In order to avoid such problem, further experiments were performed using commercial cells.

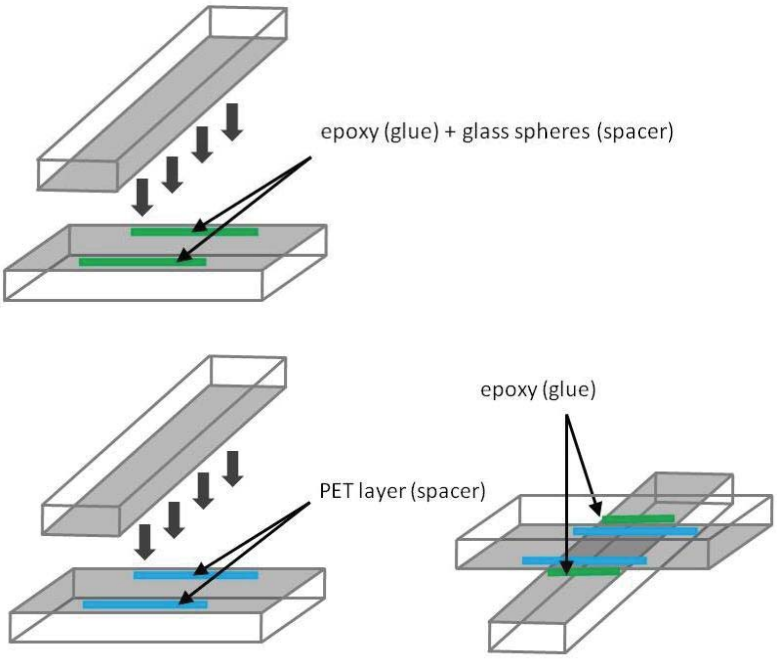

Figure 2.12. Schematic of the building process of measuring cells for liquid crystal materials using glass spheres (top) or PET layers (bottom) as spacers.

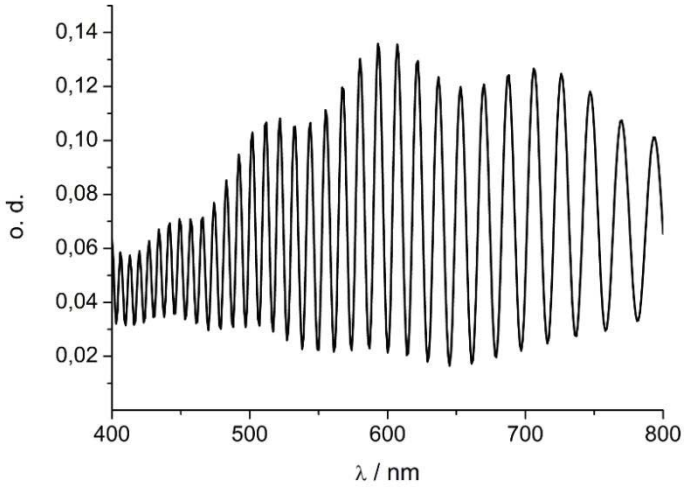

Figure 2.13. Example of the interference spectrum registered from a home-made empty cell.

Samples of material **79** prepared with the commercial cells presented different textures in the POM depending on the cooling rates applied to them from their isotropic states (Figure 2.14). Namely, lower rates led to wider homeotropic areas with a face on alignment, according to the black aspect of the samples under crossed polarizers.[14-17]

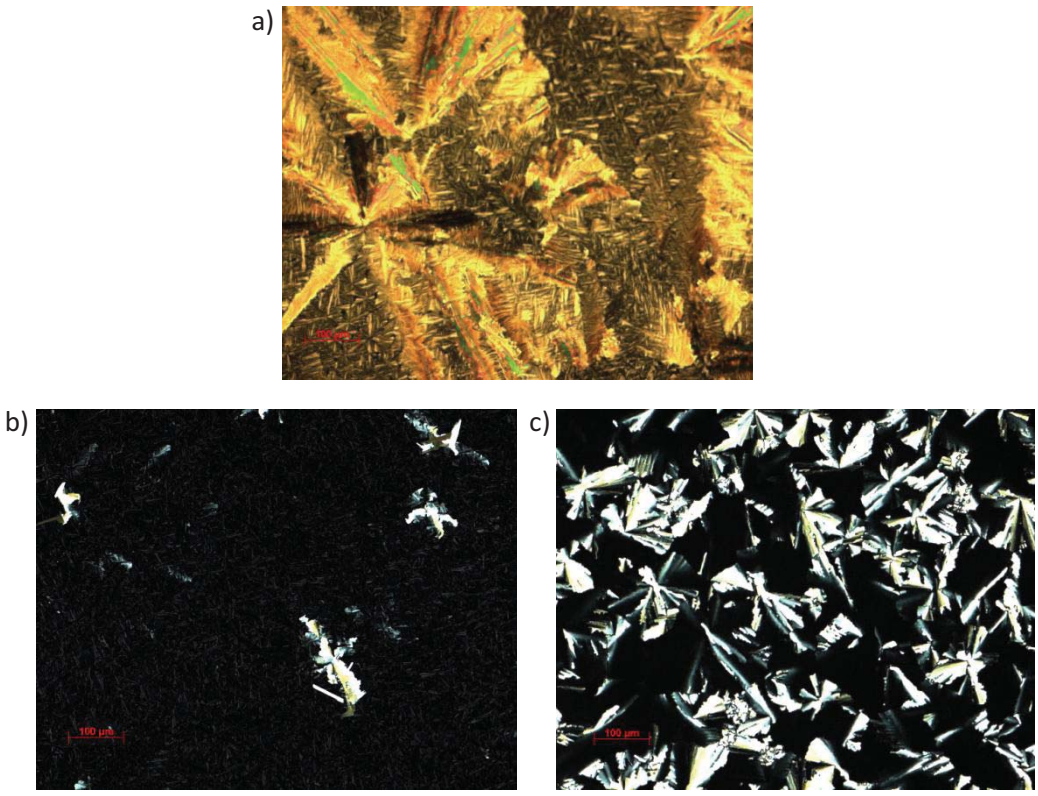

Figure 2.14. Textures found in the POM with crossed polarizers for material **79** by cooling the sample in the melted state in a home-made (10.5 ± 3 μm) cell at 0.1 °C/min (a) and in a commercial cell (4 ± 0.2 μm) at 0.2 °C/min (b) and at 2 °C/min (c)

The maximum of the absorption band of **79** overlaps with the ITO electrode absorption range. Thus the wavelength of the laser beam used to excite the material (340 nm) was chosen so that a proper absorption by the material and a minimum absorption by the ITO could be attained (Figure 2.15). Effectively, the laser pulses generated some current through the sample, thus indicating the formation of excitons within the layer. However, no inflexions were observed neither in the lineal scale nor in the logarithmic scale in any of the samples (Figure 2.16) and, consequently, transient time could not be determined for any of them.

Samples containing the complex resulting from the doping **79** with TNF in an equimolar ratio did not present any electric signal after applying the laser pulse, regardless the use of commercial cells. This result suggests that the electrons are localized at the acceptor molecules and they are not extracted from the layer. In addition, the textures formed by this material inside the cells indicated a total lack of face-on alignment (Figure 2.17)

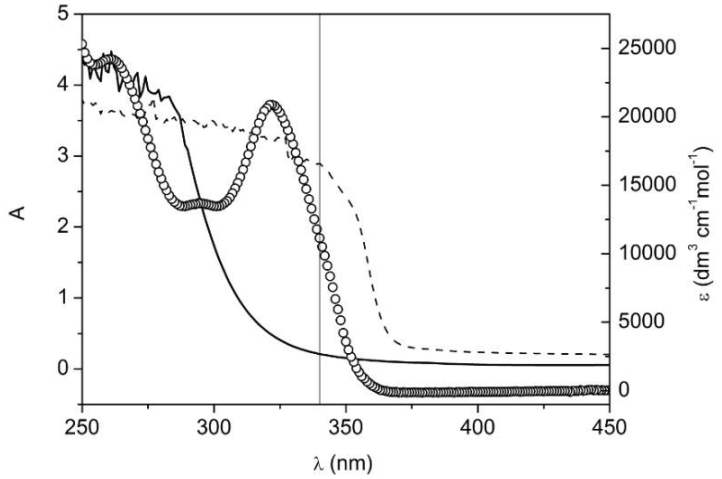

Figure 2.15. Absorption spectra of **79** in $CHCl_3$ solution (white circles) and in the liquid crystalline phase (dashed line) and of the ITO/glass substrate (solid line).

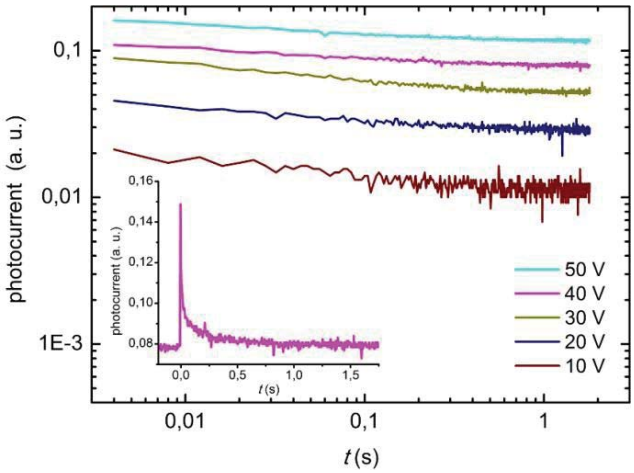

Figure 2.16. Log-log plot of the photocurrent versus time of the TOF experiment performed on material **79** at rt.

Photoexcitation of radical adduct **40** was performed with laser pulses of 355 nm, given the higher potency of the laser beam at this λ, and the absorption profile of this material. As it was discussed in section 1.2.3, radical **40** shows a wide range of light absorption. On the one hand, for a TOF experiment, a high absorption at the incident laser wavelength is preferred in order to avoid the penetration of the light into the layer. Thus, excitation of **40** in the UV region seemed more convenient. On the other hand, the absorption band that this compound presents in the visible region is attributed to the HOMO→SOMO transition, so that the injection of a hole into such an excited state is not as easy as in the case of the excited state resulting to a more energetic electronic transition that may involve the promotion of an electron to an anti-bonding MO (Figure. 2.10).

Very similar textures were obtained by slow (0.2 °C/min) and fast (2 °C/min) cooling from the isotropic state of samples of **40**. TOF measurements were performed at rt. and at 50, 60 and 70 °C in

order to detect the possible changes in the charge transport properties arising from the formation of the Col_{ho} mesophase and the temperature dependence of the mobility once the ordered mesophase is formed. Photocurrent signal presented an exponential decay both when the hole transport or the electron transport were promoted, regardless the temperature, and no transient times could be detected in any of the conditions used. Since a sand-like texture was observed in the measured samples by POM, these results were attributed to a dispersive nature of the charge transport deriving from a not complete face-on homeotropic alignment of the columns.

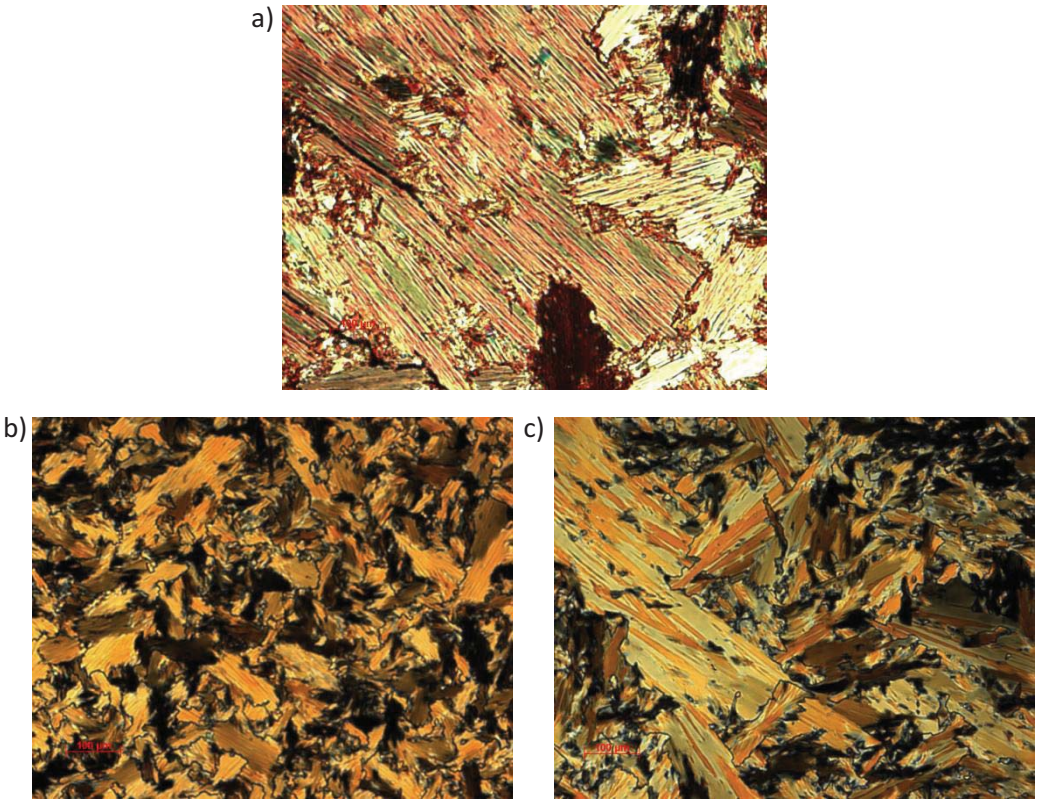

Figure 2.17. Textures observed in the POM with crossed polarizers for the **79**:TNF 1:1 complex after cooling the material from the isotropic state in a home-made cell (13 ± 1 mm) at 0.2 °C/min (a) and in commercial cells (4 ± 0.2 μm) at 0.2 °C/min (b) and at 2 °C/min (c)

Given the magnetic behavior of this material, it was decided to apply a magnetic treatment on the sample[18, 19] aiming to attain a homeotropic *face-on* monodomain and avoid any tilt angles along and within the columns, which might act as traps during the charge hopping. The sample in the isotropic state was introduced into an NMR magnet so that a strong magnetic field perpendicular to the surface of the cell acted during the cooling of the material (Figure 2.18). Namely, the magnetic spins of these discotic radicals are perpendicular to the plane containing the aromatic core, since the unpaired electron is located in the p orbital of the trivalent carbon. Thus, the magnetic field might

force the disks to be perfectly piled in a face-on fashion regarding the ITO electrodes. POM observations revealed that a face-on homeotropic alignment had been indeed attained, since no birefringence was observed (Figure 2.19).

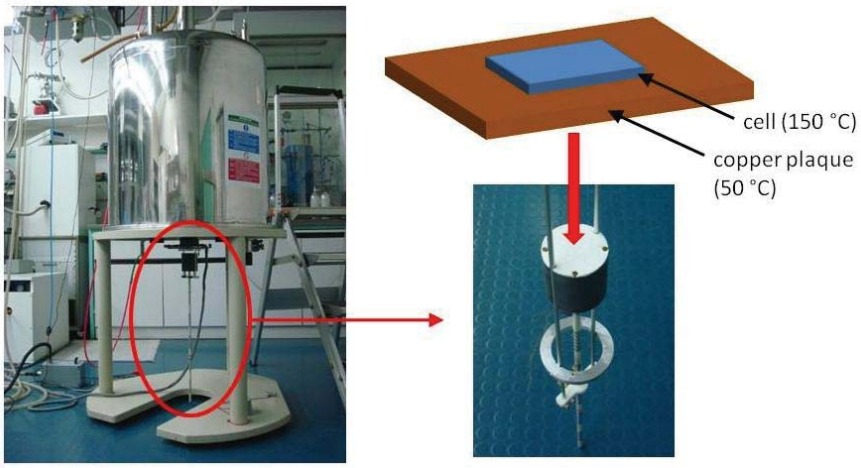

Figure 2.18. Illustration of the equipment used to align radical adduct **40** by applying a magnetic field during the cooling of the melted sample.

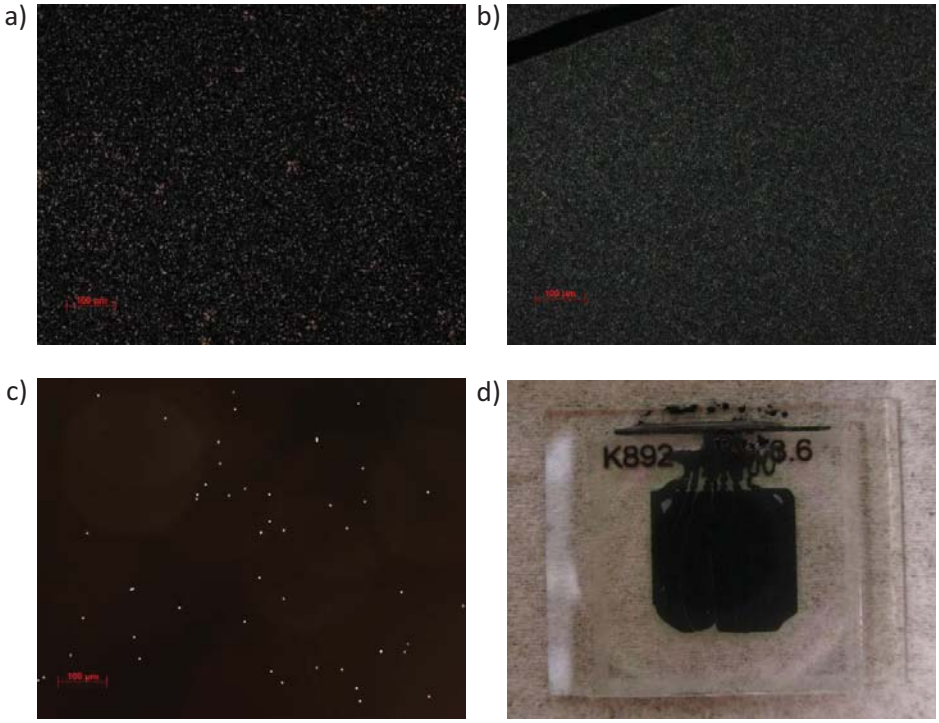

Figure 2.19. Textures observed by POM with crossed polarisers after cooling material **40** from the isotropic state in commercial cells at 0.2 °C/min (a) and at 2 °C/min (b) without applying any magnetic field and by applying a magnetic field perpendicularly to the cell plane (c). TOF cell filled with material **40**: only the area where ITO was present on both glasses was wet.

The formation of a Col_{ho} mesophase was confirmed by X-ray diffraction studies of a sample prepared in the same way on an aluminum surface (Figure 2.20). However, non-dispersive transport of holes or electrons was not detected in the TOF experiments performed at rt. or in the 50-70 °C range (Figure 2.21).

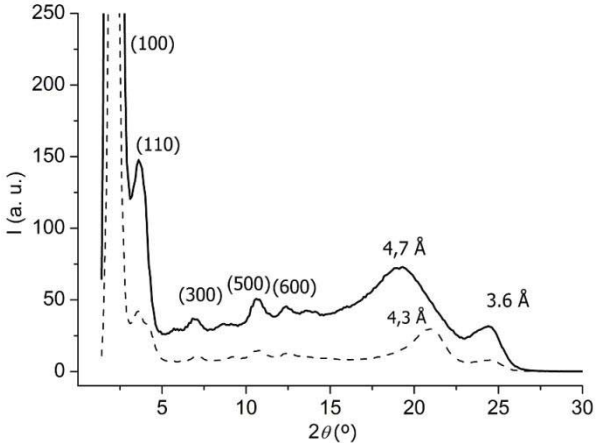

Figure 2.20. X-ray diffractogram of **40** at 30 °C (dashed line) and at 80 °C (solid line) after cooling the radical while applying a magnetic field perpendicular to the plane of the aluminum substrate.

It is difficult to find an explanation for the lack of non-dispersive charge transport in this radical, given the great number of variables that play a role in the TOF experiments, such as electrode/organic layer interfaces, thickness, number of generated charges, defects and impurities in the material, etc. Thus, more studies should be done in order to conclude if charge transport can take place along the columns of the radical.

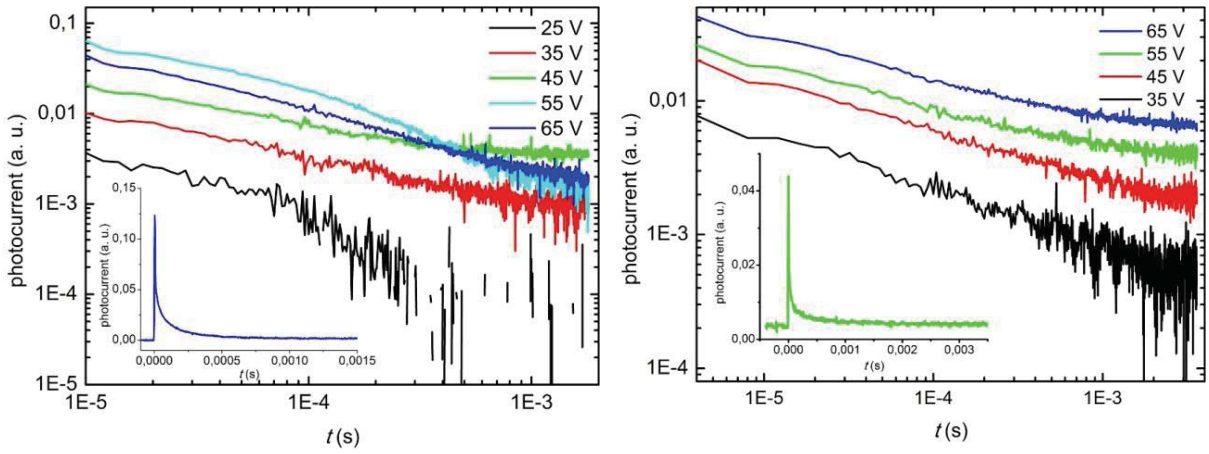

Figure 2.21. Photocurrents of **40** at 70 °C after the magnetic alignment for positive (a) and negative (b) tensions in the double logarithmic scale. Inserts show the TOF transient in the linear scale.

2.3. Summary

Bipolar charge transport was detected by XTOF techniques in radical adducts **1** and **11**. This feature is in agreement with the bipolar reversible redox characteristics observed by cyclic voltammetry, attributed to the radical nature of these compounds. The mobility values registered for both holes and electrons in these materials are among the highest reported in the literature.

The role of the heterocycle proved to be of main importance in the temporal features of the charge transport of the studied radical adducts. The lack of carbazole or indole fragments in the **TTM** radical leads to more dispersive regimes, while radical adducts **1**, **11** and **12** presented easily detectable transient times for hole-transport.

Amorphous layers of the molecular glasses based on the *N*-phenylcarbazole core, **48** and **49**, showed dispersive hole-transport in the XTOF experiments. Studies of the charge transport properties of **52** by XTOF technique were limited by the difficulties in the preparation of the corresponding layers due to solubility problems.

A complete homeotropic alignment of the columnar mesophase within the measuring cells could not be detected by POM observations for material **79** after different thermal treatments. Neither could transient time be determined the photocurrent signals of this material. Similar results were obtained for the **79**:TNF complex (1:1) and radical mesogen **40**.

A face-on homeotropic alignment of the columnar mesophase for radical adduct **40** was attained after a magnetic treatment applied to the melted material, as it was confirmed by POM observations and X-ray diffraction. However, any non-dispersive charge transport could be detected for this material for holes or electrons at different temperatures within the range of temperatures going from rt. to 70 °C.

2.4. Experimental section

2.4.1. XTOF measurements

The binding polymer used to prepare blends, bisphenol Z polycarbonate (PCZ) Iupilon Z-200, was obtained from Mitsubishi Gas Chemical Co. and methyl cellulose was obtained from Aldrich.

The samples for the charge carrier mobility measurements were prepared by casting the tetrahydrofurane solutions of the pure materials and of the molecular mixtures of the studied compound and polycarbonate in 1:1 weight proportion on polyester films and Al layer with a methylcellulose sublayer. The thickness of the charge-transporting layer were measured with a microinterferometer.

Electric field inside the material layer was created by charging of a corona. Illumination with pulses of N_2 laser (λ = 337 nm, 1 ns) generated charge carriers at the layer surface producing a decrease up to 1-5% of the initial potential before illumination. Surface potential decrease rate, dU/dt, was measured by the capacitance probe connected to the wide frequency band electrometer. Transient time (t_t) was thus determined from the kink in the log-log scale dU/dt curve or from the kink in the integral $\Delta U/t$ curves, in the case of electron transport in layers of pure radical adducts **1** and **11**. Drift mobility was then calculated according to the formula $\mu = d^2/U_0 t_t$, where d is the layer thickness and U_0 is the initial surface potential before laser pulse. Field dependences of the hole and electron mobilities were determined according to the formula $\log\mu = \beta E^{1/2}$.

2.4.2. TOF measurements

Home-made cells were built using two different spacers: a mixture of glass spheres (9-13 μm) provided by Aldrich and epoxy provided by Epoxy Technology and PET layers (10 μm). Two glass substrates (1.1 mm thickness) containing ITO (20 Ω/sq) were cleaned in an ultrasounds bath with an Alconox solution (1 g/ml, 10 min.), then with ethanol (10 min.) and afterwards with *iso*-propanol (10 min.). After drying the two electrodes with N_2, the spacers were placed on the sides of one of the substrates and the other substrate is placed parallel to the first one. The epoxyde was cured by illuminating the epoxyde with a UV lamp (366 nm, 8 W, 5 min.)

The exact thickness and uniformity of the home-made cell gap is measured using thin film interference spectra obtained with an UV spectrophotometer.

Commercial cells were purchased to Instec®. The cells belonged to the SA series and contained 10x10 mm area of no-patterned ITO (30 Ω/sq) with a 4 μm gap.

A small quantity of the organic material is deposited at the entrance of the cell and is then heated until melting. The cell gap is filled by capillarity action and the liquid crystal arrangement is attained by applying a selected cooling rate between 0.1 and 2 °C/min. under nitrogen atmosphere in a Linkam THM 600 temperature controller.

Textures of the samples were checked in a Zeiss, Axiophot Microsope polarized light optical microscope and photographied using a Zeiss, Axiocam camera. Wide angle X-ray scattering (WAXS) experiments were performed by Michael Bachs using a standard copper anode (2.2 kW) source with a pinhole collimator equipped with an X-ray mirror (Osmic type CMF15-sCu6) and a Bruker detector (High-Star).

For TOF measurements the samples were housed in a temperature controlled home-built cryostat under a dynamic vacuum of typically 10^{-5} mbar. Excitation at the selected wavelengths was provided by an Spectra Physics, Quanta Ray pumplaser equiped with a GWU Lasertechnik VISIR2 optical parametric oscillator (OPO) and a a GWU Lasertechnik second harmonic generation (SHG) The samples were illuminated from the ITO side and the current transient was detected with a Tektronix oscilloscope (TDS 524A) triggered by the laser pulse.

References

[1] S. Tiwari, N. Greenham, *Opt. Quantum Electron.* **2009**, *41*, 69-89.
[2] Y. Shirota, H. Kageyama, *Chem. Rev.* **2007**, *107*, 953-1010.
[3] V. Coropceanu, J. Cornil, D. A. da Silva Filho, Y. Olivier, R. Silbey, J.-L. Bredas, *Chem. Rev.* **2007**, *107*, 926-952.
[4] P. Strohriegl, J. V. Grazulevicius, *Adv. Mater.* **2002**, *14*, 1439-1452.
[5] I. Musubu, H. Nobuyasu, Y. Norimasa, M. Tetsuzo, N. Susumu, K. Toshiki, T. Yoshio, *Phys. Status Solidi (RRL)* **2007**, *1*, R37-R39.
[6] D. K. Oh, S. M. Hong, C. E. Lee, B. S. Kim, J. I. Jin, *Solid State Commun.* **2005**, *136*, 585-590.
[7] V. Peciuraite, V. Vaitkeviciene, S. Grigalevicius, J. V. Grazulevicius, V. Jankauskas, *Monatsh. Chem. Chem. Month.* **2006**, *137*, 1053-1062.
[8] T. H. Huang, J. T. Lin, L. Y. Chen, Y. T. Lin, C. C. Wu, *Adv. Mater.* **2006**, *18*, 602-606.
[9] P. M. Borsenberger, W. T. Gruenbaum, E. H. Magin, S. A. Visser, D. E. Schildkraut, *J. Polym. Sci. Part B: Polym. Phys.* **1999**, *37*, 349-356.
[10] V. Gamero, D. Velasco, S. Latorre, F. López-Calahorra, E. Brillas, L. Juliá, *Tetrahedron Lett.* **2006**, *47*, 2305-2309.
[11] D. Velasco, S. Castellanos, M. Lopez, F. Lopez-Calahorra, E. Brillas, L. Julia, *J. Org. Chem.* **2007**, *72*, 7523-7532.
[12] M. López, D. Velasco, F. López-Calahorra, L. Juliá, *Tetrahedron Lett.* **2008**, *49*, 5196-5199.
[13] S. Christian, R. Imma, R.-M. Daniel, Z. Yuxia, V.-G. José, W. Klaus, J. Peter, C. Koen, P. André, R. Concepció, V. Jaume, *Angew. Chem. Int. Ed.* **2004**, *43*, 5266-5268.
[14] C. Deibel, D. Janssen, P. Heremans, V. De Cupere, Y. Geerts, M. L. Benkhedir, G. J. Adriaenssens, *Org. Electron.* **2006**, *7*, 495-499.
[15] E. Grelet, H. Bock, *Europhys. Lett.* **2006**, *73*, 712-718.
[16] C.-y. Liu, A. Fechtenkotter, M. D. Watson, K. Mullen, A. J. Bard, *Chem. Mater.* **2002**, *15*, 124-130.
[17] K. Marcel, L. Frederic, M. Klaus, W. Gerhard, *Appl. Phys. Lett.* **2006**, *89*, 252103.
[18] M. I. Boamfa, S. V. Lazarenko, E. C. M. Vermolen, A. Kirilyuk, T. Rasing, *Adv. Mater.* **2005**, *17*, 610-614.
[19] R. Guo, Y. Reznikov, K. Slyusarenko, S. Kumar, *Liq. Cryst.* **2007**, *34*, 955 - 961.

Consulted bibliography

Michael C. Petty. *Molecular Electronics. From principles to practice.* Chichester, Wiley & Sons Ltd. (2008).

Markus Schwoerer, Hans Christoph Wolf. *Organic Molecular Solids*. Weinheim, Wiley-VCH (2007)

Paul M. Borsenberger, David S. Weiss. *Organic Photoreceptors in Xerography.* Vol. 49, Optical Engineering Series. New York, Marcel Dekker Inc. (1998).

3. Electronic devices

3.1. Theoretical basis

3.1.1. Organic thin film transistors (OTFTs)

Organic thin film transistors (OTFTs) are the key building block for organic electronics showing flexibility and lightness, as it was proved by the first full-color, video-rate, flexible, all plastic display reported by Sony in 2007, based on OTFTs and OLEDs devices. OTFTs consist of three-terminals (gate, source and drain), an insulator (gate dielectric) and an organic semiconductor as an active element. The voltage applied to the metallic gate affects an electric current flowing between source and drain electrodes. This control feature allows the device to be switched from an on state to an off state and back again, an operation that is the basis of many electronic functions.

Two types of structures, top-contact and bottom-contact electrode configurations, have been adopted for the fabrication of OTFTs (Figure 3.1). When there is no voltage application to the gate electrode, only small currents flow between the source and drain electrodes; this state is referred to as the *off-state* of transistor. When negative voltage, for example, is applied to the gate electrode, hole carriers in the organic semiconductor layer become accumulated at the interface with the gate dielectric, and hence, hole transport takes place from the source to the drain electrode; this state corresponds to the *on-state* of transistor. This type of device is called a p-channel device. Likewise, application of positive voltage to the gate electrode causes electron transport in the case of n-channel devices. The current flow between the source and the drain (I_D) can be modulated by the magnitude of both the gate voltage (V_G) and the source/drain voltage (V_D).

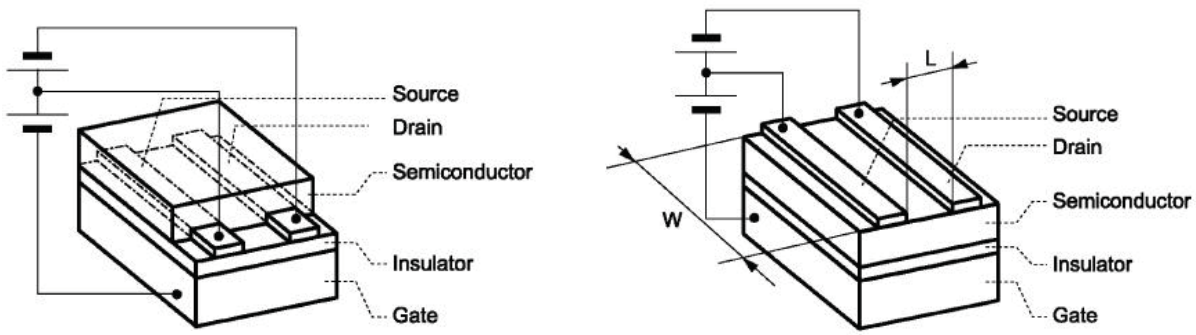

Figure 3.1. Structures of OTFTs: bottom contact (a) and top contact (b) configurations.

Since charge carriers are injected from the source electrode into the organic layer, metals with the proper work function Ψ_m (the minimum energy required to remove an electron from the solid) must be chosen for the source and drain electrode. Typical values of Al are ranged between 4.1 and 4.3 eV and of Au between 5.1 and 5.5 eV. Thus, Au is used for p-type OTFTs so that holes can be injected in

the HOMO of the organic material, since HOMO energy for hole-transporting materials is usually in the 5-6 eV range. Similarly, Al is used for n-type materials, since their LUMO energies have values around the 3 eV.

The *output* characteristics of an OTFT are obtained by plotting I_D versus V_D under a given V_G (Figure 3.2). For low drain voltage V_D, the channel acts as a resistance; I_D increases linearly with V_D (linear regime) and is given approximately by the equation

$$I_D = \frac{WC_i}{L}\mu_{FET}\left(V_{GS} - V_T - \frac{V_D}{2}\right)V_D \tag{3.1}$$

where, μ_{FET} is the field-effect mobility of the charge carrier, L is the channel length, W is the channel width, C_i is the capacitance per unit area of the gate dielectric, and V_T is the threshold voltage, a constant for a particular device.

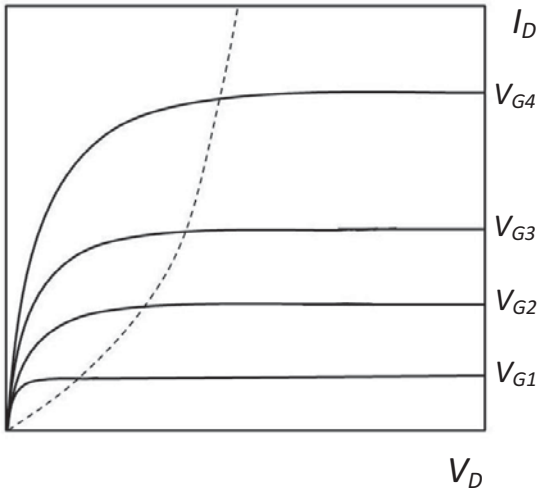

Figure 3.2. Output characteristics of an OTFT. The dashed line indicates where the channel of the OFET becomes pinched off.

As the magnitude of V_D increases, I_D tends to saturate. This is the result of *pinch-off* of the accumulation layer (Figure 3.3). The combination of the voltages applied to the gate and the drain will produce a wedge-shaped accumulation layer. At pinch-off, the effective cross-sectional area of the conduction channel becomes zero at the drain. Thus, drain current beyond the pinch-off point remains essentially the same and follows the equation

$$I_D = \frac{WC_i}{2L}\mu_{FET}(V_G - V_T)^2 \tag{3.2}$$

The transition between the saturated and the linear region is defined as $V_D = V_G - V_T$ and is indicated in Figure 3.2 with a dashed line.

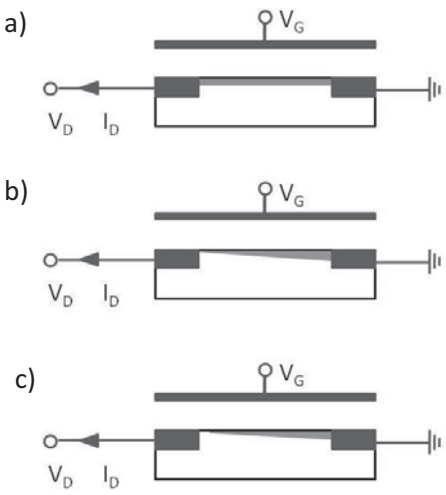

Figure 3.3. Diagram showing the effect of applying an increasing V_D to an OTFT given a constant V_G. Linear regime (a): a channel extends between the source and the drain electrodes. Pinch-off (b): the channel becomes zero at the drain electrode. Saturation region (c): carriers must cross the depletion layer to reach the drain electrode.

The *transfer* characteristics of an OTFT are obtained by measuring I_D versus V_G given a constant V_D (Figure 3.4 left) For the proper values of V_D, the current flowing from source to drain increases in an exponential regime first and in a lineal regime later with V_G. Two parameters can be calculated from this plot: the field effect mobility in the linear regime from the transconductance, g_m, for a given V_D

$$g_m = \left(\frac{\partial I_D}{\partial V_G}\right)_{V_D} = \frac{WC_i}{L}\,\mu_{FET} V_D \tag{3.3}$$

for a given V_D; and the I_{on}/I_{off} ratio of the device, as the ratio of the current flowing in the accumulation regime to that in depletion. That is, given a p-channel device and a sufficient drain tension, the ratio between the current when $V_G < 0$ (depletion regime, on) and when $V_G > 0$ (accumulation regime, off).

By applying the same tension to the drain and the gate ($V_D = V_G$) the device works in the saturation regime (Figure 3.4 right). The plot of $\sqrt{I_D}$ measured for low tensions to $V_G >> V_T$ adjust a lineal equation $y = Ax - B$, where

$$\mu_{FET} = \frac{A^2}{\frac{WC_i}{2L}} \qquad V_T = \frac{B}{A} \tag{3.4}$$

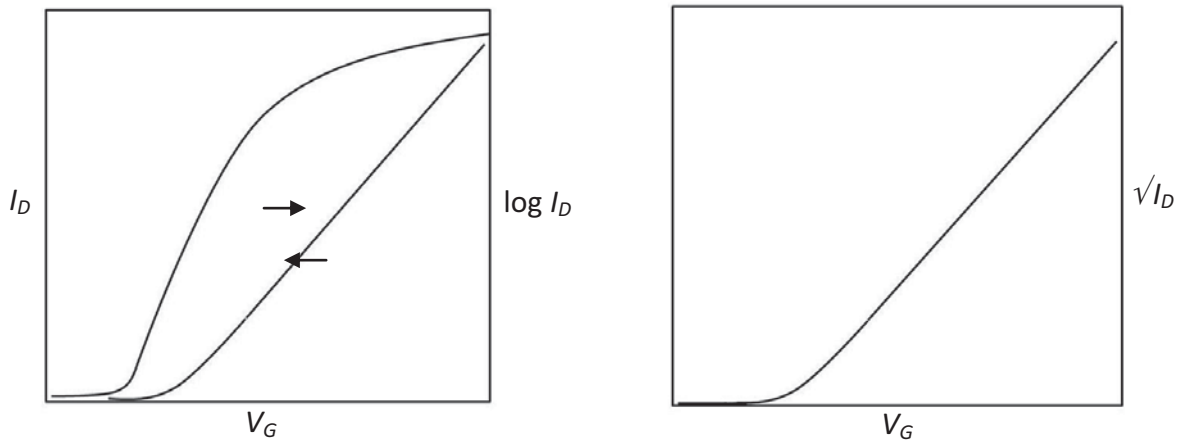

Figure 3.4. Transfer characteristics (left) and saturation characteristics (right) of an OTFT.

3.1.2. Organic solar cells.

Solar cells are devices that directly convert light into electrical current. Devices for such photoelectric conversion with organic photoactive materials are mainly classified in organic photovoltaic cells (OPV) and dye-sensitized solar cells (DSSC).

3.1.2.1. Organic photovoltaic devices (OPVs)

Organic photovoltaic devices (OPVs) consist of thin films of organic photoactive materials sandwiched between two different electrodes. When the incoming photons have energy greater than the HOMO-LUMO gap, these are absorbed, creating coulombically bound electron–hole pairs called excitons. Electric current is then created when the excitons are dissociated, something that can be conveniently done at a convenient interface (e. g. the junction between a donor organic material and an acceptor organic material).

The current versus voltage behavior of the OPV cells is shown in Figure 3.5. In the dark, the device behaves as a diode, that is, current flows only for one polarity of the external power source (forwarded bias) but not for the opposite (reverse biased) following the equation

$$I = I_0 exp\left(\frac{eV}{nk_BT}\right) \tag{3.5}$$

where *n* is the ideality factor of the diode. Thus, the plot of current versus voltage, that is, the I-V characteristics of OPVs exhibit rectifying properties.

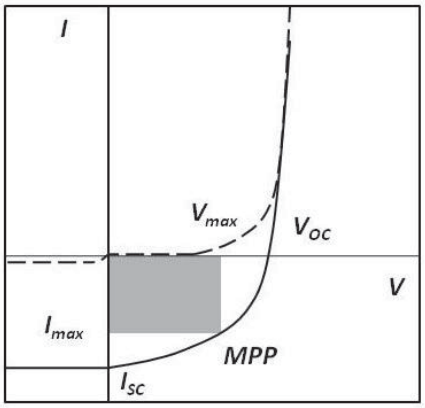

Figure 3.5. Current versus voltage characteristics for an OPV in the dark (dashed line) and under illumination (solid line). The shaded area represents the maximum power available from the cell. MPP is the maximum power point defined as the maximum value for the *I* x *V* product, I_{max} x V_{max}.

Under illumination, the I-V characteristic is moved down the current axis as photocurrent is generated. Two important device parameters are the open-circuit voltage (V_{OC}) and the short-circuit current (I_{SC}). The former represents the voltage appearing across the terminals for the solar cell when no current is drawn from the device; this is the maximum attainable voltage that the OPV cell can provide. When the device terminals are short-circuited, I_{SC} represents the maximum current that the solar cell can provide. The performance of OPVs is evaluated by power conversion efficiency (η) and field factor (*FF*) defined as:

$$\eta = \frac{I_{max} \times V_{max}}{P} \tag{3.6}$$

$$FF = \frac{I_{max} \times V_{max}}{I_{SC} \times V_{OC}} \tag{3.7}$$

where I_{max} and V_{max} are the values of current and voltage for which the maximum IxV product is obtained, the maximum power point, *MPP*. It is clearly desirable to produce devices with *FF* values as close to unity as possible.

Both single layer (Schottky-type cells) and pn-heterojuctions OPVs had been studied. In Schottky-type cells the photoactive layer consists of a single organic material. Depending on if the current flows by applying a negative or a positive voltage to the metal electrode the device is classified in p-type or n-type, respectively. In other words, p-type photodiode are fabricated by using hole-transporting photoactive materials and n-type photodiodes, by using electron-transporting photoactive materials. Schottky-type cells tend to produce a reasonable V_{OC} but their photocurrent is typically very low,[1, 2] as a consequence of the recombination of both excitons and of holes and electrons (polarons).

The origin of pn-heterojunction OPVs took place when C. W. Tang discovered in 1985 that, by making two-layer OPV cells with organic semiconductors that have offset energy bands, the efficiency of OPV cells could be improved as a result of the exciton dissociation at the interface between the two semiconductors.

Pn-heterojunction OPVs are based on a photoactive layer containing an electron-donor (p-type) and an electron-acceptor (n-type) organic material. The cells can be built in different designs, represented in Figure 3.6: bilayer, disordered bulk-heterojunktion and ordered bulk-heterojunction.[2]

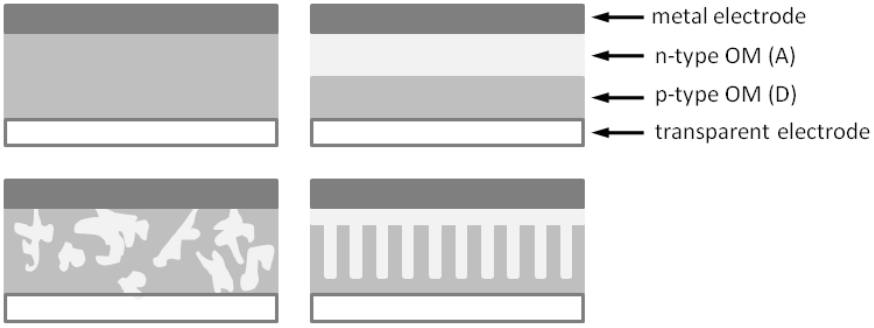

Figure 3.6. Four device architectures of conjugated polymer-based photovoltaic cells: single-layer PV cell (a); bilayer PV cell (b); disordered bulk heterojunction (c); ordered bulk heterojunction (d). OM = organic material, A =electron acceptor, D = electron donor.

The photovoltaic mechanism in these devices is illustrated in Figure 3.7 and proceeds as follows: 1) light absorption by organic semiconductors to form excitons, 2) diffusion of excitons, 3) exciton dissociation and charge carrier generation, 4) charge transport through the organic layers, and 5) charge collection at both electrodes.

Incident photons can be absorbed by either the p-type (D) or the n-type (A) material. Excitons can be dissociated into polarons (holes an electrons) at the D/A heterojunction. The energy level offset between the molecular orbitals of the donor and acceptor layers provides the driving force for elementary charge transfer. For example, when the LUMOs energy difference is greater than the exciton binding energy, subpicosecond charge transfer takes place from the donor to the acceptor. Excitons within the acceptor layer are similarly dissociated by hole transfer between the HOMOs at the heterojunction. Charge recombination pathways also exist. However, recombination rate constants in efficient heterojunctions are typically at least an order of magnitude slower than those for charge separation, giving rise to persistent, long-lived ionized states.

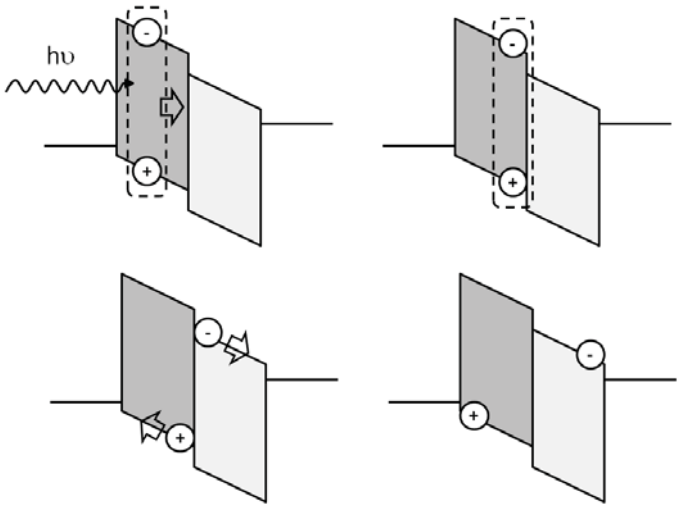

Figure 3.7. Energy diagram for a pn-heterojunction OPV during the photovoltaic mechanism. Dark grey represents the donor organic material and pale grey the acceptor donor material. The top and the bottom of the of the coloured areas represent the LUMO and HOMO levels of the materials, respectively.

Once the exciton is dissociated, holes and electrons are transported to the cathode (transparent electrode) and the anode (metal electrode) through the p-type and the n-type materials, respectively. Hence the donor and acceptor charge-carrier mobilities play an important role in this step and influence the device performance.

Another important feature of the organic materials used in the fabrication of OPVs is their optical absorption. Namely, it should match the incoming photon flux from the solar irradiation. The peak in the solar spectrum has a useful range of about 0.3-2 μm what means that, for OPVs, the most effective conversion of this radiation to electrical energy is achieved using semiconductors with a E_{gap} of around 1 μm (~1.2 eV).

Therefore, a way to evaluate the performance of an OPV is recording its spectral response, which is defined as the ratio of the current generated by the solar cell to the power incident on the solar cell. A similar evaluation is the record of the external quantum efficiency (EQE) of the device for different wavelengths, that is, the ratio of the number of charge carriers collected by the solar cell to the number of photons of a given wavelength shining on the solar cell

For many organic materials, photocurrent (EQE) and absorption spectra are either well-matched (symbatic) or almost complement one another (antibatic). If the maximum photocurrent coincides with the strongest absorption, the photocurrent response is said to be *symbatic* with the absorption spectrum. If the maximum photocurrent occurs at photon energies where absorption is weakest, the

photocurrent response is said to be *antibatic*. The symbatic and antibatic behavior arise from the low mobility of carriers in the organic material, which make the charge photogeneration and the recombination processes to be localized on certain interfaces. This results in filter effects that influence the photocurrent spectral shapes.[3]

3.1.2.2. Dye sensitized sollar cells (DSSCs)

DSSCs are artificial photosystems containing a light-harvesting antenna and were first manufactured by Grätzel's in 1991 by using a dye-sensitized titanium dioxide thin film with a redox electrolite.[4] This device operates as depicted schematically in Figure 3.8. Upon a photon absorption, a dye electron is elevated to an excited state. The dye then injects the excited electron directly into the coduction band of a semiconductor, which subsequently creates a current in an external circuit. The electrolite then reduces the dye, regenerating it.

DSSCs using nanocrystalline, porous TiO_2, on which an organic dye is adsorbed, and I_3^-/I^- redox species in solution or gels have been a topic of current intensive research and development because of the high conversion efficiencies reaching 10%. Grätzel and co-workers developed also DSSCs that use a solid electrolyte since the liquid electrolyte cells required complete encapsulation and were difficult to handle. The new electrolyte was an amorphous organic hole-transporter (OMeTAD) and the latest improved devices reached power conversion efficiencies of 2.6%.

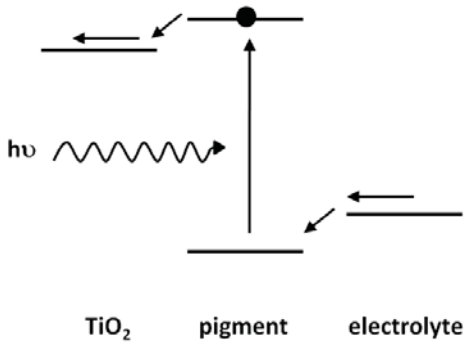

Figure 3.8. Energy diagram of a DSSC during the carrier transport.

3.1.3. Organic light emitting diodes (OLEDs)

OLEDs are current-driven devices that utilize emissions from the electronically excited states of molecules. The simplest OLED is an electroluminescent (EL) compound, such as a polymer or dye, sandwiched between metals of high and low work function, as depicted in Figure 3.9. On application of a voltage, electrons are injected from the low work function electrode (cathode) into the LUMO level of the organic compound and holes from the high work function electrode (anode) into the

HOMO level, thus generating an electronically excited state or exciton, which is followed by the emissive relaxation of the exciton. A huge improvement of the OLEDs performance is achieved, though, by separating the functions of charge transport and light emission. Electron- and hole-transporting layers can be introduced between the cathode and the emitting layer and between the anode and the emitting layer, respectively, to improve and balance the injection of charge carriers (Figure 3.9 right).

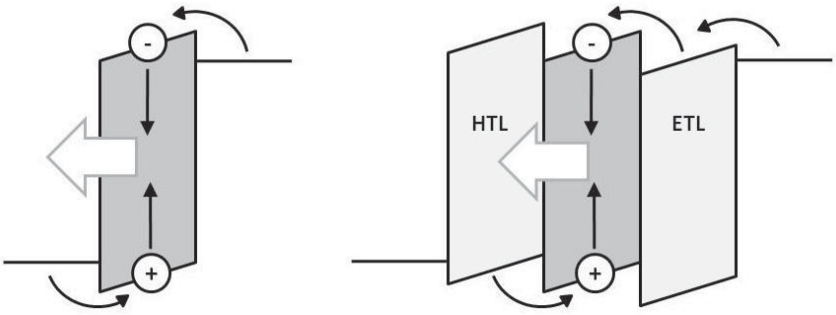

Figure 3.9. Energy band structure of a single layer (left) and a multilayer (right) OLED. HTL and ETL stand for hole-transporting layer and electron-transporting layer, respectively.

OLEDs act as rectifying devices and present I-V characteristics as those exhibited by OPVs in the dark (Figure 3.5). A convenient measure of the properties of an OLED is the luminous efficiency, η_l, in cd A^{-1}, which is calculated

$$\eta_l = \frac{AL}{I} \tag{3.7}$$

where *A* is the device active area, *I* is the current and *L* is the luminance of the OLED, in cd m^{-2}, which refers to the luminous intensity per unit area emitted by the device. Another frequently used display efficiency unit is the luminous power efficiency or luminosity, η_p, measured in lm W^{-1}. This is the ratio of luminous power emitted in the forward direction to the total electrical power required to drive the OLED at a particular voltage.

Work is focused on the use of both low molecular weight organic molecules and polymers as EL materials and there is considerable industrial interest in the application of such materials to various display technologies. Bipolar emitting materials are specially sought since this way both holes and electron can migrate through the material till the recombination takes place. In addition to such charge transport properties, the emitting materials should have high luminescence quantum

efficiencies. In table 3.1 are given the luminous efficiency and the luminous power efficiency of some commercial polymer-based OLEDs.

Table 3.1. Performance of some commercial polymer-based OLEDs.

color	voltage (V)	η_l at 400 cd m^{-2} (cd A^{-1})	η_p at 400 cd m^{-2} (lm W^{-1})
red	3.6	2.3	2.0
green	4.9	15.8	10.1
blue	5.5	9.6	5.5
white	6.8	4.5	2.1

3.2. Results and discussion

The fabrication and evaluation of the organic thin film transistors (section 3.2.1) and the organic photovoltaic devices (section 3.2.2) presented in this chapter were performed in the Departament d'Enginyeria Electrònica of the Universitat Politècnica de Catalunya (UPC) under the supervision of Dr. Puigdollers. Preliminary studies on organic emitting diodes were performed by Dr. Cheylan in the Institut de Ciències Fotòniques (ICFO) and only a summary of the results will be given in section 3.2.3.

3.2.1. Organic thin film transistors (OTFTs)

The materials used for the preparation of OTFTs were the two radicals **1** and **11** and the non-radical molecular glass, **49**. The formers were chosen given their high hole and electron mobility values observed by the XTOF technique while material **49** was chosen for its reversible redox characteristics.

OTFTs were built in a top-contact configuration using SiO_2 as the gate dielectric, metallic Si for the gate and Al and Au as metals for the drain and metal electrodes. The organic layer was deposited on the SiO_2 wafer by vacuum thermal evaporation (VTE). The equipment used is shown in Figure 3.10 and allowed the regulation of three parameters: 1) the substrate temperature; 2) the deposition rate and; 3) the thickness of the organic layer. Substrate temperature and deposition rate can influence dramatically thin film morphology and thus the electronic transport characteristics of OTFTs. Slower deposition rates and higher substrate temperatures lead to larger grains, which has a beneficial effect on the transports because grain boundaries interfere with the transports.[5] Figure 3.11 displays one of the prepared OTFTs. Table 3.2 shows the parameters used for the deposition of each compound.

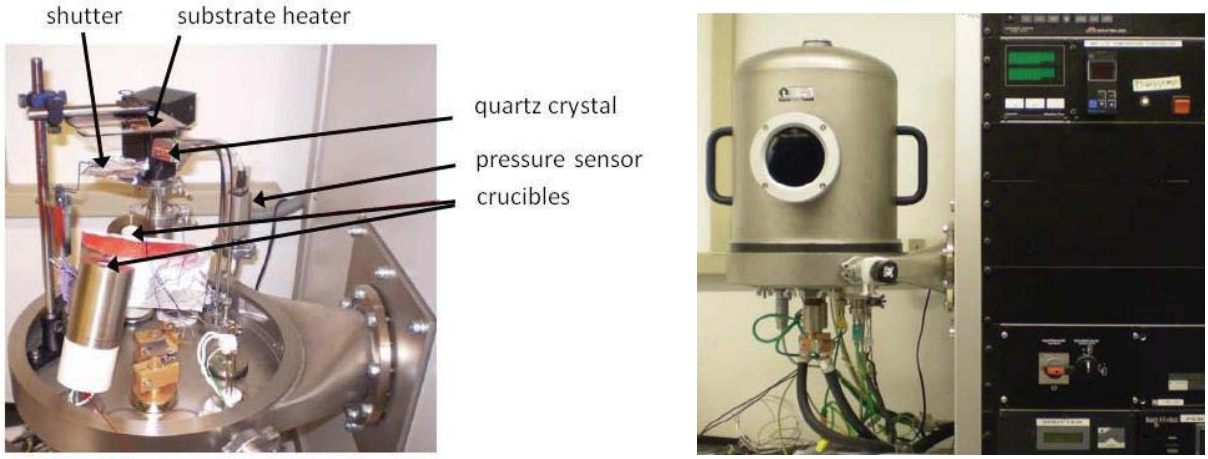

Figure 3.10. Vacuum thermal evaporation equipment: internal components (left) and external view (right).

Table 3.2. Deposition rates, substrate temperature and metals for the drain and source electrodes used for the fabrication of the OTFTs and final thickness of the organic layer.

	material	rate (Å/s)	thickness (nm)	T	electrode
D1	**1**	0.2	20	rt.	Au
D2	**1**	0.3	50	80 °C	Au
D3	**11**	0.3	50	rt.	Au
D4	**11**	0.2	50	rt.	Au
D5	**11**	0.2	50	rt.	Al
D6	**49**	0.2	50	rt.	Au

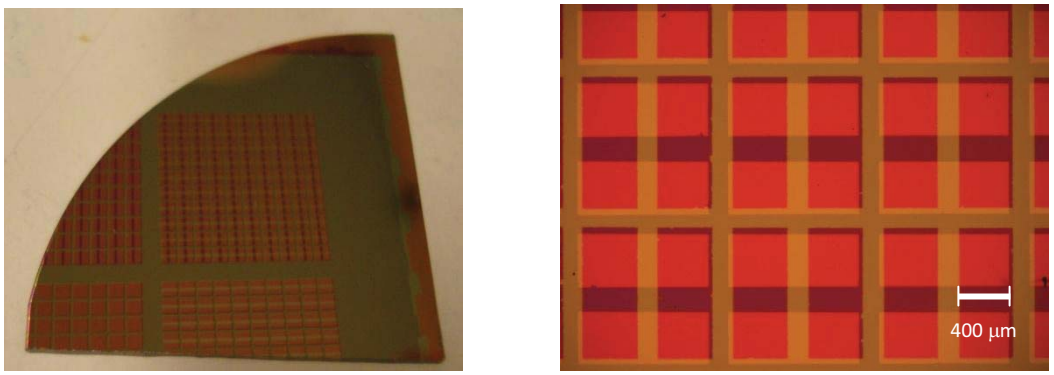

Figure 3.11. OTFTs based on radical **1** and Au electrodes. On the right, magnified aspect of the fabricated OTFTs.

It is remarkable that the molecular orbital involved in the charge transport in the radical compounds in the OTFTs is the SOMO, whether the charge carriers are electrons (n-channel) or holes (p-channel), since injection of both types of charge carriers takes place in this orbital. In other words, the oxidation and the reduction of the radical species to produce a hole or an electron, respectively, correspond to the extraction or insertion of a single electron from or into the half-filled molecular orbital, the SOMO. Accordingly, the two electrochemical parameters that should be considered in these devices are the ionization potential (IP) and the electron affinity (EA), like in the case of the traditional closed-shell systems, but with the difference that IP and EA values do not correspond to the HOMO and LUMO energies for the radical compounds.

Given their charge transport properties that radicals **1** and **11** had shown in the XTOF experiments, OTFTs based on radicals **1** and **11** were expected to be bipolar, that is, to form both n-channels and p-channels by applying positive and negative V_G, respectively. Certainly, source to drain current was detected for $V_G < 0$ in the devices based on radical **1**, D1 and D2, thus revealing hole-transport through a p-channel, despite the IP values of radical **1** in solution (5.6 eV) and in the amorphous film (5.8 eV) are higher than the work function values of Au. However, no electron-transport took place

for $V_G > 0$. Output and transfer characteristics of devices D1 and D2 are shown in Figure 3.12 and in Figure 3.13, respectively.

Devices based on radical **11**, D3 and D4, though, did not give any current signal neither for negative nor for positive V_G values, even by using Al for the drain and source electrodes (D5) in order to facilitate the electron injection (EA = 4.2 eV). The reason for these negative results is not clear and is a subject of further studies.

Device D6 proved to be a p-type OTFT, according to the redox characteristics of material **49**, which presents a reversible oxidation. Output and transfer characteristics recorded for D6 are shown in Figure 3.14.

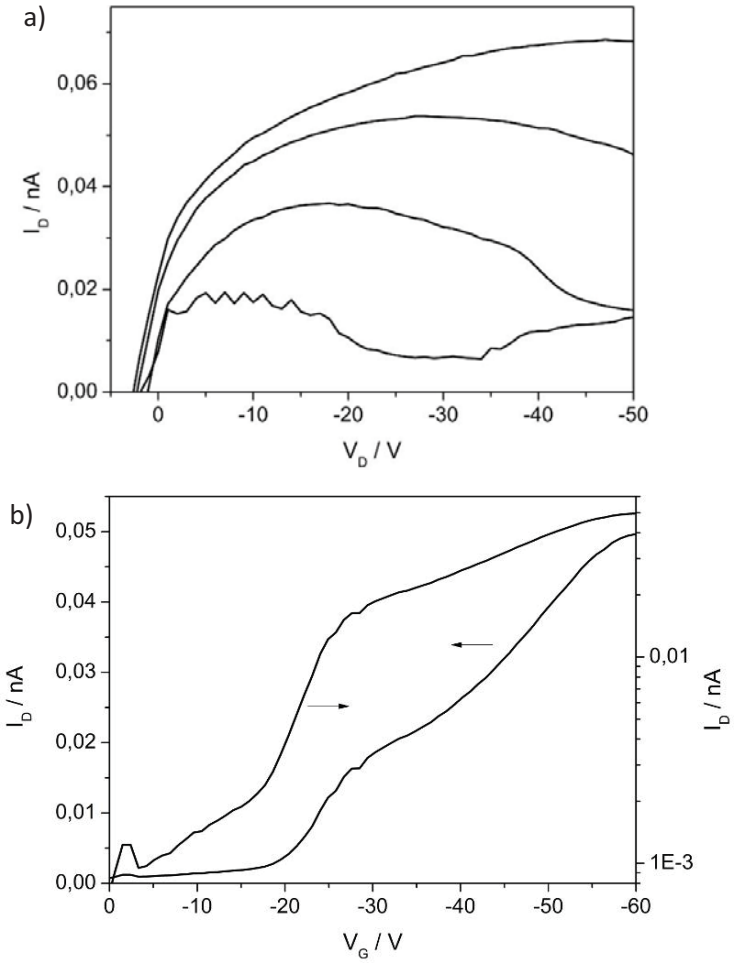

Figure 3.12. Output characteristics for V_G = -30, -55, -75 and -100 V (a) and transfer characteristics for V_D = -50 V (b) of device D1 at room temperature.

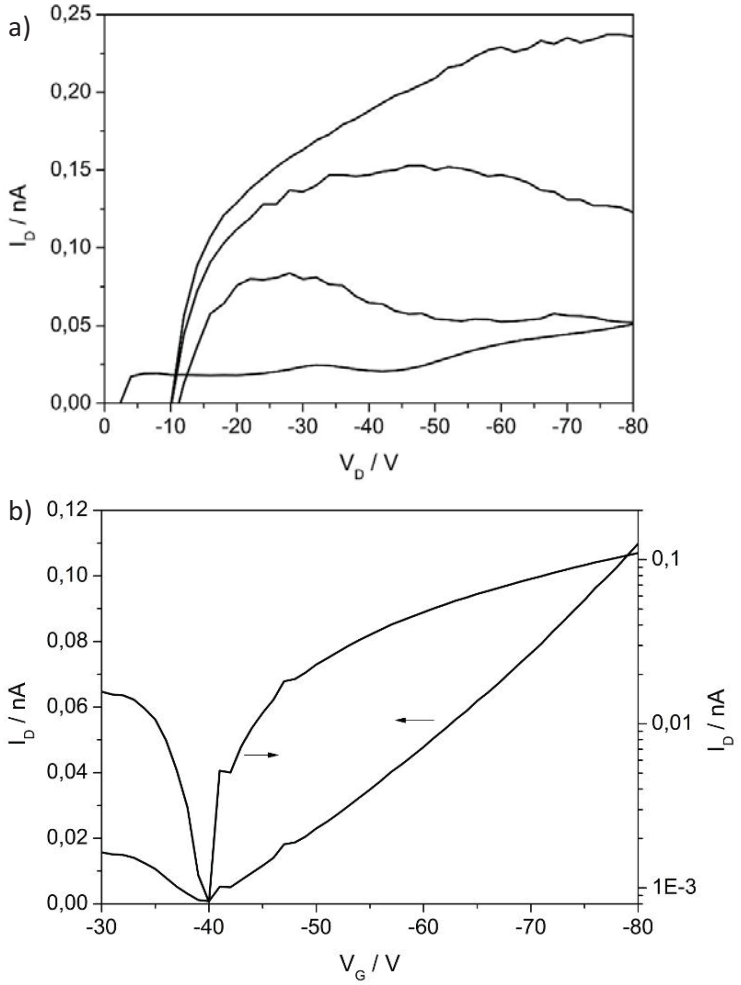

Figure 3.13. Output characteristics for V_G = -10, -40, -70 and -100 V (a) and transfer characteristics for V_D = -100 V (b) of device D2 at room temperature.

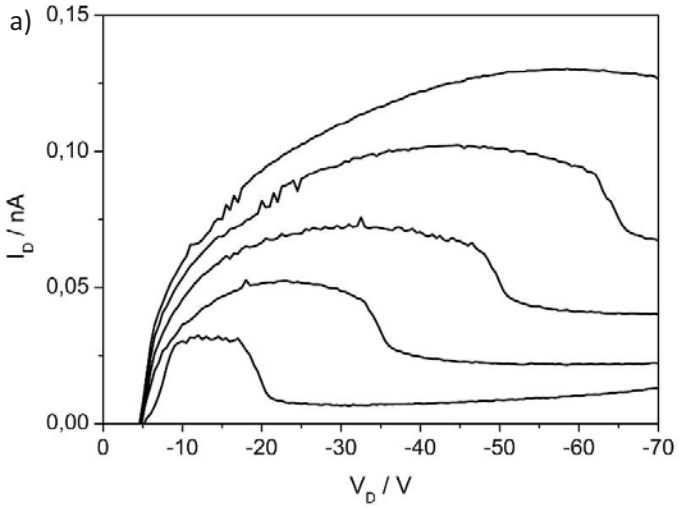

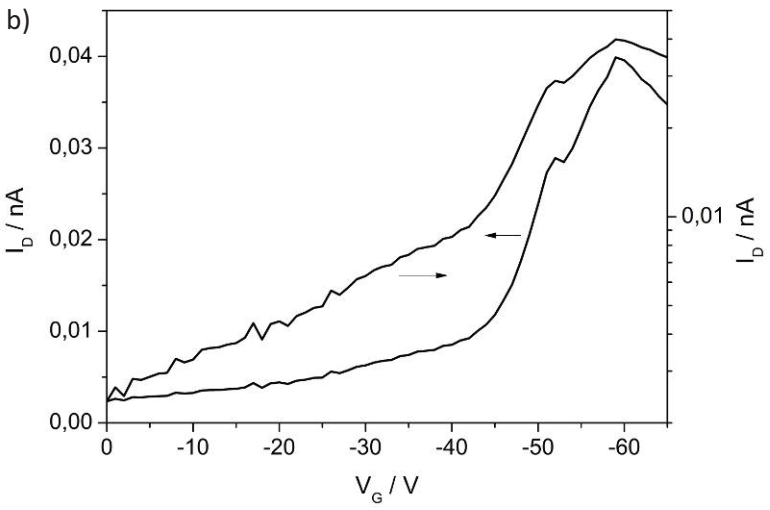

Figure 3.14. Output characteristics for V_G = -20, -35, -50, -65 and -80 V (a) and transfer characteristics for V_D = -100 V (b) of device D6 at room temperature.

Although saturation characteristics of D1, D2 and D6, shown in Figure 3.15, did not fit exactly the profile described in section 3.1.1 due to the low values of the electric currents of the devices, they presented a linear range, which was used to estimate the hole field effect mobility (μ_{FET}) according to the equation 3.4. In Table 3.3 are given the characteristics found for devices D1, D2 and D6.

Table 3.3. Channel widths (W) and lengths (L) and calculated field effect mobilities (μ_{FET}) of the fabricated OTFTs

	W / μm	**L / μm**	**μ_{FET} / cm^2 V^{-1} s^{-1}**
D1	757	182	$2x10^{-6}$
D2	671	182	$8x10^{-7}$
D6	720	190	$3x10^{-7}$

The obtained μ_{FET} values are three orders lower than the μ values registered by the XTOF technique. However it must be considered that in OTFTs the charges migrate within a very narrow channel (at most a few nanometers thick) at the interface between the organic semiconductor and the dielectric. Transport is affected by structural defects within the organic layer at the interface, the surface topology and polarity of the dielectric, and/or the presence of traps at the interface. Contact resistance at the source and drain metal/organic interfaces plays an important role as well. Also impurities at this scale could produce a dramatic drop in the current flow.

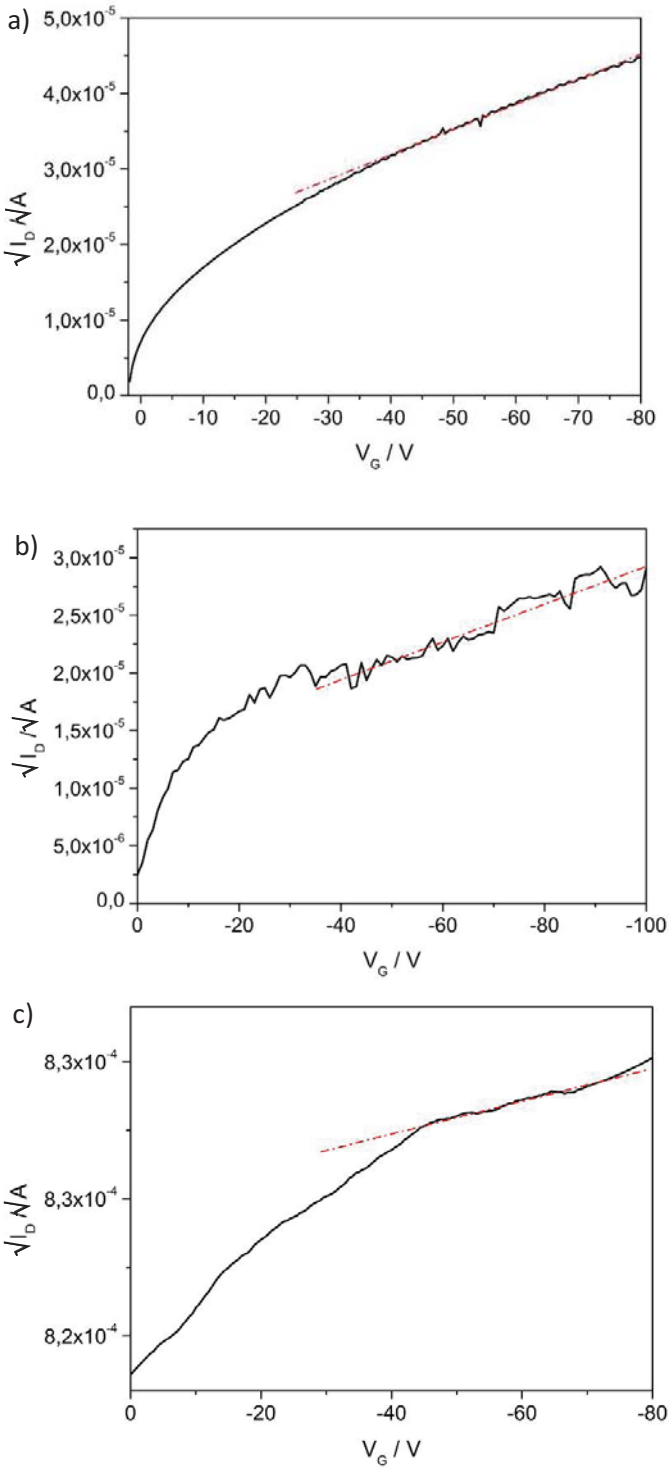

Figure 3.15. Saturation characteristics of D1 (a), D2 (b) and D6 (c) at room temperature.

3.2.2. Organic photovoltaic devices (OPVs)

Radical **1** was chosen for the fabrication of OPVs due to its electrochemical and charge transport properties and its greater availability in front of more complex radical structures. Namely, radical **1** absorbs in a wide range of the visible spectrum and presents high charge carriers mobility by XTOF measurements. Two kinds of OPVs were fabricated with this material: single layer OPVs (Schottky-

type diodes) and bulk-heterojunction OPVs. The structure of the devices were in all cases glass/ITO/PEDOT/OM/Al, where OM stands for photoactive organic material layer. Figure 3.16 displays a sample of fabricated OPVs.

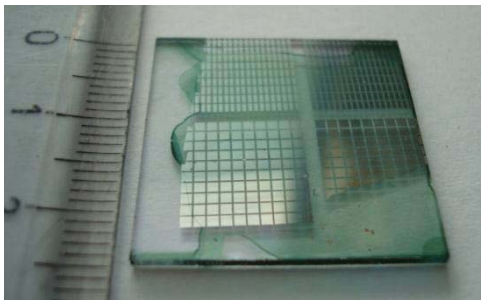

Figure 3.16. OPVs based on radical **1** on a glass/ITO/PEDOT substrate and Al electrodes on top.

3.2.2.1. Single layer OPVs

Single layer OPVs were prepared by spin-coating of $CHCl_3$ solutions of **1** in two different concentrations (25 g/l for PV1 and 50 g/l for PV2) on glass/ITO/PEDOT substrates. These devices worked as p-type photodiodes, in agreement with the performance of material **1** in the previous OTFT devices. The I-V curves recorded for the two devices are shown in Figure 3.17 and the fill factor of PV1 is represented in Figure 3.18. The parameters for each cell are given in Table 3.4.

Table 3.4. Device parameters found for cells PV1 and PV2

	thickness / nm	V_{OC} / V	I_{SC} / mA cm^{-2}	V_{max} / V	I_{max} / mA cm^{-2}	*FF*
PV1	~160 nm	0.64	1.42x10^{-4}	0.34	7.36x10^{-5}	0.28
PV2	~290 nm	0.26	5.66x10^{-5}	0.12	3.37x10^{-5}	0.28

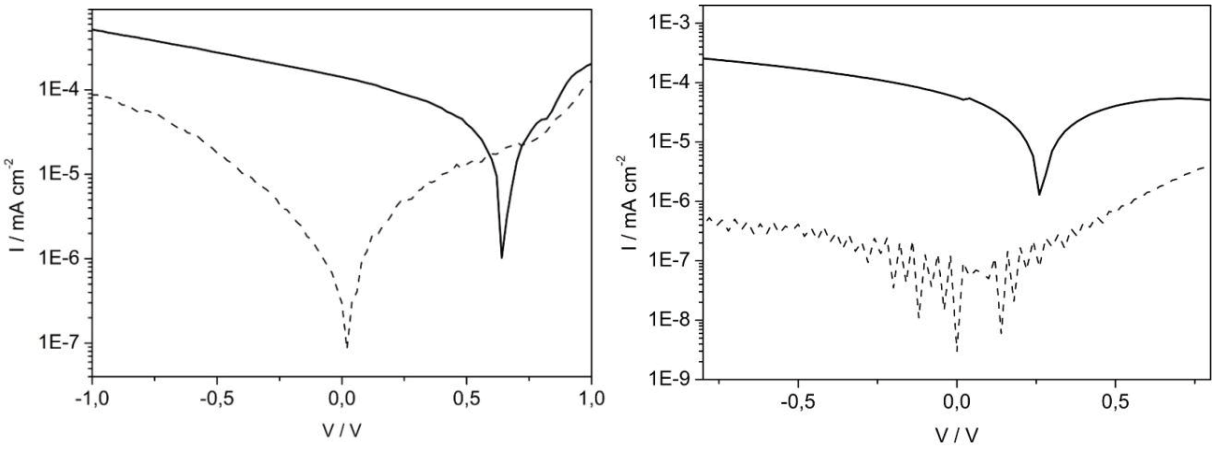

Figure 3.17. I-V characteristics of PV1 (left) and PV2 (right) in the dark (dashed line) and under illumination (solid line) in the logarithmic scale.

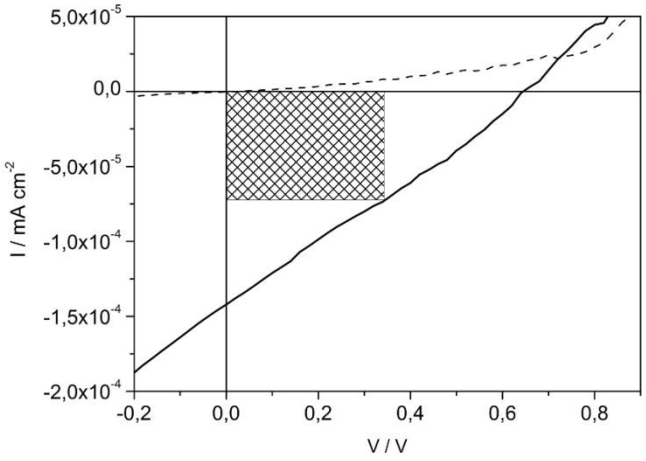

Figure 3.18. I-V characterisitcs of PV1 in the linear scale in the dark (dashed line) and under illumination (solid line). Shaded area represents the field factor.

It can be observed that an increase of the thickness of the organic layer by spin-coating of a more concentrated solution of **1** produces a drop of the V_{OC} and I_{SC} values, while the *FF* remains the same. The decrease of the current can be attributed to the longer paths that the excitons and polarons formed during the photovoltaic mechanism must travel to corresponding electrodes, which lead to recombination of these species. The differences of V_{OC} values, though, are not so easy to justify, since for single layer OPVs, the V_{OC} is related to the difference in the work function between the top and bottom electrodes.[2]

External quantum efficiency (EQE) of cells PV1 and PV2 as a function of the wavelength of the incident light resembles the absorption profile of **1** in solution, that is, these devices present a symbatic behavior (Figure 3.19).

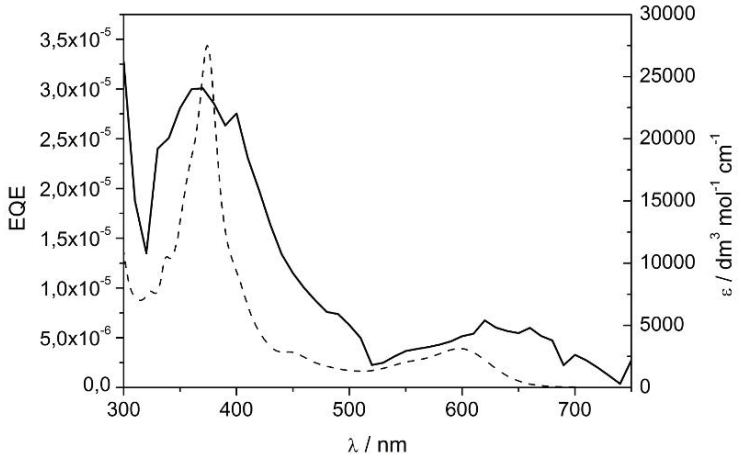

Figure 3.19. External quantum effiency (solid line) of the device PV1 and absorption spectrum of a solution of **1** in $CHCl_3$ (dashed line).

It is difficult to determine the energy levels of the excitons participating in the operation of the prepared cells given the complex electronic configuration of radical **1**. According to the interpretation of the electrochemical and photochemical properties of the compounds belonging to the *N*-carbazolylTTM family (section 1.2.3), an energy diagram like the one shown in Figure 3.20 can be proposed. This diagram might explain the photovoltaic effect in the range of shorter wavelengths (300-500 nm) because in this range an exciton involving $LUMO_2$ and SOMO levels might be formed (Figure 3.20 right). However, the exciton that might result from the absorption in the visible range of the spectrum (Figure 3.20 left) would not lead to the generation of current since the electrons might find a barrier to go from the now fully occupied SOMO to the Al electrode. It must be remarked, though, that the EA value of this radical (represented with a dashed line in the diagram), which is associated to the attainment of a full SOMO (EA is by definition the energy required to add an electron to the SOMO), is very close to the Ψ_m value of the anode.

While in closed-shell systems the less energetic absorption band is associated to the promotion of an electron to an empty MO, in the case of the HOMO→SOMO transition, the electron ends up in an already semioccupied orbital, and the final energy level of the fully occupied MO might not be the same as in the ground state. Nevertheless, future theoretical calculations will be the key to understand the experimental results.

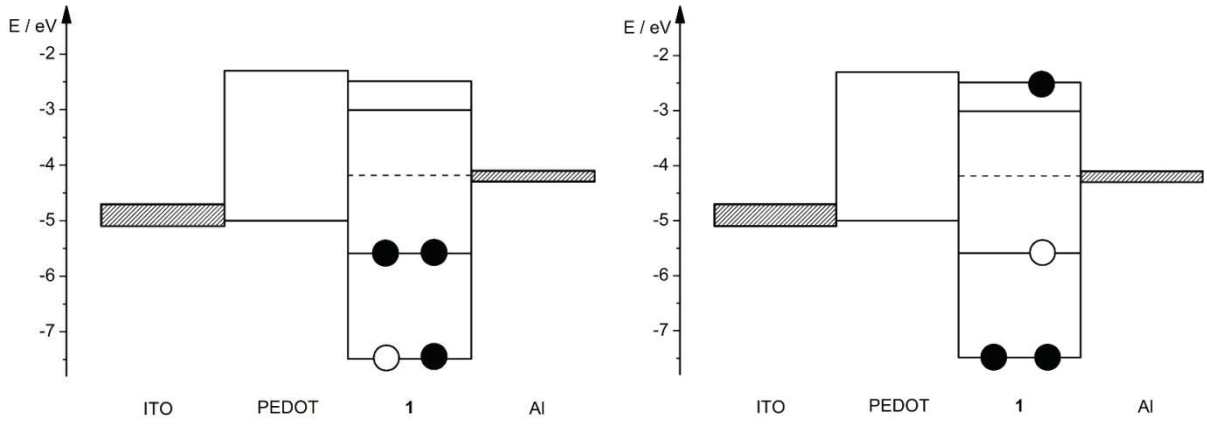

Figure 3.20. Proposed energy diagrams for single layer OPVs based on radical **1** under illumination with light in the visible range (left) and with light in the UV range (right) of the spectrum.

3.2.2.2. Bulk-heterojunction OPVs

Considering the results obtained in the studied OTFTs and the single layer OPVs, radical **1** was handled as a p-type material and thus for the fabrication of the pn-heterojunction cells. The chosen electron-transporting or n-type materials were TiO_2, an inorganic compound, and PCBM, an organic compound.

3.2.2.2.1. OPVs based on TiO_2:1

For the fabrication of this kind of OPVs the photoactive layer was deposited by spin-coating of a solution containing the titanium derivative titanium isopropyl oxide (TIO) and **1** in $CHCl_3$ in different molar ratios. Once the solvent is evaporated TIO hydrolises under atmospheric conditions to give TiO_2.[6, 7] The used TiO_2:**1** ratios were 10:1 (PV3 and PV4), 5:1 (PV5), 2.5:1 (PV6) and 1:1 (PV7).

Cell PV3 presented a clear photovoltaic effect in its I-V curves shown in Figure 3.21. Like in the case of the single layer OPVs, the EQE is symbatic with the absorption profile of **1** and of the TiO_2:**1** film (Figure 3.22). The measured V_{OC}, I_{SC} and *FF* for this cell are given at the end of this section in Table 3.5.

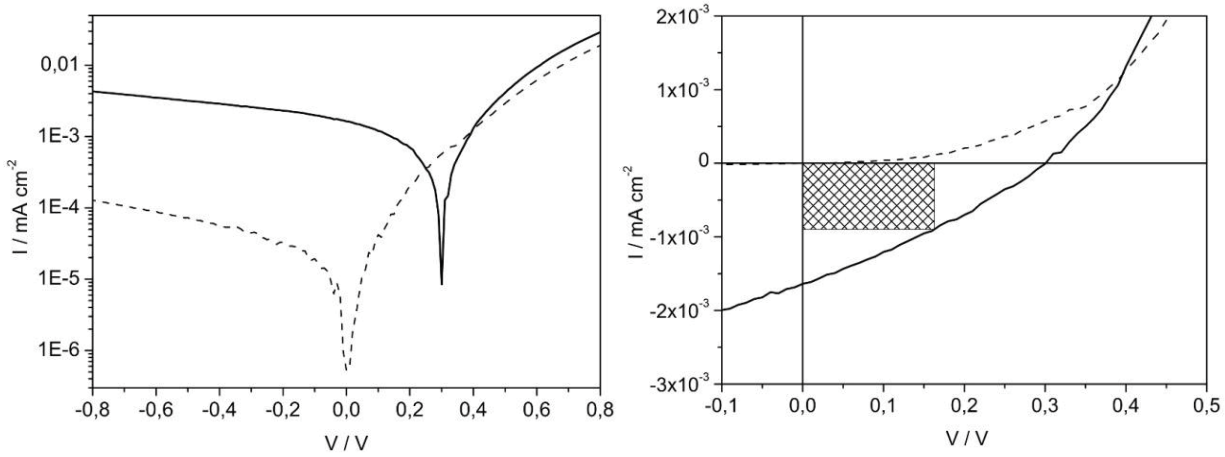

Figure 3.21. I-V characteristics of PV3 in the dark (dashed line) and under illumination (solid line) in the logarithmic scale (left) and in the linear scale in the dark (right).The shaded area represents the field factor.

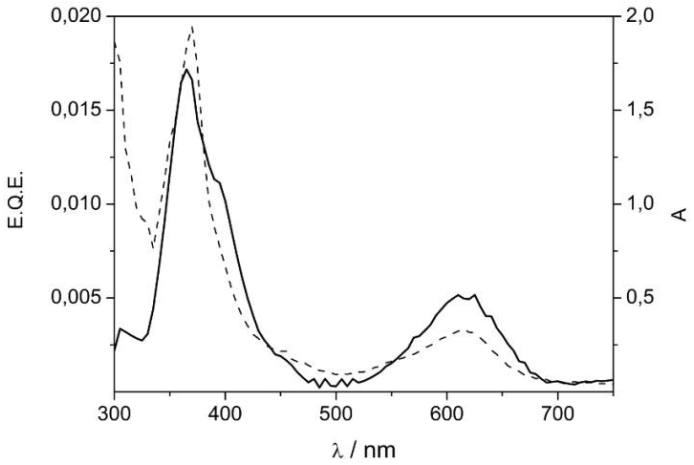

Figure 3.22. External quantum efficiency (solid line) and absorption spectrum of the TiO_2:**1** film of the device PV3.

Unfortunately, these results could not be reproduced in PV4, which only behaved as a p-type diode after the cell was exposed to light. The same behavior was observed in the rest of the cells. Apparently, some irreversible photochemical reaction took place in the first illumination, most probably an electron transfer from the radical to the TiO_2 (oxidation of the radical), and the resulting mixture of species acted as a hole-transporting material. Further experimental should be done to find an explanation for this irreproducibility of the PV3 results.

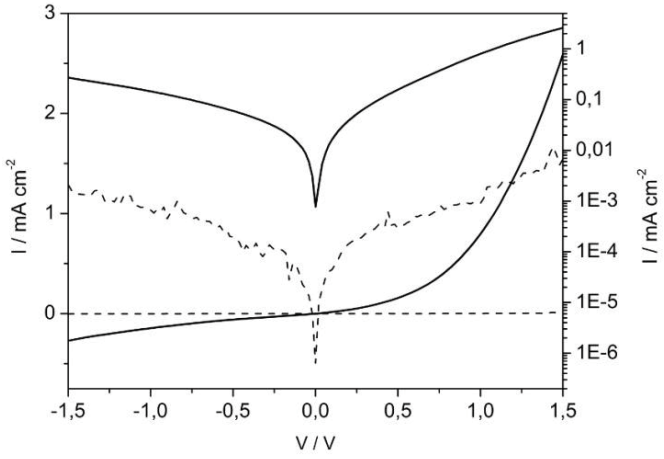

Figure 3.23. I-V characteristics of PV4 before the first exposure to light (dashed line) and after illumination (solid line) in the linear and the logarithmic scale.

The proposed energy diagrams for the two excitons expected to participate in the operation of these cells are given in Figure. 3.24. The same discussion used for the single layer OPVs could be applied for these cells and more accurate energy values should be found by computational methods in order to understand the electronic processes within these cells.

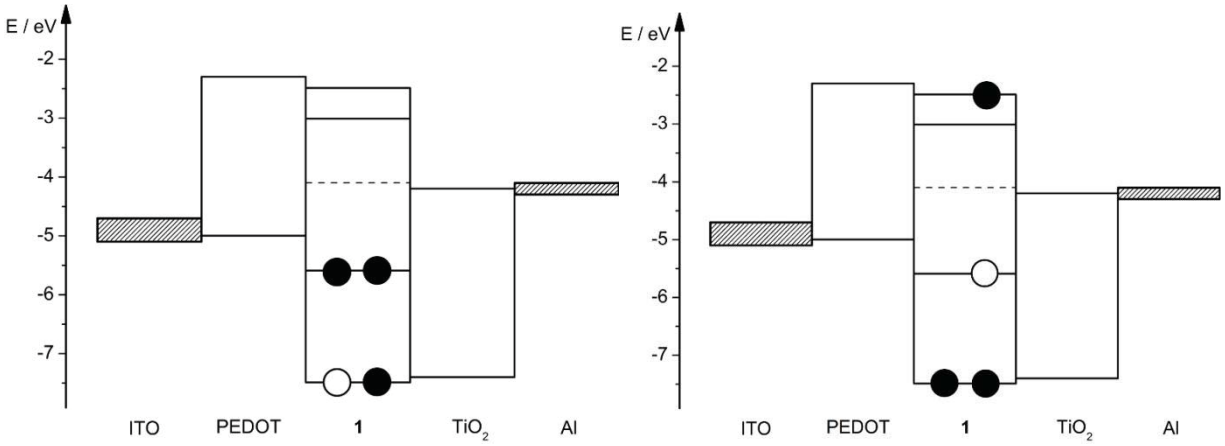

Figure 3.24. Proposed energy diagrams for bulk-heterojunction OPVs based on TiO_2:**1** under illumination with light in the visible range (left) and with light in the UV range (right) of the spectrum.

3.2.2.2.2. OPVs based on PCBM:1

Two devices were fabricated using the mixture of n-type and p-type materials PCBM and **1**. The PCBM:**1** molar ratios used for the organic layer were 1:1 (PV8) and 3:4 (PV9). Both cells showed very similar characteristics (Figure 3.25). *FF* for both similar for both samples (Figure 3.26). However PV9 seemed to have a better performance given that higher current densities and EQE were recorded for this device (Figure 3.27). The photocurrent proved to be symbatic with the absorption spectrum of radical **1** for both devices.

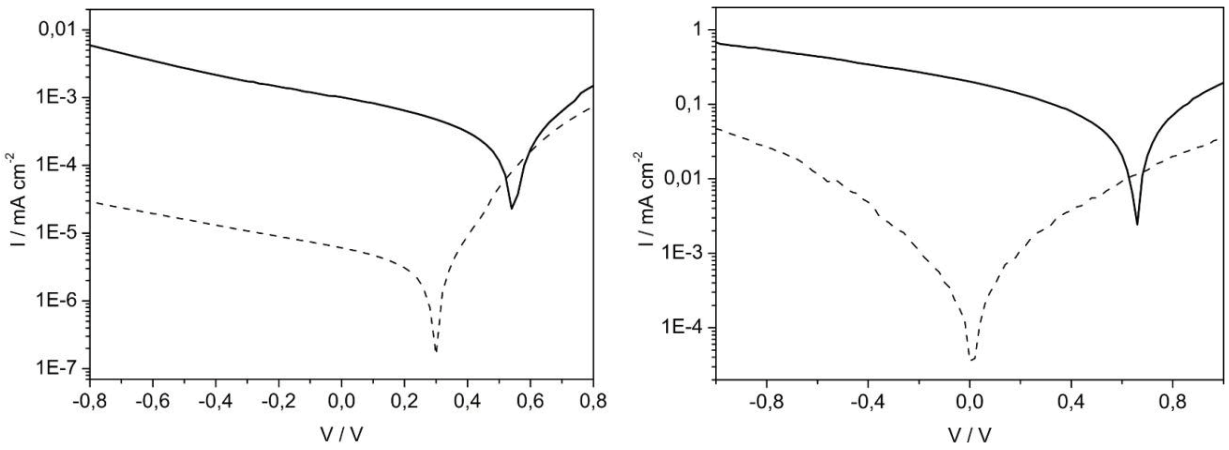

Figure 3.25. I-V characteristics of PV8 (left) and PV9 (right) in the dark (dashed line) and under illumination (solid line) in the logarithmic scale. (left) and in the linear scale in the dark (right).The shaded area represents the field factor.

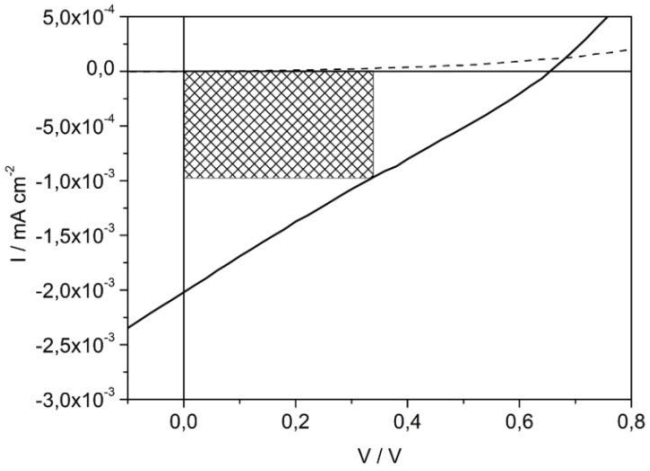

Figure 3.26. I-V characteristics of PV8 in the linear scale in the dark (dashed line) and under illumination (solid line).The shaded area represents the field factor.

The proposed energy diagram for cells PV8 and PV9 is show in Figure 3.28. As for the previous cells, computational studies are required to confirm the energetic levels of the excited states and explain the experimental results.

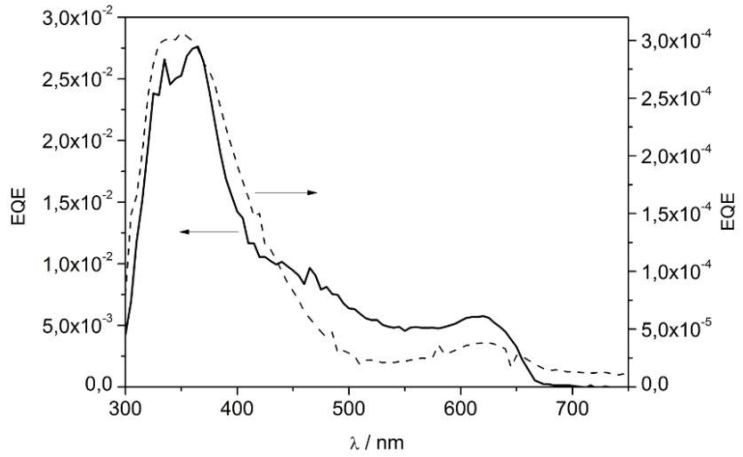

Figure 3.27. External quantum efficiency of PV8 (solid line) and of PV9 (dashed line).

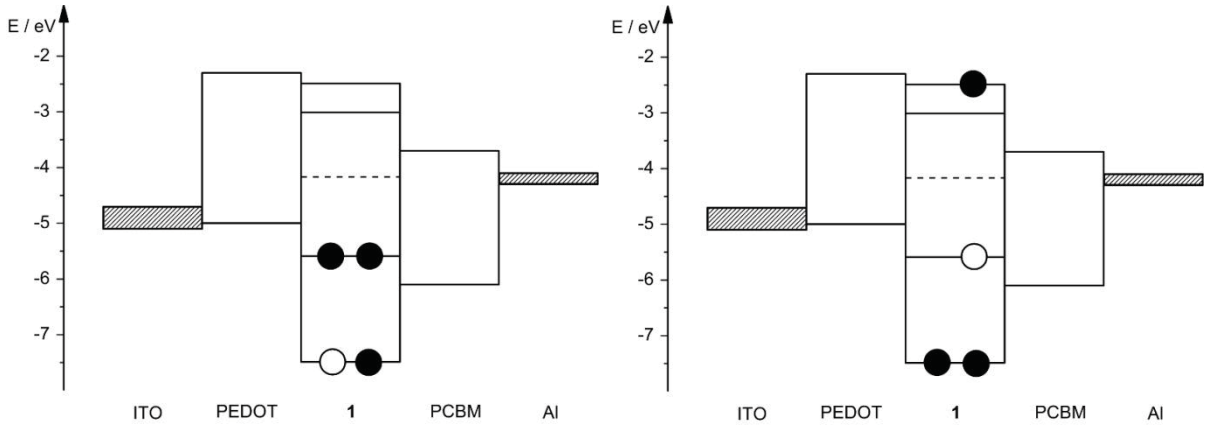

Figure 3.28. Proposed energy diagrams for bulk-heterojunction OPVs based on PCBM:**1** under illumination with light in the visible range (a) and with light in the UV range (b) of the spectrum.

3.2.2.2.3. Summary

The parameters obtained for all active bulk-heterojunction cells are listed in table 3.5.

Table 3.5. Characteristics of the photoactive layers and device parameters for the bulk-heterojunction OPVs prepared with radical **1**.

	material (ratio)	thick. /nm	V_{OC} / V	I_{SC} / mA cm^{-2}	V_{max} / V	I_{max} / mA cm^{-2}	*FF*
PV3	TiO_2:**1** (1:1)	280-290	0.3	-1.64x10^{-3}	0.16	-9.20x10^{-4}	0.31
PV8	PCBM:**1** (1:1)	90	0.54	-1.03x10^{-3}	0.30	-4.77x10^{-4}	0.26
PV9	PCBM:**1** (3:4)	130-150	0.66	-2.02x10^{-3}	0.34	-9.66x10^{-4}	0.25

It can be observed that the based on the PCBM:**1** heterojunction showed higher V_{OC} than the cell with TiO_2 as n-type material. Studies made on conjugated polymer/fullerene bulk-heterojunction solar cells support that the V_{OC} in these kind of systems is related directly to the energy difference

between the HOMO level of the donor and the LUMO level of the acceptor components.[8, 9] More specifically it had been reported that the relation is $(V_{OC})_{max} < \Delta E$, for these cells seems to hold.[10]

It can also be noticed that all pn-heterojunction OPVs presented higher current densities than the single layer OPVs, as it could be expected. Many parameters can still be modified in order to improve this kind of devices, such as annealing of the organic layer by thermal treatment, further variation of the molar ratio of p-type and n-type material and of the thickness of the layer, as well as the environment conditions during their fabrication, which was not anaerobic so far, among others.

3.2.3. Organic light emitting diodes (OLEDs)

The ambipolar transport shown by radicals **1** and **11** in the XTOF experiments and the high quantum yields of the fluorescent emissions in solution of the radical derivatives belonging to the *N*-carbazolylTTM and *N*-indolylTTM family (see section 1.2.3) prompted us to study their performance as light emitting layer in organic light emitting diodes (OLEDs).Materials **1**, **11** and **18**, were chosen due to their ability of forming amorphous think films and their greater availability

All devices were built according to the configuration ITO/PEDOT-PSS/EL/metal where EL stands for electroluminescence layer. Table 3.6 lists the studied devices according to the material acting as EL and the metal.

Table 3.6. Parameters of the fabricated OLEDs

	EL	thickness / nm	metal
O1	**1**	60	Al
O2	**11**	55	Al
O3	**18**	60	Al
O4	**18**	110	Al
O5	**1**	60	Ag
O6	**11**	60	Ag
O7	**18**	60	Ag

Despite presenting clear rectifying characteristics in the I-V curves with relatively low voltage thresholds (Figure 3.29), all devices presented very low efficiencies. The best performance was registered for devices using Al as cathode. Figure 3.30 shows the luminance, *L*, and the luminous efficiency, η_l for devices O1-O4. It can be observed that radicals bearing carbonyl chains present luminance and efficiency values three orders higher than those for radicals with bare heterocycles. This might be related to the electron-withdrawing nature of the carbonyls, which partially prevents the charge transfer from the carbazole to the trivalent carbon, thus reducing the quenching of

fluorescence in the solid state. The threshold voltage for material **18**, though, was higher, as a result of the higher IP of this compound regarding to radicals **1** and **11**.

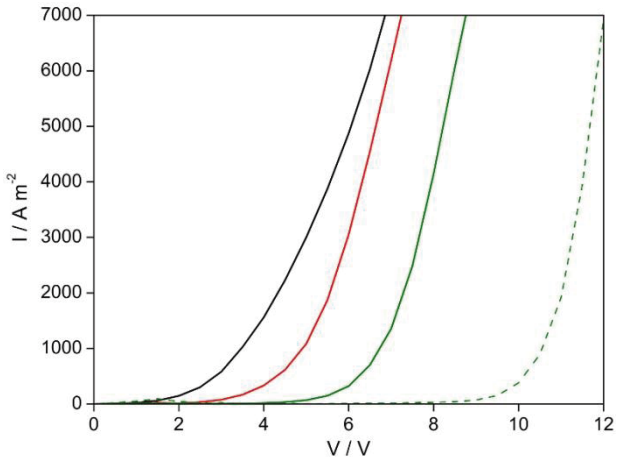

Figure 3.29. I-V characteristics of devices O1 (black), O2 [11], O3 (solid green) and O4 (dashed green).

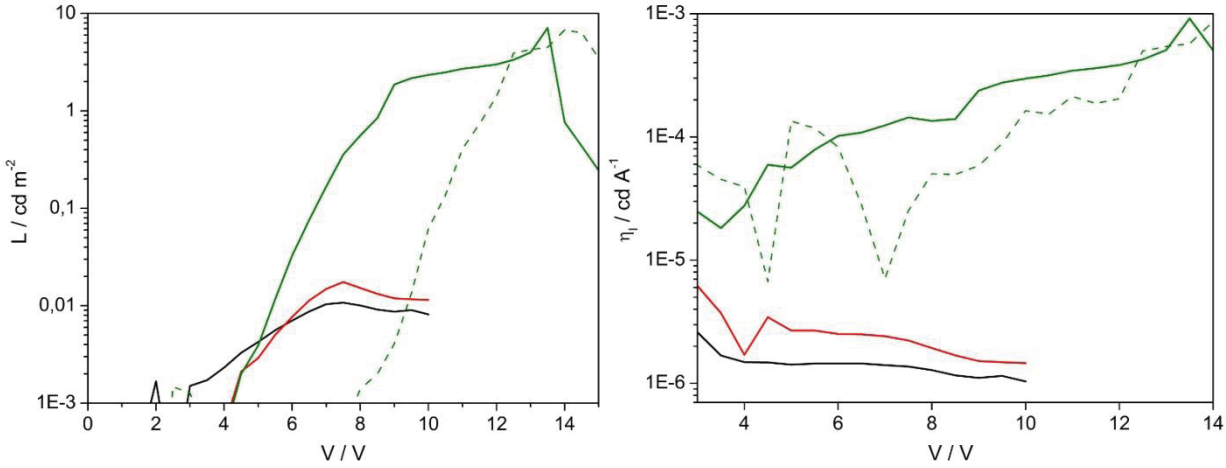

Figure 3.30. Luminance (left) and luminous efficiency (right) as a function of the applied voltage of devices O1 (black), O2 (red), O3 (solid green) and O4 (dashed green).

3.3. Summary

OTFTs fabricated with radical **1** and with material **49** showed the I-V characteristics of a p-type channel device. However, no current was observed in OTFTs based on radical **11** neither for positive nor negative gate voltage values.

Material **1** works as a photoactive material in OPVs both in single layer device configuration -where **1** acts as a p-type semiconductor- and in bulk-heterojunction device configuration -where **1** acts as a donor material. Photocurrent proved to be symbatic with the absorption spectrum of the radical.

Single layer OPVs show higher V_{OC} values (0.64 V) than most bulk-heterojunction OPVs, but lower current densities, in agreement with what is reported in the literature. In addition bulk-heterojunction OPVs that use PCBM as acceptor material presented higher V_{OC} (0.54 V and 0.66 V) and better reproducibility than the TiO_2 counterparts (V_{OC}= 0.30 V). Field factor values in all cases were around 0.30.

OLEDs fabricated with radicals **1**, **11** and **18** as emitting layer showed relatively low voltage thresholds but low efficiencies.

3.4. Experimental section.

3.4.1. Equipment

Organic layers for the OTFTs fabrication were deposited using a VTE Leybold equipment, model UNIVEX 300 consisting of a stainless steel vacuum chamber of 30 cm diameter and 40 cm height provided with a Pirani (for pressures till 10^{-4} mbar) and a Penning (for lower pressures) pressure sensors, a shutter, two ceramic crucibles and a quartz transducer to measure the evaporation rate.

Metals for the electrodes were evaporated in a home made thermal evaporator consisting of two molibdemum crucibles.

Deposition by spin-coating was performed using a Specialty Coating Systems SpinCoater model P6700.

N-doped crystalline silicon wafers, also acting as gate electrodes, (165 nm) were used for OTFTs.

For the electrical measurements of the OTFTs and the OPVs an Agilent 4256C analyzer connected to a probe station was used.

Glass/ITO substrates (12 Ω/sq) were purchased to Optical Filters. PEDOT/PSS solution was purchased to Baytron® P.

3.4.2. Devices fabrication

3.4.2.1. General procedure for the fabrication of OTFTs.

The organic layer was deposited by VTE on wafers of Si/SiO_2 (165 nm). The substrate was covered with a mask patterned so with slits of 0.5 x 1 mm separated by margins of 0.2 mm. Sublimation of the organic compounds were performed under pressure within the range $1 \times 10^{-5} – 1 \times 10^{-6}$ mbar. A shutter was placed between the masked substrate and the crucible containing the organic material and was only removed when the evaporation rate was constant. Table 3.7 shows the pressure and temperature conditions for the deposition of materials **1**, **11** and **49**.

The metallic electrodes were also deposited by VTE. The same mask was placed on the substrate with the organic layer so that the slits were perpendicularly oriented regarding the strips of the organic material so that square OTFTs consisting in two channels of organic layer connected at their extremes by the metallic electrodes resulted (Figure 3.21).

Table 3.7. Evaporation pressure (P) and temperature (T) of the organic materials used in the fabrication of OTFTs.

	P / mbar	T / °C
1	8×10^{-6}	160-175
11	2×10^{-6}	140-150
49	4×10^{-6}	120-125

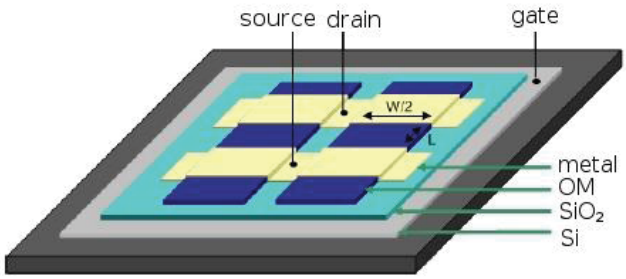

Figure 3.21. Schematic of a OTFT. OM = organic material, W = channel width, L = channel length.

3.4.2.2. General procedure for the fabrication of OPVs.

Glass substrates covered with a layer of ITO were cleaned with acetone and isopropanol and with a ultraviolet-ozone (UVO) treatment. A solution of PEDOT/PSS was spin-coated on the clean substrates (5000 rpm, 5'', 30'' followed by 3500 rpm, 1'' 10'') and the coated glasses were heated at 115 °C for 10 min. The organic layers were then deposited by spin-coating the corresponding solutions using the proper spinning conditions.

Aluminum was deposited on the organic layer by VTE technique. The organic layer was covered with a mask patterned with square slits of 1 mm^2 separated by margins of 0.2 mm. The cells were measured immediately after their preparation.

3.4.2.2.1. Deposition of the organic layer in cells PV1 and PV2

Radical **1** (PV1: 12.5 mg; PV2: 25 mg) was dissolved in spectrophotometric $CHCl_3$ (0.5 ml) and spin coated on the glass/ITO/PEDOT substrate (3000 rpm, 5'', 30''; 3500 rpm, 1'', 10'').

3.4.2.2.2. Deposition of the organic layer in cells PV3-PV7

Titanium isopropyl oxide (50 mg for PV3 and PV4; 25 mg for PV5, 16 mg for PV6 and PV7) was dissolved in spectrophotometric $CHCl_3$ (1 ml). Radical **1** (12.5 mg for PV3-PV6; 20 mg for PV7) was added to an aliquot of the prepared TIO solution (0.5 ml) and the resulting mixture was spin-coated over the glass/ITO/PEDOT substrate (3000 rpm, 5'', 30''; 3500 rpm, 1'', 10''). The deposited layer was

left 24 h in the dark under atmospheric conditions and then heated in an oven at 80 °C during 30 min.

3.4.2.2.3. Deposition of the organic layer in cell PV8

PCBM (12 mg) was dissolved in chlorobenzene (0.5 ml) under nitrogen atmosphere and protecting it from light by stirring the mixture in a sand bath at 70 °C during 1 h, then at 100 °C during 10 min. and thereafter keeping the system at 70 °C overnight. Radical **1** (8 mg) was dissolved in chlorobenzene (0.5 ml) at rt. under nitrogen atmosphere protecting the solution from light. The two solutions were mixed and the resulting solution was spin-coated (1500 rpm, 5'', 40 ''; 4000 rpm, 1'', 10'') on the glass/ITO/PEDOT substrate. The layer was finally heated in an oven at 100 °C for 10 min.

3.4.2.2.4. Deposition of the organic layer in cell PV9

PCBM (12 mg) was dissolved in chlorobenzene (0.5 ml) under nitrogen atmosphere and protecting the system from light by stirring the mixture in a sand bath at 70 °C during 1 h, then at 100 °C during 10 min. and thereafter keeping the system at 70 °C overnight. Radical **1** (12 mg) was added to the PCBM solution and kept at 65 °C for 15 min. still in the dark and under nitrogen atmosphere. The resulting solution was spin-coated (1500 rpm, 5'', 40 ''; 4000 rpm, 1'', 10'') on the glass/ITO/PEDOT substrate. The layer was finally heated in an oven at 100 °C for 10 min.

References

[1] Y. Shirota, H. Kageyama, *Chem. Rev.* **2007**, *107*, 953-1010.
[2] K. M. Coakley, M. D. McGehee, *Chem. Mater.* **2004**, *16*, 4533-4542.
[3] J. Hui, Y.-B. Hou, X.-G. Meng, T. Feng, *Thin Solid Films* **2008**, *516*, 1142-1146.
[4] B. O'Regan, M. Gratzel, *Nature* **1991**, *353*, 737-740.
[5] C. D. Dimitrakopoulos, P. R. L. Malenfant, *Adv. Mater.* **2002**, *14*, 99-117.
[6] P. A. v. Hal, M. M. Wienk, J. M. Kroon, W. J. H. Verhees, L. H. Slooff, W. J. H. v. Gennip, P. Jonkheijm, R. A. J. Janssen, *Adv. Mater.* **2003**, *15*, 118-121.
[7] C.-H. Huang, C.-H. Huang, T.-P. Nguyen, C.-S. Hsu, *Thin Solid Films* **2007**, *515*, 6493-6496.
[8] C. J. Brabec, A. Cravino, D. Meissner, N. S. Sariciftci, T. Fromherz, M. T. Rispens, L. Sanchez, J. C. Hummelen, *Adv. Funct. Mater.* **2001**, *11*, 374-380.
[9] M. C. Scharber, D. Mühlbacher, M. Koppe, P. Denk, C. Waldauf, A. J. Heeger, C. J. Brabec, *Adv. Mater.* **2006**, *18*, 789-794.
[10] T. Yamanari, T. Taima, J. Sakai, K. Saito, *Sol. Energy Mater. Sol. Cells* **2009**, *93*, 759-761.
[11] V. Coropceanu, J. Cornil, D. A. da Silva Filho, Y. Olivier, R. Silbey, J.-L. Bredas, *Chem. Rev.* **2007**, *107*, 926-952.

Consulted bibliography

Michael C. Petty. *Molecular Electronics. From principles to practice.* Chichester, Wiley & Sons Ltd. (2008)

Conclusions

The coupling between the **TTM** radical core and the *N*H-carbazole or *N*H-indole heterocycles seems to proceed through a radicalary mechanism. Radical molecular glasses that form stable amorphous films can be attained by the attachment of acyl chains of 8 carbons to radicals adducts *N*-carbazolylTTM **1** and bis(*N*-carbazolyl)TTM **2**. Discotic radical molecules showing columnar arrangements can be attained by the attachment of 18 and 12 carbon acyl chains (radical adducts **40** and **41**) to radical core **3**.

Radical adduct **40** is the first example in the literature of discotic radical bearing the unpaired electron centered in the aromatic core. The piling of radical cores shown by this radical adduct is a most interesting and sought feature for electronic applications. Moreover EPR and magnetic studies performed on this radical mesogen proved that intermolecular magnetic interactions take place in the ordered hexagonal columnar liquid crystal phase of **40**, whereas they disappear in the glassy rectangular columnar phase. Thus, control over magnetic behavior can be attained by means of the phases transitions, i. e., by temperature variation.

Providing the *N*-phenylcarbazole core with methoxy groups allows the attainment of molecular glasses showing high T_g and reversible oxidation processes (**49**). The tricyanovinyl groups attached to the carbazole fragment of the 1,3,5-tris(*N*-carbazolyl)benzene TCB core of compounds **50**, **51** and **52** confers the new systems with high stability and electron-acceptor character, as it is evidenced by the reversible reduction processes they undergo. Reduction potentials of these derivatives indicate low electron-affinities (EA) values, regarding the values found in the literature. Thus, a proper

derivatization of the *N*-phenylcarbazole core led to molecular glasses with favoring features for their application as both p-type (**49**) and n-type (**50**, **51** and **52**) organic semiconductor materials.

The presence of terminal carboxylic acids in the heptaalkoxyl *N*-phenylcarbazole mesogens (**81** and **82**) destabilizes the mesophase regarding the **79** counterpart, previously known in the group. Doping of **79** and **81** with the electron-acceptor TNF, though, promotes the formation of Col_{ho} within a wide range of temperatures.

A fine tuning of the absorption and emission wavelengths of the prepared radical adducts can be achieved by varying the number of the carbazole moieties present in the aromatic core and the electronic nature of the side groups added to the carbazole fragment. The number and length of the alkoxyl chains in the *N*-phenylcarbazole core modify only slightly the absorption and emission characteristics of the resulting derivatives. However, the attachment of tricyanovinyl groups to TCB provides the new carbazole derivatives **50**-**52** with strong absorption bands in the visible region and dual fluorescence, in certain solvents, attributed to an intramolecular charge transfer.

The combination of carbazole and indole fragments with a **TTM** radical core is an efficient strategy to obtain molecular glasses showing bipolar transport properties with high mobility values for both holes and electrons. The electron mobility values found in these particular materials by XTOF technique are among the highest reported for low molar mass amorphous materials so far. TOF measurements performed on radical mesogen **40**, non-radical mesogen **79** and on the mesogenic **79**:TNF (1:1) complex presented a very dispersive regime and did not allow the determination of any charge mobility, despite an homeotropic face-on alignment could be attained for radical adduct **40** by a magnetic treatment of the corresponding sample.

Radical adduct **1** works as p-type material both in organic thing film transistors (OTFTs) and in organic photovoltaic (OPV) devices. OPVs based on this radical show high V_{OC} values and a symbatic spectral response. These devices are the second example of devices using organic radicals as active materials in the literature. Compound **49** acts as a p-type organic material in OTFTs.

List of abbreviations

^{13}C NMR	carbon nuclear magnetic resonance
^{1}H NMR	proton nuclear magnetic resonance
A	acceptor
AcOEt	ethyl acetate
AcOH	acetic acid
αH-TTM	tris(2,4,6-trichlorophenyl)methane
Alq_3	tris-(8-quinolinolato)aluminum
β	mobility field dependence
C	Curie constant
χ	magnetic susceptibility
Col_h	hexagonal columnar mesophase
Col_{ho}	ordered hexagonal columnar mesophase
Col_r	rectangular mesophase
Col_{ro}	ordered rectangular columnar mesophase
CT	charge transfer
CV	cyclic voltammetry
D	donnor
D_0	doublet ground state
D_1	doublet first excited state
D_2	doublet second excited state
D-B-A	donor-bridge-acceptor
DCC	dicyclohexyl carbodiimide
DDQ	2,3-dichloro-5.6-dicyanobenzoquinone
DMAP	dimethylaminopyridine
DMSO	dimethylsulfoxide
DSC	differential scanning calorimetry
DSSC	dye-sensitized solar cell
e	electron
E^0	standard redox potential
EA	electron affinity
E_{gap}	HOMO/LUMO energy gap
EL	electroluminescence
E_{onset}	onset redox potential
E_{pa}	anodic peak potential
E_{pc}	cathodic peak potential
EPR	electron paramagnetic resonance
EQE	external quantum efficiency
Et_2O	ethyl ether
ETL	electron transporting layer
FET	field effect transport

Φ_f	quantum yield
FF	fill factor
$g_\perp$	g factor in the perpendicular direction to the magnetic field
$g_\parallel$	g factor in the perpendicular direction to the magnetic field
h	hole
HOMO	highest occupied molecular orbital
HTL	hole-transporting layer
ICT	intramolecular charge transfer
I_D	source to drain current
IP	ionization potential
IR	infrarred
I_{SC}	short circuit current
ITO	indium tin oxide
λ	wavelength
LC	liquid crystal
LCD	liquid crystal display
LE	locally excited state
LUMO	lowest unoccupied molecular orbital
μ	charge mobility
m.p.	melting point
MO	molecular orbital
OFET	organic field effect transistor
OLED	organic light emitting diode
OPV	organic photovoltaic
OTFT	organic thin film transistor
PCBM	[6,6]-phenyl-C61-butyric acid
PCZ	polycarbonate-Z
PDI	perylene diimide
PET	polyethylene
POM	polorized optical microscopy
PVK	poly(*N*-vinylcarbazole)
Θ	Weiss constant
S_0	singlet ground state
S_1	singlet first excited state
S_NAr	nucleophyl aromatic substitution
SOMO	semioccupied molecular orbital
T_1	triplet first excited state
TBAH	tetrabutylammonium hydroxide
TCB	1,3,5-tris(*N*-carbazolyl)benzene
T_g	glass transition temperature
TGA	termogravimetry analyses
THF	tetrahydrofurane
TNF	2,4,7-trinitrofluorenone
TOF	time-of-flight

t_t	transient time
TCNB	tetracyanobenzene
TIO	Titanium isopropoxide (IV)
TTF:TCNQ	tetrathiafulvalene: tetracyanoquinodimethane:
TTM	tris(2,4,6-trichlorophenyl)methyl radical
UV	ultraviolet
V_G	gate voltage
V_{OC}	open-circuit votage
VTE	vacuum thermal evaporation
XRD	X-ray diffraction
XTOF	xerographyc time-of-flight
Ψ_m	work function

List of publications

Scientific publications

Sonia Castellanos, Luis Juliá, Dolores Velasco, Valentas Gaidelis, Vygentas Jankauskas, Jouzas V. Grazulevicius, Enric Brillas, Francisco López-Calahorra **.Stable radical cores: a key for bipolar charge transport in glass forming carbazole and indole derivatives**. (in preparation)

Castellanos, S.; López-Calahorra, F.; Brillas, E.; Juliá, L.; Velasco, D. **All-organic discotic radical with a spin-carrying rigid-core showing intracolumnar interactions and multifunctional properties.** *Angew. Chem. Inter. Ed.* **2009**, 48, 6516-6519.

Castellanos, S.; Velasco, D.; López-Calahorra, F.; Brillas, E.; Julia, L. **Taking advantage of the radical character of tris(2,4,6-trichlorophenyl)methyl to synthesize new paramagnetic glassy molecular materials.** *J. Org. Chem.* **2008**, 73, 3759-3767.

Velasco, D.; Castellanos, S.; Lopez, M.; Lopez-Calahorra, F.; Brillas, E.; Julia, L. **Red organic light-emitting radical adducts of carbazole and tris(2,4,6-trichlorotriphenyl)methyl radical that exhibit high thermal stability and electrochemical amphotericity.** *J. Org. Chem.* **2007**, 72, 7523-7532.

Posters in conferences

New organic stable radicals bearing carbazole moieties with low band gaps and bipolar characteristics. D. Velasco, L. Julià, M. López, E. Brillas, S. Castellanos. *European Conference on Molecular Electronics 2009*, Copenhagen, September **2009**

Semioccupied molecular orbital in stable organic radicals as a key for OPV devices. Castellanos, S.; Della Pirriera, M. B.; Puigdollers J.; López-Calahorra, F.; Velasco, D.; Juliá, L. *International symposium on functional p-electron systems*, Georgia, May **2010** (accepted)

Novel N-phenylcarbazole derivatives with suitable redox and liquid crystalline properties for electronic devices. Castellanos, S.; Juliá, J.; López-Calahorra, F.; Velasco, D.; *International symposium on functional p-electron systems*, Georgia, May **2010** (accepted)

Patents

Radicales orgánicos como componentes semiconductores. Juliá, L.; Velasco, D.; Castellanos, S.; Puigdollers, J.; Alcubilla, R. **2009**, P200931217